Aeroelastic optimisation of composite plates using both deterministic and stochastic approaches

Mahshid Sharifi

Aeroelastic optimisation of composite plates using both deterministic and stochastic approaches

Mahshid Sharifi

Spécialité : Mécanique

École doctorale : SMAER ED391

Réalisé à
Institut Jean le Rond ∂'Alembert

Pour le grade de
Docteur de Sorbonne Université

Devant le jury composé de :

Marco Montemurro	Professeur, ENSAM	Rapporteur
Fabrice Thouverez	Professeur, Centrale de Lyon	Rapporteur
Paola Cinnella	Professeur, SU	Examinateur
Jean-François Deü	Professeur, CNAM	Examinateur
Olivier Montagnier	Enseignant-chercheur, CReA	Examinateur
Jean-Camille Chassaing	Professeur, SU	Directeur de thèse
Angela Vincenti	Professeur, SU	Co-directrice de thèse

Contents

List of Figures

List of Tables

Nomenclature

α_{swept}	Swept wing angle
$\boldsymbol{\kappa}$	CLPT curvature
$\boldsymbol{\varepsilon}$	CLPT in-plane strain
δW	Virtual work of the non-conservative forces
$\Delta\bar{p}$	Complex amplitude of the pressure distribution
γ	Rate of decay
$\hat{q}$	Amplitude of the structural modes
Λ	Stability margin
$\bar{\mathbf{H}}$	Matrix of the transversal modal displacement on the DLM grid
$\bar{\mathbf{u}}_z$	Vertical displacement on the DLM grid
$\hat{\mathbf{K}}$	Stiffness matrix
$\hat{\mathbf{M}}$	Mass matrix
$\boldsymbol{\Phi}$	Matrix of the structural mode shapes
AIC	Aerodynamic Influence Coefficient matrix
A	CLPT membrane stiffness matrix
$\mathbf{A}_{aero}$	Global aerodynamic matrix
$\mathbf{A}_{aero}^{I}$	Imaginary part of the aerodynamic matrix
$\mathbf{A}_{aero}^{R}$	Real part of the aerodynamic matrix

$\mathbf{B}$	CLPT membrane-bending coupling matrix
$\mathbf{C}$	CLPT homogeneity matrix
$\mathbf{c}_p$	Pressure coefficient vector
$\mathbf{D}$	CLPT bending stiffness matrix
$\mathbf{D}_{dw}$	Downwash factor matrix
$\mathbf{F_{ABD}}$	Kullback-Leibler function
$\mathbf{f}_{aero}$	Vector of the aerodynamic forces
$\mathbf{H_{dl}}$	Matrix of the transversal modal displacement at the doublet line in each panel
$\mathbf{H}$	Matrix of the transversal modal displacement on the finite-element grid
$\mathbf{K}$	Modal stiffness matrix
$\mathbf{M}$	Modal mass matrix
$\mathbf{m}$	CLPT bending moments
$\mathbf{n}$	CLPT membrane forces
$\mathbf{Q}$	CLPT base layer stiffness matrix
$\mathbf{q}$	Vector of generalised coordinates
$\mathbf{S}$	Matrix of surface values for each panel of the grid
$\mathbf{u}$	Vector of structural degrees of freedoms
$\mathbf{u}_z$	Vertical displacement on the finite-element grid
$\mathbf{w}^\star$	Vector of discrete dimensional downwash
$\mathbf{W}_{dw}$	Downwash complex matrix
$\mathbf{w}_{dw}$	Vector of discrete downwash
μ_Λ	Mean value of stability margin
μ_f	Mean value of flutter velocity
ν	Poisson's coefficient

ω	Aeroelastic frequency
ω_f	Flutter frequency
ω_s	Structural frequencies
Φ_0	Polar angle
Φ_1	Polar angle
ρ	Density of the plate material
ρ_a	Air density
σ_Λ	Standard deviation of stability margin
σ_f	Standard deviation of flutter velocity
θ	Ply angle
$\tilde{\mathbf{D}}$	CLPT modified bending stiffness matrix
b	Half chord of the wing
c	Chord of the wing
d	Total thickness of the plate
E	Elastic modulus
G	Shear modulus
g	Aeroelastic damping
K	Complex acceleration potential kernel
k_r	Modified reduced frequency
R_0	Anisotropic polar moduli
R_0^{BL}	Anisotropic polar moduli of the base layer
R_1	Anisotropic polar moduli
R_1^{BL}	Anisotropic polar moduli of the base layer
S	Half span of the wing

s	Aeroelastic eigenvalues
T	Kinetic energy
T_0	Isotropic polar moduli
T_1	Isotropic polar moduli
t_p	Ply thickness
U	Potential energy
V	Airspeed
V_d	Divergence velocity
V_f	Flutter velocity
V_{design}	Design velocity
w_{dw}	Dimensionless downwash
$\mathbf{u}_{zdl}$	Vertical displacement at the doublet line in each panel

Abstract

With the growing popularity of composite materials in aeronautics, study of the influence of their anisotropy on the aeroelastic behaviour of various structures is imminent. This type of study is referred to as aeroelastic tailoring which implies the variation of the composite structure properties in order to obtain the desired aeroelastic response. While there has been some work done in this field, the robustness of the methods used in order to deal with the anisotropy of the composite materials has not yet been at a satisfying level.

The first focus of this work is on reformulation of the aeroelastic optimisation problem, in order to achieve a faster convergence with more reliable control over the elastic properties of the final structure. For this purpose a 2-level optimisation method is presented during which a parametric formulation is employed for optimisation of the aeroelastic behaviour. The formulation is based on polar parameters which can describe the anisotropic behaviour of a given structure. The first level of the optimisation is conducted by the Genetic Algorithm. The second level study is then considered which is associated to the retrieval of a stacking sequence with 16 plies in this work that has identical properties as the optimal polar parameters.

Next, the tow-steered laminates with variable stiffnesses have been studied. This type of material can increase the rigidity of the structure and positively impact various static and dynamic responses of the latter. Using the polar parameters, the variation of the rigidity along the structure has been modelled and its aeroelastic behaviour has been optimised between $2 - 4\%$.

Finally, the stochastic response of the optimal case obtained during the deterministic optimisation process has been considered. The parametric uncertainties during the manufacturing of composite laminates can impact the aeroelastic response of the system. The parametric uncertainties have been included in the optimisation process resulting in a reliability-based design optimisation. The discontinuities present on the aeroelastic response surface render the approximation made by the surrogate model less accurate. The use of a continuous function called the stability margin is the solution to this discontinuity problem which helps with the computational time as well.

1 Introduction

Aeroelasticity can be defined as the discipline which studies phenomena caused by interaction of aerodynamic and elastic forces [1]. An illustration of interactions between these fields is given in the Collar's triangle presented in figure 1.1 in which the inertia is added to the two other forces in order to take into account the dynamics in each domain of study.

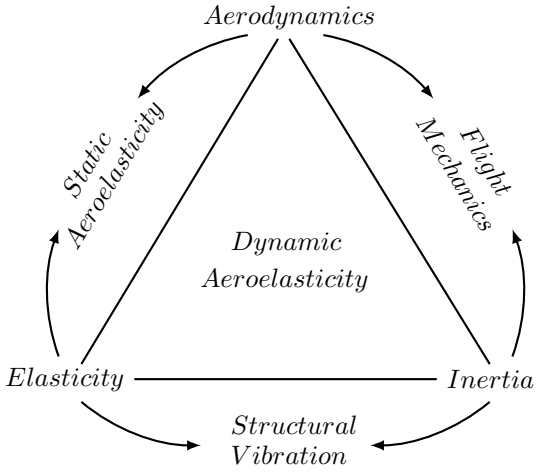

FIGURE 1.1: Collar's triangle of aeroelasticity [2].

Flight mechanics and structural vibrations are the classical dynamic studies conducted in fluids or structural domains. They respectively affect a fixed lifting surface and represent the free-structure dynamic response. Static aeroelasticity takes place when the aerodynamic forces and the structural deformations are mutually modifying one another. Phenomena such a divergence and control reversal can be fit into this category [3]. Dynamic aeroelasticity can occur when inertial effects play a crucial role on the aeroelastic response of the structure [4]. Flutter is the most common aeroelastic dynamic instability, that can be detected by running a linear analysis of the structure undergoing the aerodynamic loads. Buffeting, Limit Cycle Oscillation (LCO) which are non-linear phenomena and in general dynamic response of a structure to an aerodynamic loading such as gust or turbulence, also belong to this category.

Aeroelastic instabilities can be present in various domains, such as civil engineering (e.g., the destruction of the Tacoma bridge [5]), turbomachinery [6], wind turbines [7] or even design of Formula 1 racing cars [4]. Figure 1.2 shows the failure of the Tacoma bridge caused by torsional dominated flutter instabilities at low wind speeds of $16 - 19$ m/s.

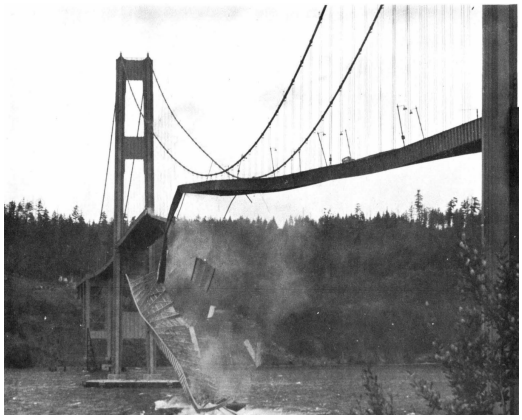

FIGURE 1.2: Collapse of Tacoma bridge due to flutter instabilities [8].

In this work, the main focus will remain in aeronautics and particularly on the flutter and divergence phenomena of simple lifting surfaces. Divergence soon became a subject of interest in aeronautical design after various incidents of the first airplanes took place in 1903 [9]. Langley had launched two powered flights in the course of that year including one, just a few days before the successful flight of the Wright brothers. Langley's last flight had failed due to torsional aeroelastic divergence and the airplane crashed in the Potomac river. Figure 1.3 shows the airplane before its crash and the torsional divergence of the rear wing. The success of Wright brothers is mainly related to the use of a warped wing which allowed them to have a better lateral control [1]. This type of wing was soon replaced by rigid ailerons as the period of biplane aircrafts ended.

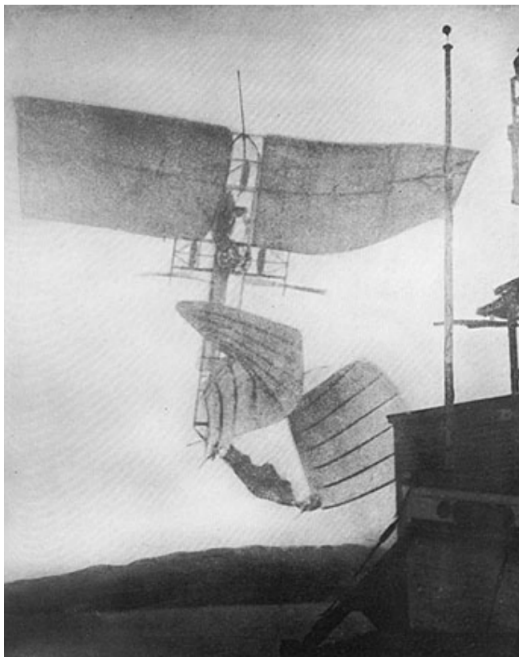

FIGURE 1.3: Incident of Langley airplane due to torsional divergence [10].

Given the presence of aeroelastic phenomena since early days of aviation, the first recorded incident took place in 1916 when the Handley-Page O/400 bomber was susceptible to a tail wing flutter [4]. A British scientist called Lanchester, with the help of Bairstow, conducted significant studies of the incident and recognised the out-of-phase oscillations of the wings as self-excited. As a measure to prevent this phenomenon, the elevators were designed with a stiffer connection [11, 12]. The latter design was also a solution to the tail flutter incidents of DH-9 airplanes in 1917 [13, 9]. It was only in the early 1930s, after an aileron reversal incident of a Bristol Bagshot, that Roxbee Cox and Pugsley at the Royal Aircraft Establishment proposed the name of Aeroelasticity to this discipline [1]. Another important step in this field was made by theoretical understanding of flutter mainly due to works of Glauert [14] and Theodorsen, who produced a report on flutter analysis of oscillating airfoils in 1934 [15].

The appearance of higher speed and larger aircrafts, resulted in new aeroelastic phenomena. Supersonic panel flutter was first observed on V-2 rocket during the war with over 70 failures [9, 16]. Similar phenomenon was repeated on the X-15 tail and side shells due to coupling between two bending modes of the plates [17]. Whirl flutter, an instability that takes place usually on a propeller of a nacelle engine was the cause of two major crashes of the Lockheed Electra [18, 19]. The instability was mainly due to a mount structure damage which required more stiffening of the mount system

[9]. Limit Cycle Oscillation (LCO) instabilities, which are famously present at the F-16 and F/A-18 fighters [20], can be interpreted as a bounded flutter [4] and they are observed on the wings, the stores and the lateral motion of the fuselage [21]. Another phenomena observed on the modern airplanes was the fin flutter. The latter caused the crash of the F-117 stealth aircraft due to flutter in control rudder shown in figure 1.4.

FIGURE 1.4: Failure of F-117 aircraft due to flutter [22].

Recent advances in aircraft design have given rise to new aeroelastic concerns. High aspect-ratio wings of drones and unmanned aerial vehicles have reports of crash due to aeroelastic instabilities. The Lockheed Martin X-56 unmanned vehicle presented some of these challenges due to its large flexible wings [23]. The High-Altitude Long Endurance flight technologies requires more innovative solutions to the possible occurrence of instabilities [24]. Figure 1.5 shows different states of the crash of the Nasa Helios drone. The data concerning the flight history, particularly near the pitch oscillations, on the wing dihedral, pitch rate and airspeed can be found in [25].

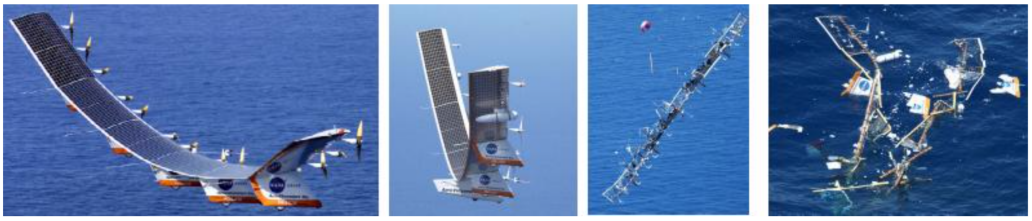

FIGURE 1.5: Crash of NASA Helios drone due to an unstable pitching mode [25].

One method amongst many others that has become more and more popular is the active flutter suppression [26]. This technology allows to overcome various instabilities that could take place throughout the flight regime.

1.1 Aeroelastic modelling

Various models have been developed to predict aeroelastic phenomena. The calculation of the response of the aeroelastic system can be carried out using analytical solutions or low-, medium- and high-fidelity numerical models. This classification is relevant to both aerodynamical and structural models. As the aeroelastic phenomena are the results of a coupled system, it is important to choose appropriate models for both structural and aerodynamic loads.

The aeroelastic studies generally begin with the free-vibration analysis of the structure [27, 28]. The latter can be done analytically for simple systems of limited number of degrees of freedom (also called *canonical models*) or using discretisation methods that are able to treat more complicated structural systems. One of the first *canonical models* was developed by Theodorsen [15] that studied a rigid wing section mounted on two springs (a linear and a torsional spring) and a flap, with pitch and plunge and rotating motions respectively. Nowadays, such configurations could be used as phenomenological models to deploy some methodological framework [29, 30, 31]. More advanced models were then employed for the modelling of the structural response such as beam models [32], panels [33] and plates [34, 35]. With improvements in the computer calculations, the structural models evolved towards the discretisation of continuous systems. Both Rayleigh-Ritz and the Finite-Element method have been employed in pure structural and aeroelastic analysis [36, 37]. The Finite-Element Method (FEM) has been more popular due to its systematic procedure and adaptability to complex geometries. Various models can be employed in the FEM, according to which would best adapt the configuration under study. Pastilha et al. [38] conducts flutter optimisation of three different structures (a circular beam, a thick plate and a flat panel) using the FEM. The beam and one of the plate configurations are subject to a non-conservative force only as an end load, and supersonic loads are applied to another plate structure. Modaress et al. [39] compare beam and plate models and their influence on the aeroelastic response of a cantilevered plate wings. Jutte et al. [40] conducted the aeroelastic optimisation of the Common Research Model (CRM) using a wing-box structure, of which they minimised the weight while maximising the flutter velocity.

The choice of an appropriate aerodynamic model is necessary for the aeroelastic analysis. These models can be chosen depending on the flow conditions in which the structure is under study. The first aeroelastic analysis were conducted with the help of analytical models. Wagner [41] introduced a model which describes the lift loads in an incompressible flow. A few years later, Theodorsen [15] presented the frequency response of these unsteady loads using a Laplace transformation, following the work of Jones [42]. The history of the evolution of analytical methods for the aerodynamics is explained in details in the work of Shams et al. [43], where the Wagner function application is compared

to the Theodorsen and Peters' [44] models. Similarly to the structural methods, the aerodynamic modelling has been influenced by increasing developments in computers. The numerical methods with different levels of accuracy have been applied to predict aeroelastic phenomena. The Doublet Lattice Method (DLM) is one of the most common aerodynamic models in aeroelastic analysis. It is considered as a medium-fidelity model, which has a higher computational cost compared to the unsteady analytical methods stated before, but it has a higher accuracy which makes it a desirable candidate for preliminary design calculations or optimisation studies needing multiple calls to the main solver. It was first introduced by Albano and Rodden [45] and later used in flutter analysis of various structures, mainly beams and plates [46, 47]. The latter is based on linearised potential theory and has the capacity to predict aerodynamic forces from incompressible to subsonic regimes. This method only considers the out-of-plane forces and motions which renders this model a less suitable candidate for more complex geometries [48]. For this type of problem, the Unsteady Vortex Lattice Method (UVLM) was introduced, which while assuming in-plane dynamics, has a sufficiently low computational cost to replace DLM for geometries such as flexible wings [49], tail wings [50] and wind turbines [51]. Eventually, with the increase in computational capacities, high-fidelity CFD models were employed to carry out the aerodynamic forces. These models are more often used in more complicated systems such as transonic regimes [52], high aspect ratio wings [53] or turbulent flows [54].

While these methods have higher accuracy, their computational cost is very high, particularly in an iterative framework such as optimisation. For this reason various methods have been developed in order to reduce the computational time. Beran et al. [55] used Reduced Order Modelling (ROM) to predict LCO instabilities. They reduced the order of both fluid and structural models using proper orthogonal decomposition and Galerkin approximation respectively. Another method applied to reduce the computational cost of high fidelity models consists on multi-fidelity design. The latter can be interpreted in different manner but it is mainly based on employing at least two models of different fidelities. This methods is mostly used to correct aerodynamic forces described by DLM using a high fidelity model such as Navier-Stokes or Euler. Thelen et al. [56] employed a cokriging-based surrogate model to approximate the Aerodynamic Influence Coefficient matrix using samples generated by the Euler and DLM modes.

Finally, the aeroelastic analysis can be conducted by coupling both structural and aerodynamic models in a time or frequency domain. The latter significantly simplifies the procedure to detect aeroelastic instabilities, it is therefore the more common method employed in a linear framework. Amongst different methods in the frequency domain, the k and p-k method are the most common solvers for prediction of flutter and divergence instabilities. The k method was first introduced by Scanlan and Rosenbaum [57] and later employed frequently in the prediction of flutter instabilities

[1, 13]. The p-k method was initially introduced by Hassig [58] in order to challenge the accuracy of the k method. He gave a better approximation of the aeroelastic damping while considering harmonic aerodynamic forces. Later Rodden [59] modified the formulation of p-k method to better represent the non-harmonic aerodynamic forces. This method is one of the most popular solvers in aeroelastic analysis [60, 61]. There have been variations over this method, for example in the work of Borglund [62] who employed the μ-k method in order to take into account aerodynamic uncertainties, or the non-iterative p-k method proposed by Pitt [63] to reduce the computational time of the aeroelastic computation.

1.2 Composite materials in aeroelasticity

One predominant part of new aircraft designs is represented by the composite materials, due to their light weight and high strength. They have been employed in various parts of the modern airplanes, since the 1960s until today, where up to 50% of the Boeing 787 (Dreamliner) consists of composite materials. They are present in many structural parts of an airplane, from wings, to the fuselage as well as engine parts. Apart from airplanes, the Unmanned Aerial Vehicle (UAV), rotorcraft or wind turbines are also hugely impacted by composite materials [64].

There are various types of composite structure mainly made of a matrix and fibres, which are used to reinforce the rigidity of the material. Each component could be made of different materials depending on the purpose of the application. In this study, composites made of multiple layers, presented in figure 1.6, are taken into account, i.e. composite laminated structures. Each layer is composed of fibres whose path can significantly impact the behaviour of the structure [65].

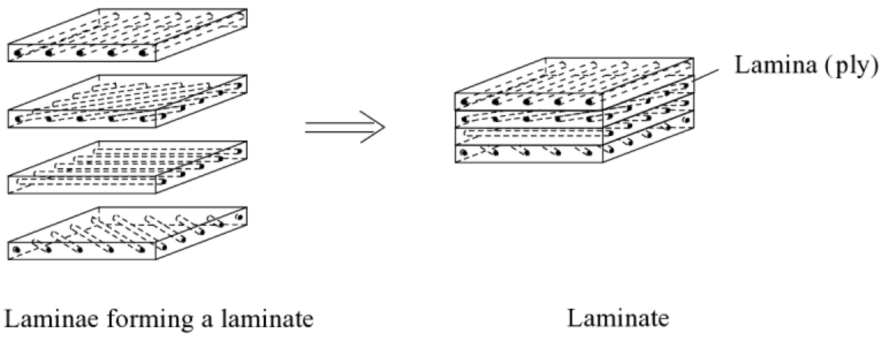

Figure 1.6: Illustration of composite plate made of Uni-Directional fibre paths [65].

One of the most simple methods to model composite structures is the Classical Laminated Plate Theory (CLPT), which is based on the Kirchhoff theory [66] and it is essentially a homogenised representation of the elastic properties of a composite laminated plate. Despite its simplicity, CLPT reveals to be effective in representing the global response of composite structures and, as such, it is widely used in works dealing with their design and optimisation. The study of the aeroelastic response of composite structures makes no exception. Lin et al. [67] have employed CLPT to model composite structures and studied the influence of composite ply angles, elastic and geometrical properties on structural and aeroelastic response of a composite plate in subsonic flow. Mahran et al. [68] studied the impact of different finite element shell models on the elastic and aeroelastic response of a plate wing and modelled the composite laminates using CLPT. Besides the necessary conditions to apply the CLPT method [66], the thickness of the plate plays an important part to neglect the effects of shear deformation. The latter is thus applied in many structural and aeroelastic studies dealing with thin laminate plates [60, 69].

In order to carry out studies using structures with non-negligible thicknesses, structural models which take into account shear deformations are employed. Koo et al. [70] studied the impact of structural damping and ply orientations on the aeroelastic response of three different geometries. They have used the First-order Shear Deformation Theory (FSDT) to model the structure of the composite laminate. Karpouzian et al. [71] studied the flutter and divergence response of a swept wing and analysed the influence of various structural effects such as anisotropy and transverse shear with the help of FSDT. While the FSDT is able to take into account the effects of the shear deformation, it does not show satisfying results in case of laminates with moderately higher thicknesses. Kapania et al.[72] discussed various methods for modelling laminate plates or beams and explained the analysis of buckling and post-buckling behaviour using Higher-order Shear Deformation Theory (HSDT). Chattopadhyay et al. [73] employed HSDT to study the aeroelastic and structural response of a composite wing box. Patil et al. [74] conducted an aeroelastic analysis of high aspect ratio wing which was modelled using the box beam with the help of HSDT.

In the late 1970s, the complexity of the anisotropic behaviour of composite materials resulted in the introduction of some parametric formulations. Tsai and Hahn [75] proposed a representation of composite materials called the *lamination parameters*. Another set of parameters were introduced by Verchery [76] which are called the *polar parameters*. *Lamination parameters* are issued from the application to the CLPT of the representation of plane anisotropic elasticity based on Tsai-Pagano parameters [77]: the latter are invariant quantities [1], obtained by trigonometric manipulations of the

[1] To be precise, not all Tsai-Pagano parameters are invariants, since one of them depends on the orientation of the reference frame [77]

Cartesian tensor components, even if they do not correspond to a proper tensorial decomposition. On the contrary, the *polar parameters* are proper tensor invariants and they can be expressed for plane tensors of any order and symmetry, and particularly for the tensors of plane elasticity representing the behaviours of a composite lamina or a laminate. On one hand, the invariant quality of these parametrisation is very helpful when dealing with the representation of plane anisotropy, compared to the cumbersome transformation rules of the Cartesian components of anisotropic tensors. Additionally, when applied to the CLPT, both parametrisation allow to reduce the number of independent variables for the description of the anisotropic response of a composite laminated plate. This is the reason why these invariants are good candidates to be used in the optimisation studies of the composite materials. Meanwhile, the lamination parameters have remained more popular in aeroelasticity as used by Kameyama et al. [60] to minimise the weight design of a composite laminate while considering aeroelastic critical velocities as constraints of the optimisation problem. Scarth et al. [69] investigated the influence of uncertainties over the ply angles on the critical velocity of a cantilevered plate wing and have employed lamination parameters to reduce the number of uncertain parameters. Nitschke et al. [29] explored this study further by considering uncertainties over ply angles and thicknesses. They used polar parameters as a tool to deal with the dimensionality of the problem and hence could consider non-symmetric and uncoupled laminates which provide a more global coverage of the anisotropic domain.

The works mentioned above are mainly focused on Uniform-Stiffness (US) composite laminates with Uni-Directional (UD) fibre paths. With the advances in the manufacturing processes, the production of composite structures is no longer restricted to the conventional laminates. Methods such as automatic fibre placement (AFP) allow placement of the fibre in curvilinear paths and therefore production of composites with Variable-Stiffness (VS) such as laminates with Tow-Steered (TS) fibres [78, 79, 80]. Figure 1.7 presents a simple illustration of the two above mentioned laminates.

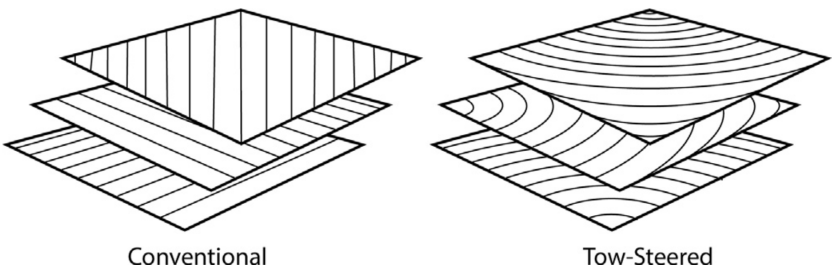

Figure 1.7: Illustration of laminates with Uni-Directional and Tow-Steered fibre paths [81].

There are many studies conducted in the structural domain using Tow-Steered laminates. Viglietti et al. [82] studied the influence of the variable angle-tow composites on the dynamic response of two structural model (beam model and a complex wing box). Pereira et al. [83] used Tow-Steered (TS) composites to conduct a multi-objective optimisation on the modal frequency and the corresponding damping. Montemurro et al. [84, 79] optimised the first buckling factor of a Tow-Steered (TS) composite laminate using polar parameters as the optimisation variables to model these types of structures. These materials have been also investigated in the aeroelasticity domain. Stodieck et al. [85] studied the influence of the tow steered laminates on the elastic axis, divergence and flutter speed and gust loads. Haddadpour et al. [86] conducted the optimisation of the aeroelastic behaviour (maximisation of the critical velocity) of a TS composite wing modelled as thin-walled beams. Guimarães et al.[87] studied TS laminates and optimised the aeroelastic and the buckling behaviours of these structures. Brooks et al. [88] compare TS and the conventional US composites by modifying the aero-structural configuration to minimise the fuel consumption.

While most studies work directly with the orientation of the fibres as design or optimisation variables, some works have been conducted using multi-scale multi-level optimisation strategies. These studies mainly focus on a first level study optimising the stiffness properties (macroscopic scale) of the structure using a parametric formulation and a second level optimisation in order to retrieve the fibre path (mesoscopic scale) on each layer. These methods are employed in both Uniform-Stiffness and Variable-Stiffness composite laminates. Setoodeh et al. [89] used lamination parameters to model Uniform- and Variable-Stiffness laminates using a 2-level strategy. Montemurro et al. [90, 91] optimised the weight design of a wing box with a 2-level procedure using polar parameters. Similar studies are carried out for the Tow-Steered fibre paths where the parametric formulation are used to describe the variation of the rigidity [79, 92, 93].

1.3 Uncertainty quantification

Uncertainties can be divided in two categories: aleatory uncertainties, which are inherent to the system and cannot be improved, and epistemic uncertainties that are due to the lack of knowledge and can thus be reduced. The latter can rise from uncertainties in the mathematical or numerical models used to describe the physics of a phenomenon [30]. This work deals with aleatory uncertainties which are due to errors on the system parameters and have to be taken into account by conducting a probabilistic study. The simplest and the most common method of uncertainty propagation is Monte Carlo, which requires a given number of samples in the space of random variables. The main algorithm is then run for each sample to obtain the distribution of the objective function. This type of approach to obtain the probabilistic response of a function is called the direct method as there is no intermediate

step between the sampling and the final stochastic result. The uncertainty propagation of a random variable in a CFD model is shown in figure 1.8. Other sampling methods such as Latin Hypercube Sampling (LHS) or Quasi-Monte Carlo (QMC) produce more uniforme samples over a given space and can insure a faster convergence rate. Kucherenko et al. [94] compared the efficiency of the mentioned sampling methods in different test cases.

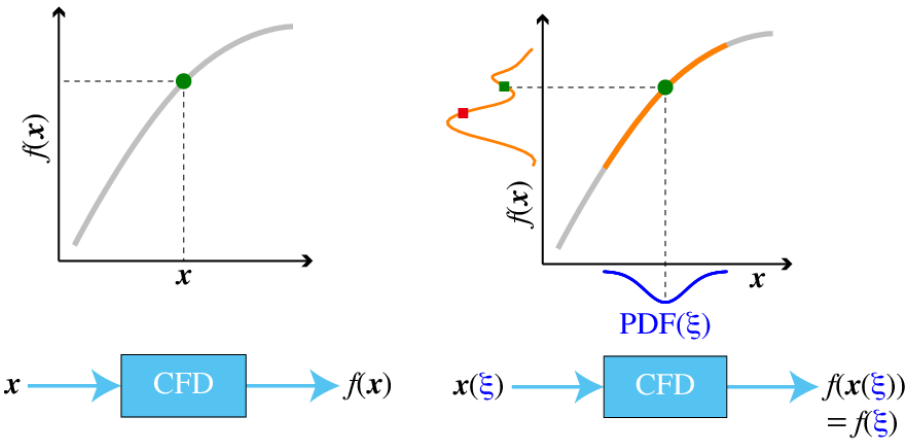

Figure 1.8: Illustration of uncertainty quantification over a CFD model with random variables [95].

The direct method can be computationally expensive particularly while using a costly algorithm for the simulation of the objective function. For this reason, surrogate models are often used to reduce the computational time, as they require smaller number of direct runs of the algorithm. Polynomial chaos is a surrogate model which appeared first in [96]. Xiu et al. [97] employed the polynomial chaos using the Askey scheme, as a generalisation of the method proposed in [96], to predict the solution of the Poisson equation. These works have remained methodological but numerous studies have employed surrogate modelling to approximate the aeroelastic response of a composite structure undergoing uncertainties over its material or geometric properties, fibre orientations, ply thicknesses and other impactful variables. Manan et al. [98] used polynomial chaos to study the stochastic aeroealstic response of a structure while considering uncertainties over the material properties, ply angles and thicknesses. Murugan et al. [99] used a high-dimensional model representation to study the effect of stiffness property uncertainties on the aeroealstic behaviour of helicopter rotors. Scarth et al. [31] approximate the aeroelastic eigenvalues with the help of Gaussian Process Regression during an optimisation process. They had also employed the same method to approximate the critical flutter or divergence instabilities speed in comparison of two different types of optimisation formulations [100].

While surrogate modelling can be helpful to reduce the computational time, working with a large number of uncertain parameters can give place to problems such as the curse of dimensionality. As mentioned previously, one of the important parametric uncertainties, present during the manufacturing of the composite structure, concerns the orientation of the ply angles. Consequently, the number of uncertain parameters grows with the layers of the laminate and cause a convergence issue due to the dimensionality of the problem. It can thus be hard to study a more realistic configuration with several layers while using a surrogate model. The parametric formulations based on *lamination parameters* or on the *polar formalism* reveal to be useful in this aspect, since they allow to limit the study of the uncertain aeroelastic response with respect to a small number of parameters independently from the number layers in the stack.

The critical velocity of the aeroelastic system, which is the indicator of the stability of the structure, is a discontinuous function of the polar or lamination parameters and hence cannot be approximated accurately by surrogate models. Multiple studies have been conducted to overcome this drawback to accurately emulate discontinuous functions using surrogate modelling. Nitschke et al. [29] used Multi Layer Perceptron Classifier to cluster the regions separated by the discontinuity and approximate each region separately using polynomial chaos. Chassaing et al. [101] used a piecewise polynomial chaos to approximate the limite cycle oscillations of a two-dimensional airfoil under uncertainties in structural properties. Becker et al. [102] carried out a sensitivity analysis of bifurcating systems using an extension of Gaussian process using a decision tree to partition the input space.

1.4 Optimisation of composite structures

The growing use of composite materials in aeronautical structures introduces some complexity, such as anisotropy and couplings, but also the freedome to explore their wide design domain, resulting from the combination of multiple material and geometric parameters (orientation angles, thicknesses, elastic properties of the base material of layers in a laminated structure). These properties can be optimised and adjusted to the required purpose in different applications which leads to the a domain of study called *tailoring*. The primary works on these materials were carried out in the structural domain, such as free vibration and buckling analysis [103, 104, 105, 106]. The tailoring of composite materials were then developed to optimise different aspects using its anisotropic properties [107, 108, 109]. Similar studies were then conducted in the aeroelasticity domain which are referred to as aeroelastic tailoring [110, 111, 112, 113]. The main objective is to optimise the aeroelastic response of the structure while taking into account its geometrical and physical aspects. Guo et al. [114] studied the influence of the geometry and the mass distribution on the aeroelastic response and used different optimisation

algorithms for this purpose. In another study, they have conducted a multi objective optimisation to minimise the weight as well as the gust response of the wing [115]. Attaran et al. [116] maximised the flutter velocity of a plate wing by variation of the fibre orientations, the swept angle and the aspect ratio of the structure. Albeit these studies lead to interesting results, they were generally limited to a few number of plies as the optimisation variables were considered to be the fibre orientations within composite laminates.

In order to conduct the optimisation problem, multiple formulations and algorithms can be employed. Some studies use lamination parameters to create a convex surface to be able to use gradient methods directly [117, 92] while other works use meta-heuristic optimisation methods to investigate the non-convex domain. There are multiple works devoted to the comparison of different optimisation algorithms. Muc et al. [118] did a review paper on several optimisation formulation and methods for aeroelastic problems. Manan et al. [119] compared four meta-heuristic optimisation algorithms based on biologically inspired methods with aeroelastic critical speed as the objective function. Ghiasi et al. [120, 121] studied various optimisation algorithms that are gradient-based or direct methods and different optimisation formulations in both uniform-stiffness and variable stiffness frameworks. Each work has argued the advantages and the disadvantages of the tested methods and provided a summary on various criteria such as convergence, simplicity and performance of the algorithm. In the present work, the Genetic Algorithm (GA) is employed which is a meta-heuristic optimisation method [112, 122, 123, 124]. It is a popular algorithm in the field of composite tailoring as the domain of investigation is extremely non-convex, however, this method can become very costly due to the wide domain of variables specially when working with high number of layers. Multiple studies have tried different strategies of formulation of the optimisation problem in order to decrease the computational cost by reducing the design space and simplifying the investigation. The original approach is the optimisation of the layer angles which are directly used as the optimisation variables. This leads to highly non-convex optimisation problems, which can be more efficiently solved when the number of optimisation variables is limited: many works in this domain are limited to consider a small number of plies and/or a small number of admissible orientation angles [125, 126, 127, 128]. In some works, only a subset of plies having the greatest impact on the laminate behaviour are considered in the optimisation process [129, 130]. Alternatively, multi-scale approaches have been developed since the early 2000s, either based on the polar formalism or on lamination parameters [131, 92, 132].

Most aeroelastic tailoring studies conduct *deterministic optimisation* of the composite laminate i.e. no uncertainty is considered on the constitutive parameters of the laminate (material or geometric properties, such as orientation angles and thicknesses). However, the construction of these structures

can be the source of multiple aleatory uncertainties such as errors over the ply angles and ply thicknesses. These variations in the laminate configuration can have large impacts on various behaviours of a structure, namely, its aeroelastic response. It is thus necessary to take into account the associated risks and the failure probability of a structure under study by conducting a *stochastic optimisation* in which the probabilistic response of the system is considered as the objective function. Surrogate models can be very helpful in this type of studies with large iterations, in order to reduce the computational cost. The stochastic optimisation can be conducted in different manners such as using the mean and variance of a parameter which leads to robust optimisation. Nikbay et al. [133] conducted a study to obtain an optimised configuration of a composite wing with a robustness criterion on the flutter velocity. Reliability-Based Design Optimisation (RBDO) is another method which controls that probability of failure remains under a given threshold. A common method of reliability optimisation is the First Order Reliability Method which approximates the most probable points on the failure surface [134, 135, 136]. Other methods using surrogate models have been employed for reliability optimisation such as Manan and Cooper [98] who used polynomial chaos to approximate the flutter velocity of a composite plate wing in an optimisation process. Scarth et al. [31] conducted a RBDO to reduce the probability of failure of a composite structure at a given velocity. Othman et al.[137] studied a 2-level optimisation problem of a wing box to minimise the weight subject to multiple probabilistic constraints both with robust and reliability nature. A comparison between these two formulations was conducted by Scarth et al. [100] using the critical aeroelastic speed as the objective function.

1.5 Thesis Layout

This work aims to address the aeroelastic optimisation of composite structures both in deterministic and stochastic framework. For this purpose, the aeroelastic model had to be first put in place. This implies a choice of different models to represent the structural response as well as the aerodynamic loads, in order to build the coupled aeroelastic system, that are explained in details in chapter 2. The structural stiffness matrix was obtained as a result of modelling the composite material using the CLPT and the Finite Element Method (FEM) was then employed for modal analysis of the structure under study. The aerodynamic forces were then computed using the Doublet Lattice Method (DLM). Finally, the aeroelastic approach used in order to solve the eigenvalue problem of the aeroelastic system is the p-k method [59]. The aforementioned model is then validated using data from the literature with both numerical and experimental results. The polar formalism is also explained at the end of chapter 2, which will then be used in the optimisation studies presented in the next chapters.

Chapter 3 presents the results of deterministic optimisations for Uniform-Stiffness (US) laminates with Uni-Directional (UD) plies. Different formulations are first compared in a fully anisotropic domain in order to conclude over the type of parameters to consider during the optimisation problem. The domain of investigation is then restrained to orthotropic laminates. Three different geometries are examined and their aeroelastic response are compared to one another.

The deterministic optimisation of these three geometries in the orthotropic domain is then extended in chapter 4 to Variable-Stiffness (VS) laminates constructed using the Tow-Steered fibre paths. Two different strategies are examined using different variations of the polar parameters [84]. The latter allowed a more targeted investigation of the orthotropic domain and the influence on the aeroelastic response of the composite structure.

Chapter 5 conducts a stochastic analysis of the entire optimal cases obtained during the deterministic optimisation. The parametric uncertainty considered in this study is the randomness over the ply angles. As the optimisation variables for both uniform and variable stiffness laminates were the polar parameters, an intermediate step is necessary to retrieve the corresponding stacking sequence. This steps allows an uncertainty propagation over the orientation of each ply.

Chapter 6 studies the aeroelastic stochastic optimisation of composite laminate with Uniform-Stiffness (US). More particularly, the objective function of this optimisation problem is the probabilistic response of the geometry under study. This process has a very high computational cost which calls for the use of surrogate modelling. As the results of approximations done by these models in a discontinuous surface are inaccurate, a new variable has been employed which is a continuous function of the material properties.

Finally, chapter 7 draws some conclusion on the entirety of the work and the results presented in the previous chapters. Subsequently, a few perspectives to the continuity of this work are introduced.

2

Numerical Modelling

The main subject of study in this work is the aeroelastic behaviour of a composite plate wing. All the results obtained are carried out using the same structural and aerodynamic models. The Finite Element Method (FEM) is used to describe the structural behaviour, the Doublet Lattice Method (DLM) models the unsteady aerodynamic forces in an incompressible flow and finally the p-k method is employed to carry out the aeroelastic response of the system. Each of these models is described in details throughout this chapter and comparisons with other studies in the literature are carried out as a validation step.

One of the peculiar aspects of this work is the use of an efficient parametric formulation for the representation of the elastic properties of composite laminates: polar parameters are presented at the end of the chapter. This formulation is necessary throughout the entire study as it is employed during the optimisation process and the uncertainty propagation. Various methods to obtain the stacking sequences corresponding to a set of polar parameters are described. These methods can be both analytical or numerical and are detailed in last section of the chapter.

2.1 Aeroelastic Problem

In this work, a 16-layer composite laminated plate is studied. It is a very common research case in the literature [85, 69]. Figure 2.1 represents the scheme of a similar configuration and its different geometrical parameters

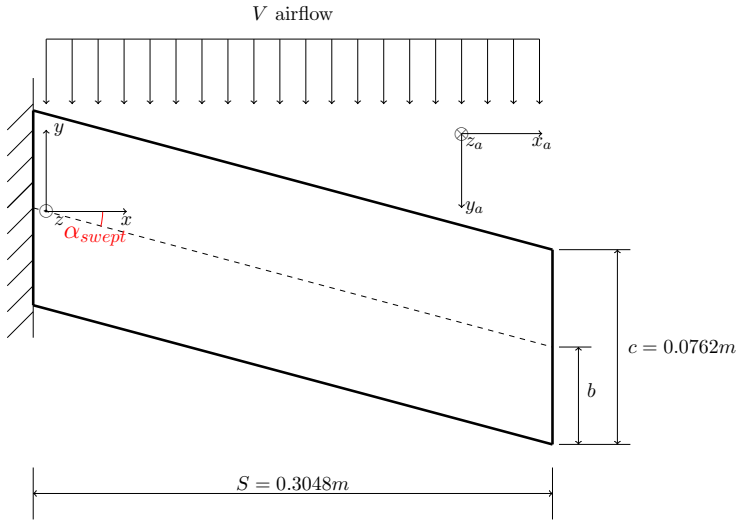

FIGURE 2.1: Representation of the reference swept-backward wing.

where S represents the half span, c the chord, and b the half chord of the wing. The reference axis placed in the mid-chord is the x axis which is also the reference axis of the fibre direction for the composite configurations, the y axis corresponds to the structural coordinate and the z axis has an upward direction. The air-flow with velocity V is aligned with the y_a axis and the z_a axis has a downward direction. The x and the x_a axis are aligned in both structural and aerodynamic coordinates. It needs to be pointed out that the entire representations in this study are placed in structural coordinates. The values considered for geometrical parameters during this study are indicated in figure 2.1. The air density is associated to the sea level for all the cases which is equal to $\rho_a = 1.225\,[kg/m^3]$.

2.1.1 Aeroelastic model

Classical Laminated Plate Theory (CLPT) has been employed to model the composite structure [138]

$$\begin{bmatrix} \mathbf{n} \\ \mathbf{m} \end{bmatrix} = \begin{bmatrix} \mathbf{A} & \mathbf{B} \\ \mathbf{B} & \mathbf{D} \end{bmatrix} \begin{bmatrix} \boldsymbol{\varepsilon} \\ \boldsymbol{\kappa} \end{bmatrix} \tag{2.1}$$

where $\mathbf{n}$ and $\mathbf{m}$ represent the membrane forces and bending moments, $\mathbf{A}$ is the membrane stiffness, $\mathbf{D}$ the bending stiffness, $\mathbf{B}$ describes the coupling between the membrane and the bending effects, $\boldsymbol{\kappa}$

and $\boldsymbol{\varepsilon}_0$ are the curvature and the in-plane strain, respectively, related to the mid-plane of the plate. These two deformation tensors are defined by means of the mid-plane displacement field (components $u_x(x,y)$, $u_y(x,y)$, $u_z(x,y)$ in the (x,y,z) Cartesian reference frame) and read

$$\boldsymbol{\kappa} = \begin{pmatrix} -\frac{\partial^2 u_z}{\partial x^2} \\ -\frac{\partial^2 u_z}{\partial y^2} \\ -2\frac{\partial^2 u_z}{\partial x \partial y} \end{pmatrix} \qquad \boldsymbol{\varepsilon}_0 = \begin{pmatrix} \frac{\partial u_x}{\partial x} \\ \frac{\partial u_y}{\partial y} \\ \frac{\partial u_x}{\partial y} + \frac{\partial u_z}{\partial x} \end{pmatrix} \tag{2.2}$$

The deformation of a given point on the plate, at coordinates (x,y,z), can thus be defined as

$$\boldsymbol{\varepsilon} = \boldsymbol{\varepsilon}_0 + z.\boldsymbol{\kappa} \tag{2.3}$$

which helps to define the plate stress as

$$\boldsymbol{\sigma} = \mathbf{Q}'(z)\boldsymbol{\varepsilon} = \begin{bmatrix} Q'_{11} & Q'_{12} & 0 \\ Q'_{12} & Q'_{22} & 0 \\ 0 & 0 & Q'_{66} \end{bmatrix} \begin{bmatrix} \varepsilon_1 \\ \varepsilon_2 \\ \varepsilon_3 \end{bmatrix} \tag{2.4}$$

where $\mathbf{Q}'(z) = \mathbf{Q}(\delta z)$ is the reduced tensor that contains the local elastic properties of the composite material under plane stress hypothesis. Supposing the plate made of a given orthotropic composite material, tensor $\mathbf{Q}$ in the local orthotropy axes reads

$$\mathbf{Q} = \begin{bmatrix} \frac{E_1}{1-\nu_{12}\nu_{21}} & \frac{E_2\nu_{12}}{1-\nu_{12}\nu_{21}} & 0 \\ \frac{E_2\nu_{12}}{1-\nu_{12}\nu_{21}} & \frac{E_2}{1-\nu_{12}\nu_{21}} & 0 \\ 0 & 0 & G_{12} \end{bmatrix} \tag{2.5}$$

where E_1 and E_2 are the Young's moduli in the orthotropy axes, G_{12} the shear modulus and ν_{12} the Poisson's coefficient.

The membrane forces $\mathbf{n}$ and bending moments $\mathbf{m}$ can be obtained by integrating the stresses and their moments over the total thickness of the composite plate

$$\boldsymbol{n} = \int_{-h/2}^{h/2} \boldsymbol{\sigma} \quad dz \qquad \boldsymbol{m} = \int_{-h/2}^{h/2} \boldsymbol{\sigma} z \quad dz \tag{2.6}$$

In the case under study in this work, pure bending condition is considered which implies neglecting the membrane forces ($\mathbf{n} = 0$). This condition simplifies the equation (2.1) so that the plate behaviour

is resumed by the following equation

$$\mathbf{m} = \left(\mathbf{D} - \mathbf{B}\mathbf{A}^{-1}\mathbf{B}\right)\boldsymbol{\kappa} \tag{2.7}$$

where the elastic response of the plate depends on the modified bending stiffness matrix ($\tilde{\mathbf{D}}$) [139]

$$\tilde{\mathbf{D}} = \mathbf{D} - \mathbf{B}\mathbf{A}^{-1}\mathbf{B} \tag{2.8}$$

Tensor $\tilde{\mathbf{D}}$ is a non-linear combination of the elastic tensors of the laminate, $\mathbf{A}$, $\mathbf{B}$ and $\mathbf{D}$, thus it can express the behaviour of coupled and non-symmetric stacking sequences. It needs to be noted that in the case of uncoupling ($\mathbf{B} = 0$), the second term of the modified bending stiffness is zero and $\tilde{\mathbf{D}}$ is equal to the bending stiffness tensor $\mathbf{D}$.

The dynamic equation of the coupled motion describing the aeroelastic system is obtained by the Lagrange equation

$$\frac{d}{dt}\frac{\partial T}{\partial \dot{\mathbf{q}}} - \frac{\partial T}{\partial \mathbf{q}} + \frac{\partial U}{\partial \mathbf{q}} = \frac{\partial(\delta W)}{\partial(\delta \mathbf{q})} \tag{2.9}$$

where T represents the kinetic energy, U the elastic potential energy, δW the virtual work of the non-conservative forces and $\mathbf{q}$ the vector of generalised coordinates. It needs to be noted that the kinetic and the potential energies are associated to the structure while the virtual work is obtained by the non-conservative aerodynamic forces. The elastic potential energy induced by the bending load reads [140]

$$U = \frac{1}{2}\int\int \mathbf{m}^{\mathsf{T}}\boldsymbol{\kappa} dxdy = \frac{1}{2}\int\int \boldsymbol{\kappa}^{\mathsf{T}}\tilde{\mathbf{D}}\boldsymbol{\kappa} dxdy \tag{2.10}$$

The kinetic energy T, while neglecting the in-plane velocities, is expressed as [85]

$$T = \frac{1}{2}\rho d\int\int \dot{u_z}^2 dxdy \tag{2.11}$$

where ρ represents the density of the material, d is the total thickness of the structure and the dot above the transversal displacement u_z is the derivative with respect to time. Using a discretised approximation method to express the energy and work terms, the above dynamic equilibrium equations (2.9) can be reformulated as

$$\mathbf{M}\ddot{\mathbf{u}} + \mathbf{K}\mathbf{u} = \mathbf{f}_{aero} \tag{2.12}$$

where $\mathbf{u} \in \mathbb{R}^{N_{dof}}$ is the vector of structural degrees of freedoms, $\mathbf{M} \in \mathbb{R}^{N_{dof} \times N_{dof}}$ the mass matrix,

$\mathbf{K} \in \mathbb{R}^{N_{dof} \times N_{dof}}$ the stiffness matrix and $\mathbf{f_{aero}}$ is the vector of the aerodynamic forces that depend on the structural movements. In the present work, the structural response is approximated using a finite-element approach, based on a Reissner-Mindlin model, as shown in [141], whilst the aerodynamic forces are represented using a DLM approach, which will be detailed in section 2.1.2. The vector $\mathbf{u}$ of structural degrees of freedoms can be expressed using the mode shapes of the structure $\mathbf{\Phi} = \left[\phi_1, ..., \phi_{N_{modes}}\right]$, $\mathbf{\Phi} \in \mathbb{R}^{N_{dof} \times N_{modes}}$ and the vector of the principal coordinates (or amplitudes) $\mathbf{q} \in \mathbb{R}^{N_{modes}}$

$$\mathbf{u} = \mathbf{\Phi}(\mathbf{x})\mathbf{q}(t) \tag{2.13}$$

thus separating the space (eigenmodes) and time (amplitudes) coordinates, as it is classically done in the mode projection methods in linear structural dynamics.

In this work, a Finite Element Method, based on the Python library FeniCs [142, 143] has been employed to compute the structural mode shapes $\mathbf{\Phi}$ of the composite laminate. The Reissner-Mindlin model has been used whose results in this case are equivalent to the Kirchhoff-Love plate theory due to the small thickness of the plate wing. Shell elements are considered due to their adaptability to thin structures. In order to discretise and approximate the system, unstructured quadratic triangular elements are chosen. Each node has 3 degrees of freedom: the transversal displacement u_z and two rotations θ_x, θ_y. It needs to be noted that according to a convergence study for the present case, the number of modes considered is $N_{modes} = 8$ and the total number of finite element nodes count $N_{node} = 617$ which with three degree of freedom per node results in $N_{dof} = 1851$.

Inserting equation (2.13) in the aeroelastic dynamic equilibrium equation (2.12) and multiplying by the transpose of the mode shapes matrix $\mathbf{\Phi}^T$, the modal form of the equation of motion (2.12) is obtained

$$\mathbf{\Phi}^T\mathbf{M}\mathbf{\Phi}\ddot{\mathbf{q}} + \mathbf{\Phi}^T\mathbf{K}\mathbf{\Phi}\mathbf{q} = \mathbf{\Phi}^T\mathbf{f}_{aero} \tag{2.14}$$

It needs to be noted that it is a common practice to neglect the structural damping in this type of study due to its small contribution to the system [3]. Introducing the modal mass matrix and the modal stiffness matrix presented by $\hat{\mathbf{M}} = \mathbf{\Phi}^T\mathbf{M}\mathbf{\Phi} \in \mathbb{R}^{N_{modes} \times N_{modes}}$ and $\hat{\mathbf{K}} = \mathbf{\Phi}^T\mathbf{K}\mathbf{\Phi} \in \mathbb{R}^{N_{modes} \times N_{modes}}$, the generalised aeroelastic dynamic equilibrium equation reads

$$\hat{\mathbf{M}}\ddot{\mathbf{q}} + \hat{\mathbf{K}}\mathbf{q} = \mathbf{\Phi}^T\mathbf{f}_{aero} \tag{2.15}$$

Next, it is possible to compute the natural frequencies and the vibration modes of the structure by imposing a harmonic motion $\mathbf{u} = \mathbf{\Phi}\, e^{i\omega_s t}$ as the solution of the homogeneous equation (free vibration

of the structure) associated to the dynamic equation of motion in (2.12)

$$\left(-\omega_s^2\mathbf{M}+\mathbf{K}\right)\mathbf{\Phi}\, e^{i\omega_s t}=\mathbf{0} \tag{2.16}$$

where ω_s represent the structural frequencies. From equation (2.16), the structural modes ($\mathbf{\Phi}$) are obtained. The interpolation of the modal shapes, gives place to the definition of the vertical displacement $\mathbf{u}_z \in \mathbb{R}^{N_{node}}$ using matrix $\mathbf{H} \in \mathbb{R}^{N_{node}\times N_{modes}}$ which reads for each mode

$$\mathbf{u}_z^k(x,y,t)=\mathbf{H}^k(x,y)\mathbf{q}^k(t) \tag{2.17}$$

where $\mathbf{q^k}(t)=\hat{q}^k e^{i\omega_s^k t}$ with $\hat{q}^k$ the amplitude of the modes and k the index of the modes going from 1 to N_{modes}. This relation will be useful in the following, when coupling the approximation of the aerodynamic forces by the DLM method with the structural model.

2.1.2 Aerodynamic model: the Doublet Lattice Method (DLM)

Various aerodynamic models can be used in the aeroelastic studies to simulate different flows and flight regimes. The incompressible flows can be simulated by analytical low fidelity models such as quasi-steady approach [4] or the fully unsteady Theodorsen model [15] but they do not provide adequately accurate results. These analytical methods with an assumption of the strip theory were employed in works of Nitschke et al. [30, 29]. Both studies were conducted on a straight cantilevered plate wing in an incompressible flow. For complex flows, higher fidelity models such as Euler [144] and RANS [145] can be employed to have a more precise description of the regime under study but these approaches can easily become very costly particularly in the optimisation framework. In this work, more complicated geometries are studied thus needing the application of the Doublet Lattice Method (DLM) that is widely used for the investigation of subsonic domain, in which the former geometries can enter [45, 146]. The DLM models the effect of pressure difference across the wing on the induced downwash using a kernel function. In this work, a parabolic approximation for the kernel numerator is considered. The dimensionless downwash $w_{dw}(x,y)$ can thus be expressed as an integral of the pressure difference $\Delta\bar{p}$

$$w_{dw}(x,y)=\frac{1}{8\pi}\iint_S K(x-\xi,y-\eta)\,\Delta\bar{p}(\xi,\eta)\,d\xi\,d\eta \tag{2.18}$$

where K is the complex acceleration potential kernel for oscillatory subsonic flow.

The area integral of equation (2.18) can be reduced to a line integral along the quarter chord of each panel, assuming that the pressure is spatially constant (for each panel) and can thus be taken out of the integral. DLM replaces the continuous $\Delta\bar{p}$ by a set of pressure doublet lines with finite

length. The doublet line lies at the quarter chord of each box whereas the downwash point is placed at 3/4 of the chord at the midspan location as presented in figure 2.2.

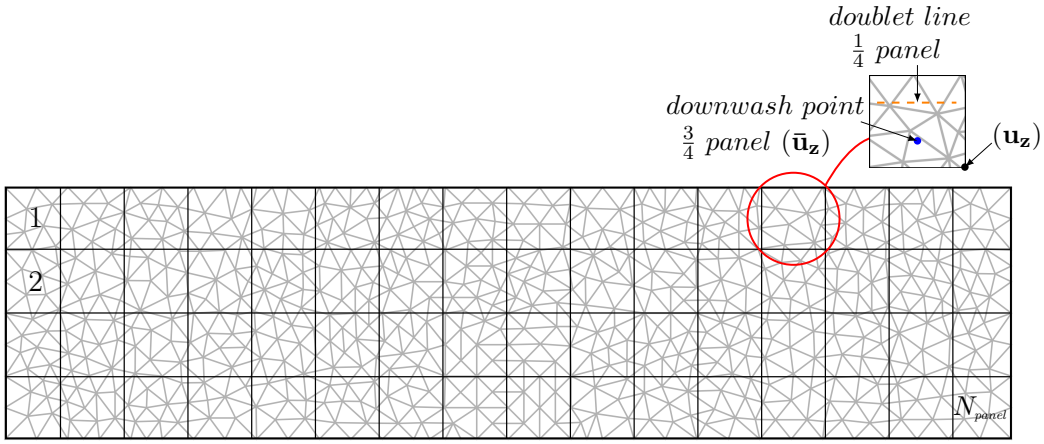

Figure 2.2: Superposition of the Finite Element and an analogues DLM mesh with lower number of panels in both directions and indication of the doublet and downwash points over a given DLM panel (this scheme is purely illustrative and it does not represent the actual refinement of the DLM mesh).

The total downwash factor is the sum between the steady downwash factor coming from the Vortex Lattice Method (VLM) and the incremental oscillatory downwash factor, thus DLM converges to the VLM at zero reduced frequency [147]. The discrete downwash $\mathbf{w}_{dw} \in \mathbb{C}^{N_{panel}} \times 1$, where N_{panel} is the total number of the panels in the DLM grid and corresponds to 300 panels in this case, can be obtained using

$$\mathbf{w}_{dw} = \mathbf{D}_{dw}\mathbf{c}_p \tag{2.19}$$

where $\mathbf{D}_{dw} \in \mathbb{C}^{N_{panel} \times N_{panel}}$ is called downwash factor matrix, and $\mathbf{c}_p \in \mathbb{C}^{N_{panel} \times 1}$ is the vector of pressure coefficients which represents the pressure coefficient at each panel. By inverting this equation, one can find the so-called Aerodynamic Influence Coefficient matrix $[\mathbf{AIC}] = \mathbf{D}_{dw}^{-1} \in \mathbb{C}^{N_{panel} \times N_{panel}}$ which allows to define the vector of pressure coefficients $\mathbf{c}_p$ as

$$\mathbf{c}_p = [\mathbf{AIC}]\, \mathbf{w}_{dw} \tag{2.20}$$

The downwash vector $\mathbf{w}_{dw}$ can be computed, starting from its definition and by using the finite-element approximation of displacements, as the composition of the partial derivatives with respect to time and the free stream direction of the transversal displacement $\mathbf{u_z}$, interpolated onto the aerodynamic points, that is $\bar{\mathbf{u}}_\mathbf{z} = \bar{\mathbf{H}}(x, y)\mathbf{q}(t)$ (with $\bar{\mathbf{u}}_\mathbf{z} \in \mathbb{R}^{N_{panel}}$ and $\mathbf{q} \in \mathbb{R}^{N_{modes}}$). Finally, the downwash

vector $\mathbf{w}_{dw}$ reads

$$\mathbf{w}_{dw} = \frac{\mathbf{w}^{\star}}{V} = \frac{1}{V}\left(\frac{\partial \bar{\mathbf{u}}_z}{\partial t} + V\frac{\partial \bar{\mathbf{u}}_z}{\partial x}\right) = \frac{1}{V}\left(\bar{\mathbf{H}}\dot{\mathbf{q}}(t) + V\bar{\mathbf{H}}_x\mathbf{q}(t)\right) \tag{2.21}$$

where $\mathbf{w}^{\star}$ is the dimensional downwash, V the free-stream velocity, $\bar{\mathbf{H}} \in \mathbb{R}^{N_{panel}\times N_{modes}}$ the transversal modal displacement matrix over each downwash point and $\bar{\mathbf{H}}_x \in \mathbb{R}^{N_{panel}\times N_{modes}}$ the matrix of the derivatives of transversal modal displacements with respect to x. The main issue faced to obtain the displacements over the DLM grid is the interpolation between the FEM and the DLM meshes. In practice, this is obtained by the modal projection over the entire domain, interpolated over the finite elements. This projection allows to extract the structural displacement over any given point, for instance the aerodynamic points (doublet and downwash points) on the DLM grid.

By imposing an harmonic motion, Eq. (2.21) becomes

$$\mathbf{w_{dw}} = i\frac{\omega_s}{V}\bar{\mathbf{H}}\mathbf{q} + \bar{\mathbf{H}}_x\mathbf{q} = \left(ik_r\bar{\mathbf{H}} + \bar{\mathbf{H}}_x\right)\mathbf{q} \tag{2.22}$$

where $k_r = \frac{\omega}{V}$ represents the modified reduced frequency. The vector of aerodynamic forces acting on the plate wing can be defined as a function of the pressure coefficients defined in equation (2.20)

$$\mathbf{f}_{aero} = \frac{1}{2}\rho_a V^2\,\mathbf{S}\,\mathbf{c}_p \tag{2.23}$$

where ρ_a is the air density, V is the free stream speed, $\mathbf{S} \in \mathbb{R}^{N_{panel}\times N_{panel}}$ is a diagonal matrix containing the surface values for each panel of the grid. Hence, $\mathbf{f}_{aero} \in \mathbb{C}^{N_{panel}\times 1}$ represents the aerodynamic forces at each panel of the DLM grid as a function of the downwash displacements, by substituting $\mathbf{c}_p$ in equation (2.23) given the expression in equation (2.20) as well as taking into account the expression of the downwash given in equation (2.22)

$$\mathbf{f}_{aero} = \frac{1}{2}\rho_a V^2\,\mathbf{S}\;[\mathbf{AIC}]\;\mathbf{w}_{dw} = \frac{1}{2}\rho_a V^2\,\mathbf{S}\;[\mathbf{AIC}]\;\underbrace{\left(ik_r\bar{\mathbf{H}} + \bar{\mathbf{H}}_x\right)}_{\mathbf{W}_{dw}}\mathbf{q} \tag{2.24}$$

where $\mathbf{W}_{dw} \in \mathbb{C}^{N_{panel}\times N_{modes}}$ corresponds to the downwash complex matrix and matrices $\bar{\mathbf{H}}$ and $\bar{\mathbf{H}}_x$ are computed at the downwash points.

The virtual work $\delta\mathbf{W}$ here is defined only with the help of the aerodynamic forces $\mathbf{f}_{aero}$ of equation (2.24) and the transversal displacement at the doublet line in each panel $\mathbf{u}_{zdl}$. The latter is extracted from the modal analysis, following the same procedure previously described for the displacements over

the downwash points

$$\delta \mathbf{W} = \delta \mathbf{u}_{zdl}^T \, \mathbf{f}_{aero} = \delta \mathbf{u}_{zdl}^T \, \frac{1}{2} \rho_a V^2 \, \mathbf{S} \; [\mathbf{AIC}] \; \mathbf{w}_{dw} = \mathbf{q}^T \frac{1}{2} \rho_a V^2 \mathbf{H}_{dl}^T \, \mathbf{S} \; [\mathbf{AIC}] \; \mathbf{W}_{dw} \mathbf{q} \tag{2.25}$$

being $\mathbf{H}_{dl} \in \mathbb{C}^{N_{panel} \times N_{modes}}$ the matrix containing the transversal displacement at midpoint of the doublet line. Once that the aerodynamic virtual work $\delta \mathbf{W}$ is defined by equation (2.25), it is possible to rewrite the complete equation of motion as defined in equation (2.15)

$$\hat{\mathbf{M}} \ddot{\mathbf{q}} + \hat{\mathbf{K}} \mathbf{q} = \frac{1}{2} \rho_a V^2 \mathbf{H}_{dl}^T \, \mathbf{S} \; [\mathbf{AIC}] \; \mathbf{W}_{dw} \mathbf{q} \tag{2.26}$$

Reminding that the modified reduced frequency is defined as $k_r = \frac{\omega_s}{V}$, equation (2.26) may help to define the global aerodynamic matrix $\mathbf{A}_{aero} \in \mathbb{C}^{N_{modes} \times N_{modes}}$ resulting from the application of the DLM. Finally, the aeroelastic governing equation of motion reads

$$\hat{\mathbf{M}} \ddot{\mathbf{q}} + \hat{\mathbf{K}} \mathbf{q} = \omega_s^2 \mathbf{A}_{aero} \mathbf{q} \tag{2.27}$$

2.1.3 Aeroelastic solver: the p-k method

The equation of the coupled motion is solved in a frequency domain considering harmonic motions of the system. One of the methods widely used in aeroelasticity in the frequency domain is called the p-k method which is an iterative frequency matching approach [148]. In order to use the p-k method, the frequency domain is expanded to the Laplace domain by replacing $i\omega$ by s, where ω is the aeroelastic frequency

$$s = \frac{pV}{b} \qquad \text{where} \qquad p = \gamma k_r + i k_r \tag{2.28}$$

Separating the real and the imaginary part of the aerodynamic matrix in equation (2.27), it can therefore be written as

$$\hat{\mathbf{M}} \ddot{\mathbf{q}} + \hat{\mathbf{K}} \mathbf{q} = \omega^2 (\mathbf{A}_{aero}^R + i \mathbf{A}_{aero}^I) \mathbf{q} \tag{2.29}$$

Rewriting the quadratic term with time derivates $i\omega^2 \mathbf{q} = \omega i \omega \mathbf{q} = \omega \dot{\mathbf{q}}$ one can define the real part of the aerodynamic matrix as the stiffness and the imaginary part as the aerodynamic damping

$$\hat{\mathbf{M}} \ddot{\mathbf{q}} - \omega \mathbf{A}_{aero}^I \dot{\mathbf{q}} + (\hat{\mathbf{K}} - \omega^2 \mathbf{A}_{aero}^R) \mathbf{q} = 0 \tag{2.30}$$

In order to be able to conduct the modal analysis of the equation (2.30), it is augmented in order to establish a first-order system

$$\begin{bmatrix} \mathbf{I} & 0 \\ 0 & \hat{\mathbf{M}} \end{bmatrix} \begin{Bmatrix} \dot{\mathbf{q}} \\ \ddot{\mathbf{q}} \end{Bmatrix} - \begin{bmatrix} 0 & \mathbf{I} \\ -(\hat{\mathbf{K}} - \omega^2 \mathbf{A}^R_{aero}) & \omega \mathbf{A}^I_{aero} \end{bmatrix} \begin{Bmatrix} \mathbf{q} \\ \dot{\mathbf{q}} \end{Bmatrix} = \begin{Bmatrix} 0 \\ 0 \end{Bmatrix} \tag{2.31}$$

Finally, by imposing harmonic motion $\mathbf{q}(t) = \hat{\mathbf{q}} e^{i\omega t}$, the system can be defined as

$$\begin{bmatrix} \mathbf{I} & 0 \\ 0 & \mathbf{I} \end{bmatrix} s \begin{Bmatrix} \hat{\mathbf{q}} \\ s\hat{\mathbf{q}} \end{Bmatrix} - \begin{bmatrix} 0 & \mathbf{I} \\ -\hat{\mathbf{M}}^{-1}(\hat{\mathbf{K}} - \omega^2 \mathbf{A}^R_{aero}) & \omega \hat{\mathbf{M}}^{-1} \mathbf{A}^I_{aero} \end{bmatrix} \begin{Bmatrix} \hat{\mathbf{q}} \\ s\hat{\mathbf{q}} \end{Bmatrix} = \begin{Bmatrix} 0 \\ 0 \end{Bmatrix} \tag{2.32}$$

For each complex conjugate eigenvalue s of system (2.32), the real part defines the aeroelastic damping g and the imaginary part the aeroelastic frequency ω

$$s = g \pm i\omega \tag{2.33}$$

These eigenvalues are used to detect the condition at which the aeroelastic system becomes unstable. When the damping becomes positive at non-zero frequency, the structure manifests a pseudo-harmonic motion with an increasing amplitude which represents an instability called flutter. The velocity at which this instability occurs is called the flutter velocity (V_f). The structure has harmonic oscillations at the critical speed which corresponds to a system with zero damping ($g = 0$). If at the critical speed where $g = 0$, the corresponding frequency is equal to zero ($\omega = 0$), the instability is a static one, called divergence, and the system no longer sustains a harmonic oscillation but an abrupt increase to the point of failure. Algorithm 1 explains the aeroelastic p-k solver.

Algorithm 1: *p-k* method

1: Obtain the mass and the stiffness matrices and the eigenmodes of the structures (equation (2.16))

$$\left(-\omega_s^2\mathbf{M}+\mathbf{K}\right)\mathbf{\Phi}\, e^{i\omega_s t}=\mathbf{0}$$

2: Compute the reduced frequency for each eigenmode $k_r=\frac{\omega_s}{V}$

3: Obtain the aerodynamic matrix using this reduced frequency (equation (2.18)-(2.25))

4: Compute the eigenvalues of the aeroelastic system and find the aeroelastic frequencies (equation (2.28)-(2.33))

$$\begin{bmatrix}\mathbf{I} & 0\\ 0 & \mathbf{I}\end{bmatrix} s\begin{Bmatrix}\hat{\mathbf{q}}\\ s\hat{\mathbf{q}}\end{Bmatrix}-\begin{bmatrix}0 & \mathbf{I}\\ -\hat{\mathbf{M}}^{-1}(\hat{\mathbf{K}}-\omega^2\mathbf{A}^R) & \omega\hat{\mathbf{M}}^{-1}\mathbf{A}^I\end{bmatrix}\begin{Bmatrix}\hat{\mathbf{q}}\\ s\hat{\mathbf{q}}\end{Bmatrix}=\begin{Bmatrix}0\\ 0\end{Bmatrix}$$

$$s=g\pm i\omega$$

5: Choose a number of steps to divide the velocity interval N_{steps}

6: **for** $i=1:N_{steps}$ **do**

7: $V=V_{interval}(i)$

8: Initial guess of the reduced frequency $k_{current}=\omega_s b/V$

9: **for** $j=1:N_{modes}$ **do**

10: $M=mass\,matrix$

11: $K=stiffness\,matrix$

12: $A(k_{current})=aerodynamic\,DLM\,matrix$

13: **Solve the eigenvalue problem** $\rightarrow s$

14: $\omega=imag(s)$

15: $k_{new}=\omega b/V$

16: **while** $|k_{current}-k_{new}|>tol$ **do**

17: $M=mass\,matrix$

18: $K=stiffness\,matrix$

19: $A(k_{new})=aerodynamic\,DLM\,matrix$

20: **Solve the eigenvalue problem** $\rightarrow s$

21: $\omega=imag(s)$

22: $k_{current}=k_{new}$

23: $k_{new}=\omega b/V$

24: **end while**

25: $\omega=imag(s)$

26: $g=real(s)$

27: **end for**

28: **end for**

2.1.4 Validation of the aeroelastic solver

In order to validate the aeroelastic solver described above, the aeroelastic instabilities are compared to a set of experimental data or other validated numerical values. It needs to be noted that before conducting the comparison, a convergence test on both FEM and DLM meshes has been carried out resulting in parameters described in section 2.1. To validate the numerical solver developed throughout this chapter, some results have been compared to the ones from the cases of Hollowell et al. [149]. The straight plate-wing configuration considered is described in table 2.1, together with the elastic properties of the base material of the laminate (elementary composite layer).

$E_{11}[GPa]$	$E_{22}[GPa]$	$G_{12}[GPa]$	ν	$\rho[kg/m^3]$	ply thickness $[mm]$	$S[m]$	$c[m]$	$\rho_a\ [kg/m^3]$
98	7.9	5.6	0.28	1520	0.134	0.305	0.0762	1.225

TABLE 2.1: Aeroelastic configuration of the anisotropic plate: Hollowell et al. [149] case studies.

The structural mode shapes resulting from the modal analysis of the dynamic system are shown in figure 2.3 (laminate of stacking sequence $[-45_2, 0]_s$). Each case represents the response of the structure, in terms of its transversal displacements, for each mode. For this configuration 5 bending-dominated and 3 torsion-dominated modes are detected.

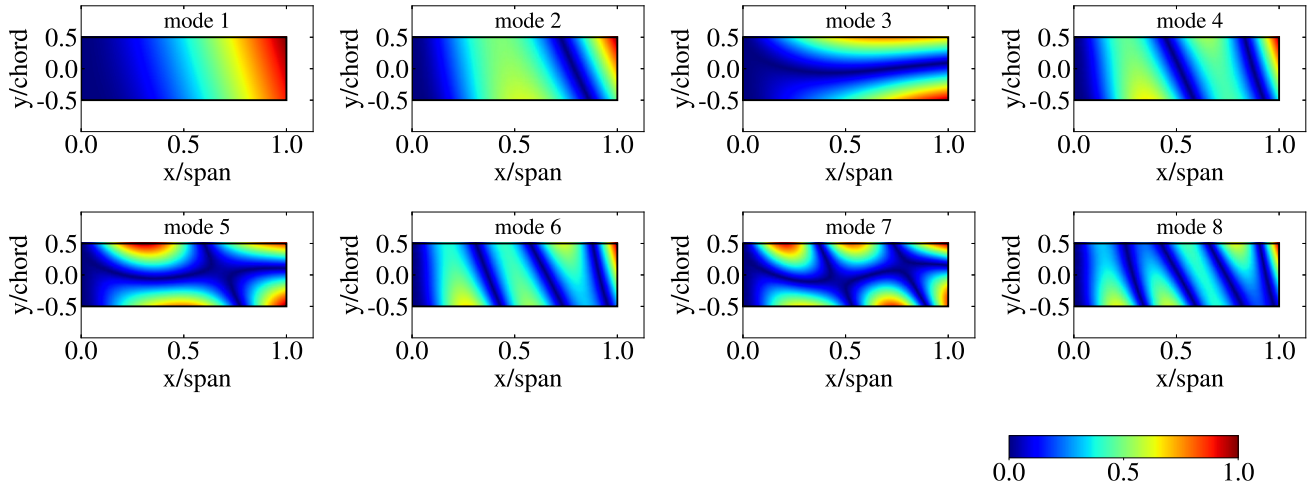

FIGURE 2.3: Structural modes obtained from the modal analysis corresponding to the stacking sequence $[-45_2, 0]_s$ in the work of Hollowell et al. [149].

The structural frequency corresponding to each mode is presented in table 2.2. These modes will be employed in the computation of the aeroelastic system, according to the FEM-DLM coupling strategy described in the previous section. It needs to be noted that the modes are arranged with increasing frequencies.

Number of mode	mode 1	mode 2	mode 3	mode 4	mode 5	mode 6	mode 7	mode 8
Frequency ($\omega_s[rad/s]$)	30.6	188.8	308.5	528.4	941.4	1034.2	1628.1	1702.7

Table 2.2: Structural frequencies of the first 8 modes corresponding to the stacking sequence $[-45_2, 0]_s$ in the work of Hollowell et al. [149].

As stated in section 2.1.3, the aeroelastic instability occurs when the damping becomes positive. In order to find the corresponding flutter velocity, the eigenvalues of the aeroelastic system are calculated for multiple velocities within a given interval. The real part of these eigenvalues represents the aeroelastic damping and the imaginary part, the aeroelastic frequency.

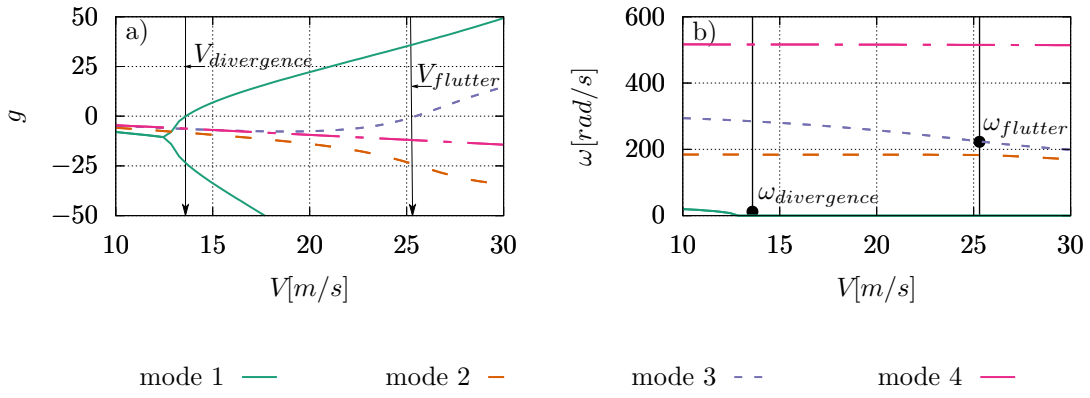

Figure 2.4: Evolution of a) damping g and b) frequency ω of the first four aeroelastic modes as a function of the airspeed V for the stacking sequence $[-45_2, 0]_s$, Hollowell's configuration [149], presented in table 2.3.

An easy way to visually detect these instabilities, is the plot of the evolution of aeroelastic damping as a function of velocity (air speed), generally known as $V - g$ diagram. Figure 2.4 presents the evolution of the real and the imaginary part of four aeroelastic modes which represent the aeroelastic damping and frequency of the given laminate respectively. As marked on the figure 2.4.a, two types of instability are present. The first instability corresponds to a divergence at $V_d = 13.7\ m/s$ and the second a flutter, observed at $V_f = 25.4\ m/s$. The difference between these two phenomena can be detected on the graph of the aeroelastic frequency in figure 2.4.b. The frequency of the static instability (divergence) is $\omega = 0.\ rad/s$ and of the dynamic instability (flutter) is $\omega = 223.4\ rad/s$. The zero frequency of the divergence is identical to the first structural mode and indicates a similar mode shape. On the other hand, the frequency of the flutter instability does not correspond to any of the structural frequencies in table 2.2 and has a value between the second and the the third mode frequencies and thus suggests a combination of these two structural modes.

Both divergence and flutter mode shapes are presented at their respective critical velocity in figure 2.5. As mentioned previously and due to similarities in the frequency values, the divergence mode shape is identical to the first structural mode. On the other hand, the flutter mode shape, does not resemble any of the structural modes. The comparison of the frequency values amongst the aeroelastic instabilities and the structural modes, suggests that the flutter frequency can be caused by the coupling of the second and the third structural modes. This coupling is exhibited in figure 2.5 (the mode shape on the right side) and can thus justify the value of the flutter frequency obtained for this configuration.

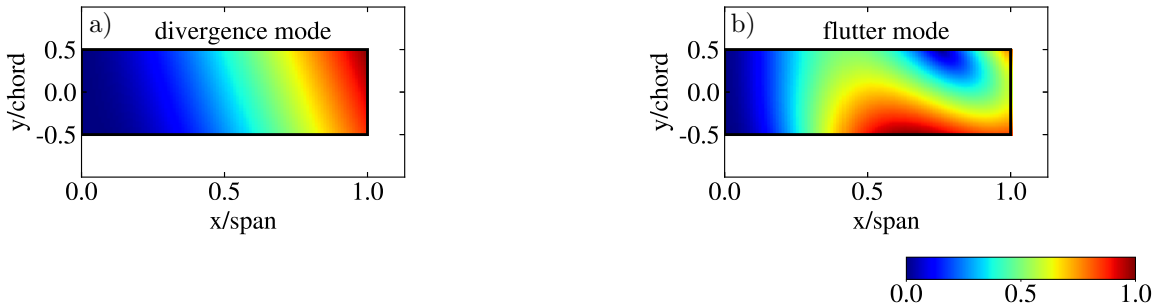

FIGURE 2.5: Aeroelastic modes for a) divergence and b) flutter instabilities corresponding to the stacking sequence $[-45_2, 0]_s$ in the work of Hollowell et al. [149].

The comparison between all the results presented in table 2.3 shows a good agreement between the present code, the experimental and the computational results in the work of Hollowell et al. [149].

Layup	V_f $[m/s]$			V_d $[m/s]$		
	present code	Ref[149] Exp.	Ref[149] Comp.	present code	Ref[149] Exp.	Ref[149] Comp.
$[-45_2, 0]_s$	25.4	-	27.8	13.7	12.5	11.1
$[0_2, 90]_s$	22.7	25	21.0	28.9	-	25.0
$[+45, -45, 0]_s$	39.6	>32	39.0	-	>32.0	-
$[+45_2, 0]_s$	26	28	27.8	-	-	-
$[+30_2, 0]_s$	25.6	27	27.8	-	-	-
$[-30_2, 0]_s$	31.7	-	30.0	13.8	11.7	11.5

TABLE 2.3: Comparison between the results of the in house code and those of Hollowell et al.[149].

The small variations between the results can be due to different structural solvers used in each study. This dissimilarities are more pronounced in the divergence velocities which is a static instability with a higher influence from the structural model. In general, it can be said that this study validates all the solvers developed in this section and permits their use in further optimisation and uncertainty quantification analyses.

2.2 Polar parameters for the representation of elastic anisotropy

The polar formulation is an algebraic technique which is able to represent any given plane tensor. It was first introduced by Verchery in 1979 [76] and it replaced the Cartesian formulation that depends on the direction of the frame in which the problem is studied. The Cartesian method can cause complexity of the problem while modelling anisotropic materials and structures, such as stacking sequences with properties that vary strongly by the direction of each layer. The polar formalism is a very advantageous replacement as it can define plane elastic tensors as a function of tensor polar invariants and polar angles, which can directly represent any given anisotropic property. More specifically, the polar angles express the directions of anisotropy of the laminate that is an essential factor in these types of materials.

For a given symmetric positive-definite fourth-order plane tensor $\mathcal{L}$, such as a plane elastic tensor, relations between the polar parameters and the tensorial Cartesian components read [150]

$$\begin{aligned} 8T_0 &= L_{xx} - 2L_{xy} + 4L_{ss} + L_{yy} \\ 8T_1 &= L_{xx} + 2L_{xy} + L_{yy} \\ 8R_0 e^{\imath 4\Phi_0} &= L_{xx} + 4\imath L_{xs} - 2L_{xy} - 4L_{ss} - 4\imath L_{ys} + L_{yy} \\ 8R_1 e^{\imath 2\Phi_1} &= L_{xx} + 2\imath L_{xs} + 2\imath L_{ys} - L_{yy} \end{aligned} \tag{2.34}$$

Here the Voigt notation of the Cartesian components $L_{ij}(i,j = x,y,s)$ is employed, where the indices x and y represent the axis coordinates and index s the shear components. The six polar parameters are defined as: the two positive-definite scalars T_0 and T_1, which represent the isotropic part of tensor $\mathcal{L}$; then, the polar modules R_0 and R_1, together with the polar angles Φ_0 and Φ_1, which are combined in complex quantities, corresponding to the anisotropic components of tensor $\mathcal{L}$. Polar angles Φ_0 and Φ_1 thus represent the principal directions of the two anisotropic components. The isotropic and the anisotropic parameters T_0, T_1, R_0 and R_1 are invariant to the rotation α of the reference frame, whilst the two polar angles Φ_0 and Φ_1 depend on the variations of the latter [150].

$$\begin{aligned} \Phi_0' &= \Phi_0 - \alpha \\ \Phi_1' &= \Phi_1 - \alpha \end{aligned} \tag{2.35}$$

On the other hand, the difference between the angles $\Phi_0 - \Phi_1$ is also an invariant to the reference frame.

The reverse relationships allow to define the Cartesian components as functions of the polar parameters [150]

$$\begin{aligned}
L_{xx} &= T_0 + 2T_1 + R_0\cos(4\Phi_0) + 4R_1\cos(2\Phi_1) \\
L_{xy} &= -T_0 + 2T_1 - R_0\cos(4\Phi_0) \\
L_{xs} &= R_0\sin(4\Phi_0) + 2R_1\sin(2\Phi_1) \\
L_{yy} &= T_0 + 2T_1 + R_0\cos(4\Phi_0) - 4R_1\cos(2\Phi_1) \\
L_{ys} &= -R_0\sin(4\Phi_0) + 2R_1\sin(2\Phi_1) \\
L_{ss} &= T_0 - R_0\cos(4\Phi_0)
\end{aligned} \tag{2.36}$$

It is worth noting that equations (2.36) can be employed to express the Cartesian components in a new reference frame, rotated of an angle θ, by simply replacing the polar angles Φ_0 and Φ_1 by their expressions Φ_0' and Φ_1' in the new reference frame, as stated in equations (2.35).

In the current study, the polar parameters can be employed to express the stiffness properties of composite laminates issued from the CLPT defined in equation (2.1). The ABD-matrix introduced in section 2.1.1 are defined by the help of the stiffness tensor $\mathbf{Q}$ of the base layer and of the orientation angle θ_k of each layer in the stacking sequence

$$\mathbf{A} = \sum_k \mathbf{Q}_k(\theta_k)\,(z_k - z_{k-1}) \tag{2.37}$$

$$\mathbf{B} = \frac{1}{2}\sum_k \mathbf{Q}_k(\theta_k)\,(z_k^2 - z_{k-1}^2) \tag{2.38}$$

$$\mathbf{D} = \frac{1}{3}\sum_k \mathbf{Q}_k(\theta_k)\,(z_k^3 - z_{k-1}^3) \tag{2.39}$$

where the sums are over the number of plies N_{plies} composing the laminate and z_k and z_{k-1} are the ply coordinates starting from the mid-plane that lies on $z = 0$. Moreover, angle θ_k implies that the tensor $\mathbf{Q}_k$ has to be calculated considering the orientation and the material of k-th ply. The three laminate stiffness tensors have different dimensions, $\mathbf{A}$ [N/m], $\mathbf{B}$ [N] and $\mathbf{D}$ [Nm] but it is usual to introduce the normalised tensors $\mathbf{A}^*$, $\mathbf{B}^*$ and $\mathbf{D}^*$ as

$$\mathbf{A}^* = \frac{1}{h}\mathbf{A} \qquad \mathbf{B}^* = \frac{2}{h^2}\mathbf{B} \qquad \mathbf{D}^* = \frac{12}{h^3}\mathbf{D} \tag{2.40}$$

where h is the total thickness of the laminate.

Once the tensor $\mathbf{Q}$ is defined, its polar parameters can be calculate using equation (2.36) and thus the polar parameters corresponding to each $\mathbf{A}$, $\mathbf{D}$ and $\mathbf{B}$ tensor can be obtained by the equations (2.37) - (2.39) and read [150]

$$\begin{aligned}
T_0^A, T_0^B, T_0^D &= \frac{1}{m}\sum_{k=1}^{N_{plies}} T_{0k}\left(z_k^m - z_{k-1}^m\right) \\
T_1^A, T_1^B, T_1^D &= \frac{1}{m}\sum_{k=1}^{N_{plies}} T_{1k}\left(z_k^m - z_{k-1}^m\right) \\
R_0^A \mathrm{e}^{4\mathrm{i}\Phi_0^A}, R_0^B \mathrm{e}^{4\mathrm{i}\Phi_0^B}, R_0^D \mathrm{e}^{4\mathrm{i}\Phi_0^D} &= \frac{1}{m}\sum_{k=1}^{N_{plies}} R_{0k}\mathrm{e}^{4\mathrm{i}(\Phi_{0k}+\theta_k)}\left(z_k^m - z_{k-1}^m\right) \\
R_1^A \mathrm{e}^{2\mathrm{i}\Phi_1^A}, R_1^B \mathrm{e}^{2\mathrm{i}\Phi_1^B}, R_1^D \mathrm{e}^{2\mathrm{i}\Phi_1^D} &= \frac{1}{m}\sum_{k=1}^{N_{plies}} R_{1k}\mathrm{e}^{2\mathrm{i}(\Phi_{1k}+\theta_k)}\left(z_k^m - z_{k-1}^m\right)
\end{aligned} \tag{2.41}$$

where m takes values of $(1, 2, 3)$ for parameters of tensors $(\mathbf{A}, \mathbf{B}, \mathbf{D})$, respectively.

An alternative approach to the representation of anisotropic elastic properties of composite laminates is represented by the so-called lamination parameters [75], issued from the Tsai-Pagano formulation of the stiffness tensor $\mathbf{Q}$. Lamination parameters, without being proper tensorial invariants, show some interesting features in the representation of the anisotropic stiffness and coupling behaviour of laminates in terms of tensors $\mathbf{A}$, $\mathbf{D}$ and $\mathbf{B}$: they essentially correspond to weighted sums of trigonometric functions of orientation angles θ_k, which also appear in the polar formalism (equation 2.41). For this reason, as well as the simplicity of their concept, they are very popular and widely employed in research works on the design and optimisation of composites structures [151], as well as in aeroelastic tailoring problems [69]. However, two critical drawbacks of lamination parameters are the facts that they are expressed only in the case of laminates made of identical layers and, more limiting than that, they only apply to the three stiffness and coupling tensors $\mathbf{A}$, $\mathbf{D}$ and $\mathbf{B}$. Particularly, when dealing with the plate-wing, the relevant elastic tensor is the reduced bending stiffness $\tilde{\mathbf{D}}$, which is a non-linear combination of the laminate's tensors $\mathbf{A}$, $\mathbf{D}$ and $\mathbf{B}$. As such, the representation based on lamination parameters would not be easy and the 12 laminations parameters representing the three separate tensors $\mathbf{A}$, $\mathbf{D}$ and $\mathbf{B}$ should be considered. This is the reason why aeroelastic studies based on the use of lamination parameters limit their scope to uncoupled and symmetric stacking sequences, even when this restrictive hypothesis is non-realistic (as in the case of Uncertainty Quantification or stochastic optimisation). On the contrary, the polar formalism can be applied to plane tensors of any order and symmetry, and the reduced bending tensor $\tilde{\mathbf{D}}$ can be represented by its 6 polar parameters $\tilde{T}_0$, $\tilde{T}_1$, $\tilde{R}_0$, $\tilde{R}_1$, $\tilde{\Phi}_0$, $\tilde{\Phi}_1$.The latter property allows to limit the domain of study to the desired elastic property of the material.

In terms of polar invariants, five independent polar quantities can be defined to describe the behaviour of a fully-anisotropic plane elastic tensor, T_0, T_1, R_{K_X}, R_{K_Y}, R_1, Φ_1 with

$$R_{K_X} = R_0 \cos 4(\Phi_0 - \Phi_1), \quad R_{K_Y} = R_0 \sin 4(\Phi_0 - \Phi_1) \tag{2.42}$$

In relation to laminates and the CLPT equations, anisotropic polar parameters can be used to represent any laminate's tensor, $\mathbf{A}$, $\mathbf{B}$, $\mathbf{D}$ or $\tilde{\mathbf{D}}$. Multiple symmetries can be defined using the polar parameters, such as isotropy, square symmetry, R_0-orthotropy and orthotropy. These properties are summarised in table 2.4.

Elastic symmetry	Polar condition	Direction of main orthotropy axis	Parameters for description of the symmetry
Isotropy	$R_0 = R_1 = 0$	none	T_0, T_1
Square Symmetry	$R_1 = 0$	Φ_0	T_0, T_1, R_0, Φ_0
R_0-Orthotropy	$R_0 = 0$	Φ_1	T_0, T_1, R_0, Φ_1
Orthotropy	$\Phi_0 - \Phi_1 = K\frac{\pi}{4}, K \in \{0,1\}$	Φ_1	T_0, T_1, $R_K = R_0 \cos 4(\Phi_0 - \Phi_1)$, R_1, Φ_1

TABLE 2.4: Elastic symmetries defined as a function of polar parameters [150]

The isotropy is simply defined when both R_0 and R_1 are zero which consequently implies that Φ_0 and Φ_1 are not defined. Square symmetry is present when only R_1 is zero meaning that Φ_1 can not be defined. The last two cases both represent an orthotropy which is specified by a condition on the difference of Φ_0 and Φ_1. Orthotropy is present when $\Phi_0 - \Phi_1 = K\frac{\pi}{4}$ where K (orthotropy shape parameter) can take the values $K = \{0, 1\}$ depending on the sign of $R_K = (-1)^K R_0$. The special case of R_0-orthotropy respects the same condition while it is only true when R_0 is zero and thus Φ_0 undefined [152].

When representing a stiffness tensor, such as $\mathbf{Q}$, $\mathbf{A}$ or $\mathbf{A}^*$, $\mathbf{D}$ or $\mathbf{D}^*$, or $\tilde{\mathbf{D}}$, polar parameters are bound by thermodynamic limits of existence [150]

$$0 < T_0 \qquad 0 < T_1 \tag{2.43}$$

$$0 \leq R_0 \qquad 0 \leq R_1 \tag{2.44}$$

$$0 < T_0 - R_0 \tag{2.45}$$

$$2R_1^2 \left[T_0 - R_0 \cos 4\left(\Phi_0 - \Phi_1\right)\right] - T_1\left(T_0^2 - R_0^2\right) < 0 \tag{2.46}$$

However, more restrictive limits have to be imposed to the anisotropic polar parameters when they represent laminate's stiffness tensors issued from the CLPT: the combination of trigonometric functions of the layers' orientation angles impose feasibility conditions over the anisotropic polar parameters, called *geometrical bounds* [150]. In the fully anisotropic case, these geometric bounds read

$$\begin{aligned} 0 &\leq \rho_1 && (2.47)\\ -1 &\leq \rho_{0_X} \leq 1 && (2.48)\\ -1 &\leq \rho_{0_Y} \leq 1 && (2.49)\\ 2(\rho_1^2) - 1 &\leq 2(\rho_1^2)(\rho_{0_X}) - (\rho_{0_X}^2) - (\rho_{0_Y}^2) && (2.50) \end{aligned}$$

where

$$\rho_{0_X} = \frac{R_{K_X}}{R_0^{BL}} \qquad \rho_{0_Y} = \frac{R_{K_Y}}{R_0^{BL}} \qquad \rho_1 = \frac{R_1}{R_1^{BL}} \tag{2.51}$$

with R_{K_X}, R_{K_Y} and R_1 represent the anisotropic moduli and Φ_1 the orientation of the anisotropic axis and R_1^{BL} and R_K^{BL} represent the Base Layer (BL) parameters. R_K^{BL} is generally identical to R_0^{BL} as it is a positive value in the most common cases of composite laminae.

For a laminate with an orthotropic base layer and a total thickness h, the geometric boundaries are defined in terms of the normalised polar parameters (polar parameters of the normalised tensors defined by equations (2.40)) as

$$\begin{aligned} 0 &\leq \rho_1 && (2.52)\\ -1 &\leq \rho_0 \leq 1 && (2.53)\\ 2(\rho_1)^2 - 1 &\leq (\rho_0) && (2.54) \end{aligned}$$

where $\rho_0 = \frac{R_K}{R_0^{BL}}$. In the case of laminates made of identical plies (i.e. same base material and same thickness for each layer), the isotropic moduli of polar parameters (T_0 and T_1) are constant. This assumption reduces the parameters required to define an orthotropic laminate using R_K, R_1 and the difference between the polar angles as described in table 2.4. The geometrical constraint defined in equation (2.54) allows to respect the orthotropic boundaries and thus the domain of study.

Figure 2.6 represents the orthotropic domain defined by the two anisotropic polar parameters: every point in this domain represents the polar parameters, i.e. the elastic properties, of feasible orthotropic laminates. In other words, any point of the domain can be realised by building one

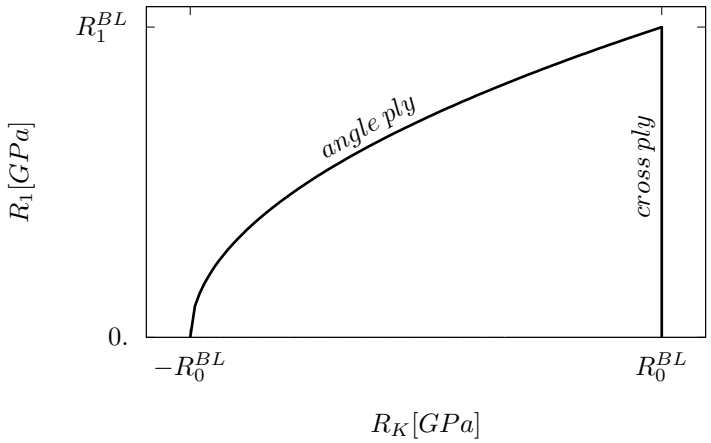

FIGURE 2.6: Orthotropic domain defined by two polar parameters R_K and R_1 for a fixed value of Φ_1 [29].

corresponding stacking sequence: this step, which can be called *stacking sequence retrieval*, is a non-trivial inverse problem that has been addressed by many authors [79, 80]. This domain includes the general orthotropy which encompasses other elastic symmetries defined previously. Each border of this domain corresponds to a specific family of orthotropic materials such as cross-ply laminates (angle of plies have 0° or 90° values) that are defined on the right edge of the domain. Another important family is on the upper parabolic limit of the domain which comprehends angle-ply laminates. This particular family have plies at angles $\pm\theta$, and they are defined as balanced when the two opposite orientations $\pm\theta$ share the number of plies in the stack. Starting from the CLPT relations in the polar formalism, the normalised in-plane stiffness polar parameters R_0 and R_1 for a balanced angle-ply laminates can be written as a function of the ply orientations θ_k

$$R_0 e^{4i\phi_0} = \frac{R_0^{BL}}{N_{plies}} \sum_k e^{4i\theta_k} = R_0^{BL}\cos(4\theta) \qquad R_1 e^{2i\phi_1} = \frac{R_1^{BL}}{N_{plies}} \sum_k e^{2i\theta_k} = R_1^{BL}\cos(2\theta) \tag{2.55}$$

the solution of the orientation associated to the angle-ply laminates reads

$$\theta = \frac{1}{4}\arccos\left(\frac{R_K}{R_0^{BL}}\right) \qquad \text{or} \qquad \theta = \frac{1}{2}\arccos\left(\frac{R_1}{R_1^{BL}}\right) \tag{2.56}$$

Particularly, the lower left corner of the domain corresponds to a balanced angle-ply laminate with $\theta = 45°$. However, these sets of remarkable stacking sequences are not the only analytical solutions that can be useful for the stacking sequence retrieval. Quasi-Trivial (QT) solutions [153, 154, 155] are another type of stacking sequence families that exist in the orthotropic domain and have been

established by solving the problem of *quasi-homogeneity* of laminates

$$\mathbf{B} = O \qquad \mathbf{C} = \mathbf{A}^* - \mathbf{D}^* = O \tag{2.57}$$

where $\mathbf{C}$ represents the homogeneity tensor. For a laminate with identical plies in material and thickness and with the help of tensors defined in equations (2.37)-(2.39), the two coupling and homogeneity matrices read

$$\mathbf{B} = \sum_k b_k \mathbf{Q}_k(\theta_k) \qquad \mathbf{C} = \sum_k c_k \mathbf{Q}_k(\theta_k) \tag{2.58}$$

with coefficients b_k and c_k defined in terms of the number of layers N_{plies} and of the index k of the layer in the stack

$$b_k = \frac{1}{N_{plies}^2}(2k - N_{plies} - 1) \tag{2.59}$$

$$c_k = \frac{1}{N_{plies}^3}\left[-2\left(6k^2 + N_{plies}^2\right) + 6N_{plies}(2k-1) + 4(3k-1)\right] \tag{2.60}$$

One can notice that coefficients b_k and c_k have an antisymmetric distribution along the plate thickness, with respect to the plate mid-plane, thus the sum of coefficients b_k and c_k over the layers is zero. Quasi-homogenetiy (QH) conditions (2.57) are achieved by assigning the same orientation angle within each *saturated group* of layers, i.e. groups of layers satisfying the partial sum of coefficients b_k and c_k equal to zero [150]. The number of saturated groups for a QTQH solution corresponds to the number of different admissible orientation angles in the stack. QTQH stacking sequences, being exact solutions of uncoupling and homogeneity, can be designed to be orthotropic by being assigned to couple of balanced saturated groups opposite orientations ($\pm\theta_i$). The in-plane elastic properties of the resulting laminate can be expressed analytically as functions of the lamination angles θ_i (the bending properties being equal to the in-plane ones by effect of the homogeneity of the stack): as such, the values of the lamination angles can be determined in order to match a given set of polar parameters, i.e. a given point, in the orthotropic domain of figure 2.7. However, because of the limited number of layers in the stack and to the limited number of saturated groups in the QTQH solutions, not every point of the domain will be feasible, and the coverage of the domain based on QTQH solutions depend on the maximum number of layers in the stack.

Figure 2.7 represents the distribution of the quasi-trivial sequences for a QTQH 20-layer laminate in the orthotropic domain. The choice for this number of plies is related to two factors. First, the aeroelastic study was formulated and validated in the incompressible regime and thus the number of

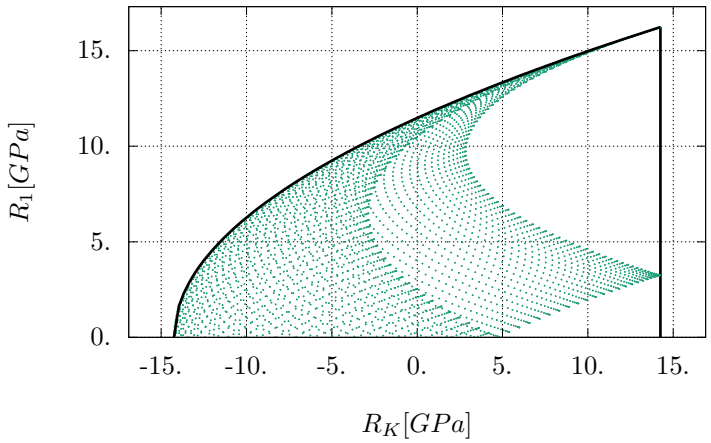

FIGURE 2.7: The coverage of the orthotropic domain using quasi-trivial stacking sequences with $N_{plies} = 20$ layers.

plies (which have a direct impact on the rigidity of the plate) have been limited so that the aeroelastic instabilities remain in this flow regime. Second, the QTQH solutions with the initial 16-ply laminate do not adequately cover the orthotropic domain. On the other hand, the 20-layer sequences have a large coverage of the domain while remaining in the incompressible regime. These staking sequences contain 4 saturated groups $\pm\theta_1$ and $\pm\theta_2$ which allow to build balanced quasi-trivial sequences for each couple of angles. They can be defined using a stacking sequence of form

$$[\theta_1, \theta_2, -\theta_2, -\theta_2, -\theta_1, \theta_2, -\theta_1, \theta_2, -\theta_2, -\theta_1, \theta_1, \theta_2, -\theta_2, \theta_1, -\theta_2, \theta_1, \theta_2, \theta_2, -\theta_2, -\theta_1] \tag{2.61}$$

where θ_1 and θ_2 are the orientations of the corresponding ply.

Using equation (2.55), the anisotropic moduli for the given balanced quasi-trivial sequences where the number of plies with the same orientation $(+/-)$ are equal, read

$$R_K = 2R_0^{BL}\frac{N_1\cos 4\theta_1 + N_2\cos 4\theta_2}{N_{plies}} \qquad R_1 = 2R_1^{BL}\frac{N_1\cos 2\theta_1 + N_2\cos 2\theta_2}{N_{plies}} \tag{2.62}$$

with N_{plies} the total number of plies, N_1 the number of plies with orientation θ_1 and N_2 the number of plies with orientation θ_2 . We note that the normalised bending anisotropic polar components will be identical to the in-plane ones, thanks to the quasi-homogeneity property. For the case presented here, the total number of plies is $N_{plies} = 20$ which divides N_1 and N_2 to two sets of 4 and 6 saturated groups respectively.

The coverage in figure 2.7 is obtained by varying the angles in an interval of $[-90°, 90°]$. It needs to be noted that over the left half of the domain, as indicated in figure 2.7, two stacking sequences correspond to the same set of polar parameters. This superposition gives the liberty to evaluate different stacking sequences corresponding to the same elastic properties with respect to other criteria, as it will be seen in the following of this work.

3

Deterministic Optimisation: Uniform-Stiffness Laminates

This chapter focuses on the deterministic aeroelastic tailoring of composite laminated plate-wings. Multiple works have deployed various methods to conduct similar optimisation problems with the objective to improve the aeroelastic response of the system [118], but they generally deal with laminates made of a small number of layers. There have been studies that use parametric formulations such as lamination parameters to render the domain more convex and easier for this investigation [60] but they usually impose a symmetry over the laminates to respect an uncoupled membrane-bending condition. The latter can affect the quality of the optimisation results and overlook some favourable properties. An original formulation based on the polar formalism of the aeroelastic optimisation problem is presented which surpasses the limitations imposed by the methods mentioned above and achieves a faster convergence with more reliable control over the elastic properties of the final structure. To this end, first an optimisation study using the ply angles is conducted. Then, the optimisation study is reformulated using the polar parameters in order to reduce the dimensionality of the problem. An investigation of the Uniform-Stiffness laminates is carried out, first, in an anisotropic domain and next in a more restrained orthotropic domain.

A 2-level optimisation problem is put in place [79, 80]. The first level focuses on the aeroelastic optimisation using the polar parameters and the second level is based on obtaining the stacking sequence corresponding to the optimal polar parameters. Multiple methods can be employed for the *stacking sequence retrieval* that are presented and explained in details.

3.1 Optimisation problem

The aeroelastic optimisation of the composite laminate, is commonly defined as the maximisation of the flutter velocity using the ply angles of the composite laminate. In this work, the Genetic Algorithm (GA) is employed to conduct the optimisation process. The use of this algorithm requires the definition of parameters such as number of generations N_{gen}, number of individuals N_{ind}, the cross-over and the mutation coefficients. These parameters vary with respect to the size of the investigation domain and the number of optimisation variables. The cross-over coefficient is usually chosen as $\frac{1}{N_{ind}}$. There is no specific rule to choose the mutation coefficient but small values of order 10^{-2} are custom to use to keep the diversity of the population but avoid a pre-mature convergence.

In this chapter, Uniform-Stiffness laminates are optimised in order to maximise the flutter velocity of the structure under study. First an anisotropic domain is considered in order to compare various formulations of the optimisation problem. These formulations are mainly based on the angles of each layer or the polar parameters presented in section 2.2. The results and the convergence speed of these formulations are compared to one another for a straight geometry in order to find the most adequate formulation. Next, using the optimisation formulation based on the polar parameters, the domain of study is limited to the orthotropic domain and the aeroelastic performance of three different geometries are optimised. This formulation is a multi-scale 2-level optimisation strategy which is based on a first-level of optimisation using the polar parameters with the purpose of maximising the flutter velocity and a second-level which is dedicated to obtain the stacking sequence that corresponds to the optimal polar parameters. To this end, the first-level is carried out and once the results of this optimisation study are obtained, the polar parameters are set as the target values of the second-level problem which can either analytically or numerically match a stacking sequence with similar elastic properties to the target polar parameters.

3.1.1 Optimisation in the anisotropic domain

The most simple and common optimisation variables used in aeroelastic tailoring, are the orientation of ply angles. The laminate can be constructed while varying the orientation of all the layers [114] or a subset of the most impactful plies [156, 157], in order to obtain an optimal performance. In this study, different formulations of the optimisation problem are proposed and tested: first of all, the direct approach is applied, where the orientations θ_k, $(k = 1, ..., N_{plies})$ of all the layers are considered as optimisation variables, thus letting the optimisation process explore the whole feasible domain of anisotropic laminates. The optimisation variables are then N_{plies} angles, being the laminate composed of N_{plies} layers. However, the direct formulation in terms of orientation angles admits no control over any specific laminate tensor and, particularly, it can give rise to laminate solutions which

are elastically coupled (i.e. $\mathbf{B} \neq O$). Anisotropy and couplings are often avoided in the composite materials as they overcomplicate the structural response of the laminate, but it seemed interesting to explore the optimal aeroelastic response of composite laminated structures over the whole anisotropic domain. Further on, aeroelastic optimisation can be limited to fully anisotropic uncoupled solutions by adding a constraint on the membrane-bending coupling matrix ($\mathbf{B}$), which can be expressed thanks to the polar formalism depending on orientation angles as optimisation variables, without the need to apply the classical and restrictive hypothesis of symmetric stacking sequences. Alternatively, one can impose uncoupling by optimising over symmetric stacking sequences, thus reducing the number of optimisation variables to $\frac{N_{plies}}{2}$ orientation angles and solving an unconstrained optimisation problem. Finally, it is possible to compare the resulting optimal solutions in case of different direct formulations of the aeroelastic optimisation problem.

It is well known that the direct approach has two drawbacks: on one hand, the objective and constraint functions are highly non-linear and non-convex in terms of the orientation angles, and, on the other hand, the dimension of the optimisation problems increases with the number N_{plies} of layers in the laminated structure [158]. Alternatively, it is possible to propose a formulation of the aeroelastic optimisation study in an anisotropic domain with the help of the polar parameters. This formulation of the optimisation problem allows to fix the number of the optimisation variables independently from the number of layers in the stacking sequence, as well as to render the optimisation and constraint functions less non-linear and non-convex (the main non-convexity being associated to the global orientation of the material anisotropy with respect to the global structural reference frame). This greatly simplifies the problem at structural level, which is generally the most complex and computationally expensive. A second step of the optimisation will be the search of stacking sequences corresponding to the optimal elastic parameters issued from the first-level structural optimisation step: this problem has been widely addressed in the literature [91] and it will be dealt with later on in this work (see section 3.2).

At the moment, it is important to recall that, as already explained in section 2.2, isotropic parameters are not to be considered as variables in the case of a composite laminate made of identical plies (layers made of the same base material and of same thickness). The optimisation variables correspond to the relevant polar parameters R_{K_X}, R_{K_Y}, R_1, Φ_1 needed to express the homogenised elastic properties of a fully anisotropic laminate and R_{K_X} and R_{K_Y} can be defined as

$$R_{K_X} = R_0 \cos 4(\Phi_0 - \Phi_1), \quad R_{K_Y} = R_0 \sin 4(\Phi_0 - \Phi_1) \tag{3.1}$$

where R_{KX}, R_{KY}, R_1 are the invariant elastic polar parameters representing the homogenised anisotropic

elastic properties of the laminate and Φ_1 is the orientation angle of the laminate with respect to the global reference frame associated to the structure.

Furthermore, feasibility constraints must be added to the first-level structural optimisation problem, which expresses the limits of the anisotropic domain of laminates in terms of their homogenised polar parameters, as written in equations (2.52) - (2.54)

$$\begin{aligned} 0 &\leq R_1 && (3.2)\\ -R_K^{BL} &\leq R_{K_X} \leq R_K^{BL} && (3.3)\\ -R_K^{BL} &\leq R_{K_Y} \leq R_K^{BL} && (3.4)\\ 2(\rho_1^2) - 1 &\leq 2(\rho_1^2)(\rho_{0_X}) - (\rho_{0_X}^2) - (\rho_{0_X}^2) && (3.5) \end{aligned}$$

where R_{K_X}, R_{K_Y} and R_1 represent the anisotropic moduli and Φ_1 the orientation of the anisotropic axis. The optimisation is subject to a constraint that defines the limits of the anisotropic domain in equation (3.5) in which the domain of investigation is restrained. The variables used to define the constraint read

$$\rho_{0_X} = \frac{R_{K_X}}{R_0^{BL}} \qquad \rho_{0_Y} = \frac{R_{K_Y}}{R_0^{BL}} \qquad \rho_1 = \frac{R_1}{R_1^{BL}} \tag{3.6}$$

and the anisotropic moduli R_0 can be decomposed to R_{K_X}, R_{K_Y} as

$$R_0^2 = R_{K_X}^2 + R_{K_Y}^2 \tag{3.7}$$

Formulations of the aeroelastic problem

Following the polar formalism, as expressed by parameters R_{K_X}, R_{K_Y}, R_1 and Φ_1, any optimisation problem for the composite laminated structure depends on 4 variables only in the fully anisotropic domain and it is independent from the number N_{plies} of laminate's layers. Furthermore, the polar formalism can be applied to any laminate tensor, which is relevant to represent the structural response: in the problem at stake in this work, the structure is subject to bending loads only, thus the relevant tensors are $\mathbf{D}$ or $\tilde{\mathbf{D}}$ for an uncoupled or a coupled laminate, respectively. Therefore, when running the optimisation problem, the resulting optimal solution terms of polar parameters can be interpreted as a coupled or uncoupled laminate, according to the hypothesis that the designer chooses to apply. This way, the hypotheses on elastic (un)coupling and other symmetries can be easily imposed at the

first level of structural optimisation and they result in a coherent parametrisation in terms of polar components, whilst the search of the optimal stacking sequences that satisfy these properties is postponed to the second-level optimisation step, i.e. the stacking sequence retrieval. Before addressing this aspect in the last section of this chapter, different formulations of the aeroelastic optimisation problem are tested and their influence on the optimisation results are compared.

Four preliminary study of the aeroelastic optimisation in the fully anisotropic domain has been conducted on a classical case issued from the literature [85, 69] in order to conduct comparison of results with the existing ones based on different strategies from different authors: the study case is a straight laminated-plate wing, as depicted in figure 3.1, composed of N_{plies}=16 layers.

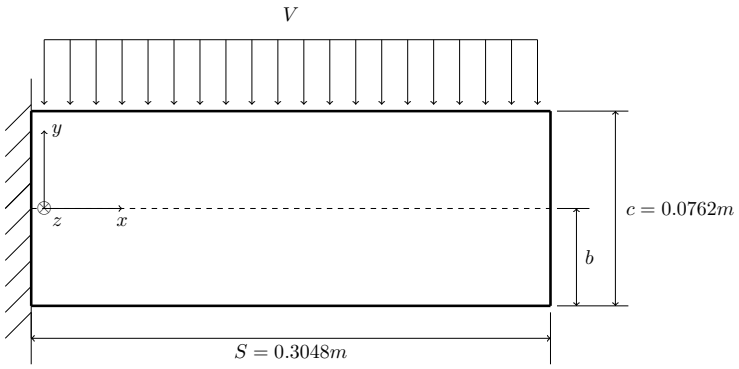

Figure 3.1: Representation of the straight cantilevered plate wing

These optimisation strategies are summarised in the following and for each case the optimisation formulations including the variables and the constraints employed are stated.

- Case 1 (direct approach, fully anisotropic and coupled domain): Optimisation of the flutter velocity using N_{plies}=16 ply angles, resulting in a fully anisotropic non-symmetric coupled laminate, which can show elastic coupling. For this purpose the optimisation can be formulated as an unconstrained non-convex optimisation problem as

$$\underset{\Theta}{\text{maximize}} \quad V_f \tag{3.8}$$

  where V_f represents the flutter velocity and Θ the N_{plies}-dimension vector of variables, i.e. stacking sequence with ply angles that vary from $-90°$ to $90°$ with an increment of $5°$.

- Case 2 (direct approach, fully anisotropic domain with uncoupling constraint): Optimisation of the flutter velocity using N_{plies}=16 ply angles while imposing a constraint on the degree of coupling using the polar components of the rigidity matrix ($\mathbf{B}$), resulting in a fully anisotropic

non-symmetric uncoupled laminate

$$\begin{aligned} \underset{\Theta}{\text{maximize}} \quad & V_f \\ \text{subject to} \quad & \frac{||R_0^{\mathbf{B}} + 2R_1^{\mathbf{B}}||}{||R_0^{BL} + 2R_1^{BL}||} - \epsilon < 0, \end{aligned} \tag{3.9}$$

where $R_0^{\mathbf{B}}$ and $R_1^{\mathbf{B}}$ represent the anisotropic moduli of the normalised coupling rigidity matrix $\mathbf{B}^*$, R_0^{BL} and R_1^{BL} indicate the anisotropic moduli of the Base Layer (BL) and $\epsilon = 10^{-3}$. Formulation (3.9) corresponds to a constrained non-convex optimisation problem.

- Case 3 (direct approach, anisotropic domain limited to uncoupled symmetric stacking sequences): Optimisation of the flutter velocity using $\frac{N_{plies}}{2} = 8$ ply angles, resulting in a symmetric uncoupled laminate

$$\underset{\Theta_{\text{sym}}}{\text{maximize}} \quad V_f \tag{3.10}$$

Formulation (3.10) corresponds to an unconstrained non-convex optimisation problem in terms of the reduced vector of variables Θ_{sym} representing only half of the stacking sequence. The optimal solutions are limited to the symmetric set of stacking sequences.

- Case 4 (multi-scale approach, fully anisotropic domain of $\tilde{\mathbf{D}}$): Optimisation of the flutter velocity using 4 polar parameters (R_{K_X}, R_{K_Y}, R_1, Φ_1) that are able to define the entire anisotropic domain of the bending stiffness tensors $\mathbf{D}$ or $\tilde{\mathbf{D}}$ and for which a laminate with desired properties can be retrieved at the second level of the optimisation process

$$\begin{aligned} \underset{R_{K_X}, R_{K_Y}, R_1, \Phi_1}{\text{maximize}} \quad & V_f \\ \text{subject to} \quad & 2(\rho_1^2)(1 - \rho_{0_X}) + (\rho_{0_X}^2) + (\rho_{0_Y}^2) - 1 \leq 0, \end{aligned} \tag{3.11}$$

The anisotropic moduli R_{K_X}, R_{K_Y}, R_1 and the polar angle Φ_1 represent the optimisation variables and the constraint defines the limits of the admissible anisotropic domain. These variables and relationships have been introduced in section 2.2 and reminded at the beginning of this section.

Results

The optimisation problems expressed by equations (3.8)-(3.11) are all solved by the use of a Genetic Algorithm (GA) [122] with the numerical parameters fixed to $N_{ind} = 100$ individuals (i.e. search points in the design space) and $N_{gen} = 50$ generations (i.e. optimisation iterations). The material properties of the base US composite layer composing the laminate are described in table 3.1 and stay the same throughout the entire study.

$E_1[GPa]$	$E_2[GPa]$	$G_{12}[GPa]$	$\nu_{12}[-]$	$\rho[kg/m^3]$	Ply thickness $t[mm]$
138.0	8.96	7.1	0.3	1600	0.1

Table 3.1: Engineering elastic properties of AS4/3502 base Uniform-Stiffness (US) lamina.

The stiffness tensor $\mathbf{Q}$ of the base layer can be calculated using the engineering elastic properties. Table 3.2 represents the polar parameters of this tensor.

$T_0[GPa]$	$T_1[GPa]$	$R_0[GPa]$	$R_1[GPa]$	$\Phi_0[^\circ]$	$\Phi_1[^\circ]$
21.35	19.15	14.25	16.23	0	0

Table 3.2: Polar parameters of AS4/3502 base Uniform-Stiffness (US) lamina.

Table 3.3 represents the domain of definition for each optimisation variable defined for the bending behaviour of a 16-layer laminate (polar parameters representing tensor $\mathbf{D}$ or $\tilde{\mathbf{D}}$). It needs to be noted that variables R_{K_X}, R_{K_Y} and R_1 are treated as continuous variables by the optimisation algorithm while Φ_1 is a discretised variable with a 1° step and the ply angles discretised with a step of 5°.

	$R_{K_X}[GPa]$	$R_{K_Y}[GPa]$	$R_1[GPa]$	$\Phi_1[^\circ]$	angles $[^\circ]$
Variable bounds	[-14.25,14.25]	[-14.25,14.25]	[0,16.23]	[-90,90]	[-90,90]
Variable nature	continuous	continuous	continuous	discrete, step = 1°	discrete, step = 5°

Table 3.3: Ranges of definition and nature of the optimisation variables in the anisotropic domain.

Table 3.4 presents the results obtained by the four optimisation studies described previously. For all cases, the optimisation was carried out in an anisotropic domain. The first result corresponds to the formulation of Case 1, with N_{plies}=16 orientation angles as optimisation variables and no constraint

on the elastic coupling. The polar parameters of the final optimal sequence indicate that it is fully anisotropic with no elastic symmetries (R_0 and R_1 are not zero, and the angular invariant $\Phi_0 - \Phi_1$ is not a multiple of $\frac{\pi}{4}$).

The second result is obtained using the N_{plies}=16 ply orientations as optimisation variables but this time a constraint is imposed to trigger the uncoupled laminates (formulation of Case 2). The corresponding sequence is again fully anisotropic with no preferred direction of symmetry (R_0 and R_1 are not zero, and the angular invariant $\Phi_0 - \Phi_1$ is not a multiple of $\frac{\pi}{4}$). In comparison to the previous case, the flutter velocity can not reach values as high as the coupled case but the flutter frequencies are in close intervals which suggests that the same aeroelastic modes have caused the instability. It needs to be noted that the value of constraint on the degree of coupling is 4×10^{-3}, which can be considered sufficiently small to satisfy the uncoupled condition. The lower value of the optimal flutter velocity in the case of an uncoupled solution obtained by imposing a constraint on the degree of coupling in the direct approach (optimisation formulation in terms of the laminate's orientation angles) can also be justified by the fact that the optimisation problem is highly non-convex and the optimisation algorithm might get stuck in a local minimum.

Case	$R_0[GPa]$	$R_1[GPa]$	$\Phi_1[^\circ]$	$\lvert\Phi_0 - \Phi_1\rvert[^\circ]$	$V_f[m/s]$	$\omega_f[rad/s]$	sequence [°]
1	10.80	4.01	4.7	39.0	144.7	482.6	**[40, -35, -40, 35, -50, 75, 45, 15, -80, 25, 45, 50, 30, -35, -40, 30]**
2	8.25	2.83	33.7	10.1	137.0	469.2	**[40, -25, 40, -65, -35, -80, 50, -90, -50, 0, -30, -35, 30, 75, -50, 40]**
3	12.24	4.12	-1.4	44.8	146.7	469.5	$\mathbf{[35, -40, -40, 40, -35, 35, 30, 0]_s}$
4	**12.60**	**3.47**	**8.0.**	**34.8**	146.8	459.3	-

TABLE 3.4: Results of the deterministic optimisation in the anisotropic domain. In the first three cases, the optimisation variables are the orientation angles (the corresponding polar parameters are calculated a posteriori), whilst in the last case polar parameters are the optimisation variables.

The third case in table 3.4 corresponds to an exact uncoupled laminate, since symmetry is imposed on the stacking sequence. In this case, the difference between the polar angles is very close to $\frac{\pi}{4}$: this value indicates that the laminate has very close properties to an orthotropic symmetry. The flutter velocity is increased by about 1% compared to the fully anisotropic coupled laminate. This rise can be due to the faster convergence of this strategy because of the number of the optimisation variables which is half of the previous cases as a results of the symmetric laminate.

Finally, the optimal case obtained using the polar parameters is presented. The flutter velocity is very close to the Case 3 (symmetry imposed on the stacking sequence) with less than 1% difference.

The flutter frequencies are almost 2% apart but can be considered to belong to the same aeroelastic mode. While the anisotropic moduli (R_K and R_1) between the configuration obtained by the polar parameters (Case 4) and the symmetric configuration (Case 3) are close, the polar angles show large differences. More specifically the difference of polar angles $|\Phi_0 - \Phi_1|$ corresponding to the last strategy is not close to 0° or $\frac{\pi}{4}$ which indicates a fully anisotropic behaviour of the laminate. Almost equal critical flutter velocities for the optimal points in cases 3 and 4 allows to understand that the optimisation problem has several, almost equivalent, optimal solutions.

An important factor in choosing an optimisation strategy can be the speed of convergence. Given the three highest flutter velocities in table 3.4, their convergence of mean and maximum values of the objective function are compared in figure 3.2. The maximum flutter velocity obtained at the first generation, belongs to the strategy conducted with polar parameters (Case 4). This maximum value evolves in different manners for each strategy, either by stagnating over multiple generations or sudden jump of the objective function from one generation to the other as shown for the non-symmetric configuration. The mean values indicate that the case with polar parameters have the lowest mean velocity at the beginning of the optimisation compared to the cases obtained with ply angles. On the other hand, at the last generation, the mean value of the former is significantly higher than the other strategies. This observation indicates that the optimisation conducted using the polar parameters investigates a larger domain and has a lower chance of obtaining a local maximum. Comparing both cases 1 and 3 (formulated in terms of ply angles), the non-symmetric configuration has a slower convergence speed which is expected due to its large number of optimisation variables. It can be concluded that given its optimal flutter velocity and the convergence speed, the non-symmetric configuration of Case 1 is the least efficient strategy.

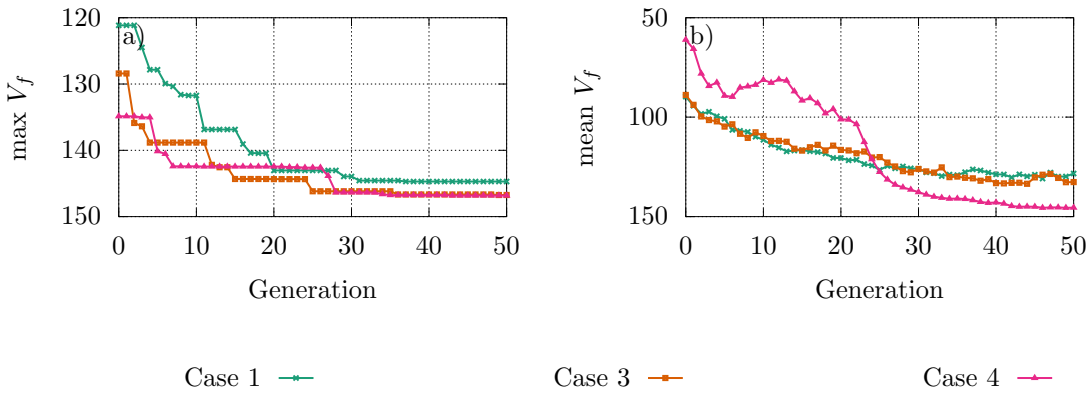

Figure 3.2: Convergence of the optimisation algorithm for three formulations. a) max V_f and b) mean V_f

The elastic and aeroelastic behaviour of the last two cases (Case 3: symmetric ply angles and Case 4: polar parameters) will next be compared in order to obtain the ideal optimisation formulation. Figure 3.3 represents the second and the third aeroelastic modes of these two optimal configurations. Both cases demonstrate similar behaviours, with the second mode that becomes unstable and the third mode that is close to the flutter boundary (zero horizontal axis). The damping plots for mode 2 (green curves in figure 3.3.a) in the two cases, angles and polar parameters, completely overlap, and the corresponding curves for the frequency plots (green curves in figure 3.3.b keep in a very close interval, as well. Concerning the third mode (red curves in figure 3.3), frequency plots are almost confused between the angle and polar parameter cases, whilst interestingly a difference can be observed in the damping plot (figure 3.3.a): the damping curve of mode 3 for the angle case solution stays farther from the zero horizontal axis, i.e. it keeps a greater margin of stability compared to the optimal solution of Case 4, based on the polar parameter formulation.

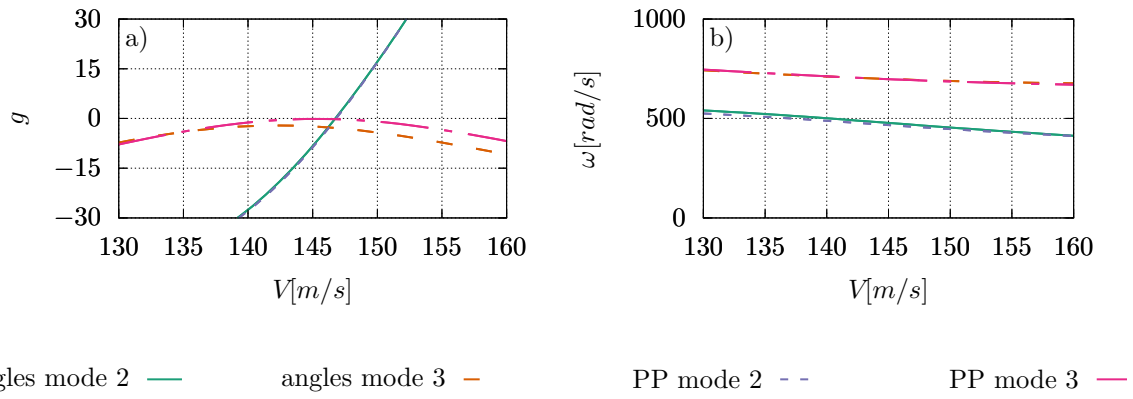

FIGURE 3.3: The evolution of a) aeroelastic damping and b) aeroelastic frequency for the optimal Uni Directional composite laminated straight wings obtained in Case 3, symmetric ply angles and , and in Case 4, Polar Parameters (PP).

Figure 3.4 visualises both unstable modes for the optimal solutions of cases 3 and 4 (last two lines in table 3.4): as mentioned before via the interpretation of the similar values of flutter frequencies, the unstable modes are almost identical, resulting from the coupling between the two structural modes, first torsion and second bending.

Figure 3.5 represents the anisotropic elastic properties of the optimal laminates, namely their bending and torsional moduli. The Young modulus shape (green curve in figure 3.5.a), representing the bending stiffness for the symmetric configuration obtained by ply angles (Case 3) is very similar to an

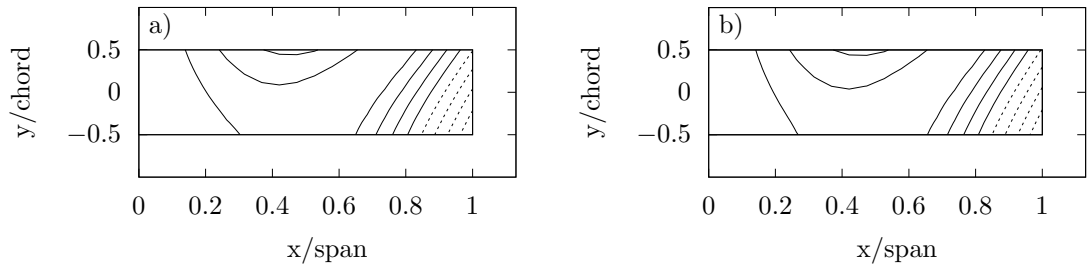

Figure 3.4: Shape of the unstable aeroelastic mode for the optimal US solutions of composite laminated straight wings: a) Case 3, of ply angles and b) Case 4, polar parameters.

orthotropic symmetry with two preferred directions (this is coherent with the value of the polar angular difference in table 3.4: for Case 3 $\Phi_0 - \Phi_1 = 44.8°$). On the other hand, the optimal case obtained using polar parameters (Case 4, red discontinuous line in figure 3.5.a) is more definitely anisotropic in agreement with the value of the polar angular difference in table 3.4: $\Phi_0 - \Phi_1 = 34.8°$). The torsional moduli of both cases (figure 3.5.b) are very similar both in shapes and values, but one can note the small deviation from the principal global axes (0°-90° directions) of the optimal solution obtained in Case 4, formulation based on the polar parameters: table 3.4 gives for this case the stiffness polar angles $\Phi_1 = 8°$ and $\Phi_0 - \Phi_1 = 34.8°$, meaning $\Phi_0 = 42.8°$, which approximatively corresponds to the weak direction for the torsional modulus (red discontinuous curve in figure 3.5.b).

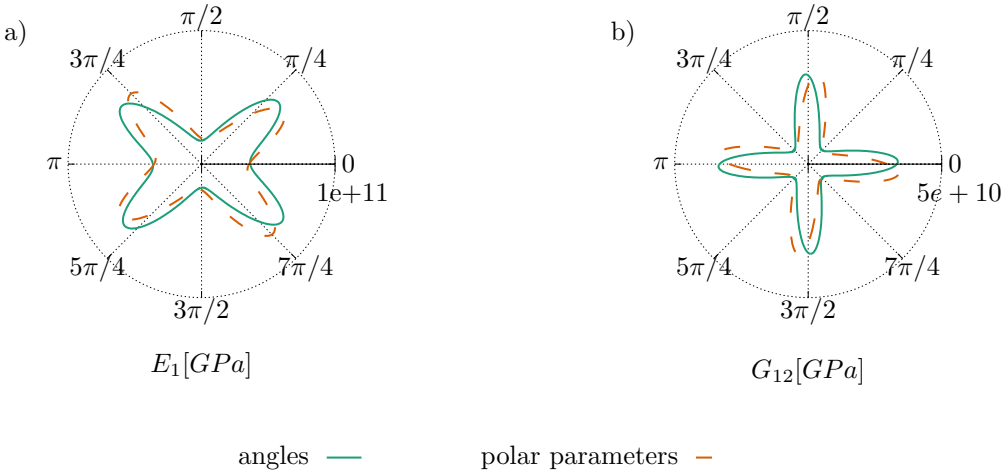

Figure 3.5: Elastic properties of the two optimal cases obtained with symmetric ply angles and polar parameters as optimisation variables.

Given the comparison conducted in aeroelastic, elastic and convergence behaviour of the previous optimisation strategies, two configurations stand out: The case obtained by the symmetric ply angles (Case 3) and the one obtained by the polar parameters (Case 4). They both converge toward similar flutter velocities with analogous speed of convergence. These comparable results were obtained while the strategy using the polar parameters investigates a larger domain since the anisotropic moduli (R_{K_X}, R_{K_Y} and R_1) are treated as continuous functions. It also needs to be pointed out that the latter strategy has examined a larger sample of configurations (as it was observed on the convergence plot of the mean flutter velocities per generation) which avoids convergence to a local maximum. It can be concluded that the study conducted by polar parameters is more accurate, more diverse and more efficient to investigate a domain of elastic symmetry, even if it does not result in an explicit result in terms of a laminate stacking sequence. The strategies to retrieve optimal stacking sequences are detailed in section 3.2.

3.1.2 Optimisation in the orthotropic domain

The domain of investigation is restrained to orthotropy as this symmetry was observed for one of the previous optimal configurations with the highest flutter velocity, but also because it is generally admitted that the design of composite laminated structures requires some basic elastic symmetries, namely orthotropy. It is quite rare to investigate the fully anisotropic space of laminates and the objective of the previous section was to explore the aeroelastic response of simple structures, such as straight wings, in order to compare the results with the more standard case of orthotropic laminates. The advantage of using the polar formulation is to be able to trigger orthotropy by simply adapting the parametrisation of the problem, as explained in section 3.1.1: whilst the fully anisotropic case is represented by the polar parameters R_{K_X}, R_{K_Y}, R_1 and Φ_1 (see equations (3.2)- (3.5)), in the orthotropic case R_{K_Y} vanishes and the orthotropic behaviour only depends only on two elastic moduli R_K (which is the equivalent of R_{K_X} in the anisotropic space) and R_1, and one polar angle Φ_1. Thanks to this further simplification of the polar parametrisation of orthotropic laminates, an introductory parametric study can be conducted over the orthotropic domain in the case of a straight laminated plate wing of identical configuration as in section 3.1.1. For this purpose, the principal orthotropy axis Φ_1 of the laminate is considered fixed and aligned with the wing axis, i.e. $\Phi_1 = 0°$, whilst the parameters at study are the polar moduli R_K and R_1, varying within the same definition intervals given in table 3.3 for a 16-layer laminate made of the base layer AS4/3502 of table 3.1 (for the parametric study, the intervals are divided into 200 and 100 steps, respectively for R_K and R_1). In addition, R_K and R_1 must satisfy the geometric constraints for the orthotropic behaviour of the laminate, as expressed by equations (2.52)- (2.54).

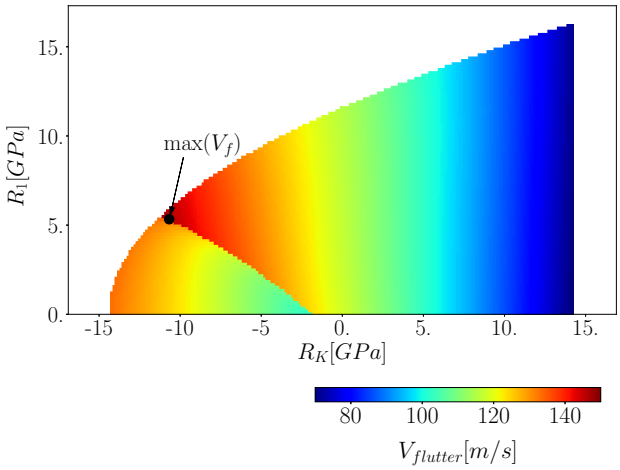

Figure 3.6: Variation of the flutter velocity in an orthotropic domain as a function of the anisotropic moduli R_K and R_1 where $\Phi_1 = 0$ for a straight wing.

Figure 3.6 represents the response surface of the variation of the flutter velocity V_f for the straight plate wing defined in section 3.1.1, as a function of the anisotropic moduli R_K and R_1 in the orthotropic domain of 16-layer laminates made of AS4/3502 for $\Phi_1 = 0°$. One can note that the upper bound of the domain corresponds to the geometric constraint on orthotropic laminates, defined in equation (2.54). The response surface indicates the separation of the two modal regions by a mode switch causing a discontinuous surface. The maximum flutter velocity obtained following the discretisation of the parametric study (V_f = 147.1 m/s, R_K = -11.83 GPa, R_1 = 5.44 GPa), presented on the response surface, is located next to this discontinuity (black dot in figure 3.6).

To further investigate the orthotropic domain, an optimisation study is carried out considering variations of the polar angle Φ_1. The formulation of the problem is presented in (3.12) with the polar parameters employed as the optimisation variables. These parameters allow a direct control over the elastic properties of the laminates and permit a restriction of the anisotropic domain. These restrictions reduce the domain of study while ensuring the elastic symmetries of the optimal laminate. In this optimisation study, the geometrical bound of the orthotropic domain expressed as a function of the polar parameters defines the constraint of the research interval

$$\begin{aligned} &\underset{R_K,R_1,\Phi_1}{\text{maximize}} \quad V_f \\ &\text{subject to} \quad -(\rho_0) + 2(\rho_1^2) - 1 \leq 0, \end{aligned} \tag{3.12}$$

where

$$\rho_0 = \frac{R_K}{R_0^{BL}} \qquad \rho_1 = \frac{R_1}{R_1^{BL}} \tag{3.13}$$

Once the optimal case is obtained by means of the polar parameters, a second-level study can be carried out to retrieve the corresponding stacking sequence. There are multiple ways to conduct the second-level optimisation and they will be explained in details in section 3.2, however different families in the orthotropic domain (angle-ply, cross-ply, quasi-trivial) can help to find analytical solutions identical to the optimal polar parameters.

The optimisation formulation developed using the polar parameters in (3.12) is generalised to a larger number of configurations, including a great variety of geometries with forward and backward swept wings. In the first place, a fixed value of the deviation angle is considered, $\alpha_{swept} = 15°$, which is positive in the case of swept-forward wing and negative in the case of swept-backward. Table 3.5 summarises the optimisation results for all Uniform-Stiffness (US) configurations studied in this work with orthotropic laminates, i.e. elastic properties belonging to the orthotropic domain of figure 2.6. The bold coloured values, indicate that those variables are fixed and not optimised during the optimisation process.

Case ID	Wing configuration	$R_K[GPa]$	$R_1[GPa]$	$\Phi_1[°]$	$\alpha_{swept}[°]$	$V_f[m/s]$	$\omega_f[rad/s]$
st1	straight	-10.68	5.33	0.	**0.**	146.5	499.0
st2	straight (variable α_{swept})	-12.63	3.58	-2.	0	146.7	459.8
swb1	swept-backward	-13.46	2.68	**-15.**	**-15**	130.5	411.7
swb2	swept-backward	14.25	1.31	-56.	**-15**	140.8	711.5
swf1	swept-forward	4.13	12.70	**15.**	**15**	92.0	0.
swf2	swept-forward	13.63	4.09	47.	**15**	137.0	394.5

TABLE 3.5: Results of deterministic optimisation for different US configurations using polar parameters and swept-angle as optimisation variables where the bold red coloured values indicated constant parameters during the optimisation process.

The first case (*st1* in table 3.5) concerns the optimisation of a straight plate wing in the orthotropic domain. The optimisation variables are the anisotropic moduli R_K and R_1 and the orientation of the orthotropic axis Φ_1. The optimal case obtained corresponds to a laminate with its orthotropic axis aligned with the principle axis of the wing. With an additional variable that defines the angle of swept wings α_{swept}, an optimisation problem with 4 variables is then carried out. The second optimal configuration (case *st2* in table 3.5) corresponds to a straight wing with an orthotropic axis that is slightly deviated. While this deviation increases the flutter velocity, this augmentation remains limited to less than 1%. The anisotropic moduli of both optimal straight cases are in close intervals which indicates similarities in elastic properties. While both the flutter velocities and the polar parameters of these two configurations are analogous, the flutter frequencies exhibit a difference of about 8%.

After performing the most general optimisation study, some special cases have been considered. A swept-backward wing with a swept angle of 15° is the first configuration to investigate. Initially, the optimisation problem is formulated for a swept-backward wing with the orthotropic axis aligned with the main axis of the structure (case case *swb1* in table 3.5). In this case the flutter velocity (V_f = 130.5 m/s) decreases compared to the straight case (V_f = 146.5 m/s). On the other hand, including the orientation of the orthotropic axis in the optimisation problem (case *swb2* in table 3.5), increases the flutter velocity (V_f = 140.8 m/s) by more than 7%. Comparing the flutter frequencies of both swept-backward cases, it is observed that they are not in the same range of values (ω_f = 411.7 rad/s, ω_f = 711.5 rad/s). This difference might indicate that the unstable aeroelastic mode is not the same for both cases. These observations show that for a swept-backward wing, the direction of the orthotropic axis is more influential than for a straight wing. The same type of study is then carried out for a swept-forward wing with a swept angle of 15°. Similar behaviour is observed while varying the alignment of the orthotropic axis. In this case V_f increases by about 48%(between case *swf1* and case *swf2* in table 3.5). This improvement is more significant than the swept-backward case and proves the importance of the orientation of the orthotropic axis (Φ_1). Concerning the flutter frequencies, the unstable mode switches from divergence (ω_f = 0. rad/s) to an unsteady flutter mode (ω_f = 394.5 rad/s). The latter behaviour renders the swept-forward case with an unaligned orthotropic axis to the reference axis more favourable because the case *swf2* configuration avoids the divergence instability which is a recurring event in the swept-forward wings.

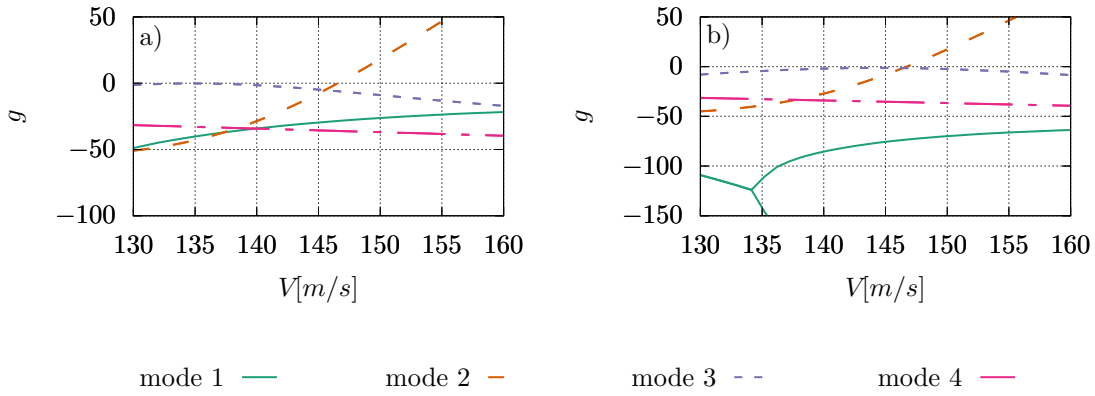

Figure 3.7: The evolution of aeroelastic damping. a) case *st1* and b) case *st2*.

Figure 3.7, shows the evolution of damping and frequency of the first four aeroelastic modes of the optimal case *st1* and case *st2* cases. The instability appears on the second mode for both cases but the third mode is very close to the zero axis thus the instability. Contrary to the second configuration,

when the orthotropic axis is completely aligned with the reference axis (case *st1*), the third mode is closer to instability at the lower velocities while for the second configuration with a slight change of Φ_1 value (case *st2*), the third mode approaches the axis at higher speeds near the flutter velocity V_f.

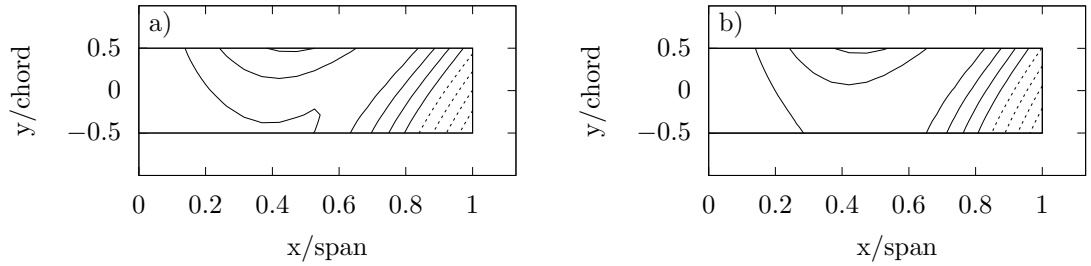

FIGURE 3.8: The aeroelastic mode shapes: a) case *st1* and case *st2*.

As shown in figure 3.8, both configurations exhibit the same unstable mode shape which corresponds to the second aeroelastic mode, that for this case is obtained with a combination of second bending and first torsion structural modes.

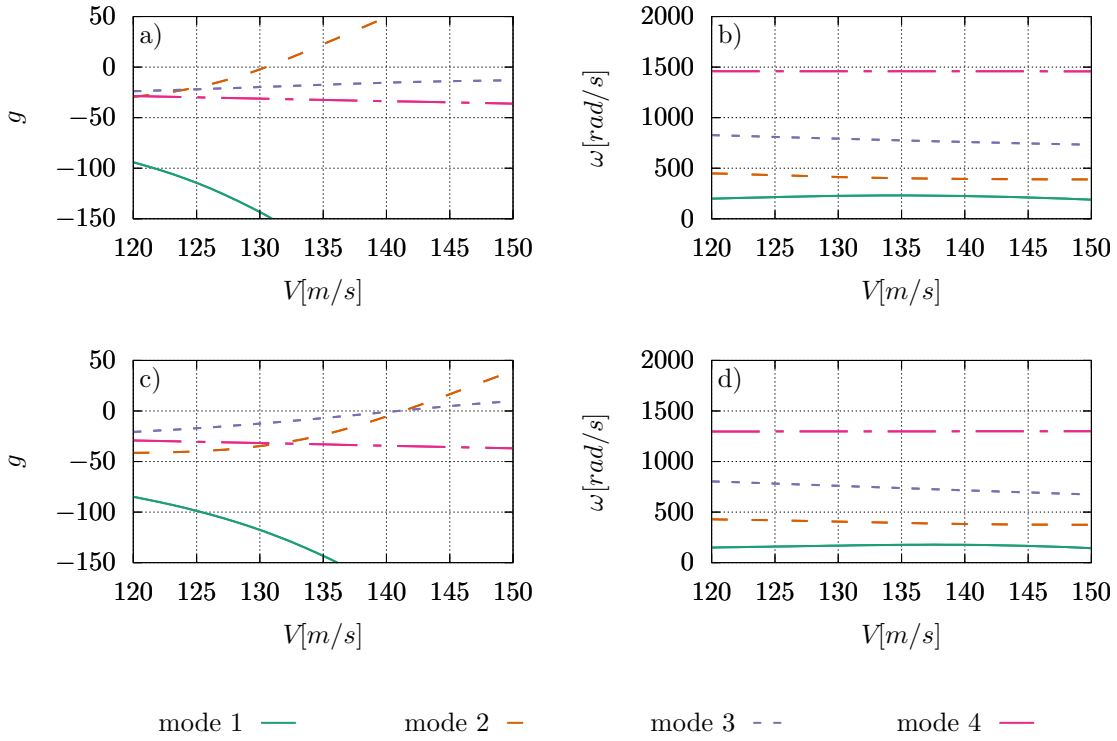

FIGURE 3.9: The evolution of (a,c) aeroelastic damping and (b,d) aeroelastic frequency. (a,b) case *swb1* and (c,d) case *swb2*.

The aeroelastic evolutions of both optimal swept-backward configurations in figure 3.9 manifest differences in the unstable mode. For swept-backward case with aligned orthotropic axis and main reference axis (case *swb1*), the second aeroelastic mode becomes unstable but for the case with a Φ_1 unaligned with the reference axis (case *swb2*), the third mode becomes positive. On the other hand, in the latter case (case *swb2*), the second mode becomes immediately unstable after the third mode while in the case of case *swb1*, other modes are quite far from the axis zero meaning far from instability. The unstable modes for both optimal cases are presented in figure 3.10.

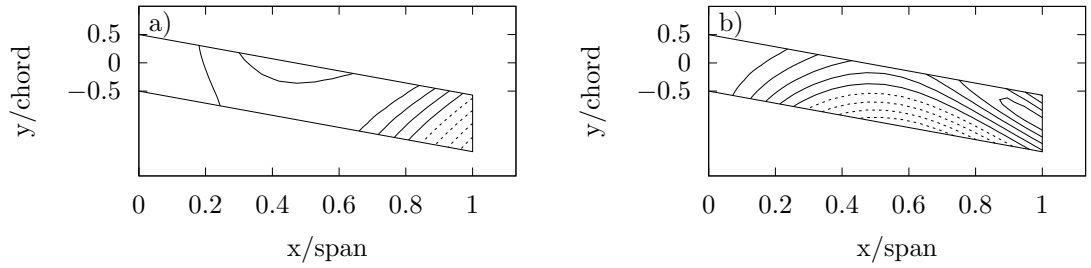

Figure 3.10: The aeroelastic mode shapes: a) case *swb1* and case *swb2*.

The second aeroelastic mode which is a combination of the second bending and the first torsion mode, is demonstrated in figure 3.10.a). The third aeroelastic mode is presented in figure 3.10.b), corresponding to a first torsion and the third bending mode.

The same comparison has been made for the swept-forward cases in figure 3.11. While the orthotropic axis is aligned with the main axis of the wing (case *swf1*), the instability occurs on the first mode which results in an aeroelastic divergence. On the contrary, when the angle Φ_1 is included in the optimisation process (case *swf2*), the divergence mode is far from instability and the same behaviour as the previous cases is observed. This time again, the second aeroelastic mode is unstable and while the third mode is close to instability, unlike the swept-backward case, it does not become unstable.

Figure 3.12 represents the corresponding unstable modes. A divergence mode corresponding to a pure bending shape is observed for the swept-forward configuration with aligned orthotropic axis to the principle axis (case *swf1*) and the second aeroelastic mode for the unaligned case (case *swf2*).

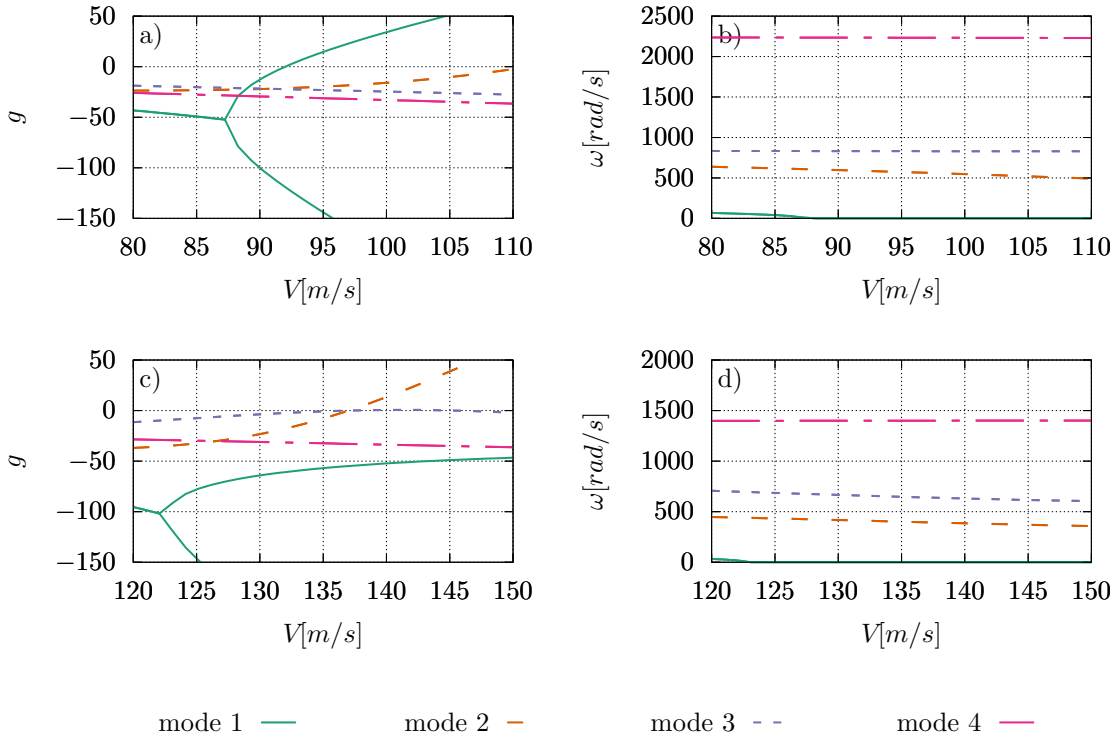

FIGURE 3.11: The evolution of (a,c) aeroelastic damping and (b,d) aeroelastic frequency. (a,b) case *swf1* and (c,d) case *swf2*.

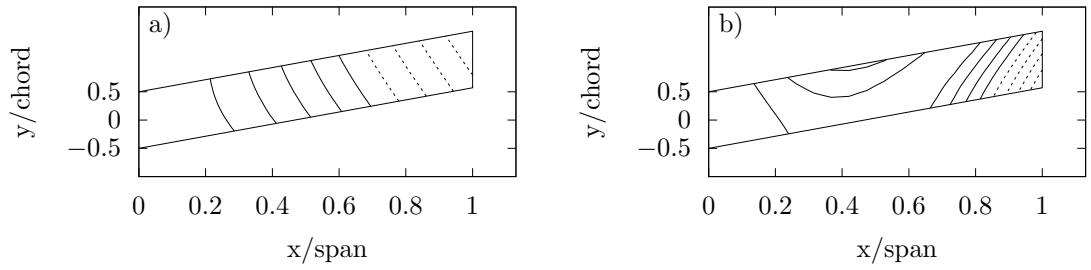

FIGURE 3.12: The aeroelastic mode shapes: a) case *swf1* and b) case *swf2*.

3.2 Stacking sequence retrieval

The optimisation using polar parameters has been conducted previously for multiple configurations and the optimal aeroelastic behaviours have been obtained. The second level of this study is naturally to retrieve stacking sequences that correspond to the optimal polar parameters. As explained in section 2.2, there are multiple families in the orthotropic domain which allow the construction of

the stacking sequence for a given set of polar parameters analytically. These stacking sequences are called the quasi-trivial sequences due to their elastic properties. These solutions cover the majority of the orthotropic domain and have the advantage of giving an exact solution matching the given polar parameters. However, there are parts of the domain that do not correspond to a quasi-trivial sequence and thus another solution needs to be established to construct a matching stacking sequence for the given set of polar parameters.

A solution that is widely used in the study of composite structures, is a numerical optimisation study in which a cost function is minimised that measures the similarity between the target set of polar parameters and the corresponding stacking sequence. This cost function can be defined with different formulations [79]. In this study the Kullback-Leibler function defined by Moakher [159] is used to minimise the difference between the rigidity properties of a set of polar parameters and a given stacking sequence

$$\mathbf{F_{ABD}}(\Theta, \mathbf{L_T}) = \mathrm{tr}(\mathbf{L}(\Theta)\mathbf{L_T^{-1}}) + \mathrm{tr}(\mathbf{L}(\Theta)^{-1}\mathbf{L_T}) - 12 \qquad \text{with} \qquad \mathbf{L} = \begin{bmatrix} \mathbf{A} & \mathbf{B} \\ \mathbf{B} & \mathbf{D} \end{bmatrix} \tag{3.14}$$

where subscript $\mathbf{T}$ represents the Target matrices associated to the optimal polar parameters, all $\mathbf{L}$ matrices are defined as a function of the rigidity tensors of the composite structure.

In order to choose the best method for the stacking sequence retrieval (analytical or numerical), all the optimal cases are positioned in the orthotropic domain as presented in figure 3.13.

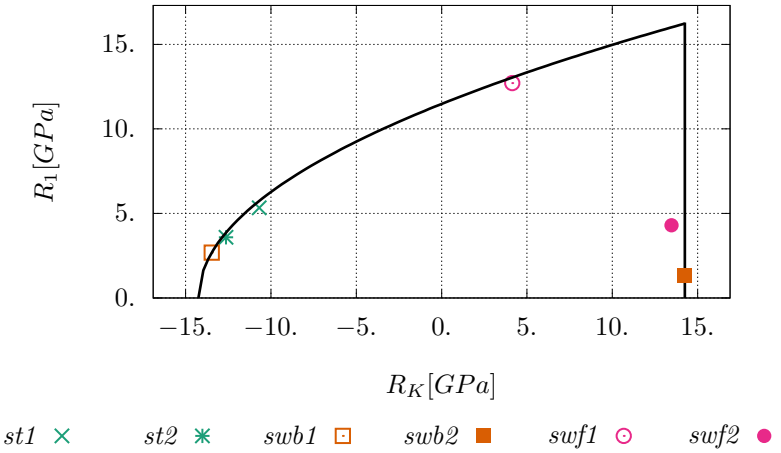

Figure 3.13: Placement of the anisotropic moduli of Uniform-Stiffness optimal cases in the orthotropic domain given the anisotropic moduli in table 3.5.

Most of the optimal configurations (solutions *st1*, *st2*, *swb1*, as depicted in figure 3.13) are close to the angle-ply curve and the stacking sequence can thus be analytically calculated. For two cases on the far right side of the domain, an optimisation problem is conducted. Figure 3.14 details the 2-level optimisation process.

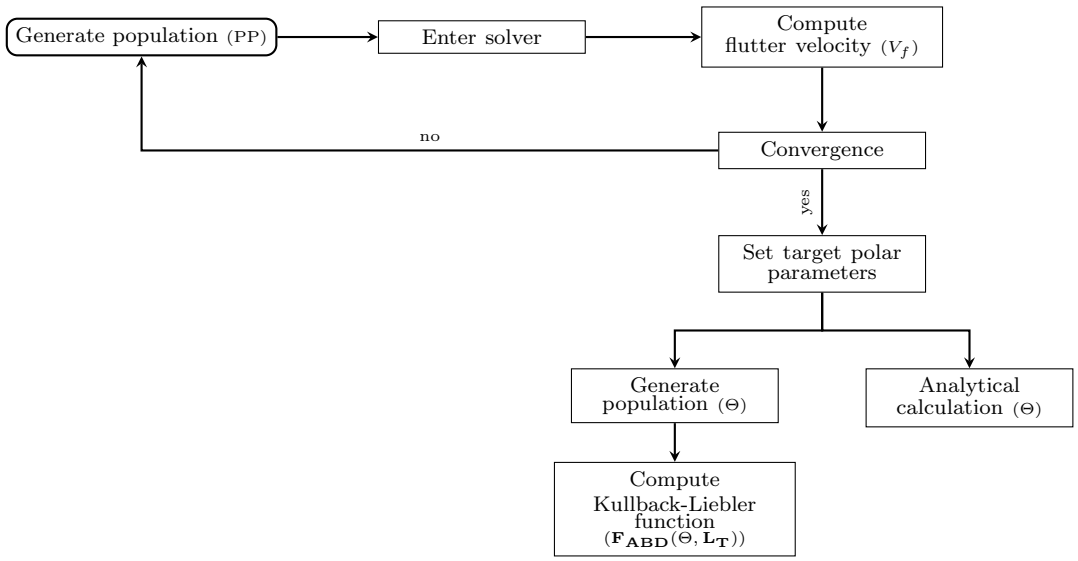

FIGURE 3.14: 2-level optimisation algorithm using polar parameters.

For the cases over the angle-ply curve (*st1*, *st2*, *swb1* in table 3.5 and in figure 3.13), the relationships defined in equation (2.56) can be employed to find the angle θ used to construct the stacking sequence, which must be itself selected amongst the available quasi-trivial solution in order to satisfy both properties of uncoupling and homogeneity (being the bending and in-plane behaviours are identical, the choice of the lamination angle defined by equation (2.56) assures the optimal orthotropy for the bending behaviour as well). The results for these four cases are thus summarised in table 3.6.

Case ID	stacking sequence [°]	$R_K[GPa]$	$R_1[GPa]$	$V_f[m/s]$	$\omega_f[rad/s]$
st1	$[35_2, -35_4, 35_2, -35_2, 35_4, -35_2]$	-10.91 + ∼ 2%	5.54 + ∼ 1%	147.0 + ∼< 1%	497.4 − ∼< 1%
st2	$[36_2, -40_4, 36_2, -40_2, 36_4, -40_2]$	-12.58 − ∼< 1%	3.92 + ∼ 2%	146.2 + ∼< 1%	462.7 + ∼< 1%
swb1	$[25_2, -55_4, 25_2, -55_2, 25_4, -55_2]$	-13.39 − ∼< 1%	2.81 + ∼< 1%	130.5 + ∼< 1%	413.8 + ∼< 1%
swf1	$[33_2, -3_4, 33_2, -3_2, 33_4, -3_2]$	4.40 + ∼ 2%	13.12 + ∼ 3%	92.0 + ∼< 1%	0.

TABLE 3.6: Stacking sequence retrieval results for optimal configurations over the angle-ply curve. The polar parameters are calculated from the stacking sequence which is a result of rounded analytical angles. Small percentages in front of each parameter, indicate the difference between the approximated stacking sequence and the optimal configurations presented in table 3.5.

The flutter velocities in this table correspond to the approximation applied to θ in order to obtain an integer for the orientation of the plies. It must be noted that the stacking sequences presented in this study are all rotated to the frame of orthotropy, meaning according to the value of Φ_1 and lamination angles are rounded to the closest integer. The aeroelastic responses between the optimal cases and the retrieved stacking sequences are quite close. The elastic properties between the results of these two levels are compared in figure 3.15 to visualise the error this second step can produce. The comparison of the bending and shear moduli manifests a good agreement between the elastic properties of both levels, because the quasi-trivial quasi-homogeneous angle-ply optimal laminates are exact solutions for uncoupling and orthotropy but the values of lamination angles are rounded to the closest integer.

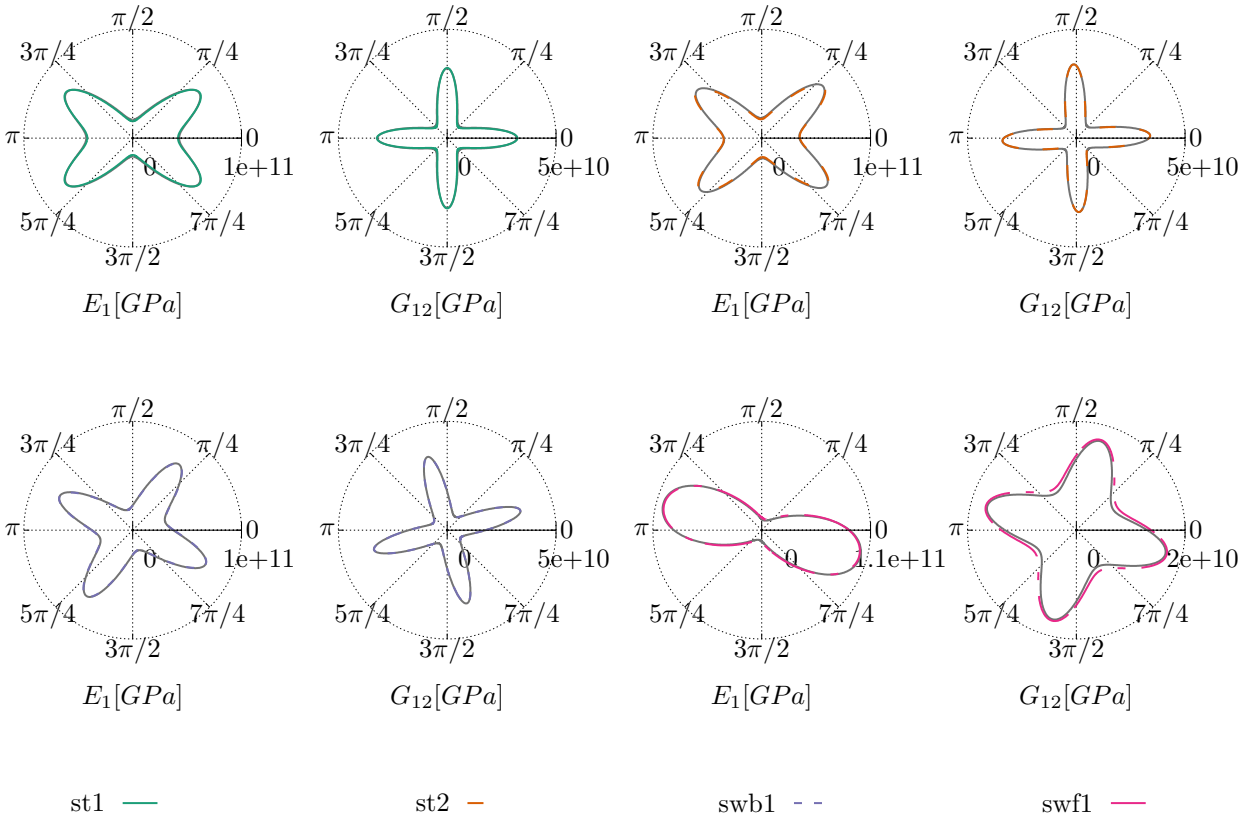

Figure 3.15: Comparison of the young moduli between the results of the optimisation and their corresponding stacking sequences obtained analytically. The gray lines on each figure correspond to the target properties and the each coloured line corresponds to the configuration indicated on the label.

For the two cases on the right side of the orthotropic domain (case *swb2* and case *swf2* in table 3.5 and in figure 3.13), the Genetic Algorithm is employed to minimise the Kullback-Leibler function and find an optimal stacking sequence.

$$\underset{\boldsymbol{\Theta}}{\text{minimize}} \quad \mathbf{F_{ABD}}(\Theta, \mathbf{L_T}) \tag{3.15}$$

The optimisation parameters used for this process are identical for all cases and equal to 300 individuals in 200 generations. The stacking sequences equivalent to these two optimal cases are retrieved with the help of the numerical optimisation method and the results are summarised in table 3.7. A good agreement between the aeroelastic response of the stacking sequences and their target polar parameters is obtained.

Case ID	stacking sequence [°]	$R_K[GPa]$	$R_1[GPa]$	$V_f[m/s]$	$\omega_f[rad/s]$	$\mathbf{F_{ABD}}$
swb2	[-55, 38, 29, -59, -56, 34, 38, -59, -53, 33, 29, 30, -55, -59, -55, 38]	13.91 – ∼ 2%	1.24 – ∼< 1%	139.1 – ∼ 1%	708.9 – ∼< 1%	0.002
swf2	[-43, 48, 45, 51, -42, 37, -43, 55, 53, 37, -45, -43, 37, -43, 52, 47]	13.79 + ∼ 1%	4.69 + ∼ 4%	136.4 – ∼< 1%	392.6 – ∼< 1%	0.0009

TABLE 3.7: Stacking sequence retrieval results for two swept wing configurations with variable Φ_1 (*swb2* and *swf2*, from table 3.5 and in figure 3.13). The polar parameters are calculated from the stacking sequence which is a result of numerical optimisation. Small percentages in front of each parameter, indicate the difference between the approximated stacking sequence and the optimal configuration presented in table 3.5.

For further comparison, the elastic behaviours are superposed in figure 3.16.

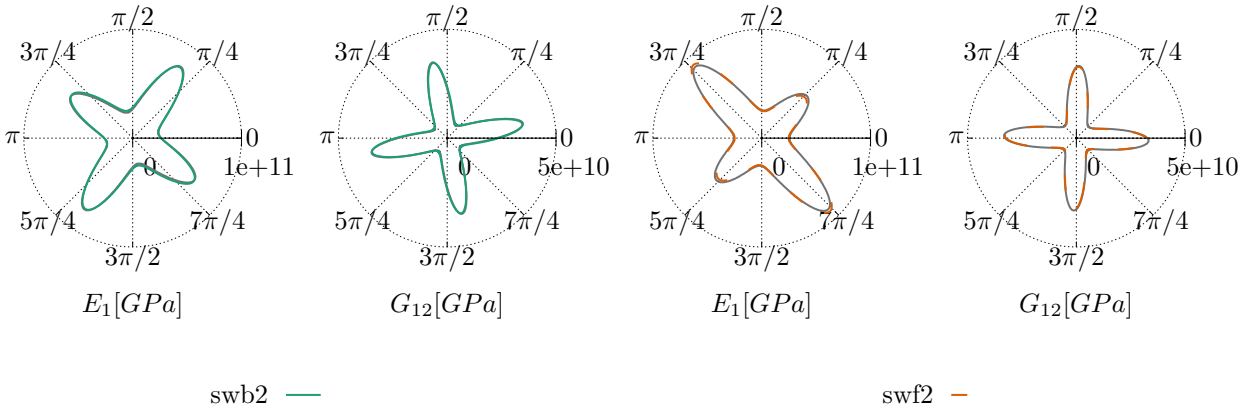

FIGURE 3.16: Comparison of the young moduli between the results of the optimisation and their corresponding stacking sequences obtained numerically. The gray lines on each figure correspond to the target properties and the each coloured line corresponds to the configuration indicated on the label.

The elastic moduli show similar tendencies for both cases in direction and norm. However, for the stacking sequence corresponding to the swept-backward wing (case *swb2*), a small difference in the flutter velocity between the two levels is observed in table 3.7. This gap is mainly due to the placement of this optimal laminate in the orthotropic domain. As mentioned in section 2.2, the right border of this domain corresponds to the cross-ply laminates which contain only 0° and 90° orientations. This limitation can be respected by restraining the discretisation of the angles during the optimisation process.

Case ID	stacking sequence [°]	$R_K[GPa]$	$R_1[GPa]$	$V_f[m/s]$	$\omega_f[rad/s]$	$\mathbf{F_{ABD}}$
swb2	[34, -56, -56, 34, -56, -56, 34, -56, 34, 34, -56, -56, 34, -56, -56, 34]	14.24 + ∼< 1%	1.17 − ∼< 1%	140.9 + ∼ 3%	711.5 + ∼ 3%	0.003

Table 3.8: Stacking sequence retrieval result for the swept-backward wing configurations with variable Φ_1 over the cross-ply border. The polar parameters are calculated from the stacking sequence which is a result of numerical optimisation. Small percentages in front of each parameter, indicate the difference between the approximated stacking sequence and the optimal configuration presented in table 3.5.

Table 3.8 represents the stacking sequence obtained during the optimisation process while limiting the angles to 0° and 90°. A more exact solution is obtained while restraining the search over the cross-ply laminates. It is thus important to identify the type of composite laminate before proceeding to the stacking sequence retrieval. It needs to be noted that for *swb2* the 0° and 90° angles had to be rotated by Φ_1 in order to match the orthotropic reference.

A good agreement is achieved between the polar parameters and their corresponding stacking sequences as shown in table 3.5, 3.7 and 3.8 . One question remains open at the end of this study which is related to the computational cost of the 2-level optimisation process. The second level conducted numerically to retrieve the stacking sequences has a very low cost of 4 seconds [1]. It can thus be negligible in comparison to the entire optimisation process for which the aeroelastic solver is resolved multiple times and each flutter calculation lasts 5 minutes.

It can thus be concluded that it is more beneficial to employ the optimisation formulation using polar parameters rather than directly using ply angles. The former provide simple mathematical relationships in order to define the elastic symmetries. Moreover, they reduce the number of generations required during the optimisation process and thus lowers the total computational cost.

[1] Intel Xeon Silver 4114 Processor with 40 cores

3.3 Conclusion

A deterministic optimisation has been conducted in order to maximise the flutter velocity of a given composite plate. The aeroelastic model has been developed and explained in details which was then used to compute the objective function of the optimisation problem. The polar parameters were presented as a type of parametric formulation in order to simplify the study of the composite laminates. These parameters can express the properties of a plane tensor using only 6 parameters which significantly lowers the number of variables required to express the anisotropy of a laminate. In case of anisotropy, the optimisation variables were decreased from 16 for each ply angle to 4 and to 3 for the investigation of the orthotropic domain. In addition to the reduction of variables, polar parameters can give mathematical relationships to define different elastic properties of composite structures and the value of each invariant carries a physical information as well.

The optimisation study has been carried out by means of the Genetic algorithm. First, four optimisation strategies were compared in the anisotropic domain, three using the ply angles as the optimisation variables and another one using the polar parameters. It has been shown that three strategies achieved similar results in terms of the objective function. Comparing the speed of convergence amongst these three cases, two strategies stood out. One using ply orientations with symmetric laminates and another optimisation formulation using the polar parameters. The symmetric optimal configuration obtained by the ply angles showed a clear superiority to the case obtained by polar parameters. This difference can be explained by the size of the domain which was larger for the polar parameters considering that the anisotropic moduli were treated as continuous variables. Despite the larger domain of investigations, the polar parameters could converge to high flutter velocities, similar to those obtained by the symmetric laminate with a difference of 1%.

The optimisation study using the polar parameters was then generalised to multiple geometric configurations (swept-backward and swept-forward). For each configuration the impact of the orientation of the orthotropic axis and the angle of swept wing was investigated. It has been shown that the highest flutter velocity corresponds to a straight wing with an orthotropic axis aligned with the main axis of the structure. On the other hand, other configurations have exhibited important improvements in their aeroelastic behaviour while including the orientation of the orthotropic axis as an optimisation variable. Specifically, the swept-backward wing had an increase of about 7% for the optimised value of Φ_1 and the swept-forward wing an improvement of more than 48%.

Finally, a second-level optimisation study was carried out in order to retrieve the stacking sequences corresponding to the optimal polar parameters obtained during the optimisation study. Two methods

were tested for this purpose. First, an analytical method was employed with the help of which the angles of the matching stacking sequences were calculated. The relationships used were based on the elastic behaviour of the target composite laminates. Next, a numerical optimisation using the Kullback-Leibler function was put in place. This method was employed for those laminates that were not included in the families defined by the analytical relationships. The two-level optimisation methods based on the polar parameters and the second level study to retrieve the corresponding stacking sequence has proved to have a faster convergence with a better control over the domain of study.

4

Deterministic Optimisation: Variable-Stiffness Laminates

The developments in automated fibre placement technology have facilitated the construction of non-conventional composite laminates. Variable-Stiffness (VS) composites could easily be added in this category as they rise multiple difficulties during their manufacturing process. There are multiple techniques to produce these types of laminates but in this chapter, Tow-Steered (TS) composites are the subject of interest. Tow-Steered composites are laminates with varying fibre path through each ply. The curvilinear fibres are the reason why these laminates possess a variable-stiffness property. The popularity of TS laminates is continuously growing and more studies are focusing on their numerical simulation and examine their impact on various structural and aerodynamic responses. There exist various works of aeroelastic tailoring using TS composites [160, 86]. Most of these studies define the fibre path using a polynomial in which a given number of angles are defined on certain control points along the structure. As discussed previously, using fibre orientations can easily increase the computational cost, particularly in optimisation problems as the number of variables are high and the domain of investigation is very large. To overcome the stated issues, studies such as [79, 80] have generalised the multi-scale optimisation methods based on the use of polar parameters (presented in section 2.2) to model the variable angle-tow laminates. The former studies focus on the structural behaviour of the laminate, particularly the buckling. On the other hand, these methods have not often been employed in an aeroelastic framework. For this reason, this chapter focuses on aeroelastic tailoring of Tow-Steered (TS) laminates using polar parameters and the optimisation study of these materials.

4.1 Numerical modelling of tow-steered laminates

As defined previously, tow-steered laminates, being reinforced by curvilinear fibres with different paths within each ply, result in a continuously varying stacking sequence throughout the structure and, as a consequence, a point-wise variation of the elastic properties of the laminated structure. The idea is to represent this variation in terms of fields of polar parameters. It is therefore implied that during their numerical simulation, each finite element node holds a different stiffness tensor. Polar parameters can thus be employed to express these tensors for each finite element node which simplifies the numerical modelling of the TS laminates. As the plies are identical in this study, the isotropic moduli (T_0 and T_1) remain the same for all the laminates. The three parameters used in the last chapter (R_K, R_1 and Φ_1) are considered as the optimisation variables and the domain of study is limited to elastic symmetries, including orthotropy, square-symmetry and isotropy (which are all represented in the definition domain expressed by equations (2.52)-(2.54) and depicted in figure 2.6).

A computational limit of associating a set of polar parameters to each finite element node, is the number of optimisation variables. As the number of the nodes on the finite element grid is very high, the optimisation algorithm can become easily saturated. A simple solution to this problem is the use of interpolation methods such as B-spline curves [161].

A B-spline surface can be defined as

$$\mathbf{S}_{BS}(\eta,\gamma) = \sum_{i=0}^{n}\sum_{j=0}^{m} N_{i,p}(\eta)N_{j,q}(\gamma)\mathbf{P}_{i,j} \tag{4.1}$$

where $\mathbf{P}_{i,j}$ represents the control points, $N_{i,p}(\eta)$ and $N_{j,q}(\gamma)$ the pth and qth degree B-spline basis function in η and γ directions and finally $n+1$ and $m+1$ are the number of control points.

The basis functions are defined on non-periodic, non-uniform knot vectors which read

$$\mathcal{E} = \{\underbrace{0,\ldots,0}_{p+1},\eta_{p+1},\ldots,\eta_{r-p-1},\underbrace{1,\ldots,1}_{p+1}\} \tag{4.2}$$

$$\Gamma = \{\underbrace{0,\ldots,0}_{q+1},\gamma_{q+1},\ldots,\gamma_{s-q-1},\underbrace{1,\ldots,1}_{q+1}\} \tag{4.3}$$

and have a length of $r+1$ and $s+1$. The number of knots, r and s are calculated using the number of control points, n and m, and the degree of polynomials, p and q such as

$$r = n+p+1 \qquad\qquad s = m+q+1 \tag{4.4}$$

In order to use B-spline surfaces during the optimisation of TS laminates, the set of control points need to be defined over the structure. In this study, $n = 6$ control points are considered along the span and $m = 4$ along the chord which gives place to $n.m = 24$ control points in total. These points are presented on the FEM mesh in figure 4.1. They do not match the FEM nodes because they are based on the B-spline grid.

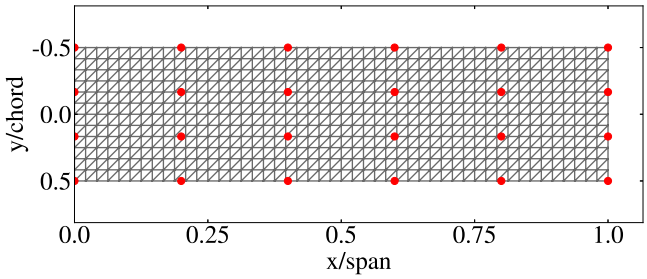

Figure 4.1: Control points located over the FEM mesh.

Genetic Algorithm (GA) generates the demanded number of optimisation variables (for the number of control points) which in this case are the polar parameters. Each parameter is then associated to a control point and the distribution of the latter over the structure is interpolated using the B-spline method. The value of the polar parameter over each finite element node can then be extracted and consequently compute the related stiffness matrix. This process could rise the question of the discontinuities of the parameters over the structure and thus the feasibility of the fibre paths. However, the B-spline property of strong convex hull insures that the optimisation constraints over the curvature of the fibre paths are satisfied. Given a 2D variation of one anisotropic modulus (R_1) over the 24 control points, the B-spline surface presented in figure 4.2 is obtained. The dashed lines connect the control points to the adjacent one and the colormap represents the final interpolated surface carried out from these points using second order polynomials in both directions (p and q).

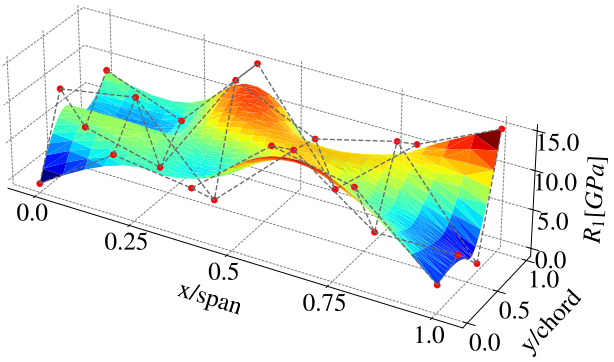

Figure 4.2: Interpolation of a B-spline surface from the control points.

The combination of the polar-based representation of the elastic properties together with the B-spline formulation, significantly reduces the number of optimisation variables and allows the consideration of laminates with high number of plies, which is impossible if working with angles, as the latter need to be defined for each layer. In the next section, the optimisation formulation and the results for each case are presented and analysed. The variations in the optimisation problem regarding the variables or other optimisation parameters are pointed out for each case.

4.2 Optimisation formulation

Using the polar parameters and the B-spline surface interpolation, an optimisation problem is put in place. The objective function remains the maximisation of flutter velocity V_f and the domain of investigation is limited to the orthotropic symmetry. The polar parameters are used as the optimisation variables and vary over each control point in order to model the variation of the stiffness throughout the structure. The upper limit of the geometric domain of orthotropy (figure 2.6) is considered as the constraint of the optimisation problem. As a result, the general optimisation problem in the orthotropic domain given the two anisotropic moduli R_K and R_1 that vary throughout the structure and the polar angle Φ_1 that is optimised but kept constant over the plate reads

$$\begin{aligned} \underset{R_K(x,y),R_1(x,y),\Phi_1}{\text{maximize}} \quad & V_f \\ \text{subject to} \quad & -(\rho_0(x,y)) + 2(\rho_1(x,y)^2) - 1 \leq 0, \end{aligned} \tag{4.5}$$

where

$$-R_K^{BL} \leq R_K \leq R_K^{BL} \qquad 0 \leq R_1 \leq R_1^{BL} \tag{4.6}$$

4.2.1 Evaluation of the objective function: critical flutter speed

The computation of the flutter velocity requires the calculation of the stiffness matrix which is a function of the modified bending stiffness matrix, $\tilde{\mathbf{D}}$. The latter matrix is calculated as a function of the polar parameters and in the case of laminates with Tow-Steered fibre paths, varies over each finite element node. The steps required, in order to compute the flutter velocity of a variable-stiffness laminate is described in algorithm 2.

Algorithm 2: Aeroelastic study of Tow-Steered laminate

1: Set the Control Points (CP) over the structure
2: Associate the polar parameters to each CP
3: Interpolate the polar parameters using B-spline surface (equation (4.1))

$$\mathbf{S}_{BS}(\eta,\gamma) = \sum_{i=0}^{n}\sum_{j=0}^{m} N_{i,p}(\eta)N_{j,q}(\gamma)\mathbf{P}_{i,j}$$

4: Extract the polar parameters on each finite-element node
5: Compute the modified bending tensor $\tilde{\mathbf{D}}$ on each finite-element node (equation (2.1)-(2.8))

$$\tilde{\mathbf{D}} = \mathbf{D} - \mathbf{B}\mathbf{A}^{-1}\mathbf{B}$$

6: Compute aeroelastic eigenvalues s (equation (2.28)-(2.33))

$$\begin{bmatrix}\mathbf{I} & 0\\ 0 & \mathbf{I}\end{bmatrix} s\begin{Bmatrix}\hat{\mathbf{q}}\\ s\hat{\mathbf{q}}\end{Bmatrix} - \begin{bmatrix}0 & \mathbf{I}\\ -\hat{\mathbf{M}}^{-1}(\hat{\mathbf{K}} - \omega^2\mathbf{A}^R) & \omega\hat{\mathbf{M}}^{-1}\mathbf{A}^I\end{bmatrix}\begin{Bmatrix}\hat{\mathbf{q}}\\ s\hat{\mathbf{q}}\end{Bmatrix} = \begin{Bmatrix}0\\ 0\end{Bmatrix}$$

$$s = g \pm i\omega$$

4.2.2 Definition of constraints: orthotropic symmetry

In order to limit the optimisation investigation to the orthotropic symmetry, the definition of a constraint is required. As shown in equation (4.5), in case of Tow-Steered laminates, the constraint has a spatial dependency. The latter condition is due to the association of a different set of polar parameters to each control point which requires the calculation of a new constraint. The number of constraints can eventually be too high and too costly for the optimisation algorithm to take into account. To remedy this problem, a mapping has been put in place, which determines the orthotropic domain using two new parameters α_0 and α_1 defining a unit square [162, 163]

$$0 \leq \alpha_0 \leq 1 \qquad 0 \leq \alpha_1 \leq 1 \tag{4.7}$$

These two variables can be computed using the anisotropic moduli

$$\alpha_0 = \frac{\rho_0 - 1}{2(\rho_1^2 - 1)} \qquad \alpha_1 = \rho_1 \tag{4.8}$$

where

$$\rho_0 = \frac{R_K}{R_K^{BL}} \qquad \rho_1 = \frac{R_1}{R_1^{BL}} \tag{4.9}$$

The response surfaces in figure 4.3 represent the variation of R_K and R_1 as a function of the two mapping variables α_0 and α_1.

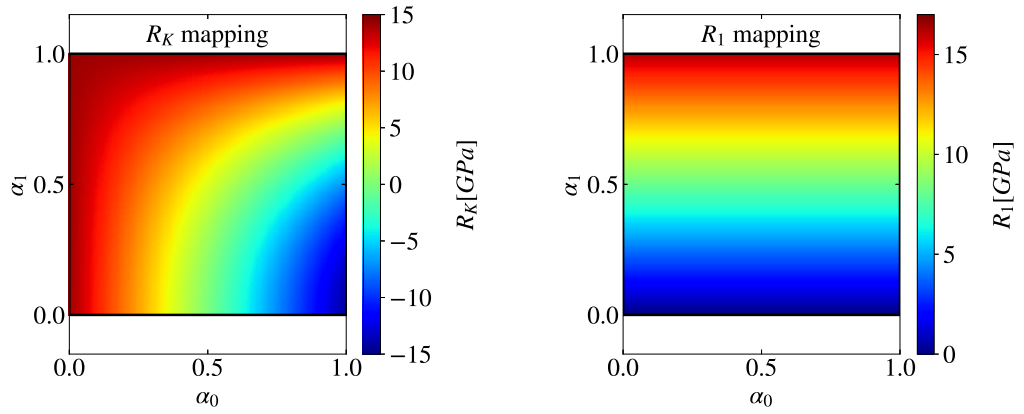

FIGURE 4.3: Mapping of the orthotropic domain using the anisotropic moduli to a unit square [163].

4.2.3 Optimisation strategies

A general optimisation problem with an orthotropic symmetry is introduced in equation (4.5) which allows a thorough investigation of this domain. On the other hand, the results of the optimisation study in chapter 3 showed that multiple optimal configurations belong to the angle-ply sequences. This observation gave place to a limited formulation of the optimisation problem which limits the investigation to the angle-ply laminates. Thus, two optimisation strategies are considered.

- Optimisation A : Anisotropic moduli (R_K and R_1) optimised over the angle-ply curve and variable per finite element node

$$\underset{R_1(x,y),\Phi_1}{\text{maximize}} \quad V_f \tag{4.10}$$

where

$$0 \leq R_1 \leq R_1^{BL} \tag{4.11}$$

$$R_K = R_K^{BL}\left(2\left(\frac{R_1}{R_1^{BL}}\right)^2 - 1\right) \tag{4.12}$$

- Optimisation B : Anisotropic moduli (R_1 and R_K) optimised over the whole orthotropic domain and variable per finite element node

$$\underset{\alpha_0(x,y),\alpha_1(x,y),\Phi_1}{\text{maximize}} \quad V_f \tag{4.13}$$

where

$$0 \leq \alpha_0 \leq 1 \qquad 0 \leq \alpha_1 \leq 1 \tag{4.14}$$

4.3 Optimisation results

The two optimisation strategies A and B, respectively the one restricted to the angle-ply curve as expressed by equations (4.10) - (4.12), and the general one over the whole orthotropic domain, as expressed by equations (4.13)-(4.14) are applied to three different geometries, one straight and two swept wings. The parameters that are variable throughout the structure, are the ones that are responsible for the variation of the rigidity. Once the variation of each parameter is obtained using the B-spline surface, the value on each finite element node is extracted. Using this value, the rigidity matrix ($\tilde{\mathbf{D}}$) is calculated for each FEM node. Finally using a mapping method, each rigidity matrix is associated to its corresponding node using their coordinates and finally the eigenvalue problem is solved in order to carrie out the modal analysis of the structural system.

4.3.1 Optimisation over the angle-ply curve

The first strategy considered, concerns the variation of the anisotropic moduli over the angle-ply curve of the orthotropic domain (equations (4.10) - (4.12)). The reason for choosing this optimisation formulation is due to the numerous optimal cases over this curve obtained during the US optimisation study and presented in figure 3.13. The optimisation variables are thus 6 values of R_1 as the variation of the parameters are considered in a span-wise direction. The four control points over the same axis position are therefore identical. The latter further restricts the optimisation study for an initial simplification but can be easily expanded to a 2D variation along both span and chord.

As the optimisation is restrained to the angle-ply curve, the values of R_K can be obtained analytically from R_1 using the relationship expressed in equation (4.12), initially introduced as the upper limit of the geometrical definition of the orthotropic domain in figure 2.6 [1]. It needs to be pointed out that during this optimisation strategy, the principal orthotropy axis, represented by the polar angle Φ_1, is fixed and aligned to the reference axis of the wing for the straight case as it was proven during the Uniform-Stiffness optimisation study that this orientation was the optimal angle for this geometry. The polar angle is then included for the two swept configurations, since its influence was shown in the investigation of Uniform-Stiffness (US) laminates. For these types of geometries, an aligned orthotropic axis to the reference axis of the wing can drastically decrease the flutter velocity. The optimisation problem expressed by equations (4.10) - (4.12) was solved by the use of a Genetic Algorithm, with genetic parameters set at $N_{ind} = 100$ individuals and $N_{gen} = 50$ generations. Table 4.1 presents the results of this optimisation strategy for the plate configuration in the domain of angle-ply laminates. For each case, the anisotropic moduli are variable along the span, the polar angle Φ_1 is optimised for the two swept wings. The red bold coloured values are not optimised and predefined

[1] demonstration of the relationship in [150]

for each variable.

Case ID	Wing configuration	$R_K[GPa]$	$R_1[GPa]$	$\Phi_1[^\circ]$	$\alpha_{swept}[^\circ]$	$V_f[m/s]$	$\omega_f[rad/s]$
st1	straight	variable	variable	**0.**	**0.**	151.8 + ∼ 4%	499.5
swb1	swept-backward	variable	variable	-9.	**-15.**	145.1 + ∼ 3%	457.5
swf1	swept-forward	variable	variable	89.	**15.**	127.6 − ∼ 7%	607.6

TABLE 4.1: Deterministic optimisation results of the Tow-Steered configurations obtained by variation of anisotropic moduli (R_K and R_1) over the angle-ply curve throughout the structure and optimised polar angle (Φ_1) for two cases, with red bold coloured variables indicating constant parameters during the study and the small grey percentages presenting the difference between the current case and their Uniform-Stiffness analogue.

Straight wing

The first geometry is noted *case st1* (cfr table 4.1) and corresponds to the straight case with the orthotropic axis Φ_1 aligned to the principle axis of the wing. The flutter velocity is increased beyond any values obtained previously for the straight wing and has a 4% gain compared to the US configuration ($V_f = 146.5m/s$). The flutter frequency, on the other hand, remains very close to the US configuration presented in table 3.5.

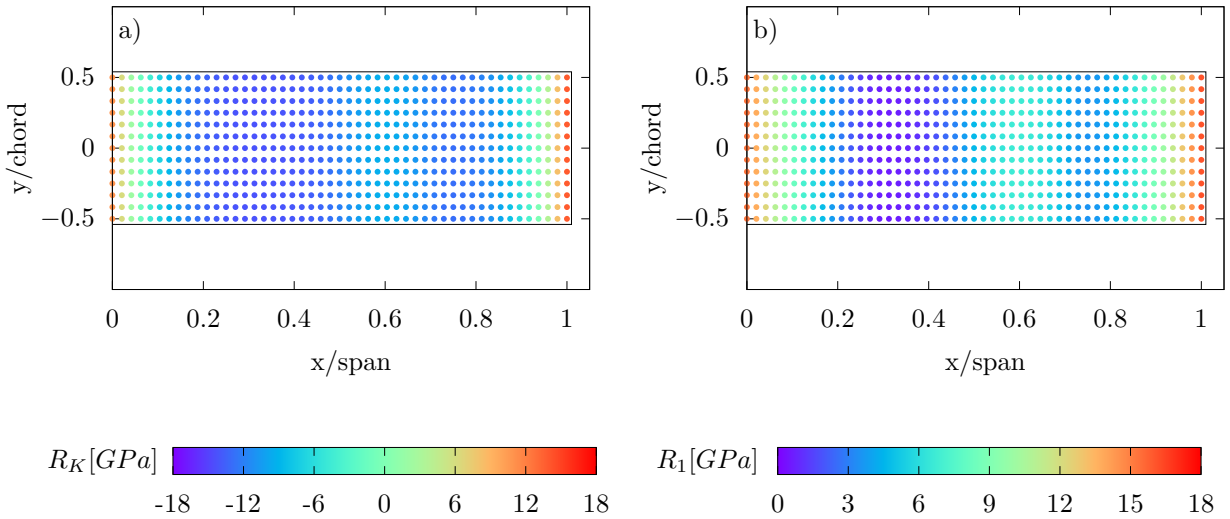

FIGURE 4.4: a) variation of R_K and b) variation of R_1 presented by the colour map over the span for the straight wing with the orthotropic axis aligned with the main axis of the wing (case *st1*) while optimising the anisotropic moduli over the angle-ply curve.

Figure 4.4 represents the variation of the anisotropic moduli over the structure. The colour map shows the value of each variable over every finite element node. The variations of both moduli remain

in a small interval in the center of the structure. A large shift in the values is seen near the borders particularly at the outer edge.

The small variations of the anisotropic moduli is directly translated to the variations of the ply angles. As explained before in section 2.2, the stacking sequence of a set of polar parameters over the ange-ply curve can be calculated analytically using equation (4.15)

$$\theta = \frac{1}{4}\arccos\left(\frac{R_K}{R_0^{BL}}\right) \qquad \text{or} \qquad \theta = \frac{1}{2}\arccos\left(\frac{R_1}{R_1^{BL}}\right) \tag{4.15}$$

This stacking sequence is assembled by layers of $\pm\theta$ where θ is the calculated ply angle. In the case of Tow-Steered fibres, each FEM node corresponds to a different value of θ and the latter varies throughout the structure. This variation is presented in figure 4.5 over the entire domain. As shown in the colormap of the anisotropic moduli in figure 4.4, a small variation is observed in the midsection of the wing which implies a roughly Uniform-Stiffness behaviour in this region. A larger variation of the ply orientation can be noticed near the edges of the structure.

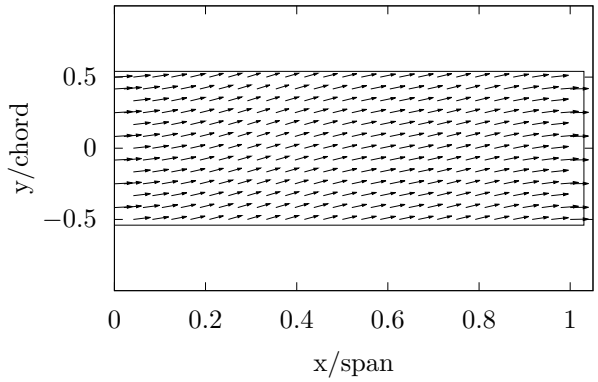

Figure 4.5: Variation of θ over the span presented by arrows for the straight wing with the orthotropic axis aligned with the main axis of the wing (case *st1* in table 4.1).

The evolution of aeroelastic damping presented in figure 4.6, follows the same behaviour as the straight US case of figure 3.7, with the second mode that becomes unstable and the third mode close to instability. It needs to be noted that the first aeroelastic mode corresponding to static instabilities, has an increasing tendency in the damping values and can become unstable as well, in larger velocities. The isolines of the unstable mode demonstrated in the same figure are a combination of the second bending and first torsion modes.

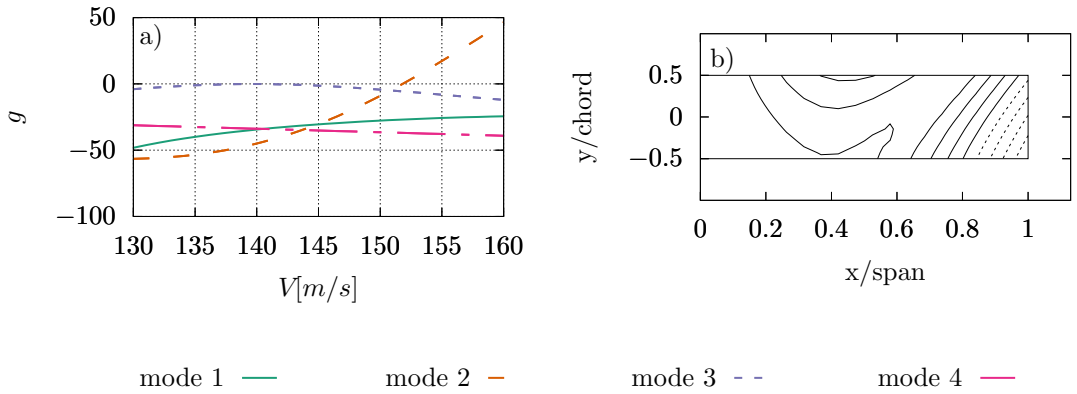

FIGURE 4.6: Aeroelastic response of the TS straight wing (case *st1*) with span-wise variations of R_K and R_1 over the angle-ply curve. a) evolution of aeroelastic damping and b) the unstable mode shape.

Swept wings

The last two cases mentioned in table 4.1 concern optimisation problems over swept configurations, where the polar angle Φ_1 is added as an optimisation variable but, differently from variables R_K and R_1, is not a variable field in the space coordinates x and y, i.e. it stays constant throughout the structure. For the swept-backward wing, an increase of 3% in the flutter velocity is observed compared to the US configuration. The flutter frequency of the TS case is not in the same interval as the US optimal configuration ($\omega_f = 711.5$ rad/s) which indicates that the instability does not occur on the same aeroelastic mode for both cases. The swept-forward case does not surpass the V_f value obtained during the US optimisation ($V_f = 137.0$ m/s) and its flutter frequency is not in the same interval as the former configuration which again points out the difference in the unstable mode. The flutter frequency of the swept-forward wing is significantly higher than the swept-backward case which indicates a difference in unstable modes.

Figure 4.7 represents the variation of the anisotropic moduli over both swept-backward and swept-forward configurations. Similarly to the straight wing (case *st1*), the TS configurations possess a limited variation of the anisotropic moduli. Unlike case *st1*, the borders of the wings do not have an impact of the values of the moduli. It is noteworthy that the variations of R_K and R_1 are not in an interval close to the values obtained for the optimal US cases. Similar observations can be carried out concerning the polar angle Φ_1 for both geometries. The Φ_1 values mentioned in table 4.1 are far from those obtained in the Uniform-Stiffness optimisation presented in table 3.5. These remarks can indicate that the domain of investigation is strongly non-convex and another optimal zone exists for

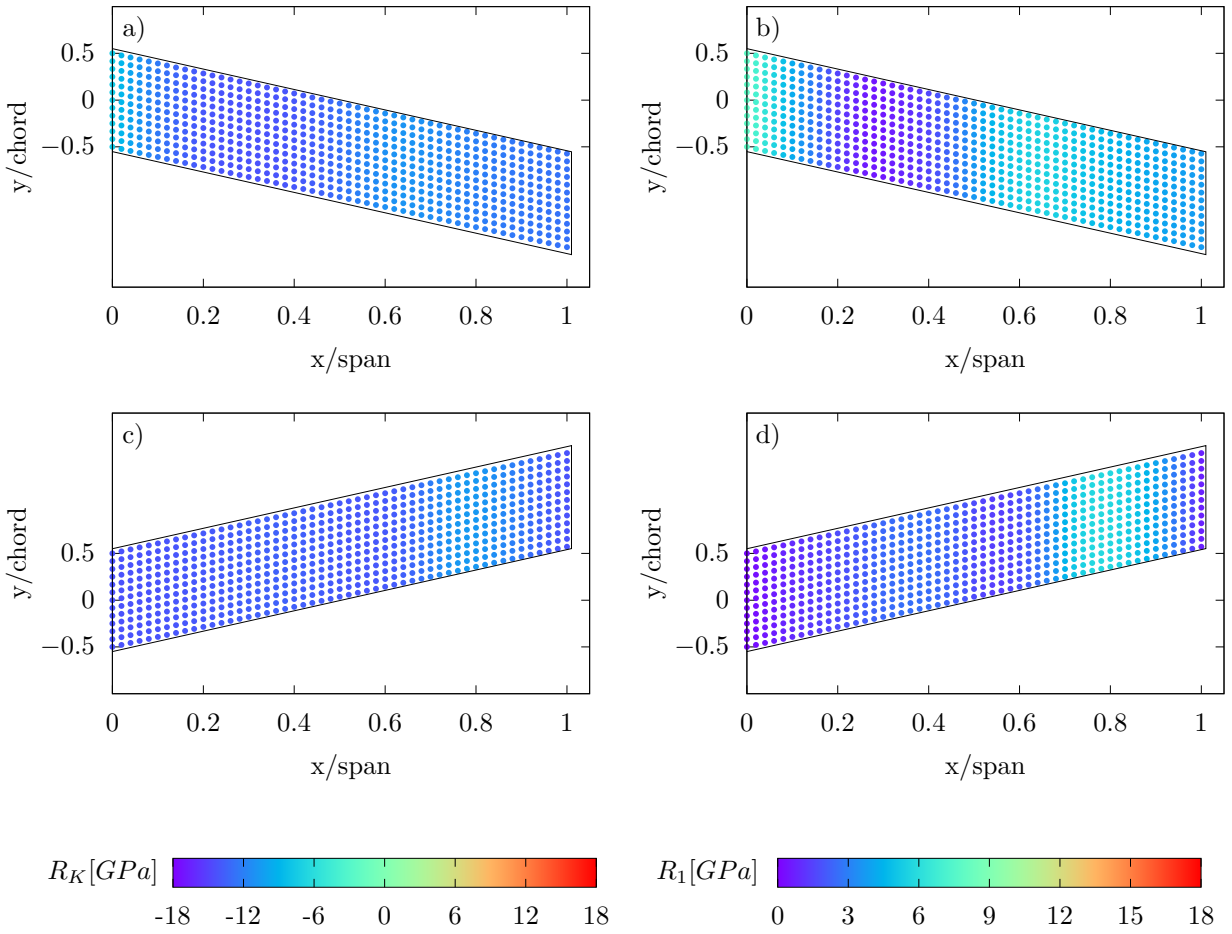

Figure 4.7: (a,c) variation of R_K and (b,d) variation of R_1 presented by the colour map over the span. (a,b) the swept-backward wing (case *swb1*) and (c,d) the swept-forward wing (case *swf1*) while optimising the anisotropic moduli over the angle-ply curve.

both swept geometries.

The ply angles are calculated for both geometries using equation (4.15). The value of angle (θ) is presented in figure 4.8. Limited variations of the angles are observed due to similar behaviours in the anisotropic moduli.

The aeroelastic responses of these two optimal cases are presented in figure 4.9. For the swept-backward case the second aeroelastic mode becomes unstable and the third mode is very close to the aeroelastic instability. On the other hand, for the swept-forward wing, the third mode becomes unstable first and soon after the second mode becomes positive. The occurrence of instability in two different aeroelastic modes can explain the large variations of the flutter frequencies from one case to another. The instability occurs on the third mode for a swept-forward wing unlike the US case. This

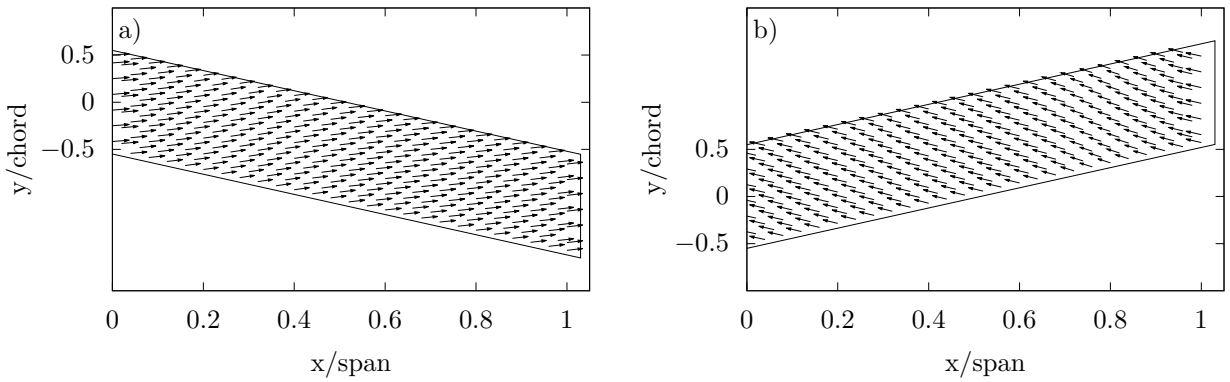

FIGURE 4.8: Variation of θ over the span presented by arrows while optimising the anisotropic moduli over the angle-ply curve. a) the swept-backward wing (case *swb1*) and b) the swept-forward wing (case *swf1*).

behaviour indicates the variation of the aeroelastic response of this geometry over the angle-ply curve.

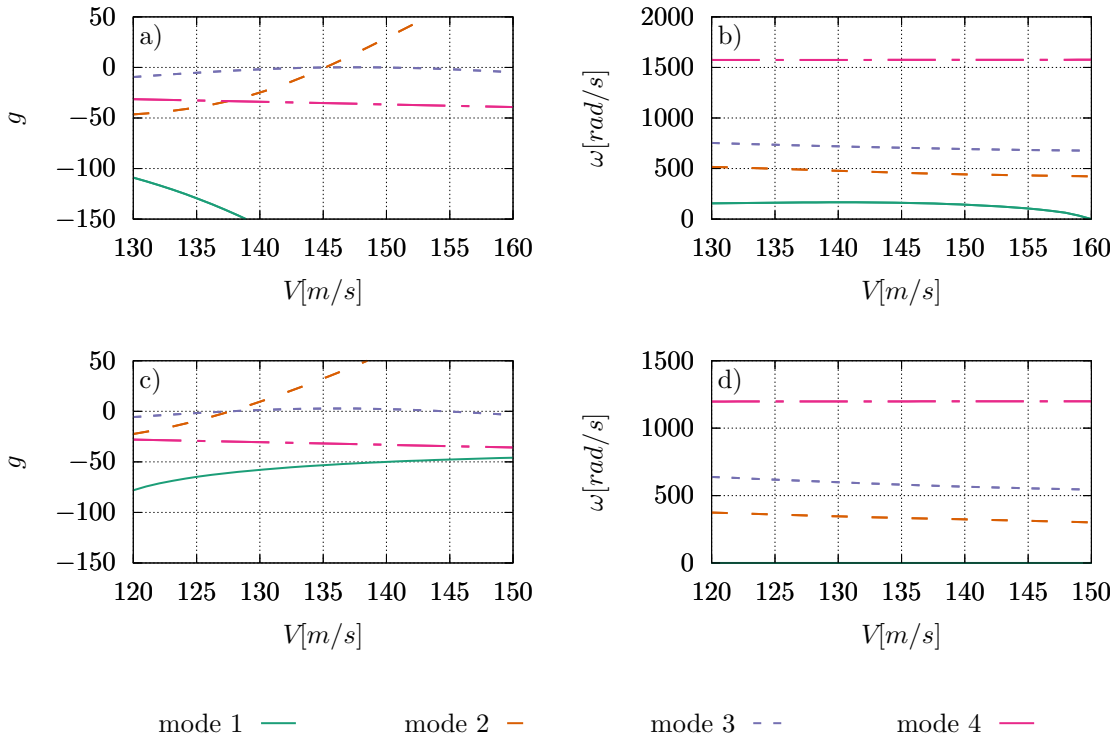

FIGURE 4.9: Evolution of (a,c) aeroelastic damping and (b,d) aeroelastic frequency of the TS swept wings with span-wise variations of R_K and R_1 over the angle-ply curve and optimising Φ_1. (a,b) case *swb1* and (c,d) case *swf1* in table 4.1.

The representation of these modes are demonstrated in figure 4.10. The swept-backward wing is a combination of the second bending and the first torsion modes and the swept-forward wing, a combination of the second torsion and the first bending mode.

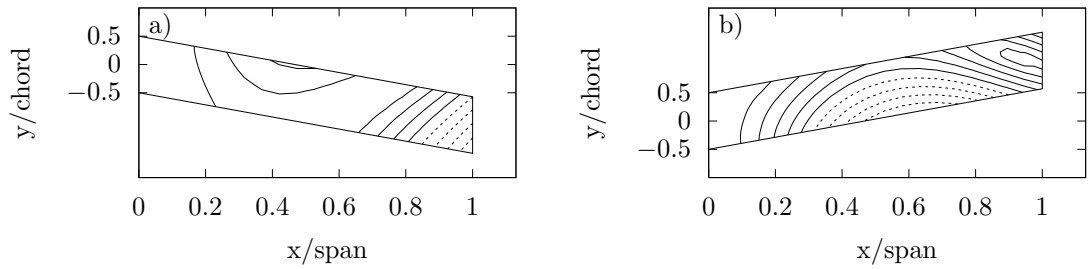

Figure 4.10: Aeroelastic mode shapes of the TS swept wings for variation of R_K and R_1 over the angle-ply curve and optimising Φ_1. a) case *swb1* and b) case *swf1* in table 4.1.

While some improvements have been observed during this optimisation strategy, particularly for the straight and the swept-backward wings, the question on the impact of the other orthotropic symmetries on the aeroelastic behaviour of the TS laminates, is still present. For this purpose the next strategy is formulated to further explore this domain for the three chosen geometries.

4.3.2 Optimisation over the orthotropic domain

In this section, the anisotropic polar moduli are employed in the formulation of the optimisation problem in order to investigate the entire orthotropic domain to form a Tow-Steered (TS) laminate according to formulation of equations (4.13)-(4.14). The difference between this strategy and the one defined in the previous section is the domain of investigation. In the previous optimisation problem, the anisotropic moduli R_K and R_1 were dependent on one another as the domain was limited to the angle-ply curve. In this strategy, both moduli can vary independently inside the orthotropic domain and do not have any dependencies on each other. The variation of the fibre path remains 1D along the span direction. The optimisation variables (R_K and R_1) are doubled which gives place to 12 parameters (2 variables per control point and 6 control points along the span) and 13 when the polar angle is optimised.

Table 4.2 presents the results obtained with this strategy for three different geometries. The optimisation problem is solved using the GA with the same settings for the genetic parameters (N_{ind} = 100 and $N_{gen} = 50$), as in the previous case (cfr. section 4.3.1). The orthotropic axis Φ_1 is considered aligned with the main axis of the wing for the straight case. The polar angle is optimised for two swept wings as the optimal US cases do not have an aligned orthotropic and reference axis, however

it is not a variable field but a variable constant with respect to which all the TS laminate has to be oriented. All the results will eventually be compared to the previous strategy based on the angle-ply domain (section 4.3.1), as well as to the US cases.

Case ID	Wing configuration	$R_K[GPa]$	$R_1[GPa]$	$\Phi_1[^\circ]$	$\alpha_{swept}[^\circ]$	$V_f[m/s]$	$\omega_f[rad/s]$
st1	straight (1D)	variable	variable	**0.**	**0.**	146.9 + ∼< 1%	502.7
swb1	swept-backward (1D)	variable	variable	-53.	**-15.**	140.6 + ∼< 1%	680.0
swf1	swept-forward (1D)	variable	variable	49.	**15.**	140.4 + ∼ 3%	402.0

TABLE 4.2: Deterministic optimisation results of the Tow-Steered configurations obtained by variation of anisotropic moduli (R_K and R_1) inside the orthotropic domain throughout the structure and optimised polar angle (Φ_1) for two cases, with red bold coloured variables indicating constant parameters during the study and the small grey percentages presenting the difference between the current case and their Uniform-Stiffness analogue.

Straight wing

The optimisation study for orthotropic TS laminates, as expressed by equations (4.13)-(4.14), is first applied to a straight wing. The anisotropic moduli R_K and R_1 are chosen in the entire orthotropic domain but the maximum flutter velocity ($V_f = 146.9m/s$) fails to surpass the previous TS results ($V_f = 151.8m/s$, given in table 4.2) and can only rise as high as the US case ($V_f = 146.5m/s$, given in table 4.2). The flutter frequency remains adequately close to the previous results, so that it can be considered corresponding to the same aeroelastic mode.

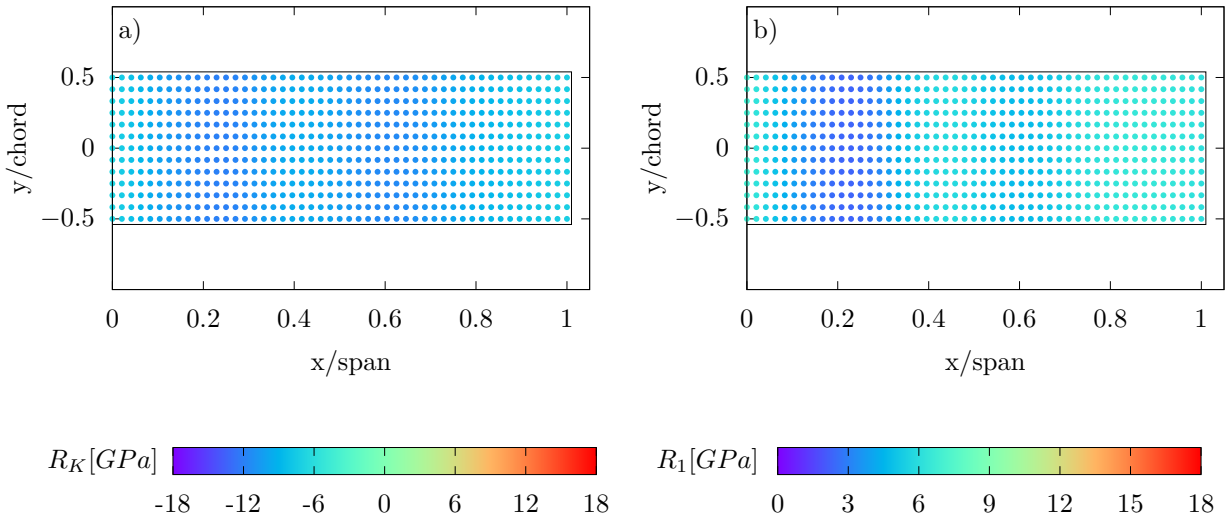

FIGURE 4.11: Variation of a) R_K and b) R_1 over the span presented by the colour map for the straight wing with aligned orthotropic and main axis (case *st1)* while optimising the anisotropic moduli inside the orthotropic domain.

Figure 4.11 represents the variations of the anisotropic moduli over the studied structure. The colormap on this figure indicates small variations for both R_K and R_1 throughout the structure. On the other hand, the variation for both moduli is limited to a given zone which has similar values to the optimal case of the US configuration. In this strategy the arrows corresponding to the orientation of the layers are not presented. The reason is that the orientations can no longer be analytically calculated for all the nodes and each layer has therefore a different fibre path which is not possible to present with only one value (such as θ for the previous strategy).

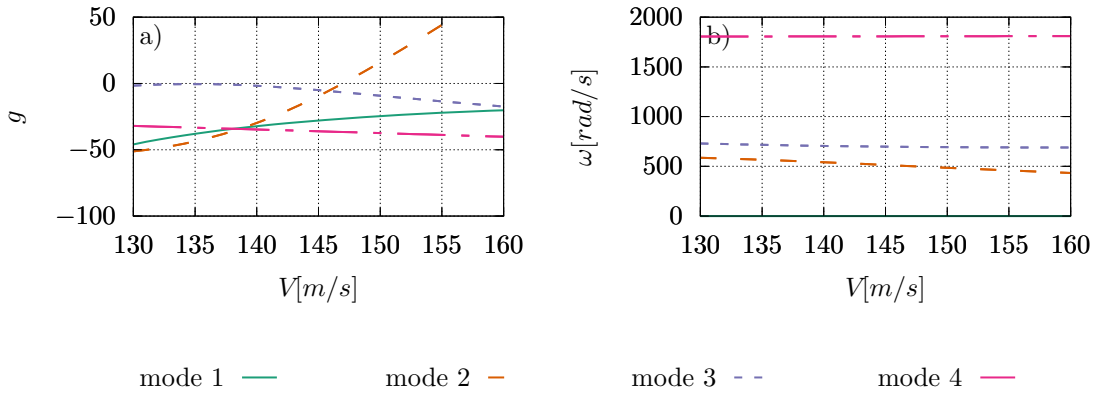

Figure 4.12: Evolution of a) aeroelastic damping and b) aeroelastic frequency of the TS straight wing (case *st1*) with span-wise variations of R_K and R_1 inside the orthotropic domain.

The aeroelastic damping and frequency presented in figure 4.12 have comparable behaviours to the previous optimal cases obtained with different strategies. The aeroelastic damping in figure 4.12.a) shows instabilities over the second mode and the third mode which is close to the zero axis. Similarly to the previous case, the damping of the first mode corresponding to divergence instability approaches the zero axis as the velocity increases. It can be predicted that an instability occurs over this mode at higher speeds.

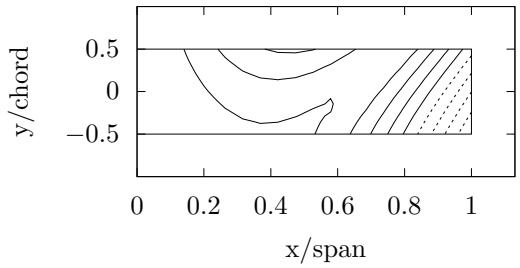

Figure 4.13: Aeroelastic mode shape of the TS straight wing for variation of R_K and R_1 inside the orthotropic domain for case *st1* in table 4.2.

The mode shape presented in figure 4.13 depicts the unstable mode for the straight optimal configuration which is a combination of the second bending and first torsion mode similarly to the previous optimal cases.

Swept wings

Once more, due to the high influence of the orientation of the orthotropic axis on the aeroelastic behaviour of swept wings, the polar angle Φ_1 is included in the optimisation problem. The latter is optimised but kept constant throughout the structure, thus all the tow-steered laminates have to be oriented according to the same principal orthotropy axis Φ_1. When optimising the polar angle for the swept-backward wing, a flutter velocity ($V_f = 140.6$ m/s) close to the one obtained by the US optimisation is attained ($V_f = 140.8$ m/s). The latter fails to exceed the values obtained in the last strategy over the angle-ply curve ($V_f = 145.1$ m/s). This analysis confirms that the optimal TS laminates for a swept-backward wing are located over this curve. On the other hand, flutter velocity of the swept-forward wing ($V_f = 140.4$ m/s) is increased higher than any of the previous studies. It shows about 3% increase with respect to the US case ($V_f = 137.0$ m/s) and about 10% compared to the TS configuration obtained over the angle-ply curve ($V_f = 127.6$ m/s). Similarly to the observations made during the US optimisation of the swept-forward wing, the optimal TS laminate for this configuration is not placed on the angle-ply curve on the contrary to all the other geometries. It needs to be noted that for both swept cases, the optimal value of the polar angle or the orientation of the orthotropic axis, is close to the US case, i.e. constant stiffness laminates (cfr. section 3.1.2 and table 3.5). This observation can help reduce the computational time as the domain of investigation is restricted to a given value of Φ_1. Finally, comparing the flutter frequencies between tables 4.2 and 3.5, all three geometries have up to 4% increase with respect to their equivalent US configuration. While the values remain within the same interval and thus correspond to the same mode, it can be concluded that the TS laminates have higher frequencies over the same flutter mode.

The distribution of the anisotropic moduli R_K and R_1 over the structure for both swept configurations is presented in figure 4.14. In case of the swept-backward wing (figure 4.14.(a,b)), the distributions for both moduli remain limited to a given interval but this time larger than the previous cases. The effect of the outer edge is more visible for this configuration compared to the one obtained over the ply-angle curve. It needs to be pointed out that this zone is around the elastic values of optimal US case with optimised value for Φ_1 which belonged to the cross-ply laminates. The swept-forward wing has also limited variation for R_K (figure 4.14.c) and the values are limited to the higher extremity of this parameter, meaning that the optimal laminates correspond to cross-ply laminates (right border of the orthotropic domain). On the other hand, the values of R_1 (figure 4.14.d) are more

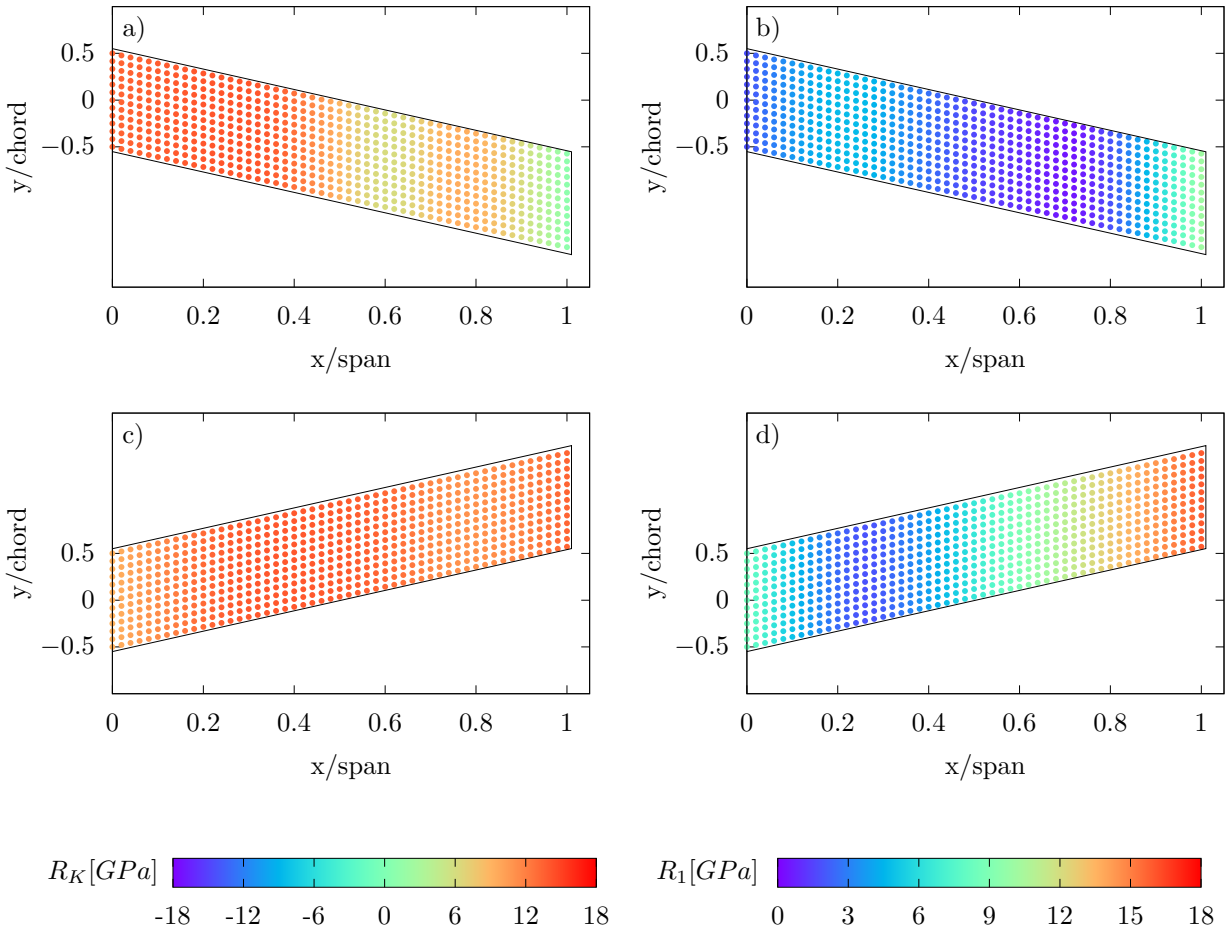

Figure 4.14: Variation of (a,c) R_K and (b,d) R_1 presented by the colour map over the span. (a,b) the swept-backward wing (case *swb1*) and (c,d) the swept-forward wing (case *swf1*) for variation of R_K and R_1 inside the orthotropic domain while optimising Φ_1.

dispersed and vary through the entire domain of definition. This case corresponds to the variations of the tow-angles in the cross-ply laminates throughout the structure, implying a discontinuous variation of the orientation angles through the ply, switching from 0° to 90°, which is not really feasible considering tow-steered laminates.

Figure 4.15 represents the aeroelastic response of both wings. The swept-backward (case *swb1*) configuration shows similar behaviours as previous cases but this time the instability first occurs on the third mode. The second mode becomes unstable shortly after the third mode. For the swept-forward wing, the instability takes place on the second mode but again with a third mode that is close to instability and the divergence mode that follows the same trend.

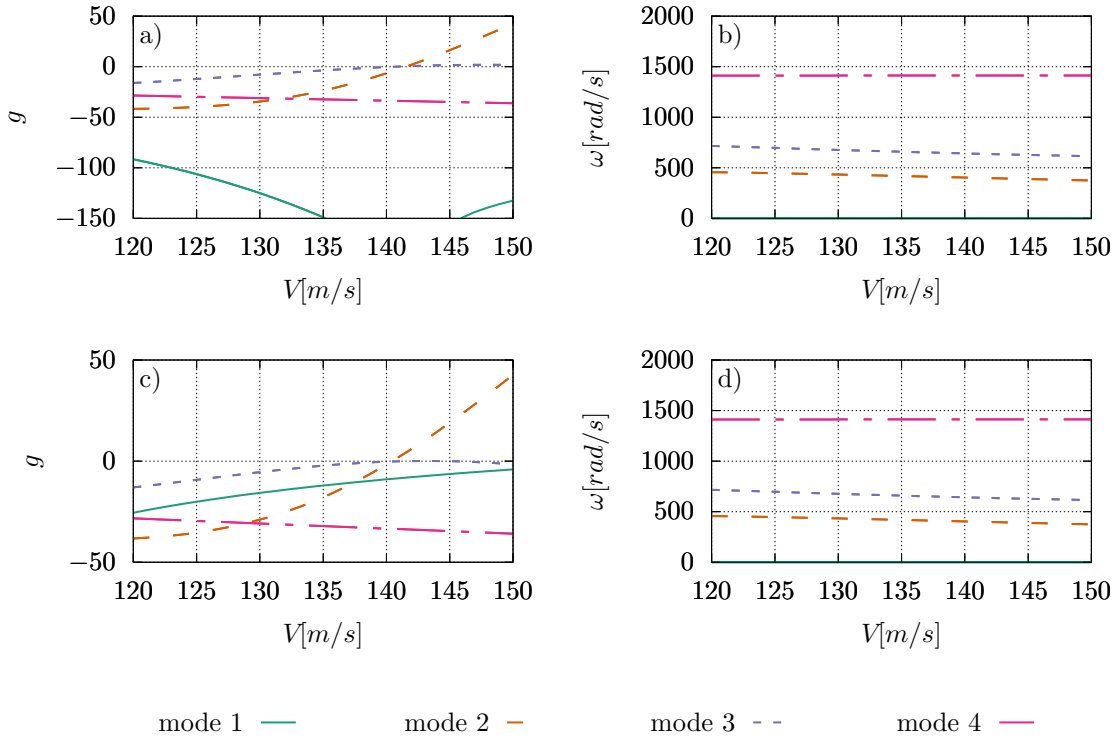

FIGURE 4.15: Evolution of (a,c) aeroelastic damping and (b,d) aeroelastic frequency of the TS swept wings with variations of R_K and R_1 in the orthotropic domain while optimising Φ_1. (a,b) case *swb1* and (c,d) case *swf1*.

The unstable modes are presented in figure 4.16. The third aeroelastic mode is demonstrated for the swept-backward wing which is a combination of the first torsion and the third bending mode. For the swept-forward case, the second aeroelastic mode is presented as well in figure 4.16.b).

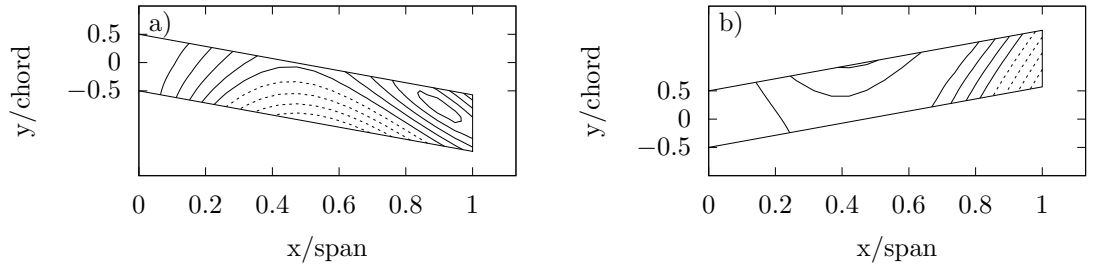

FIGURE 4.16: Aeroelastic mode shapes of the TS swept wings for variation of R_K and R_1 in the orthotropic domaine while optimising Φ_1. a) case *swb1* and b) case *swf1*.

The optimisation inside the orthotropic domain was conducted for all three geometries, straight, swept backward and forward. No improvement has been shown regarding the straight and the swept-backward cases. On the other hand, interesting results were obtained concerning the swept-forward wing. It has increased the flutter velocity of the structure by more than 2% but also confirmed the results concerning the optimal elastic properties obtained during the US optimisation.

4.3.3 Optimisation over span and chord

The previous cases were optimised in the span-wise direction which implies a 1D variation of the tow angles. While some improvements have been observed, a further gain in the aeroelastic performance could be achieved by applying a 2D variation of the fibre path. Considering the most efficient strategy with variation of the anisotropic moduli R_K and R_1 over the angle-ply curves defined in equation (4.10), a 2D optimisation can be carried out. Table 4.3 presents the results of 2D optimisations for the straight wing and recalls the span-wise (1D) optimisations of the same configuration. In both cases a slight improvement in the results of the flutter velocity (V_f) is observed during the 2D optimisation.

Case ID	Wing configuration	$R_K[GPa]$	$R_1[GPa]$	$\Phi_1[^\circ]$	$\alpha_{swept}[^\circ]$	$V_f[m/s]$	$\omega_f[rad/s]$
st1	straight (1D)	variable	variable	**0.**	**0.**	151.8	499.5
st2	straight (2D)	variable	variable	**0.**	**0.**	152.2	468.2

Table 4.3: Deterministic optimisation results of the Tow-Steered configurations obtained by 2D variation of anisotropic moduli (R_K and R_1) over the angle-ply curve throughout the structure with red coloured variables indicating constant parameters during the study.

The straight wing with 2D fibre variation presents an improvement of less than 1% in the flutter velocity in comparison to the 1D case. On the other hand, this small increase of V_f implies more than 6% decrease of the flutter frequency (ω_f).

The 2D variations of the anisotropic moduli (R_K and R_1) are presented in figure 4.17. The values remain within a limited interval particularly in the middle of the structure. An increase can be observed towards the leading and trailing edge of the wing. The 2D optimisation strategy has added multiple variation zones on the structure which increases the complexity of the fibre paths.

Similarly to the previous cases in section 4.3.1, the fibre orientations are calculated analytically using the anisotropic moduli over the angle-ply curve according to equation (4.15) and presented in figure 4.18.

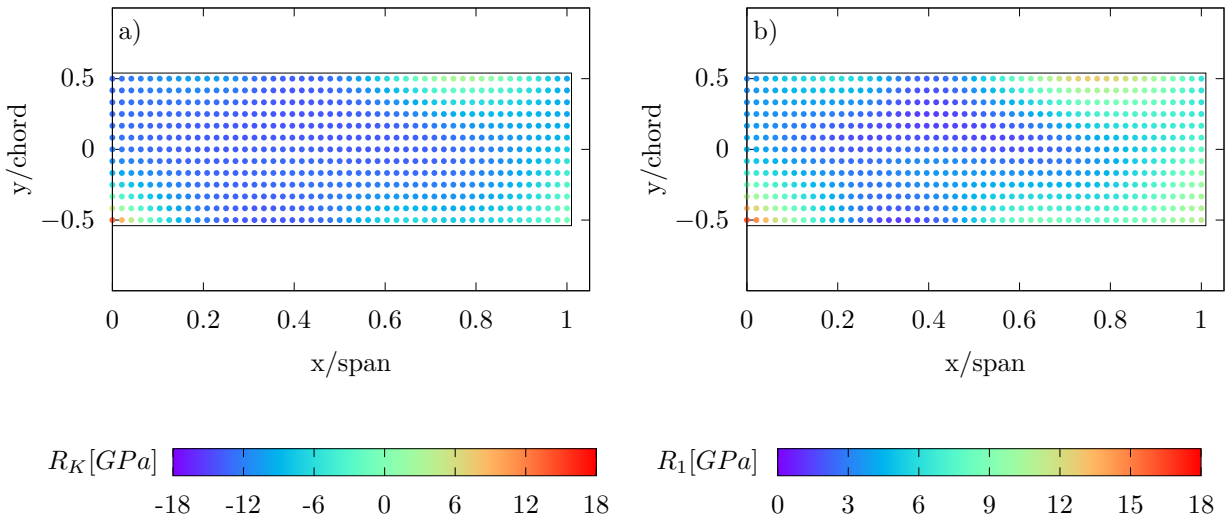

FIGURE 4.17: Variation of a) R_K and b) R_1 over the span and chord (2D) for the straight wing with the orthotropic axis aligned with the main wing axis (case *st2* in table 4.3) while optimising the anisotropic moduli over the angle-ply curve.

The lamination angle theta is represented, thus figure 4.18 depicts the fibre path along one ply, which will be alternated to plies aligned to the opposite angle $-\theta$, where the orientation is defined with respect to the main orthotropy axis Φ_1 (here, $\Phi_1 = 0$, the orthotropy axis is aligned with the main wing axis) The orientations vary both along the chord and the span. On the other hand, they remain nearly constant ($\theta \sim 40°$) over a large part of the structure the structure with slight changes towards the edges.

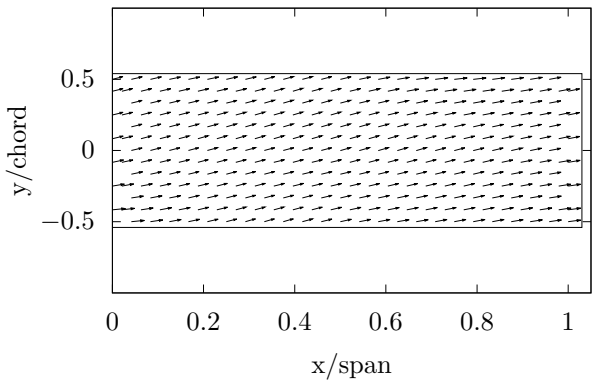

FIGURE 4.18: Variation of the lamination angle θ for the angle-ply stacking sequence over the span and chord presented by arrows for the straight wing with the orthotropic axis aligned with the main axis of the wing (case *st2*) in table 4.3.

Figure 4.19.a) represents the evolution of the aeroelastic damping and Figure 4.19.b) the unstable mode shape.

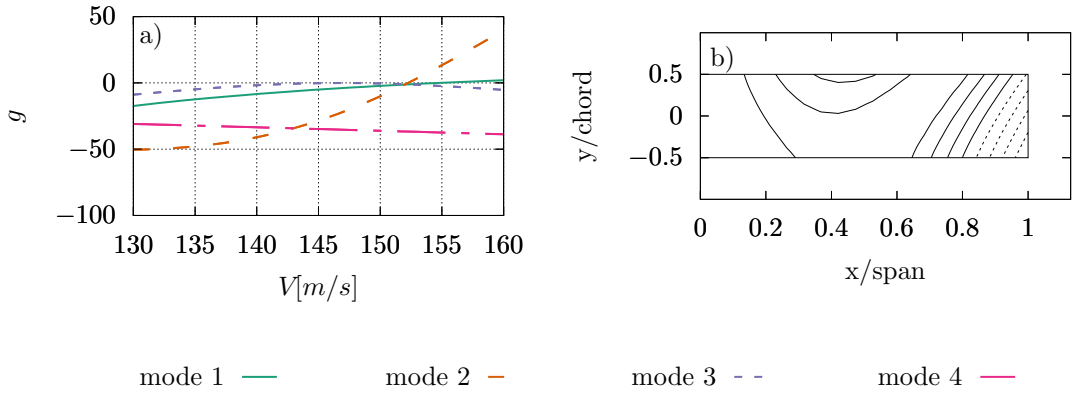

Figure 4.19: Aeroelastic response of the TS straight wing (case *st1*) with 2D variations of R_K and R_1 over the angle-ply curve. a) evolution of aeroelastic damping and b) the unstable mode shape.

The damping diagram indicates an instability over the second aeroelastic mode. However, the third mode remains very close to the flutter boundary (zero horizontal axis) and the first mode (divergence mode) becomes positive and thus unstable immediately after the instability of the second mode. This suggests that small perturbations of the optimal deterministic parameters can give raise to a mode switch and the emergence of unstable modes at lower velocities. It can be said that while the 2D variation of the fibre paths has increased the flutter velocity of about 1% compared to the 1D configuration, it has modified the rigidity of the structure in a way that the instability can occur over multiple mode shapes.

4.4 Conclusion

In the continuation of the previous chapter, multiple optimisation problems were formulated in order to maximise the flutter velocity of three different geometries. The optimisation problem was based on laminates with Variable-Stiffnesses (VS) and in particular the Tow-Steered composite plies. The latter are usually described using a direct parametrisation on the stacking sequence angles, and the orientation field over the geometric domain was approximated by polynomials [86, 82]. In this study, the polar parameters were employed to replace the traditional methods. Two different strategies were developed to study the impact of each parameter on the aeroelastic performance of the structure.

The first strategy put in place during this study was the variation of the anisotropic moduli over

the angle-ply curve (upper border of the orthotropic domain: only one anisotropic modulus is considered as an optimisation variable, since the second one is linked to it by the angle-ply curve relation). This choice was made due to the large number of optimal cases placed on this curve during the US optimisation. This strategy was carried out for all three geometries (straight, swept-backward, swept-forward). A gain of 4% over the flutter velocity was observed compared to the US case for the straight wing. Both swept cases showed a large gain for an optimised Φ_1 during their US optimisation. For this reason, the polar angle was included as an optimisation variable while staying constant throughout the structure. The flutter velocity of the swept-backward wing increased by 3% for an optimised value of the polar angle Φ_1 compared to the US case. On the other hand, the swept-forward wing did not have an increase of the flutter velocity compared to its US case during this optimisation study.

A more general strategy was then conducted over the entire orthotropic domain, thus letting the anisotropic moduli vary as independent variables over the whole domain. In this case, the straight wing could only attain similar velocities as the US configuration. The polar angle Φ_1 was included in the optimisation problem for the swept wings but kept constant over the structure. While the swept-backward wing matched the value of the V_f obtained during the US optimisation, the swept-forward wing could surpass this value. The latter resulted in a gain of about 3% for this configuration compared to the US case.

Finally, an optimisation study was conducted considering the variation of the tow angles in both span-wise and chord-wise directions. This strategy was applied to a straight wing by varying the anisotropic moduli over the ply-angle curves. The latter helped increase the flutter velocity by less than 1% which resulted in a decrease of the flutter frequency by 6%. The evolution of the aeroelastic damping of this configurations shows that three aeroelastic modes surpass or approach the flutter boundary (instability) around the flutter velocity. It can then be concluded that given the complexity in the fabrication of 2D fibre paths and the small improvement of flutter velocity, this configuration was one of the less interesting cases.

5

Uncertainty Quantification

In the present chapter, the stochastic behaviour of the optimal solutions obtained by various deterministic optimisation problems is investigated. These analyses are conducted mainly due to the multiple sources of uncertainties in the manufacturing of composite materials, as well as the observed potential risks of mode switches in the aeroelastic behaviour of the optimal solutions in the previous chapters. Scarth et al. [69] conducted similar studies on the aeroelastic behaviour of composite structures using quasi-steady aerodynamic models and approximating the aeroelastic response of the structure by means of polynomial chaos [96, 164, 165]: this study was restrained to symmetric distributions of errors on the ply orientation angles. Nitschke et al. [29] completed these studies by generalising the distribution of angular errors over the entire stacking sequence, thus getting rid of the unrealistic hypothesis of symmetry, and by including uncertainties on ply thicknesses, thanks to the use of the polar formalism. They both proved the importance of stochastic analysis on the aeroelastic response of a structure. On the other hand, both these studies were limited to straight cantilevered plate wings with Uniform-Stiffness laminates and very low-fidelity aerodynamic models.

Hereafter, broader geometries and composite configurations are explored using a higher fidelity aerodynamic model. The deterministic aeroelastic behaviour of these cases were studied in the previous chapters, however, the influence of the parametric uncertainties present during the manufacturing process was entirely neglected. This chapter is dedicated to the study of the impact of parametric uncertainties on all the optimal cases and a comparison between the probabilistic aeroelastic responses is conducted.

5.1 Uniform-Stiffness Laminates

The main parametric uncertainty taken into account is the uncertainty over the ply angles. These parameters have a considerable influence on the stiffness of the structure and its aeroelastic behaviour. The ply thicknesses can also be affected by uncertainties thus their impact on the aeroelastic response of the structure is measured. As explained in chapter 3, the optimisations have been conducted using polar parameters and the corresponding stacking sequences are obtained using different methods explained in section 3.2. The same strategy is employed for the Tow-Steered laminates which will be explained in details in the next section. The parametric uncertainties are then considered over the retrieved optimal stacking sequences.

At first, uncertainties over ply angles are considered for each stacking sequence. The uncertainties are propagated using the Latin Hypercube Sampling (LHS) with a standard deviation (std) of 5 degrees ($\sigma = 5°$) for each ply. For a given stacking sequence, a convergence study has been carried out by varying the number of samples in order to find the appropriate number of sampling to use. Table 5.1 summarises the mean of the flutter velocity, μ_f, and its standard deviation, σ_f, as well as their associated computational time for each case. The mean values of the 1000 and 5000 sample cases are identical to the order 10^{-3} and with less than 1% difference in comparison to the case with 10000 samples. The standard deviations of the first two cases are further apart but the general variations between the three cases remains about 2%.

Number of samples	$\mu_f[m/s]$	$\sigma_f[m/s]$	Computational time [1] [h]
1000	134.409	4.123	83
5000	134.408	4.225	416
10000	134.502	4.196	833

TABLE 5.1: Stochastic properties of the stacking sequence $[-45, 40, -55, 35, 40, 10, -60, -50]_s$ for three different LHS sampling population.

Figure 5.1 compares the probability density function (pdf) of the three sampling cases of table 5.1. The general shape of the pdfs remain similar to one another, whilst a small difference in the peak of the three pdfs is observed. The latter reduces as the number of the samples increases and gives place to a wider pdf which explains the difference in the values of the standard deviations. Given the similarities in the mean and standard deviation of the three cases presented in table 5.1 and the shape of the pdfs demonstrated in figure 5.1, it can be said that the 1000 samples can provide adequately accurate results. Furthermore, the high computational time of these simulations is an added justification to

[1] Intel Xeon Silver 4114 Processor with 40 cores

choose the lowest number of sampling to conduct the stochastic analysis.

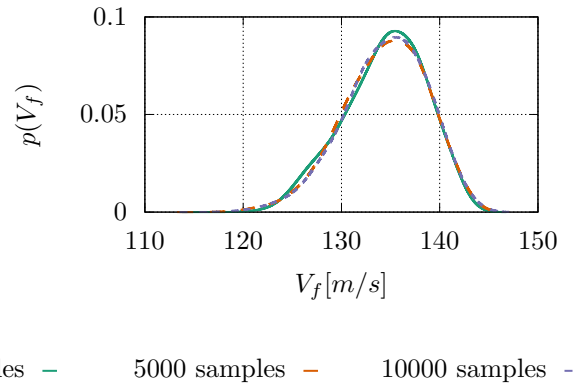

Figure 5.1: Probability distribution function of the flutter velocity corresponding to the stacking sequence $[-45, 40, -55, 35, 40, 10, -60, -50]_s$ for three different sampling population.

As a result of the previous study, 1000 samples are propagated using the LHS through the optimal configurations obtained in the previous chapters and their flutter velocity (V_f) is computed using the same method explained in section 2.1.3. In this section, the stochastic behaviour of all the orthotropic cases presented in chapter 3 are analysed. The first case to consider is the straight configuration obtained while optimising the anisotropic moduli (R_K and R_1) and the polar angle (Φ_1) (configuration *st1* of table 3.5). Table 5.2 presents the optimal and mean flutter velocity, V_f and μ_f respectively, as well as the standard deviation σ_f resulting from the uncertainty propagation. The flutter velocity corresponding the the 0.01^{th} percentile, $(V_f[m/s], 0.01)$, of each case has been presented in the far right column of table 5.2, in order to facilitate the comparison of the stochastic response of different configurations.

Case ID	Wing configuration	$V_f[m/s]$	$\mu_f[m/s]$	$\sigma_f[m/s]$	$(V_f[m/s], 0.01)$ [2]
st1	straight	146.5	132.8	10.0	102.2
st2	straight (variable α_{swept} [3])	146.7	138.0	5.8	119.0
swb1	swept-backward	130.5	129.1	4.0	116.5
swb2	swept-backward (variable Φ_1)	140.8	135.9	2.8	122.9
swf1	swept-forward	92.0	91.6	3.5	80.9
swf2	swept-forward (variable Φ_1)	137.0	130.2	4.3	101.3

Table 5.2: Stochastic properties of the deterministic optimal cases obtained with US ply laminates due to randomness in the ply angles with a standard deviation of 5°.

The pdf obtained from the uncertainty propagation on the ply angles of the first straight configuration treated in section 3.1.2 (*st1* already presented in table 3.5 and recalled in table 5.2) is presented in figure 5.2. The latter pdf exhibits a bi-modal behaviour which can be easily explained using the response surface in figure 5.3.a).

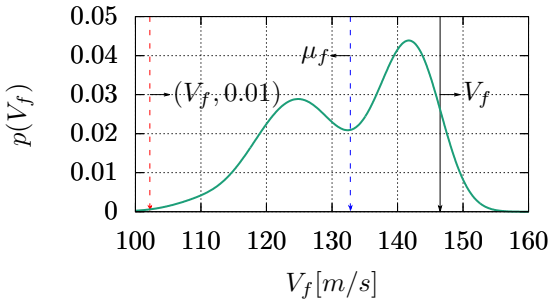

FIGURE 5.2: Probability distribution function of flutter velocity corresponding to the optimal straight US case *st1* where $\Phi_1 = 0$. The vertical solid black line represents the deterministic optimal flutter velocity, the vertical dashed blue line is the mean flutter velocity μ_f and the vertical dashed red line, the flutter velocity at 0.01^{th} percentile $(V_f[m/s], 0.01)$.

Figure 5.3 shows the complete response surface of the critical flutter velocity V_f for the straight configuration *st1*, considered as made of an orthotropic laminate with the main orthotropy axis Phi_1 aligned with the main wing axis (Phi_1= 0). When varying the values of the anisotropic moduli R_K and R_1 over the orthotropic domain, a discontinuity caused by a mode switch is present on the response surface and the maximum flutter velocity is placed right next to this discontinuity. Thus, when applying angular errors to the deterministic optimal stacking sequence, given in table 3.5, the resulting laminates can show much lower aeroelastic performances if their elastic parameters fall beyond the discontinuity. As a consequence, the higher peak of the pdf in figure 5.2 corresponds to the values around the optimal deterministic flutter velocity ($V_f = 146.5\ m/s$) which are observed on the right side of this discontinuity. In figure 5.2 the second peak around the smaller values of V_f is related to the values on the left side of the discontinuity. These observations can explain the difference of 10% between the mean and the optimal flutter velocity (μ_f and V_f, respectively, in table 5.2) as well as the large value of the standard deviation. The flutter velocity at 0.01^{th} percentile ($V_f = 102.2\ m/s$) is more than 30% lower than the optimal flutter velocity which is another implication of the bi-modality of this pdf. The high probability of the lower peak indicates a high risk behaviour. The latter can easily fall in the flying region of the airplane given the current safety standards and cause severe damages to the wing structure [29].

[2] flutter velocity value at 0.01^{th} percentile
[3] α_{swept} is referred to the angle of the swept wing

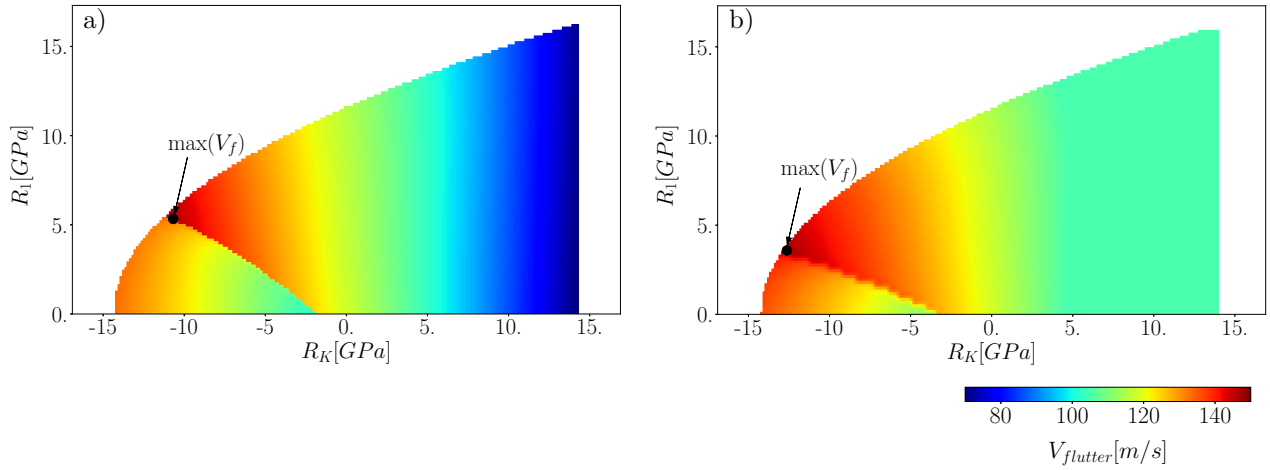

Figure 5.3: Variation of the flutter velocity in an orthotropic domain as a function of the anisotropic moduli R_K and R_1. a) $\Phi_1 = 0°$ and b) $\Phi_1 = -2°$. The black dot represents the configuration with the highest flutter velocity for a straight wing.

The stochastic behaviour of other configurations have thus been studied. The *st2* case of straight wing obtained from the optimisation of the anisotropic moduli (R_K and R_1), as well as the polar angle (Φ_1) and the swept angle (α_{swept}) is now considered (results shown in table 3.5). In this case, the mean value of the flutter velocity ($\mu_f = 138.0\ m/s$) is 4% higher than the previous configuration ($\mu_f = 132.8\ m/s$). The standard deviation of *st2* is about 40% lower than *st1*. As a result of this difference, this configuration has a flutter velocity at 0.01^{th} percentile ($V_f = 119.0\ m/s$) that is about 15% higher than the previous straight wing ($V_f = 102.2\ m/s$) .

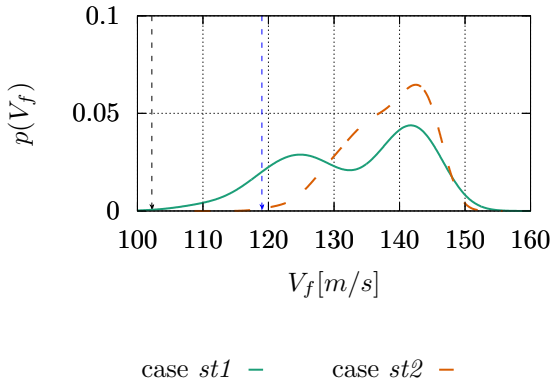

Figure 5.4: Comparison of probability distribution functions of flutter velocity corresponding to the optimal straight US cases (*st1* and *st2* in table 5.2) where $\Phi_1 = 0°$ and $\Phi_1 = -2°$ respectively. The vertical dashed black line represents the flutter velocity at 0.01^{th} percentile of case *st1* and the vertical dashed blue line is the flutter velocity at 0.01^{th} percentile of case *st2*.

Figure 5.4 compares the two pdf of this optimal laminate *st2* to the previous case *st1* presented in figure 5.2. The probability density function once again exhibits bi-modal behaviours but in comparison to the case with $\Phi_1 = 0°$, the lower peak falls in larger values of V_f and closer to the higher peak which can explain the 40% decrease of the standard deviation. This behaviour can be explained using figure 5.3.b) which exhibits a discontinuity in the response surface, but the difference between values on either side of the discontinuity (V_f^{high}=147 m/s, V_f^{low}=142 m/s) is lower than in the *st1* case of figure 5.3.a) (V_f^{high}=147 m/s, V_f^{low}=133 m/s). On the other hand, the values of the flutter velocity on both sides of this discontinuity remain in a closer interval in comparison to the case with $\Phi_1 = 0°$. This proximity of values results in a smaller variance in the pdf of the optimal case despite the existence of a mode switch on the response surface.

The forward uncertainty propagation of a swept-backward wing obtained while optimising only the anisotropic moduli (case *swb1* given in table 3.5) and when including the polar angle as an optimisation variable (case *swb2* given in table 3.5), are compared in figure 5.5. First of all, one can remark a bimodal shape for the pdf of the *swb1* case (green curve in figure 5.5), whilst the bi-modality seems to be absent in the *swb2* case. Coherently with the deterministic optimisation results (cfr. table 3.5), the mean flutter velocity ($\mu_f = 135.9\ m/s$) of case *swb2* is higher than case *swb1* ($\mu_f = 129.1\ m/s$) but this difference is only of 5%, while the optimal flutter velocities are 7% apart. Moreover, the standard deviation is 30% smaller for the case with optimised Φ_1 (case *swb2*). The same observations are made, by comparing the pdfs: the latter case has a lower variance and a pdf with higher probabilities around the mean value. The long tail in the pdf of case *swb2* lowers the value of flutter velocity at 0.01^{th} percentile ($(V_f[m/s], 0.01) = 122.9\ m/s$, dashed blue line in figure 5.5) compared to the optimal flutter velocity ($V_f = 140.8\ m/s$, solid blue line in figure 5.5). On the other hand, the latter has a higher flutter velocity at 0.01^{th} percentile compared to case *swb1* ($(V_f[m/s], 0.01) = 116.5\ m/s$, dashed black line in figure 5.5) and thus remains the more reliable case.

Figure 5.6 presents the response surfaces of the flutter velocity and the flutter frequency of the swept-backward wing with an optimised polar angle (case *swb2* in table 5.2), which help to explain the stochastic analysis of this configuration. Similarly to the previously discussed straight geometries, the optimal case is located next to a discontinuity. The latter is more visible on the frequency response surface (figure 5.6.b) due to the sharp jump between the values of two modes. This surface is more complex than the one corresponding to the straight wing as it has two mode-switches including a region with zero frequency (represented by the blue region in the upper part of the domain, corresponding to divergence instabilities). On the other hand, the discontinuity next to which the optimal case is located, does not show a variation between the flutter velocities from one side to the other, which avoids the bi-modality on the pdf of the swept-backward wing.

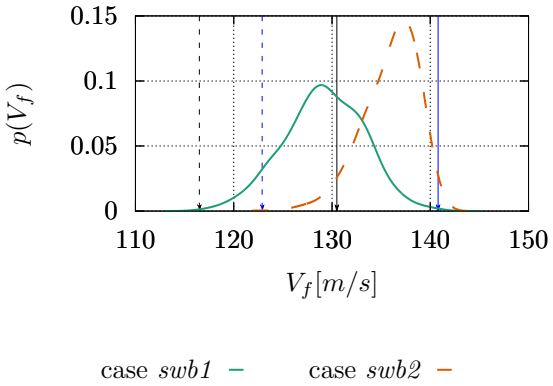

Figure 5.5: Comparison of probability distribution functions of flutter velocity corresponding to the propagation of uncertainties over the optimal swept-backward US cases (*swb1* and *swb2*) , with, respectively, Φ_1 = -15 (orthotropy axis aligned with the swept wing axis) and Φ_1=-56 (optimised value of Φ_1). The solid and the dashed black lines represent the optimal and the 0.01^{th} percentile flutter velocity of case *swb1*, and the solid and the dashed blue lines are the optimal and the 0.01^{th} percentile flutter velocity of case *swb2*, respectively.

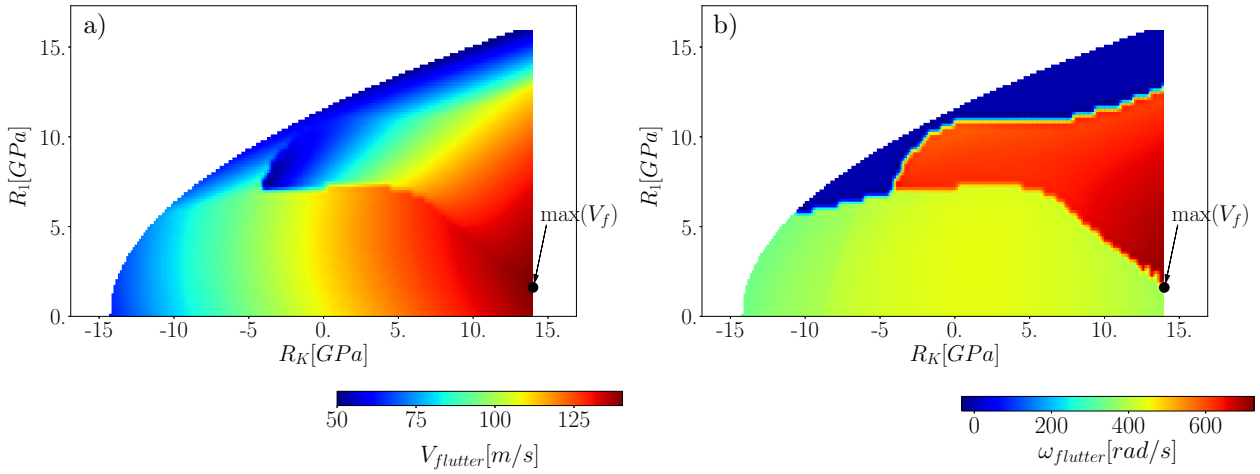

Figure 5.6: Variation of a) the flutter velocity and b) the flutter frequency in an orthotropic domain as a function of the anisotropic moduli R_K and R_1 for the optimal solution of *swb2* case, where $\Phi_1 = -56°$. The black dot represents the configuration with the highest flutter velocity for the considered configuration of swept-backward wing.

The comparison of swept-forward cases, *swf1* and *swf2* is given in figure 5.7 and it shows the significant difference of about 30% in the optimal flutter velocities (cfr. the deterministic optimal results in table 3.5). Unlike the swept-backward wings, case *swf1* has a lower variance ($\sigma_f = 3.6\ m/s$) compared to case *swf2* ($\sigma_f = 4.3\ m/s$). The difference in the variance is of 22% which is not negligible, even if both values of variance are small. However, case *swf2* has a flutter velocity at 0.01^{th} percentile

($(V_f[m/s], 0.01) = 101.3\ m/s$, dashed blue line in figure 5.7) that is more than 20% higher than case *swf1* ($(V_f[m/s], 0.01) = 80.9\ m/s$, dashed black line in figure 5.7) which renders the former the more reliable configuration. These observations are presented in figure 5.7 with the pdf of case *swf2* whose range of observability is obtained for larger values of V_f than case *swf1*.

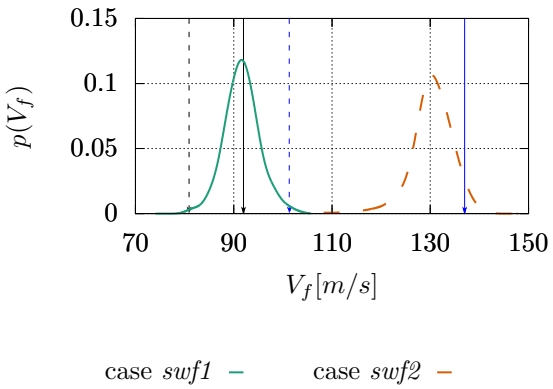

FIGURE 5.7: Comparison of probability distribution functions of flutter velocity corresponding to the optimal swept-forward US cases (*swf1* and *swf2*) with, respectively, $\Phi_1 = 15$ (orthotropy axis aligned with the swept wing axis) and $\Phi_1 = 47$ (optimal direction of the orthotropy axis). The solid and the dashed black lines represent the optimal and the 0.01^{th} percentile flutter velocity of case *swf1*, and the solid and the dashed blue lines are the optimal and the 0.01^{th} percentile flutter velocity of case *swf2*, respectively.

It needs to be noted that, for both swept cases (backward, *swb1* and *swb2*, and forward, *swf1* and *swf2*), when the polar angle is aligned with the main axis of the structure, the mean and the optimal values of the flutter velocity are very close to one another with less than 1% difference. The reason for the proximity of these values is the impact of Φ_1 on the swept geometries. It was shown during the optimisation process (in section 3.1.2) that the swept cases have higher flutter velocities once their orthotropic and reference axis are not aligned. Thus, when an uncertainty is imposed over the aligned cases, it influences the values of the polar angles and reaches higher flutter velocities than the optimal case. This increase is not observed for configurations with unaligned orthotropic and main axis. For these cases, the polar angle is included in the optimisation process and the deterministic case has already reached the maximum flutter velocity and it can only be reduced by uncertainties over Φ_1.

Finally, the comparison of the pdf of V_f is presented in figure 5.8 for cases *st1*, *swb2* and *swf2*. It can be observed that, despite the highest optimal flutter velocity of the straight wing, the swept-backward configuration remains the best compromise between the performance and reliability as it possesses the largest mean value and the smallest variance which directly implies the higher flutter velocity at 0.01^{th} percentile ($(V_f[m/s], 0.01) = 122.9\ m/s$, dashed blue line in figure 5.8).

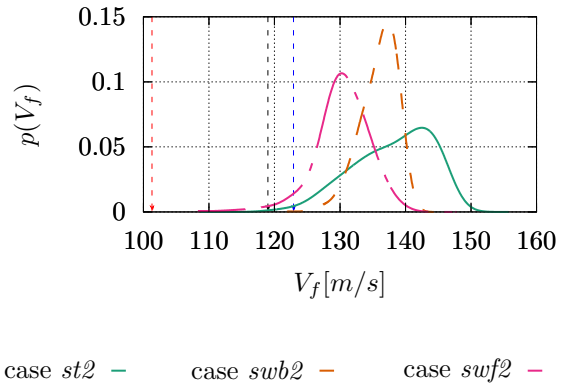

Figure 5.8: Comparison of probability distribution functions of flutter velocity corresponding to all optimal US cases with variable Φ_1 (cases *st1*, *swb2* and *swf2*). The dashed black line represents the flutter velocity at 0.01^{th} percentile of case *st2*, the dashed blue line is the flutter velocity at 0.01^{th} percentile of case *swb2* and the dashed red line is the flutter velocity at 0.01^{th} percentile of case *swf2*.

5.2 Tow-Steered Composites

Before considering the parametric uncertainties for the Tow-Steered (TS) composite materials, spatially variable uncertainties need to be modelled, which was not the case for Uniform-Stiffness composites, where angular and thickness perturbations can be directly taken into account as parametric uncertainties. However, if the direct sampling methods, applied in section 5.1, were employed in the case of Variable-Stiffness Tow-Steered composites, they could simply provide uncertainties over each node of the FE model, and are not able to include the spatial dependency present in the TS plies. In this context, Scarth et al. [166] have employed the Karhunen-Loève expansion which separates the spatial and random dependency of the uncertainties, and they have presented an intrusive polynomial chaos method which conserves these properties of the K-L expansion. Another example of uncertainty propagation using a random field can be observed in the work of De Larrard et al. [167], where spatial and random variations of the Young modulus are considered over the mechanical behaviour of a nuclear containment vessel and a study is conducted on the impact of the correlation length over the covariance function and its different parameters. Guimarães et al. [168] applied this expansion in the framework of aeroelasticity to impose uncertainties over a Tow-Steered composite laminate in both subsonic and supersonic flow conditions.

In this work, a similar approach is considered to investigate the stochastic response of Variable-Stiffness (VS) laminates made of Tow-Steered (TS) plies. As the entire optimisation studies have been carried out using the polar parameters, the corresponding tow angles need to be calculated for each case. In this section, the stacking sequence retrieval of the Tow-Steered laminates is first explained.

Next the numerical modelling of the uncertainty propagation using the Karhunen-Loève expansion is presented. Finally the results of these studies are analysed and discussed in detail.

5.2.1 Stacking Sequence Retrieval of Tow-Steered plies

In the following, the methods applied in section 3.2 are adapted in the case of Variable Stiffness (VS) laminates. Two different optimisation strategies are employed during the optimisation of these materials. Each strategy requires a specific approach to obtain a stacking sequence with similar elastic properties as the target polar parameters.

- **Variation of the anisotropic moduli over the angle-ply curve**

  The first optimisation strategy, adopted in section 4.2.3 varies R_K and R_1 over the structure but limits the parameters to the angle-ply curve where most optimal configurations from US cases are placed. In this case, each finite-element node (i), with $i = 1, ..., N$, corresponds to a set of polar parameters which result in a corresponding (i)-th node stacking sequence, which is defined over the angle-ply curve. The angle-ply lamination angle θ can be calculated analytically using equation (5.1).

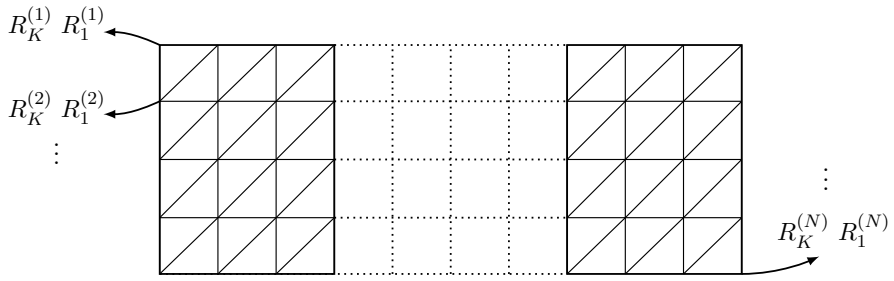

FIGURE 5.9: The corresponding set of anisotropic moduli over each node of the Finite Element mesh.

$$
\begin{aligned}
\theta^{(1)} &= \frac{1}{2}\arccos\left(\frac{R_1^{(1)}}{R_1^{BL}}\right) \quad \Rightarrow \quad [\theta_2^{(1)}, -\theta_4^{(1)}, \theta_2^{(1)}, -\theta_2^{(1)}, \theta_4^{(1)}, -\theta_2^{(1)}] \\
\theta^{(2)} &= \frac{1}{2}\arccos\left(\frac{R_1^{(2)}}{R_1^{BL}}\right) \quad \Rightarrow \quad [\theta_2^{(2)}, -\theta_4^{(2)}, \theta_2^{(2)}, -\theta_2^{(2)}, \theta_4^{(2)}, -\theta_2^{(2)}] \\
&\vdots \\
\theta^{(N)} &= \frac{1}{2}\arccos\left(\frac{R_1^{(N)}}{R_1^{BL}}\right) \quad \Rightarrow \quad [\theta_2^{(N)}, -\theta_4^{(N)}, \theta_2^{(N)}, -\theta_2^{(N)}, \theta_4^{(N)}, -\theta_2^{(N)}]
\end{aligned}
\tag{5.1}
$$

where the (i)-th line (or subscript (i)) indicates the stacking sequence corresponding to the (i)-th node of the FE model illustrated in figure 5.9. The subscript in the stacking sequences denote the number of repetition of that orientation in consecutive plies.

This case could rise the question of the feasibility limits on the fibre path for each ply. On the other hand, the B-spline method, applied to model the TS laminates, explained in section 4.1, has a strong convex hull property which insures the admissible limits on the value of the anisotropic moduli. As these values have a direct relationship with angle (θ) used to build the corresponding stacking sequence, the convex hull property insures the limits on the fibre paths of each ply as well.

- **Variation of the anisotropic moduli inside the orthotropic domain**

The second optimisation strategy in section 4.2.3 was conducted by variation of the anisotropic moduli all over the orthotropic domain. For this case, each finite element node, as depicted in the FE model of figure 5.9, corresponds to a different set of polar parameters in the orthotropic domain. Contrary to the previous strategy, the corresponding stacking sequence retrieval will require a numerical investigation by minimising the Kullback-Leibler function defined in equation (5.2).

$$\mathbf{F_{ABD}}(\delta, \mathbf{L_T}) = \mathrm{tr}(\mathbf{L}(\delta)\mathbf{L_T^{-1}}) + \mathrm{tr}(\mathbf{L}(\delta)^{-1}\mathbf{L_T}) - 12 \tag{5.2}$$

where subscript $\mathbf{T}$ represents the Target matrices associated to the optimal polar parameters, all $\mathbf{L}$ matrices are defined as a function of the rigidity tensors of the composite structure

$$\mathbf{L} = \begin{bmatrix} \mathbf{A} & \mathbf{B} \\ \mathbf{B} & \mathbf{D} \end{bmatrix} \tag{5.3}$$

This study can become very costly due to the large number of finite-element nodes and the limits on the fibre path curves cannot be easily satisfied. For these reasons, the optimal cases obtained by this strategy are not analysed in this chapter.

Once the stacking sequences corresponding to each case are obtained, they can be employed in the uncertainty quantification analysis. For this purpose, the Karhunen-Loève expansion is used in order to take into account the spatial dependency of the random variables.

5.2.2 Karhunen-Loève Expansion

The Karhunen-Loève (K-L) expansion which decomposes the random and the spatial dependency of the uncertainties, can be defined as [169]

$$\mathbf{K}(\mathbf{x}, \Theta) = \bar{\Theta}(\mathbf{x}) + \sum_{i=1}^{m} \sqrt{\lambda_i} \kappa_i(\mathbf{x}) \zeta_i(\Theta) \tag{5.4}$$

where $\mathbf{K}(\mathbf{x}, \Theta)$ is a random process (in this case the uncertainties over the tow-angles), $\bar{\Theta}(\mathbf{x})$ the mean of the process (deterministic optimal fibre paths), λ_i and $\kappa_i(\mathbf{x})$ the eigenvalues and the eigenvectors of the covariance function ($\mathbf{C}(\mathbf{x_1}, \mathbf{x_2})$), $\zeta_i(\Theta)$ the uncorrelated random variables obtained with unit variance and m is the number of K-L terms. It needs to be noted that $\mathbf{x}$ represents the coordinate of a FEM node and the $\mathbf{C}(\mathbf{x_1}, \mathbf{x_2})$ translates to the value of covariance function calculated between two nodes. The covariance function [170] chosen for this study can be defined with the help of the correlation length (l_c) and the variance of the random process (V_c), which is related to the standard deviation σ on the angular errors

$$\mathbf{C} = V_c \exp\left(-\frac{\|\mathbf{x_1} - \mathbf{x_2}\|^2}{l_c^2}\right) \tag{5.5}$$

In this study, a correlation length of $l_c = \frac{chord}{2}$ is considered with a variance of $V_c = \sigma^2$ (previously set to 5° for the errors on fibre angles). The covariance function $\mathbf{C}$ is thus computed amongst all FEM nodes using their coordinates, and its eigenvalues λ_i and eigenvectors κ_i are computed. For the truncated K-L expansion given in equation (5.4), the number of terms are limited to m whose value is determined by a convergence study over the eigenvalues. Defining an error as the fraction of the sum of truncated terms over the total sum of eigenvalues $\frac{\sum \lambda_m}{\lambda_{tot}}$, figure 5.10 represents the evolution of the latter with respect to the number of K-L terms.

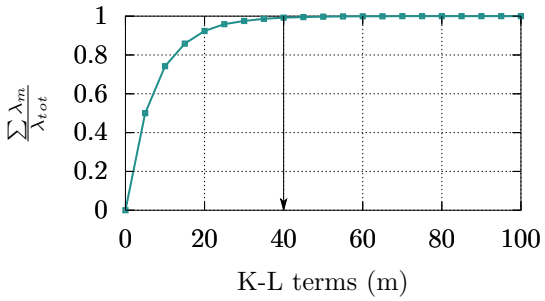

FIGURE 5.10: Convergence of the eigenvalue error with respect to the number of K-L terms.

Considering the convergence test conducted above, $m = 40$ K-L terms are chosen to present the random process of equation (5.4). The covariance matrix mode shapes of the first 8 terms are presented in figure 5.11.

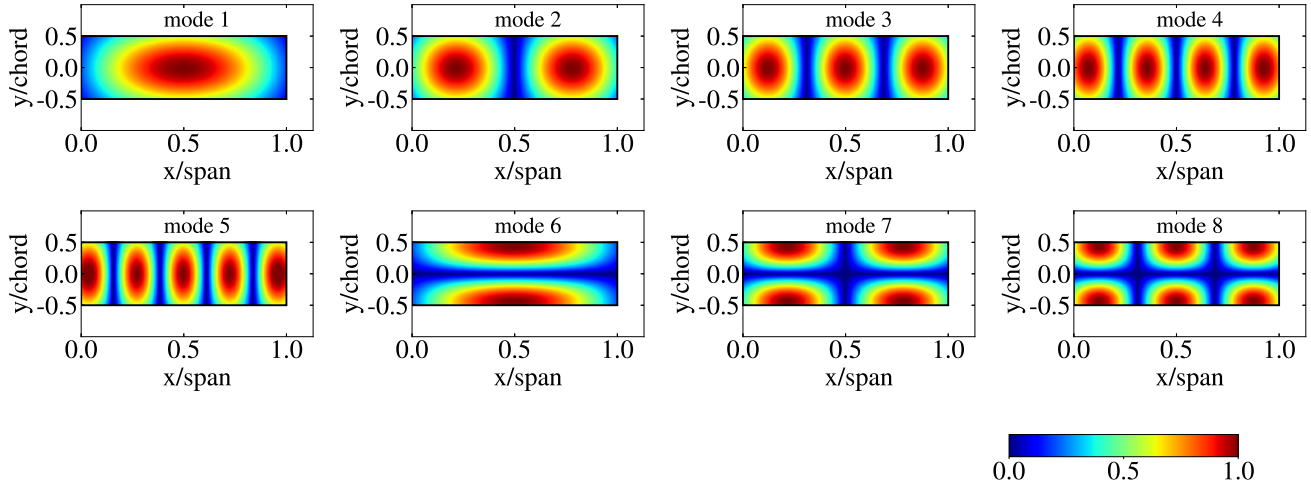

Figure 5.11: Mode shapes (eigenvectors) of the K-L covariance matrix.

Algorithm 3: Karhunen-Loève Expansion for generation of uncertainty over TS laminates

1: Define the Covariance matrix (equation (5.5))

$$\mathbf{C} = V_c \exp\left(-\frac{\|\mathbf{x_1} - \mathbf{x_2}\|^2}{l_c^2}\right)$$

2: Compute the eigenvalues λ and the eigenvectors κ of the Covariance matrix
3: **for** $i = 1 : N_{plies}$ **do**
4: Generate a set of random variables with unit variance $\zeta_i(\Theta)$
5: **for** $i = 1 : N_{random}$ **do**
6: Compute the B-spline surface (equation (5.4))

$$\mathbf{K}(\mathbf{x}, \Theta) = \bar{\Theta}(\mathbf{x}) + \sum_{i=1}^{m} \sqrt{\lambda_i}\kappa_i(\mathbf{x})\zeta_i(\Theta)$$

7: **end for**
8: **end for**

5.2.3 Effect of uncertainties on the aeroelastic response of angle-ply TS laminates

As shown in section 5.2.1, the optimal angle-ply TS laminates are retrieved by application of an analytical approach. Using the K-L expansion method, the uncertainties on ply angles with a standard deviation of $\sigma = 5$ are propagated in order to obtain perturbed angle-ply TS laminates. The aeroelastic performances of such uncertain TS laminates are evaluated and the results are presented in table 5.3.

Case ID	Wing configuration	$V_f[m/s]$	$\mu_f[m/s]$	$\sigma_f[m/s]$	$(V_f[m/s], 0.01)$
$st1$	straight	151.8	138.4	10.4	117.4
$swb1$	swept-backward	145.1	139.8	3.6	124.1
$swf1$	swept-forward	127.6	123.9	2.7	116.2

TABLE 5.3: Stochastic properties of the optimal cases obtained with angle-ply TS laminates: deterministic maximum flutter velocity V_f, mean μ_f and standard deviation σ_f of the flutter velocity after propagation of errors, and flutter velocity at 0.01^{th} percentile, $(V_f[m/s], 0.01)$.

The straight wing has a mean velocity μ_f that is more than 8% lower than its optimal deterministic flutter velocity V_f. The standard deviation of this case indicates a large variation of the flutter velocity around the mean value which implies a more dispersed probability density function (pdf) resulting into a flutter velocity at 0.01^{th} percentile that is more than 20% lower than the optimal V_f. The swept-backward wing, while having a lower optimal flutter velocity compared to the straight case, has a mean value that is only about 3% lower than the optimal V_f. Given the value of the standard deviation (std) which is more than 65% lower than the std of the straight case, it can be concluded that the pdf of case *swb1* is much narrower than the *st1* with a higher probability over the mean value. The flutter velocity at 0.01^{th} percentile of case *swb1* ($V_f = 124.1\ m/s$) is 5% higher than the one corresponding to the straight wing ($V_f = 117.4\ m/s$). The previous observation shows that, while the swept-backward wing has a lower optimal flutter velocity, it is a more reliable configuration compared to the straight wing. Finally, the swept-forward case with the lowest optimal flutter velocity in comparison to the other cases, has a mean velocity that is 3% lower than its optimal V_f. This configuration has the lowest standard deviation compared to the other geometries which implies that it has the highest probability of having the flutter velocity around the calculated mean value μ_f. Moreover, the flutter velocity at 0.01^{th} percentile of case *swf1* is only less than 1% lower than the straight case while its optimal flutter velocity is more than 15% lower than case *st1*. While these values provide multiple indications concerning the probabilistic response of each optimal case, the pdf of each configuration allows a more visual and explicit comparison of the aeroelastic behaviour.

Figure 5.12 compares the three pdfs of the cases presented in table 5.3. The pdf of the straight wing exhibits a bi-modal behaviour which explains the large value of the standard deviation corresponding to this configuration. As mentioned previously, the position of the optimal straight case next to a discontinuity present on the orthotropic surface can results in a first peak on the pdf around the higher values of the flutter velocity and a second peak related to the lower velocities on the other side of the discontinuity. This mode switch which gives rise to the bi-modal probabilistic behaviour can become dangerous with the current safety measures which takes into account a 15% security margin below the maximum flutter velocity.

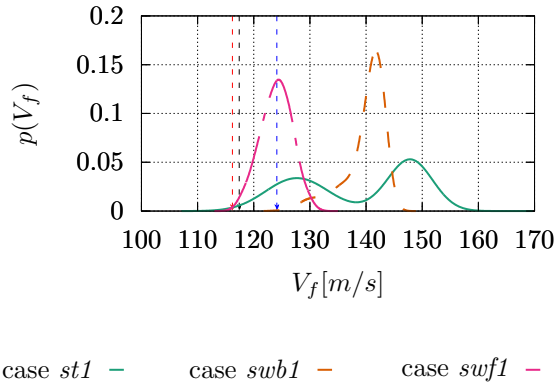

Figure 5.12: Comparison of probability distribution function of flutter velocity corresponding to the optimal Tow-Steered cases with variations of R_K and R_1 over the angle-ply curve with optimised Φ_1 for swept cases. The dashed black line represents the flutter velocity at 0.01^{th} percentile of case *st1*, the dashed blue line is the flutter velocity at 0.01^{th} percentile of case *swb1* and the dashed red line is the flutter velocity at 0.01^{th} percentile of case *swf1*.

The swept-backward configuration does not show bi-modal behaviour but the corresponding pdf has a long tail which explains the value of the standard deviation. The tip of the density function has a narrower shape and it has a high probability on the mean flutter velocity. On the other hand the large tail reduces the reliability of the configuration. The swept-forward wing has the ideal shape with a high probability over the mean flutter velocity and a narrow pdf with short tails on both ends. However, the optimal flutter velocity of this case is lower than both other configurations and while it is reliable, the performance is not adequate.

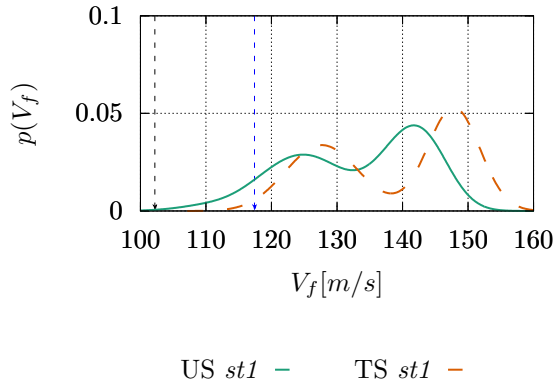

Figure 5.13: Comparison of probability distribution function of flutter velocity corresponding to the Uniform-Stiffness (US) case and the Tow-Steered (TS) laminate with span-wise variation of R_K and R_1 over the angle-ply curve for a straight wing. The dashed black line represents the flutter velocity at 0.01^{th} percentile of the US configuration and the dashed blue line is the flutter velocity at 0.01^{th} percentile of the TS case.

The stochastic response of the Tow-Steered configuration obtained by optimisation of the anisotropic moduli over the angle-ply curve is compared to the Uniform-Stiffness straight case in figure 5.13. Both pdfs present a bi-modal response which confirms that the maximum flutter velocity is located near the mode switch discontinuity. The Tow-Steered fibres allowed an increase of the flutter velocity regarding both peaks. It was observed that the maximum flutter velocity of the TS configuration is 4% higher than its US counterpart. However the stochastic response has higher values of velocities for both peaks and the lower probability over the gap between the two peaks.

Figure 5.14 shows that the swept-backward wings both present a mono-modal pdf of V_f. The Uniform-Stiffness case has a wider pdf that is more uniformly spread. The Tow-Steered configuration on the other hand, has a narrower tip with higher probabilities but a longer tail that covers a higher range of the lower velocities. This behaviour is the reason why the standard deviation of the TS case is about 25% higher than the US optimal laminate.

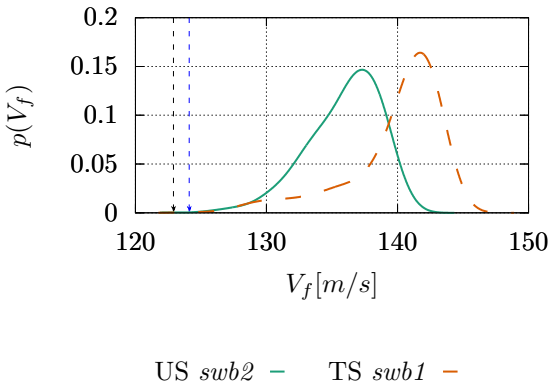

FIGURE 5.14: Comparison of probability distribution function of flutter velocity corresponding to the Uniform-Stiffness (US) case and the Tow-Steered (TS) laminate with span-wise variation of R_K and R_1 over the angle-ply curve and optimised Φ_1 for a swept-backward wing. The dashed black line represents the flutter velocity at 0.01^{th} percentile of the US configuration and the dashed blue line is the flutter velocity at 0.01^{th} percentile of the TS case.

Unlike the previous cases, the swept-forward wing could not surpass the maximum flutter velocity obtained with the optimal Uniform-Stiffness configuration during the Tow-Steered optimisation over the angly-ply curve. The comparison of the stochastic response of both cases in figure 5.15 confirms the difference in the mean velocities. On the other hand, the TS configuration has a narrower pdf with higher probability over the corresponding mean velocity. The latter explains the 35% reduction in the standard deviation of the TS case. It can be concluded that the latter is a more reliable configuration than the US laminate with lower performance.

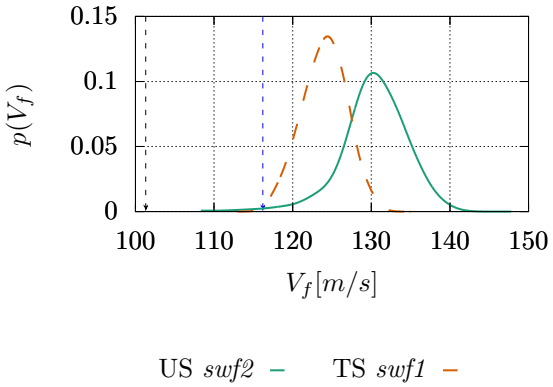

Figure 5.15: Comparison of probability distribution function of flutter velocity corresponding to the Uniform-Stiffness (US) case and the Tow-Steered (TS) laminate span-wise variation of R_K and R_1 over the angle-ply curve and optimised Φ_1 for a swept-forward wing. The dashed black line represents the flutter velocity at 0.01^{th} percentile of the US configuration and the dashed blue line is the flutter velocity at 0.01^{th} percentile of the TS case.

5.3 Conclusion

The stochastic analysis of the optimal configurations obtained with various formulations was conducted. The Uniform-Stiffness laminates have been subject to a direct uncertainty propagation using the Latin Hypercube Sampling (LHS) method. A standard deviation of 5° over 1000 samples was considered to carry out the probability density function of each case. Unlike the results of the deterministic optimisation for which the highest flutter velocity was achieved by the straight wing, the stochastic analysis suggested different conclusions. The mean flutter velocity of the straight wing indicated a difference of 8% compared to the optimal V_f which was significantly larger than other cases. This reduction can be explained by the large value of the standard deviation and the bi-modal pdf of this case. This bi-modality reduced the reliability of the optimal deterministic results and proved the necessity of the stochastic investigation.

Other geometries such as swept wing were then subject to similar analysis. The impact of the polar angle over both swept configurations was demonstrated in previous chapters, the mean values of the stochastic study confirmed these conclusions. The swept-backward wing showed higher mean values for the case with optimised polar angle Φ_1 and a reduced standard deviation for the latter case. On the other hand, the swept-forward wing indicated an increase in the standard deviation of the configuration with unaligned orthotropic and main axis. While this increase is of about 22%, the latter configuration remained more robust due to its 30% increase in the mean flutter velocity.

Conducting similar studies for the Tow-Steered laminates, first, the corresponding stacking sequences needed to be obtained. Only the results of one strategy were considered for the stochastic studies due to numerical and manufacturing limitations. The retrieval method employed was similar to the Uniform-Stiffness laminates. Due to the spatial dependency of the fibre paths, the uncertainties imposed on angles had to be decomposed using the Karhunen-Loève (K-L) expansion. An exponential covariance function was chosen for this purpose and 40 K-L terms were conserved to model the random processes.

Three geometries were investigated during which the Tow-Steered laminates were optimised by means of variation of anisotropic moduli over the angle-ply curve. The straight wing again had the highest flutter velocity in comparison to other cases. On the other hand, the large difference of more than 8% between the optimal and mean values as well as the high standard deviations for both cases, indicated a wide pdf. The latter presents bi-modal behaviours and while the deterministic values of the flutter velocity were higher than other configurations, the stochastic results were not sufficiently reliable. While the swept cases did not achieve as high values as the straight wing, they had more reliable stochastic responses with a low variance and high probability over their optimal flutter velocity.

Finally, the stochastic behaviour of both optimisation formulations were compared for each geometry. The straight wing preserved its bi-modal behaviour for both Uniform-Stiffness and Tow-Steered cases with higher velocities for the latter. The pdf of the swept-backward wing exhibited the higher values of the optimal and mean flutter velocities of the TS case. On the other hand the long tail of the latter resulted in higher standard deviations and thus lower reliability of this configuration. The TS strategy could not increase the flutter velocities of swept-forward case. On the other hand, it rendered the pdf narrower with higher probabilities on the corresponding mean value. This case, while less efficient, was more reliable with respect to the obtained optimal deterministic results.

6

Stochastic Optimisation

In this chapter, an optimisation study, based on the probabilistic aeroelastic behaviour of the structure, is carried out. The optimal deterministic aeroelastic response of various geometries and the probability density function (pdf) of optimal cases were presented and compared in the previous chapters. Some of these studies demonstrated bi-modal stochastic behaviours near the maximum flutter velocity. These behaviours are the source of motivation for investigations conducted in this chapter. The objective is to obtain a laminate configuration which owns an optimal probabilistic response defined by a given number of criteria.

The stochastic optimisation problem can be defined in multiple manners. Muc et al. [118] gave a thorough review of various optimisation formulations in aeroelasticity using composite materials. Some formulations are based on the mean and the variance of the objective function which result in a robust optimisation [171]. Another type of stochastic optimisation is reliability-based which focuses on the probability of failure that can be measured by a given threshold [172]. Both approaches have been compared in an aeroelastic framework in the work of Scarth et al. [100] and the reliability-based method showed results with lower probability of failure while the robust formulation had lower variance but higher probability of failure. In this chapter, the optimisation studies are based on the Reliability-Based Design Optimisation (RBDO). The formulation of this problem and the employed tools will be explained in details hereafter.

6.1 Optimisation formulation

The first step of the Reliability-Based Design Optimisation (RBDO) is to define the threshold after which the response of the system will not be acceptable. As the main objective function considered in this work is the flutter velocity, a design velocity (V_{design}) is designated as the threshold. The latter is chosen as the highest velocity at which the structure is engaged. Given this limit, the RBDO can be formulated as the minimisation of the probability (P) that the flutter velocity V_f of a laminate is lower than a given design velocity (V_{design}). This formulation is expressed as

$$\underset{\Theta}{\text{minimize}} \quad P(V_f < V_{design}) \tag{6.1}$$

where Θ represents the stacking sequence with ply angles that vary from $-90°$ to $90°$ by an increment of $5°$. The objective function of this stochastic optimisation is called the Probability of Failure (PoF) and it is minimised to obtain a more reliable configuration [31].

This general formulation of the RBDO, can easily become very costly, as the calculation of the probabilistic behaviour of V_f requires the computation of not less than 1000 samples (83 hours per individual resulting in 4150 hours per generation and thus for multiple generations). The computational cost of the LHS direct method is manageable for analysis of one case, it cannot be employed in an optimisation framework with multiple iterations of individuals and generations. It is thus necessary to reduce this computational cost with methods such as surrogate modelling which can approximate a large number of samples using fewer calculations of the aeroelastic system.

6.1.1 Surrogate model

The surrogate model used during this study, is the Gaussian Process Regression (GPR) [173]. The latter, follows the same process as a linear regression method which fits a linear function to the input datas (also called the training samples)

$$y_t = f(x_t) + \epsilon_t \tag{6.2}$$

where x_t and y_t are the input and output of the training samples, $f(x_t)$ is a linear function and $\epsilon_t \sim \mathcal{N}(0, \sigma_\epsilon^2)$ is the noise function with a normal distribution (0 mean and standard deviation σ_ϵ).

First, the linear function f needs to be fitted to the training samples in order to obtain the best pair of coefficients (also called weights) to emulate the given data

$$f(x_t) = a_0 + a_1 x_t \Rightarrow \mathbf{f} = \mathbf{x}_t^T \mathbf{w} \quad \text{with} \quad \mathbf{x}_t = \begin{bmatrix} 1 & x_t \end{bmatrix} \quad \text{and} \quad \mathbf{w} = \begin{bmatrix} a_0 & a_1 \end{bmatrix} \tag{6.3}$$

where $\mathbf{w}$ can be called the weight vector. The output vector $\mathbf{y}_t \in \mathbb{R}^{N_{obs}}$ can thus be written using $\mathbf{X}_t \in \mathbb{R}^{N_{obs} \times 2}$ and $\mathbf{w} \in \mathbb{R}^2$

$$\mathbf{y}_t = \mathbf{X}_t \mathbf{w} + \epsilon_t \quad \text{with} \quad \mathbf{X}_t = \begin{bmatrix} 1 & x_t^{(1)} \\ 1 & x_t^{(2)} \\ \vdots & \vdots \\ 1 & x_t^{(N_{obs})} \end{bmatrix} \quad \text{and} \quad \mathbf{y}_t = \begin{bmatrix} y_t^{(1)} \\ y_t^{(2)} \\ \vdots \\ y_t^{(N_{obs})} \end{bmatrix} \tag{6.4}$$

A gaussian prior is considered for the weight vector ($P(\mathbf{w}) = \mathcal{N}(0, \sigma_w^2)$) with 0 mean and standard deviation σ_w, using which the conditional probability of $\mathbf{y}_t$ vector ($P(\mathbf{y}_t|\mathbf{X}_t, \mathbf{w})$) is calculated. With the help of the Bayesian approach defined by the prior probability of the weight vector and the conditional probability of $\mathbf{y}_t$, the posterior probability of the weight vector ($P(\mathbf{w}|\mathbf{y}_t\mathbf{X}_t)$) can be calculated and then used to make predictions of other unknown samples [174].

For unknown samples with non-linear behaviour, the Gaussian Processes Regression (GPR) can be a suitable replacement for the linear regression. The latter defines a function to fit the input data similarly as the linear regression method. On the other hand, a Gaussian Process considers the uncertainties directly over the functions and not the weights constructing the coefficients of this function. It thus defines a distribution in which any given number of point have a joint gaussian distribution. The output function is determined in a similar manner as the linear regression in equation (6.2). This time, the function has a prior distribution defined by a Gaussian Process $f(x_t) \sim \mathcal{GP}(0, \mathcal{K}(x_1, x_2))$. The prior mean is custom to be considered equal to 0 to facilitate the posterior computations. The covariance function $\mathcal{K}(x_1, x_2)$ defines the dependency between various points. This function is commonly called a kernel and its choice is based on prior assumptions. One commonly chosen kernel which depends on the distance between the points is called the radial basis function and is the kernel employed in this work

$$\mathcal{K}(\mathbf{x_1}, \mathbf{x_2}) = exp\left(-\frac{1}{2}\frac{|\mathbf{x_1} - \mathbf{x_2}|^2}{l_s^2}\right) \tag{6.5}$$

where l_s represents the length scale parameter.

The hyper-parameters of the kernel (in this case only l_s) need to be deduced from the training samples. These parameters are usually chosen by the maximisation of the log marginal likelihood [174]

$$\log P(\mathbf{y}_t|\mathbf{X}_t, \lambda_p) = -\frac{1}{2}\mathbf{y}_t^T \mathbf{K}_y^{-1} \mathbf{y}_t - \frac{1}{2}\log|\mathbf{K}_y| - \frac{n}{2}\log 2\pi \tag{6.6}$$

where λ_p is the vector of hyper-parameters and $\mathbf{K}_y = \mathcal{K}(\mathbf{X}_t, \mathbf{X}_t) + \sigma_\epsilon^2 \mathbf{I}$ is the covariance matrix of the

noisy outputs. The hyper-parameters are then obtained using a gradient-based optimisation (partial derivatives of the log marginal likelihood with respect to λ_p).

Finally, based on the Bayesian approach, the mean and the prior covariance function (kernel), a gaussian posterior distribution over the target function is defined and its mean value is used for prediction.

6.1.2 Stability margin

Despite their advantage on the reduction of the computational time, surrogate models cannot accurately approximate discontinuous functions such as the flutter velocity which a discontinuous function of the material properties. There are multiple solutions to overcome this problem such as the use of machine learning methods which are able to cluster separately the different sections on each side of the discontinuity. While the machine learning methods such as Multi Layer Perceptron Classifier are very efficient as the results show in the work of Nitschke et al. [29], they can be computationally expensive when used during an iterative optimisation process.

Another solution proposed by Scarth et al. [31] is to reformulate the RBDO problem using a continuous variable called the stability margin which measures the distance of the largest value of damping to the axis zero (the damping of the mode closest to instability) at a given velocity, V_{design}

$$\Lambda(\theta, V_{design}) = -\, max_{i=1,...,N_{modes}} \quad g_i(\theta, V_{design}) \tag{6.7}$$

where g_i represents the aeroelastic damping of the i-th aeroelastic mode ($i = 1, ..., N_{modes}$) which corresponds to the real part of the eigenvalues of the aeroelastic system defined in equation (2.33) evaluated for the stacking sequence θ and at a given velocity V_{design}..

Moreover, the use of stability margin Λ in the optimisation problem has a significant effect on the computational time as the aeroelastic system is solved only at a given velocity [1] and there is no iteration needed unlike the process to obtain the critical velocity [2]. This variable is computed by the means of the eigenvalues over the design velocity which are continuous functions of the material properties. For this reason, the surrogate model is fitted to the eigenvalues of the aeroelastic system for a few training data points and can predict these values for a larger number of samples.

[1] Calculation of the stability margin Λ: 20 seconds with single core computation over Intel Xeon Silver 4114 Processor with 40 cores

[2] Calculation of the flutter velocity ($V_{flutter}$): 5 minutes with single core computation over Intel Xeon Silver 4114 Processor with 40 cores

6.1.3 Eigenvalue sorting

One of the problems that can be faced during the fitting of the surrogate model to the eigenvalues of various samples, is that the calculated eigenvalues are not always in the same order which can falsify the prediction of the surrogate model. Therefore, the modes of all samples need to be rearranged before being fitted by the Gaussian process. Modal Assurance Criterion (MAC) is one of the tools that is widely used in order to sort the modes by identifying and comparing their mode-shapes to a reference sample. There are different formulation of MAC with small variations in the literature [175]. In this work, the formulation of Beaverstock et al. [176] is employed

$$MAC_{ij} = \frac{|Z_i^T Z_j^*|^2}{(Z_i^T Z_i^*)(Z_j^T Z_j^*)} \tag{6.8}$$

where Z is the eigenvector of the aeroelastic system projected over the DLM grid, the * indicates the complex conjugate vector and ^{T} represents the transpose vector. The i index distinguishes the reference sample, which in this study is randomly chosen as the first sample, and other samples that are going to be compared to the latter, are represented by j.

6.2 Deterministic optimisation using stability margin

Before proceeding to the RBDO of composite laminates, a deterministic optimisation is conducted. The objective function of the optimisation problem is to maximise the stability margin Λ calculated at a given design velocity, V_{design}

$$\underset{\theta \in \Theta}{\text{maximize}} \quad \Lambda(\theta, V_{design}) \tag{6.9}$$

where Θ represents the set of stacking sequences θ with ply angles that vary between $-90°$ and $90°$ at $5°$ increments. The composite laminates are constructed by 16-ply symmetric stacking sequences which ensure the uncoupled membrane-bending condition and a faster convergence of the optimisation problem as the number of variables are half of the number of plies (due to symmetry).

As mentioned before, the stability margin Λ defined in Eq. (6.7) is used as the optimisation objective which is the opposite value of the highest damping at a given velocity. As flutter occurs when damping becomes positive, the stability margin is positive when the structure is stable and negative in the case of instability. By maximising this values at a given velocity, the chance of having an instability is reduced on that velocity. It is therefore, justified to carry out a deterministic optimisation by directly maximising the stability margin.

The response surface corresponding to the variation of the stability margin in the orthotropic domain as a function of polar parameters is presented in figure 6.1.b). The design velocity considered for computation of stability margin is $V_{design} = 145m/s$ close to the optimal flutter velocity in the same domain. Unlike the response surface presented in figure 6.1,a), this surface is continuous over the entire domain. The optimal case with maximum Λ indicated on the surface, is close to the case with maximum flutter velocity ($V_f = 146.5$ m/s) which confirms the efficiency of the new optimisation formulation if the design velocity is carefully chosen.

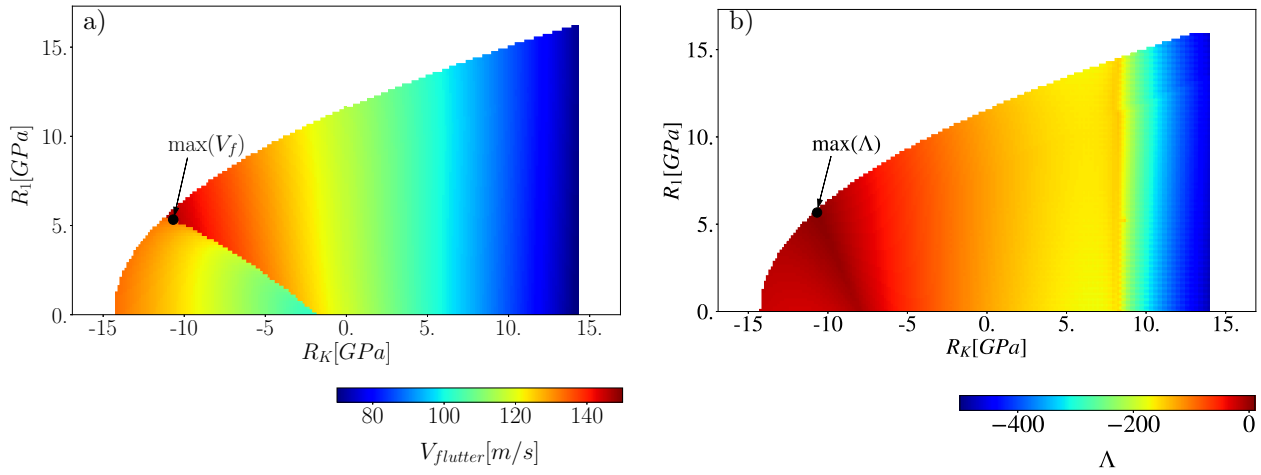

FIGURE 6.1: Variation of a) the flutter velocity and b) the stability margin for $V_{design} = 145m/s$ in an orthotropic domain as a function of the anisotropic moduli R_K and R_1 where $\Phi_1 = 0°$ for a straight wing. The black dot represents the optimal case obtained during the deterministic optimisation of the flutter velocity.

6.2.1 Deterministic optimisation results

The optimisation process is conducted in a larger anisotropic domain, compared to the orthotropic cases in the previous chapters, and is limited to the uncoupled laminates by imposing a symmetry over the plies. This gives place to 8 optimisation variables with 50 individuals per generation. The values of the design velocity V_{design}, whose range is between $[120, 150]m/s$, were chosen with respect to the pdf of the optimal US straight case in an orthotropic domain with maximum flutter velocity. The values are distributed evenly from the lowest peak to the highest and even surpassing the maximum flutter velocity obtained with US straight wing as indicated in figure 6.2.

Table 6.1 summarises the results of the deterministic optimisation where optimal configurations are presented in terms of stacking sequences and their elastic properties defined using the polar parameters. The difference between the two polar angles ($|\Phi_0 - \Phi_1|$) is a good indicator of the orthotropic

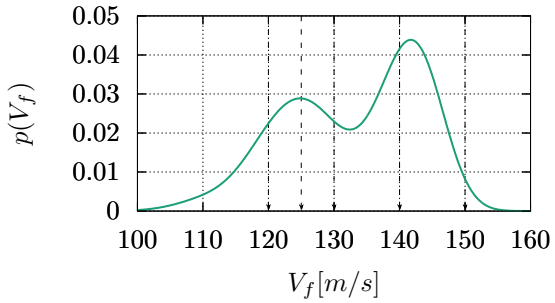

Figure 6.2: Values of five design velocities chosen according to the optimal straight wing with Uniform-Stiffness fibre paths, ranging from $V_{design} = 120m/s$ to $V_{design} = 150m/s$.

symmetry as explained in the previous chapters. Finally, for each optimal case the corresponding flutter velocity and frequency are calculated which can help evaluate the efficiency of the stability margin as the objective function.

V_{design} $[m/s]$	Λ	sequence [°]	R_0 $[GPa]$	R_1 $[GPa]$	Φ_1 [°]	$\lvert\Phi_0 - \Phi_1\rvert$ [°]	V_f $[m/s]$	ω_f $[rad/s]$
120	21.2	$[35, 35, -55, -50, -45, -25, 15, 40]_s$	13.04	3.66	23.8	12.8	127.8	431.0
125	19.4	$[30, -45, 35, -50, -25, -45, 45, 25]_s$	11.60	4.10	1.15	37.0	131.1	465.7
130	18.3	$[35, -35, -30, 20, 25, 50, 0, 90]_s$	7.80	7.12	6.0	37.0	135.2	522.6
140	9.1	$[35, -25, 40, -25, -45, -50, -60, 0]_s$	8.53	6.12	6.3	49.8	115.2	740.5
150	-1.2	$[-40, 40, -30, 30, 45, 15, 55, -55]_s$	10.82	4.49	-3.0	40.9	124.4	733.2

Table 6.1: Deterministic optimal cases obtained by maximising the stability margin Λ with five different V_{design} for a straight wing.

The first observation in table 6.1, indicates a decrease in this value as the design velocity increases. This behaviour is expected as the highest value of damping approaches instability for values near the maximum flutter velocity. For the design velocity of $V_{design} = 150m/s$ which is the only case that surpasses the flutter velocity, the stability margin has a negative value as the mode with highest damping has reached instability. Concerning the flutter velocities, these values increase along with the design velocities up to the case with $V_{design} = 140m/s$. At this velocity, a sudden increase of the flutter frequency takes place which can indicate a switch in the unstable mode.

Figure 6.3 shows the aeroelastic response of the last two optimal cases with $V_{design} = 140m/s$ and $V_{design} = 150m/s$. In both cases the instability first occurs over the third mode while the second mode becomes unstable in larger velocities and the first mode has an increasing tendency. The latter

reaches instability at the same time as the second mode for $V_{design} = 150m/s$ but remains stable at higher speeds for $V_{design} = 140m/s$. Both cases posses a so called hump mode which is associated to modes that become unstable but regain stability at higher velocities. In the case obtained by $V_{design} = 140m/s$ the unstable mode goes back to stability before the design velocity while for the $V_{design} = 150m/s$ case it remains unstable over the design velocity. This type of behaviour can show the limitations of deterministic optimisation. As the latter variable is computed over one velocity, it does not regard for phenomena taking place before this speed and for instabilities such as hump mode. The consequences can be dangerous if the design velocity is chosen in values much higher than the maximum flutter velocity of the structure.

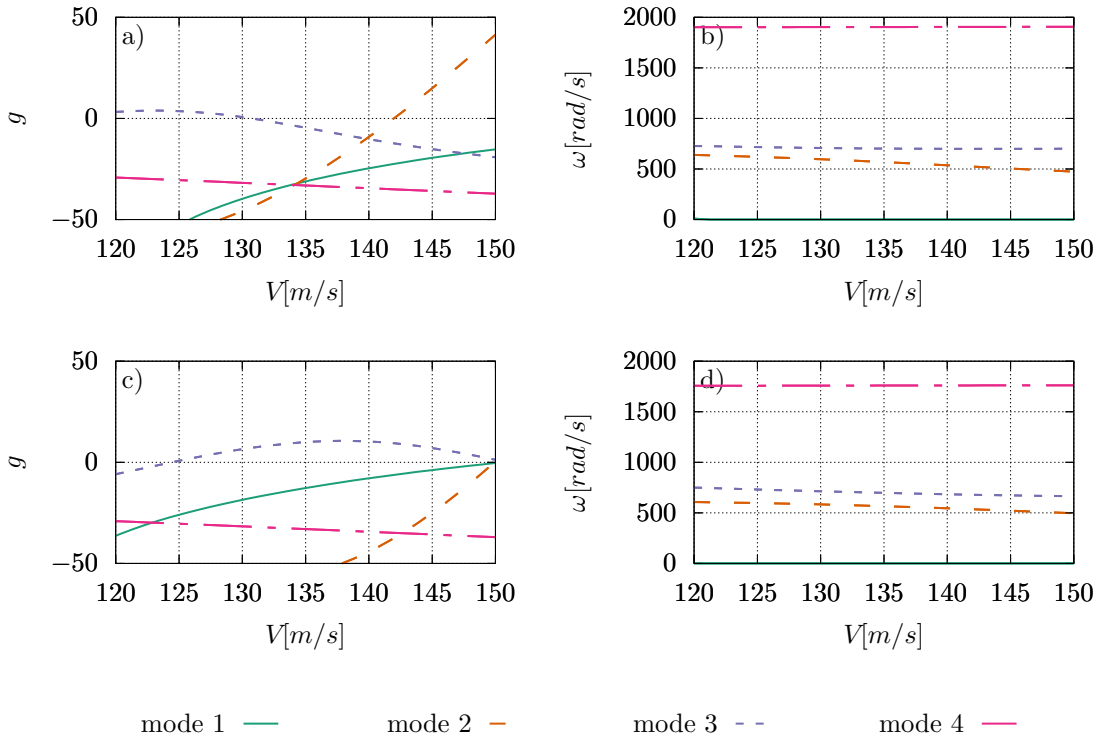

FIGURE 6.3: Comparison of the evolution of damping and frequency as a function of velocity for the last two optimisation cases. The (a,b) represents the cases of $V_{design} = 140m/s$ and (c,d) represents the cases of $V_{design} = 150m/s$.

The shape of the unstable mode for both cases is demonstrated in figure 6.4 representing the third aeroelastic mode as combination of the third bending and first torsion mode.

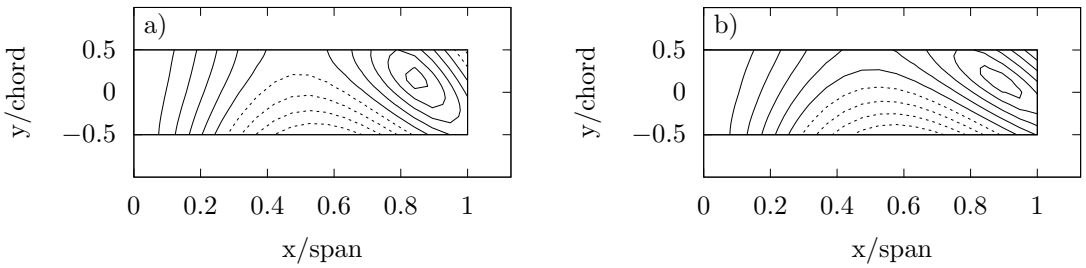

Figure 6.4: Mode shapes corresponding to the unstable mode for each optimal configurations. a) $V_{design} = 140m/s$ and b) $V_{design} = 150m/s$.

The polar parameters corresponding to each optimal case presented in table 6.1 show a strong anisotropic behaviour for the first three cases. On the other hand, for the last two optimal configurations the difference between the polar angles approaches $\frac{\pi}{4}$ that is one of the indicators of orthotropic symmetry. Figure 6.5 compares the bending young moduli and the torsional moduli of the last two cases which manifest asymmetric shapes of E_1 and higher values of G_{12} for the optimal case obtained with $V_{design} = 150m/s$. Despite the small variations in the elastic symmetries of these configurations, both cases present close properties to orthotropic symmetry as indicated by their polar parameters in table 6.1.

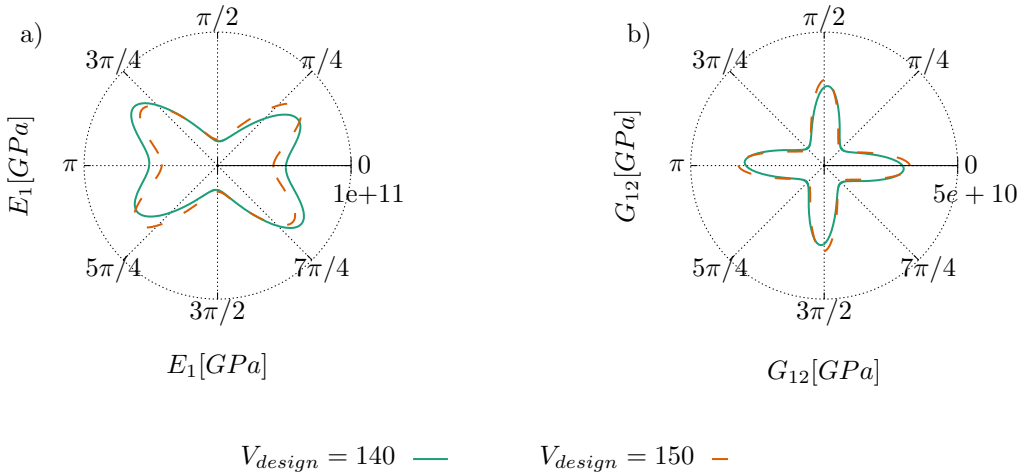

Figure 6.5: Elastic properties for optimal cases of the deterministic optimisation with $V_{design} = 140m/s$ and $V_{design} = 150m/s$.

6.2.2 Stochastic analysis

Following the reasoning of the previous chapter, the stochastic behaviour of these optimal cases obtained by forward uncertainty propagation, are now analysed and compared. The probabilisitic response of the stability margin Λ and the flutter velocity V_f are obtained using 1000 LHS samples. A standard deviation of $\sigma = 5°$ is considered over the optimal sequence which also represents the mean value in a normal distribution ($\bar{\Theta}$).

Table 6.2 summarises the stochastic response of the cases studied during the deterministic optimisation. The optimal (Λ, V_f), mean (μ_Λ, μ_f) and standard deviation (σ_Λ, σ_f) of both stability margin and flutter velocity are represented for the set of studied V_{design}.

$V_{design}[m/s]$	Λ	μ_Λ	σ_Λ	$V_f[m/s]$	$\mu_f[m/s]$	$\sigma_f[m/s]$	$(V_f[m/s], 0.01)$ [3]
120	21.2	14.9	7.9	127.8	127.3	4.8	111.1
125	19.4	9.6	11.6	131.1	130.4	5.2	115.1
130	18.3	6.8	10.0	135.2	131.4	7.2	92.0
140	9.1	-12.2	15.4	115.2	122.2	12.7	96.6
150	-1.2	-27.5	15.7	124.4	125.0	10.1	96.1

TABLE 6.2: Stochastic properties of the deterministic optimal US straight cases obtained by maximisation of the stability margin for different design velocities due to a 5° variation of the ply angles.

Comparing the mean values of the stability margin for each case, the same tendency as the optimal values is observed. The values decrease as the design velocity increases but it is worth mentioning that as the design velocity grows, the gap between the optimal values and the mean values of the stability margin increases. This observation can be explained by the standard deviations of the stability margin which also grow along with the design velocities. Concerning the flutter velocity, the mean values remain lower than the optimal cases for the three first cases. On the other hand, the mean values of the last two cases are higher than the optimal values. The standard deviation of the flutter velocities of these two cases are significantly higher than the first three cases but it can be said that the standard deviation increases with growing design velocities even if an opposite behaviour is observed between the last two cases. In order to get an indicator about the reliability of the optimal cases, table 6.2 presents the 0.01th percentile of V_f. The latter increases when the design velocity is set to $125m/s$ instead of $120m/s$. On the other hand, the flutter velocity at 0.01th percentile is significantly lower for the last three cases which can be explained by the high values of the standard deviations.

[3] flutter velocity value at 0.01th percentile

Figure 6.6 compares the pdfs of all the optimal cases for both the stability margin and the flutter velocity. The pdfs of the stability margin, become wider with lower peaks as the design velocity increases which explains the values of the mean and standard deviation observed in table 6.2. Regarding the flutter velocity, the pdfs of the first three cases have quite similar shapes with growing variance. On the other hand, the last two cases present bi-modal pdfs with the value of the optimal flutter velocity on the lower peak. This type of behaviour explains the larger values of mean compared to the deterministic flutter velocity. The higher peak corresponds to cases with greater flutter velocities but lower margins at the given design velocities. The bi-modality of the pdfs of the last two cases can explain the large jump of the standard deviation for the flutter velocity.

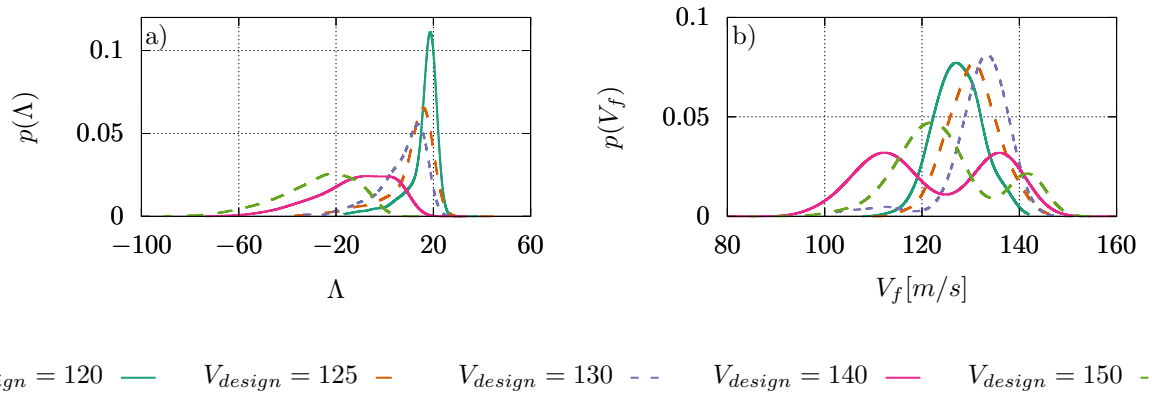

FIGURE 6.6: Comparison of a) the pdf of stability margin and b) the pdf of flutter velocity for optimal deterministic cases with five different V_{design}.

The results presented on the deterministic optimisation of the stability margin prove the inefficiency of this variable as the objective function. Stability margin is only calculated at a given design velocity whose value can be higher than the flutter velocity of a hump mode that has already becomes stable. On the other hand, the stochastic analysis showed that the probabilistic behaviour of this variable is a good indicator of the reliability of a structure. It is thus a suitable candidate for the RBDO as it is computed from continuous functions of the material properties and reduces the computational time of the optimisation process.

6.3 RBDO using ply angles

The formulation of the RBDO problem can be expressed as the minimisation of probability of having a negative stability margin at a given design velocity

$$\underset{\theta \in \Theta}{\text{minimize}} \quad P(\Lambda(\theta, V_{design}) < 0) \tag{6.10}$$

This problem translates the minimisation of probability of failure (PoF) as the negative stability margin indicates instability of the structure. The orientation of ply angles are chosen as the design variables and thus only symmetric laminates are taken into account to facilitate the satisfaction of the uncoupled bending-membrane condition. The ply angles simplify the propagation of uncertainties with a direct method but the large number of layups can result in the curse of dimensionality while working with the surrogate model. The polar parameters are therefore employed to reduce the number of uncertain parameters. The uncertainty is first propagated over the nominal stacking sequence and the number of required samples are then generated. Once the sample of layups are obtained, the corresponding polar parameters are computed. Consequently, the dimension of the problem decreases from 16 uncertain parameters to 6.

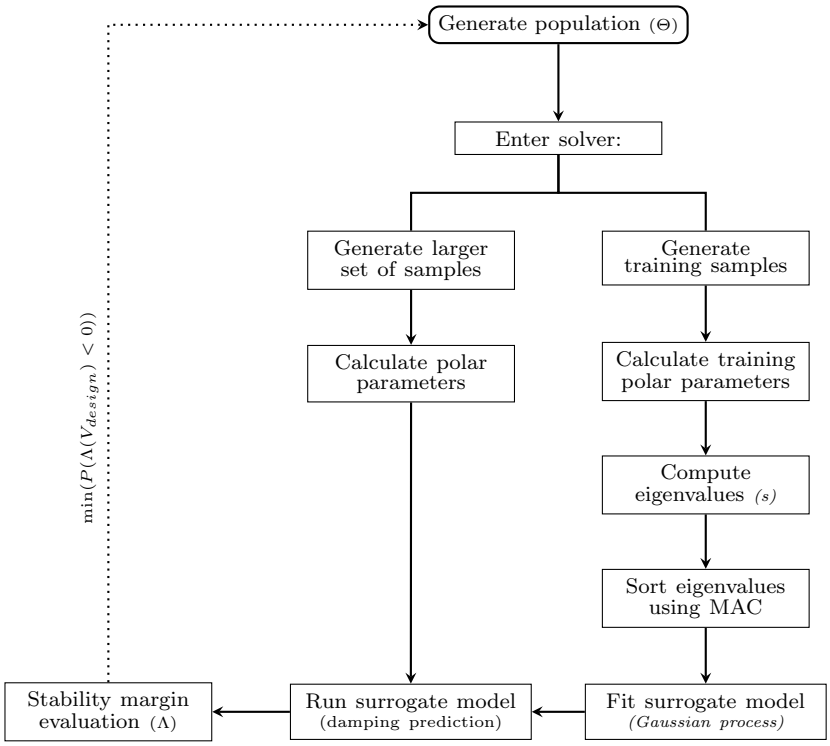

FIGURE 6.7: Reliability-Based Design Optimisation (RBDO) algorithm using ply angles.

Figure 6.7 and algorithm 4 detail the different steps involved in the RBDO process. For each individual in a population generated by the Genetic Algorithm, the main solver is executed. First, a set containing 30 samples, in this study, is used to train the surrogate model. Then the larger set with 1000 samples is generated for which the aeroelastic dampings are predicted. The polar parameters and the aeroelastic dampings of the smaller set are calculated and the damping values of each mode

are sorted amongst the samples. The surrogate model is then fitted to the training values (polar parameters) and their aeroelastic damping. Next, it can be used to predict the damping of the larger set for which the polar parameters are computed as well. Finally, using the damping of the larger set, the probability of the stability margin is calculated and the loop goes on until this value in minimised.

Algorithm 4: Reliability-Based Design Optimisation (RBDO)

Generate initial population (Θ) (using the Genetic Algorithm)
for $i = 1 : N_{ind}$ **do**
  Generate training samples ($N_{training}$)
  for $i = 1 : N_{training}$ **do**
    Calculate polar parameters $T_0, T_1, R_K, R_1, \Phi_0, \Phi_1$ (equation (2.34))
    Compute aeroelastic eigenvalues s (equation (2.28)-(2.33))

$$\begin{bmatrix}\mathbf{I} & 0\\ 0 & \mathbf{I}\end{bmatrix} s \begin{Bmatrix}\hat{\mathbf{q}}\\ s\hat{\mathbf{q}}\end{Bmatrix} - \begin{bmatrix}0 & \mathbf{I}\\ -\hat{\mathbf{M}}^{-1}(\hat{\mathbf{K}} - \omega^2\mathbf{A}^R) & \omega\hat{\mathbf{M}}^{-1}\mathbf{A}^I\end{bmatrix} \begin{Bmatrix}\hat{\mathbf{q}}\\ s\hat{\mathbf{q}}\end{Bmatrix} = \begin{Bmatrix}0\\ 0\end{Bmatrix} \qquad s = g \pm i\omega$$

  end for
  Sort eigenvalues using MAC (equation (6.8))

$$MAC_{ij} = \frac{|Z_i^T Z_j^*|^2}{(Z_i^T Z_i^*)(Z_j^T Z_j^*)}$$

  Fit surrogate model (Gaussian Process) to $g_{training}$
  Generate larger set of samples ($N_{prediction}$)
  for $i = 1 : N_{prediction}$ **do**
    Calculate the polar parameters $T_0, T_1, R_K, R_1, \Phi_1, \Phi_0$
    Predict damping values $g_{prediction}$ using the surrogate
    Compute the stability margin using $g_{prediction}$ (equation (6.7))

$$\Lambda = -max(g_{prediction}(i))$$

  end for
  Set the probability of failure to zero ($PoF = 0$)
  for $i = 1 : N_{prediction}$ **do**
    if $\Lambda < 0$ **then**
      $Pof = Pof + 1$
    end if
  end for
  Minimise objective function (PoF) using the GA

$$\underset{\Theta}{\text{minimize}} \quad P(\Lambda(V_{design}) < 0)$$

end for

6.3.1 Parametric uncertainties over ply angles

The Genetic Algorithm (BIANCA) [177] with 50 individual per generation is employed for the optimisation process [4]. The orientation of the layers which vary between $-90°$ to $90°$ with an increment of $5°$ are subject to an uncertainty of $\sigma = 5°$. Table 6.3 shows the results of the RBDO process expressed in equation (6.10) using the models and parameters explained previously.

[4] using Λ as objective function: 15 minutes per individual, 12 hours per generation and thus for multiple generations

$V_{design}[m/s]$	$P(\Lambda < 0)$	sequence [°]	$R_0[GPa]$	$R_1[GPa]$	$\Phi_1[°]$	$V_f[m/s]$	$\omega_f[rad/s]$
120	< 0.01	$[30, -35, -55, 45, 65, 50, 60, -15]_s$	9.67	2.75	19.70	138.5	470.8
125	0.03	$[-45, 40, -55, 35, 40, 10, -60, -50]_s$	12.88	1.54	-24.09	137.1	424.2
130	0.09	$[45, 35, -55, -45, -40, 30, -30, 45]_s$	12.98	3.83	13.91	138.3	418.7

TABLE 6.3: Optimal results obtained by the RBDO algorithm for three different V_{design}.

All three cases have similar values of flutter velocity and frequency as well as anisotropic moduli.

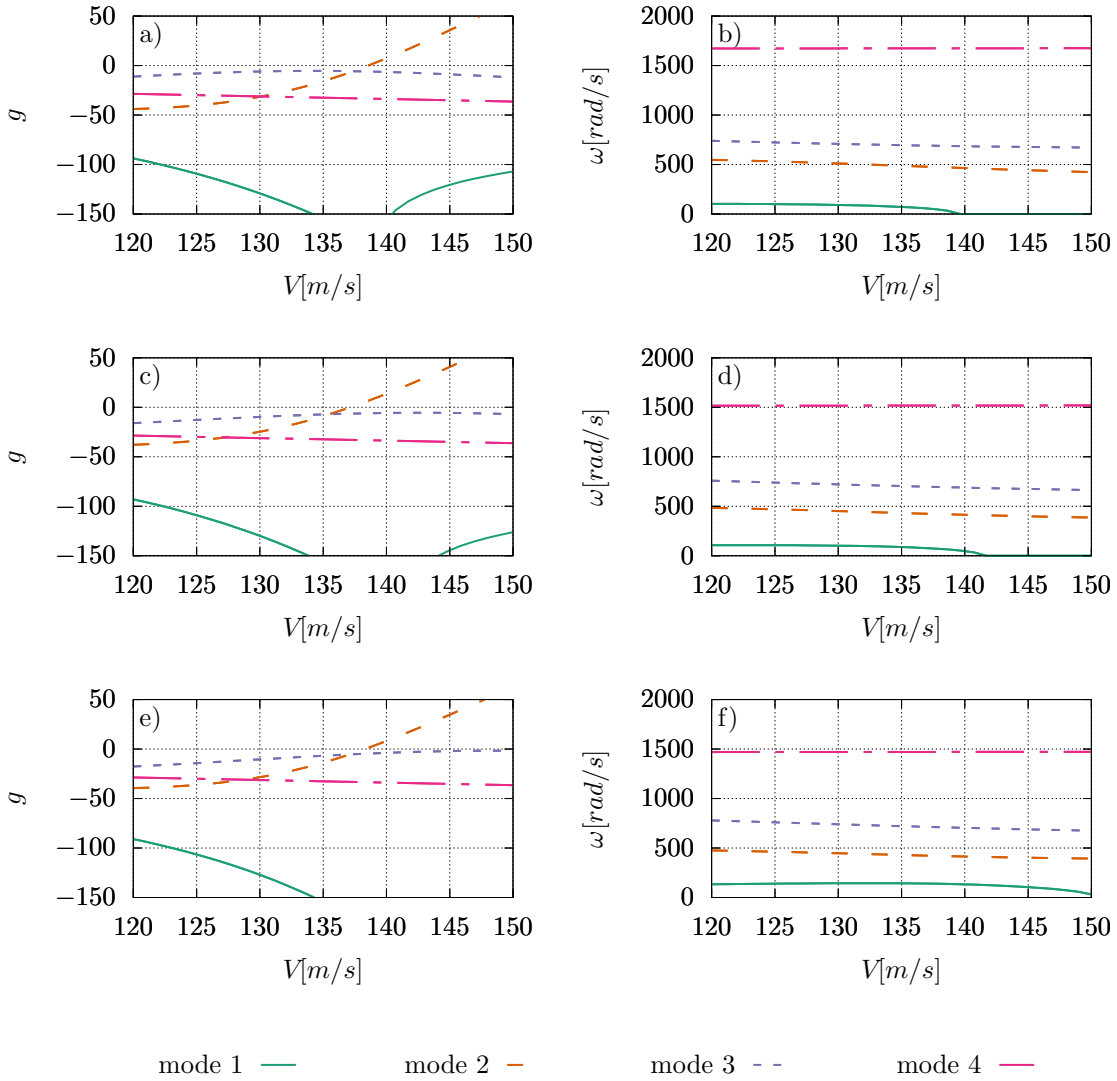

FIGURE 6.8: Damping and frequency diagrams as a function of velocity for all optimisation cases. (a,b) the case of $V_{design} = 120m/s$, (c,d) the case of $V_{design} = 125m/s$ and (e,f) the case of $V_{design} = 130m/s$.

Their aeroelastic response is demonstrated using the evolution of damping and frequency in figure 6.8. Each row represents a different value of V_{design}. The left column shows the evolution of aeroelastic damping over the velocity and the right column presents the values of aeroelastic frequency over the same interval of speed. For all three values of V_{design}, the instability occurs on the second aeroelastic mode with the third mode that approaches the axis zero. On the other hand, the modes that become unstable are not the modes closest to instability (zero axis) at the given V_{design} which can indicate the influence of aeroelastic modes on one another.

Table 6.3 also summarises the polar parameters corresponding to each optimal case. The values of R_0 and R_1 are not close for any of the cases meaning that they do not belong to the same optimal region. However, the value of Φ_1 changes drastically between the cases with $V_{design} = 120m/s$ and $V_{design} = 125m/s$ and the values of R_0 and R_1 are not very far from one another which indicates that these two configurations can have similar elastic behaviours.

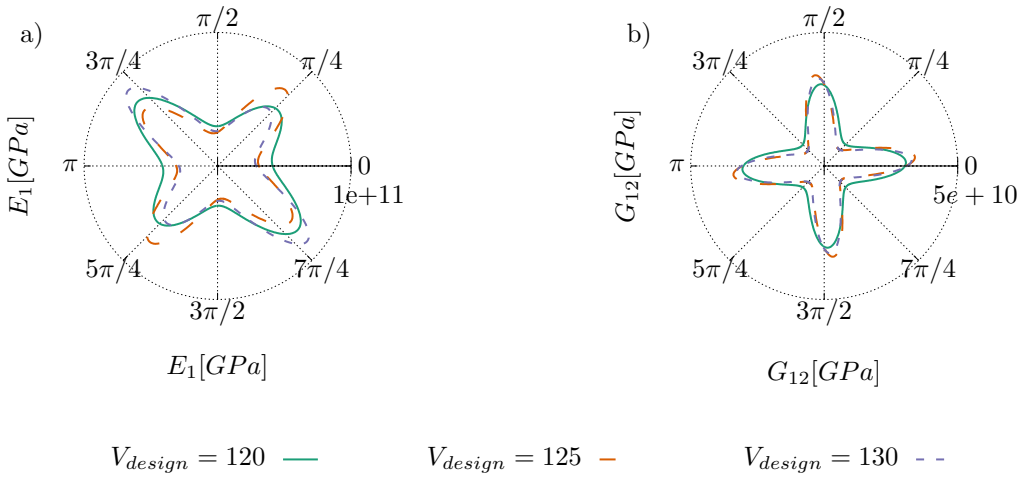

FIGURE 6.9: Elastic properties for RBDO cases obtained for three different V_{design}.

Figure 6.9 shows the variation of the young moduli E_1 and the shear moduli G_{12} between the three cases. According to the values of the polar parameters presented in table 6.3, all configurations are anisotropic. On the other hand, the plot of E_1 shows behaviours close to orthotropic structures as there are two dominated directions for all cases. Similar behaviours can be seen in the plot of G_{12}. While there are small variations in the value of these moduli, there are many analogous properties that prove proximities in the elastic behaviours of the three configurations.

Table 6.4 presents the stochastic properties of the all three cases for both the stability margin and the flutter velocity.

$V_{design}[m/s]$	Λ	μ_Λ	σ_Λ	$V_f[m/s]$	$\mu_f[m/s]$	$\sigma_f[m/s]$	$P(\Lambda < 0)$	$(V_f[m/s], 0.01)$
120	11.1	10.7	3.0	138.5	134.0	4.4	< 0.01	116.9
125	12.8	10.4	4.3	137.1	134.4	4.1	0.03	120.8
130	10.4	6.7	5.9	138.3	134.9	3.4	0.09	123.5

TABLE 6.4: Stochastic properties of the optimal cases obtained by RBDO for different design velocities.

The nominal stability margins of three cases are in the same range and do not show a particular tendency with respect to the value of the design velocity. On the other hand, the mean value decreases and the standard deviation increases as the V_{design} grows. Unlike the stability margin, the mean values μ_f of the flutter velocity increase with the design velocity while the standard deviations decrease with respect to latter. The variation of the stability margin standard deviation σ_Λ is also observed on the probability of failure which increases with the value of the design velocity. This observation is expected as the modes approach the zero axis along with the speeds near the maximum flutter velocity. While the probability of failure is a good indicator to learn about the reliability of a case at a given velocity, it is not efficient to compare the three cases amongst themselves. The flutter velocity at 0.01th percentile can be a good indicator of general reliability of a structure. This value presented in table 6.4 increases with the design velocity proving that the choice of this parameter (V_{design}) can affect performance of the final result.

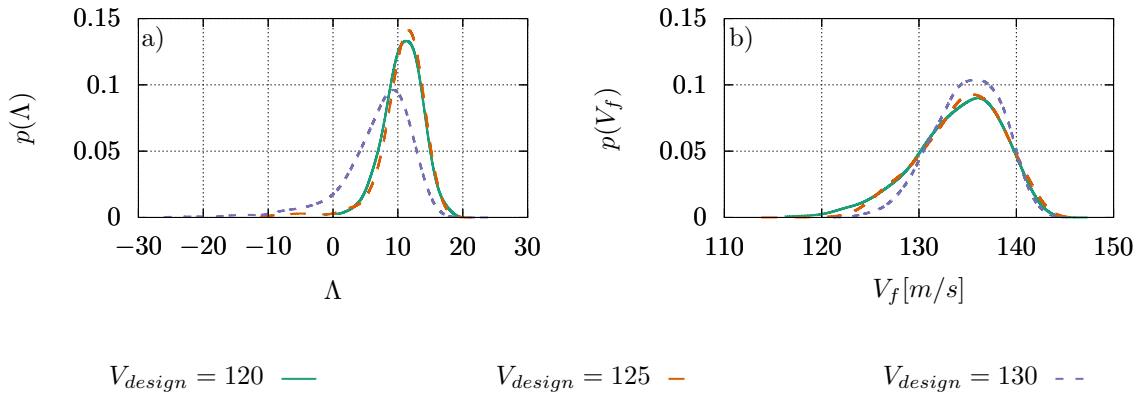

FIGURE 6.10: Comparison of pdfs of a) the pdf of stability margin and b) the pdf of flutter velocity for RBDO cases.

The stochastic behaviour of the optimal RBDO cases obtained by different V_{design} are compared in figure 6.10. The probability of failure increases with respect to the V_{design} as observed in table 6.4. The pdfs of the stability margin become wider with longer tails as the design velocity grows. Consequently, the last case has the highest probability of failure. On the other hand, when this probability is calculated at the same design velocity the all the cases, the last configuration reaches lower probabilities than others. This behaviour can also be observed on the pdfs of the flutter velocity. The kernels become narrower with higher peaks on the mean values as the design velocity increases. This observation is an explanation for the high flutter velocity at the 0.01th percentile of the last optimisation study. It can be concluded that the case with $V_{design} = 130m/s$ is the most reliable configuration with the best aeroelastic performance.

While the results presented show interesting behaviours that indicate robust aeroelastic properties, they have not yet been compared to the deterministic cases studied during the chapter 3 for which the formulation is reminded in equation (6.11)

$$\begin{aligned} &\underset{R_K, R_1, \Phi_1}{\text{maximize}} \quad V_f \\ &\text{subject to} \quad -(\rho_0) + 2(\rho_1^2) - 1 \leq 0, \end{aligned} \tag{6.11}$$

As shown in section 3.1.2, the Uniform-Stiffness case with the highest flutter velocity is the orthotropic straight wing. The stochastic behaviour of the latter is compared to the optimal RBDO case obtained with $V_{design} = 125m/s$ hereafter in figure 6.11.

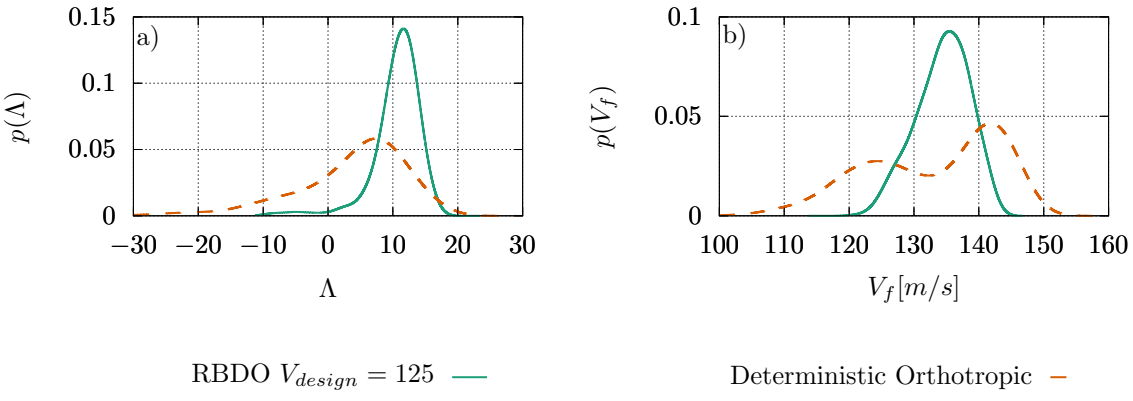

FIGURE 6.11: Comparison of forward uncertainty propagation of the RBDO and the optimal orthotropic case of: a) pdf of stability margin and b) pdf of flutter velocity.

The principle advantage of configurations found with the RBDO is the mono-modal shapes which eliminates the probability of failure at unexpected speeds. Furthermore, the optimal RBDO configuration lowers the PoF from 25% to 3% compared to the optimal orthotropic case at the same V_{design}. While the nominal flutter velocity of the optimal RBDO laminate is lower than the orthotropic case, its mean value remains in the same range and its standard deviation is almost 60% lower. It can then be concluded that RBDO succeeds to obtain a safer sequence with improved stochastic performance compared to the deterministic case.

6.3.2 Parametric uncertainties over ply angles and thicknesses

The influence of additional parametric uncertainties have been considered for a given composite sequence in the optimisation framework, such as random thicknesses. For this purpose, a 5% variation over the thickness of each ply is considered. In order to have an initial perception of the impact of this uncertainty over the aeroelastic results, a comparison of the probability density function is carried out over the same configuration with and without including the uncertainty over the thicknesses. The optimal case obtained for the straight Uniform-Stiffness wing in the orthotropic domain has been considered (see section 3.1.2).

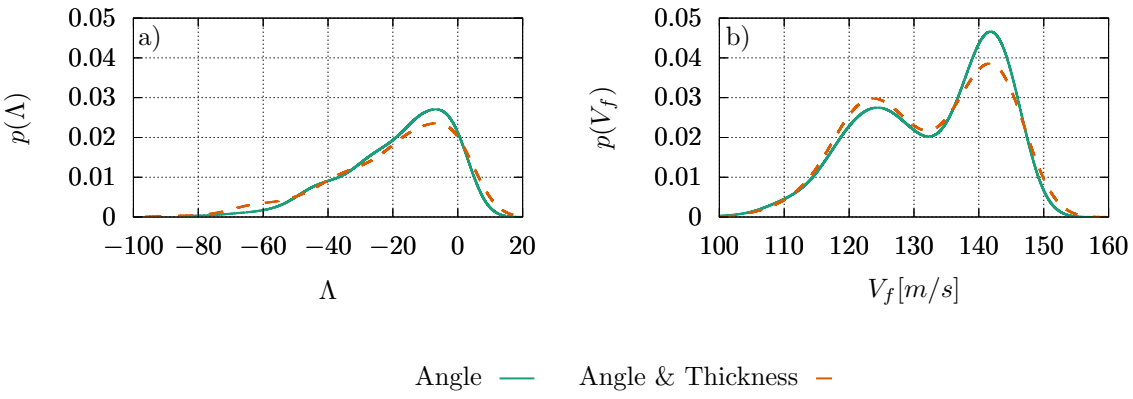

FIGURE 6.12: Comparison of stochastic results for forward uncertainty propagation study: a) pdf of stability margin and b) pdf of flutter velocity for the initial optimal deterministic case in the orthotropic domain while considering uncertainties over only angles or both angles and thicknesses.

Figure 6.12 shows a comparison between two pdfs for the stability margin at $V_{design} = 125m/s$ and the flutter velocity obtained using 1000 LHS samples. The influence of the uncertainty over the thicknesses is present but rather marginal on the pdf of Λ but the difference is significant on the pdf of V_f particularly around the peaks. These results raise the question on the impact of these variation on the RBDO results.

For the sake of simplicity, only a case of $V_{design} = 125m/s$ is studied. The initial RBDO case obtained using this design velocity is compared to the optimal configuration carried out while conducting RBDO (see algorithm 4) considering uncertainties over both ply angles and thicknesses.

Two optimisation studies are performed [5]

- Case A: Optimisation while considering uncertainties over angles (Θ)

$$\underset{\Theta}{\text{minimize}} \quad P(\Lambda(V_{design}, \delta\Theta) < 0) \tag{6.12}$$

- Case B: Optimisation while considering uncertainties over angles and thicknesses (Θ and t_p)

$$\underset{\Theta}{\text{minimize}} \quad P(\Lambda(V_{design}, \delta\Theta, \delta t_p) < 0) \tag{6.13}$$

Table 6.5 summarises the elastic and aeroelastic properties of both RBDO results. The first remark made between the two cases, is the proximity of the flutter velocity values but the large difference in the flutter frequencies. This jump in the values can be due to a switch in the unstable modes.

Type of uncertainty	$R_0[GPa]$	$R_1[GPa]$	$\Phi_1[^\circ]$	$V_f[m/s]$	$\omega_f[rad/s]$	Nominal Sequence
Case A	12.88	1.54	-24.09	137.1	424.2	$[-45, 40, -55, 35, 40, 10, -60, -50]_s$
Case B	13.54	4.61	46.5	137.9	697.8	$[40, -50, 50, 40, -45, -60, 45, 65]_s$

TABLE 6.5: Optimal results obtained by the RBDO algorithm for two optimal cases with and without uncertainties over the thicknesses with $V_{design} = 125m/s$.

Figure 6.13 shows the plots of damping and frequency of the nominal optimal cases for both optimisation formulations. Unlike the previous cases, the optimal RBDO case obtained by considering uncertainty over the thicknesses causes an instability on the third aeroelastic mode. This mode switch explains the higher value of the flutter frequency for this case. The second aeroelastic mode becomes quickly unstable right after the third mode.

[5] where δ represents the uncertainties over each parameter

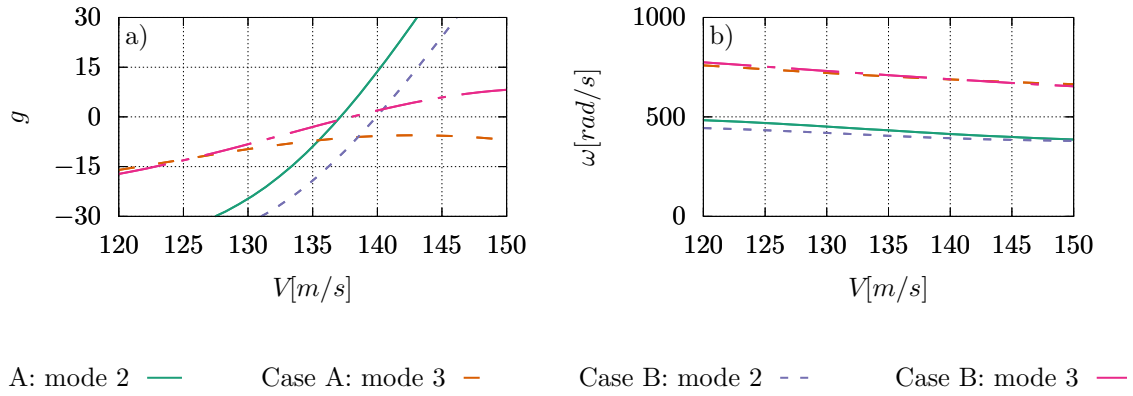

FIGURE 6.13: Comparison of the evolution of: a)damping and b)frequency as a function of velocity for both RBDO studies.

Figure 6.14 gives an illustration of the mode shapes for both RBDO cases. The second aeroelastic mode which is a combination of the second bending and the first torsion mode associated to the optimal case obtained with imposing uncertainties over angles. The third aeroelastic mode obtained by combination of the first torsion and the third bending mode corresponding to the optimal case achieved by uncertainties over both angles and thicknesses.

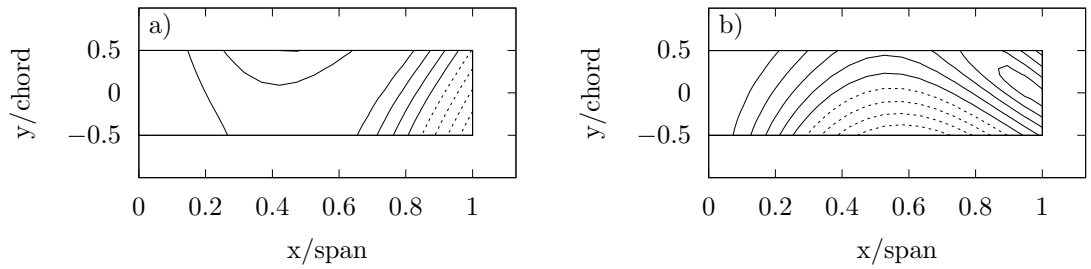

FIGURE 6.14: Mode shapes corresponding to the unstable mode for each optimal configuration. a) Case A (uncertainties over Θ) and b) Case B (uncertainties over Θ and t_p)

The elastic properties of these two configurations using the polar parameters and the elastic moduli are compared in figure 6.15. The polar parameters indicated in table 6.5 are not similar and do not belong to the region in the anisotropic domain. Figure 6.15 showed that Case B also has a similar elastic properties to orthotropic symmetry. On the other hand, the young moduli has a strong domination in one direction while for Case A, symmetries in both directions are more balanced. The shear moduli of both cases are very similar with a slight rotation for the configuration obtained by considering uncertainties over angles.

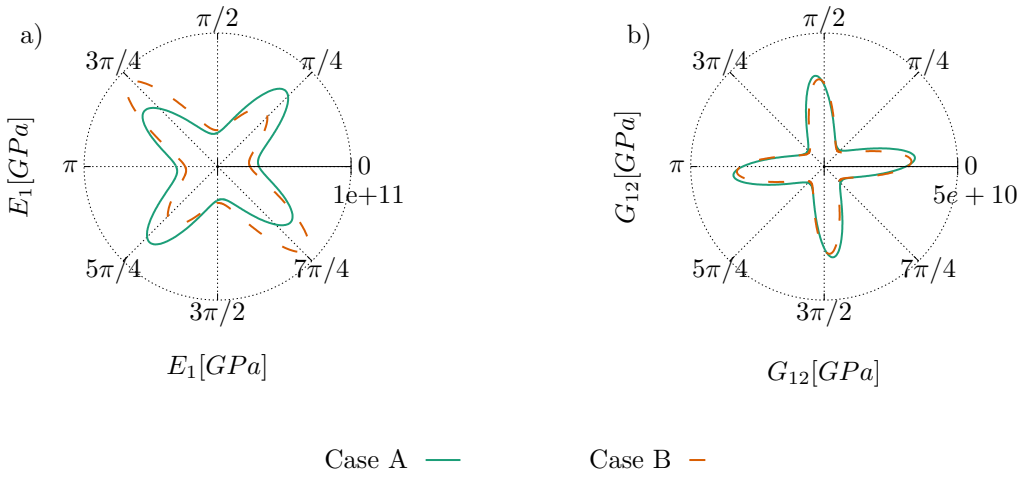

FIGURE 6.15: Elastic properties for RBDO cases with $V_{design} = 125m/s$. a) Case A (uncertainties over Θ) and b) Case B (uncertainties over Θ and t_p)

In order to deeper investigate the stochastic behaviour of the optimal cases, a direct uncertainty propagation study has been conducted a posteriori. For each optimal case, two uncertainty quantification studies have been carried out to further understand the influence of different uncertainties over the aeroelastic response of a laminate. Thus, each nominal optimal configuration has been subjected to an uncertainty quantification process, one considering only uncertainties over angles and another considering both uncertainties over angles and thicknesses. For each case, the pdf of Λ and V_f are compared. All studies are summarised in the following and the ID associated to each case is cited for each study

1. Case A.1: RBDO considering uncertainties over angles and a posteriori Uncertainty Quantification using angles (RBDO (Θ) + forward UQ (Θ))

$$\underset{\Theta}{\text{minimize}} \quad P(\Lambda(V_{design}, \delta\Theta) < 0) \quad \Rightarrow \quad \text{a posteriori} \quad UQ(P(\Lambda(V_{design}, \delta\Theta)) \tag{6.14}$$

2. Case B.1: RBDO considering uncertainties over angles and thicknesses and a posteriori Uncertainty Quantification using angles (RBDO (Θ + t_p) + forward UQ (Θ))

$$\underset{\Theta}{\text{minimize}} \quad P(\Lambda(V_{design}, \delta\Theta, \delta t_p) < 0) \quad \Rightarrow \quad \text{a posteriori} \quad UQ(P(\Lambda(V_{design}, \delta\Theta)) \tag{6.15}$$

3. Case A.2: RBDO considering uncertainties over angles and a posteriori Uncertainty Quantification using angles and thicknesses (RBDO (Θ) + forward UQ (Θ+ t_p))

$$\underset{\Theta}{\text{minimize}} \quad P(\Lambda(V_{design}, \delta\Theta) < 0) \quad \Rightarrow \quad \text{a posteriori} \quad UQ(P(\Lambda(V_{design}, \delta\Theta, \delta t_p)) \tag{6.16}$$

4. Case B.2: RBDO considering uncertainties over angles and thicknesses and a posteriori Uncertainty Quantification using angles and thicknesses (RBDO (Θ + t_p) +forward UQ (Θ+ t_p))

$$\underset{\Theta}{\text{minimize}} \quad P(\Lambda(V_{design}, \delta\Theta, \delta t_p) < 0) \quad \Rightarrow \quad \text{a posteriori} \quad UQ(P(\Lambda(V_{design}, \delta\Theta, \delta t_p)) \tag{6.17}$$

Table 6.6 summarises a posteriori uncertainty propagation over RBDO results for all configurations. The main observation concerns the standard deviations of both variables. Albeit, for the same optimal case with two different UQ strategy, the mean values (μ_Λ) remain identical or very close, the standard deviations systematically increase when considering the uncertainties over thicknesses. The probability of failure is higher for the Case A compared to Case B for both uncertainty propagation strategies. The latter also shows higher flutter velocities at 0.01th percentile indicates that it is a more reliable case with higher performance.

Type of uncertainty	Λ	μ_Λ	σ_Λ	$V_f[m/s]$	$\mu_f[m/s]$	$\sigma_f[m/s]$	$P(\Lambda < 0)$	$(V_f[m/s], 0.01)$
Case A.1	12.8	10.4	4.3	137.1	134.4	4.1	0.03	120.8
Case B.1	13.1	11.2	2.9	137.9	133.9	3.0	< 0.01	122.6
Case A.2	12.8	10.4	5.0	137.1	134.4	4.9	0.03	117.3
Case B.2	13.1	11.0	3.9	137.9	133.8	3.9	0.01	120.2

TABLE 6.6: Stochastic properties of the optimal cases obtained by RBDO for two optimal cases with and without uncertainties over the thicknesses with $V_{design} = 125m/s$.

Figure 6.16 shows a comparison of the forward uncertainty propagation of both optimal cases under uncertainties over ply angles (cases followed by .1) or uncertainties over both ply angles and thicknesses (cases followed by .2). On the pdf of Λ, the pdfs of the cases obtained by a posteriori propagation over both angles and thicknesses are wider with lower peaks on the mean values of the stability margin. It needs to be noted that the Λ pdfs of cases with same uncertain parameters in a posteriori propagation are very close to one another. On the other hand, the pdfs of V_f exhibit narrower shapes with higher

peaks over the mean for optimal cases obtained during RBDO with uncertainties imposed over both angles and thicknesses.

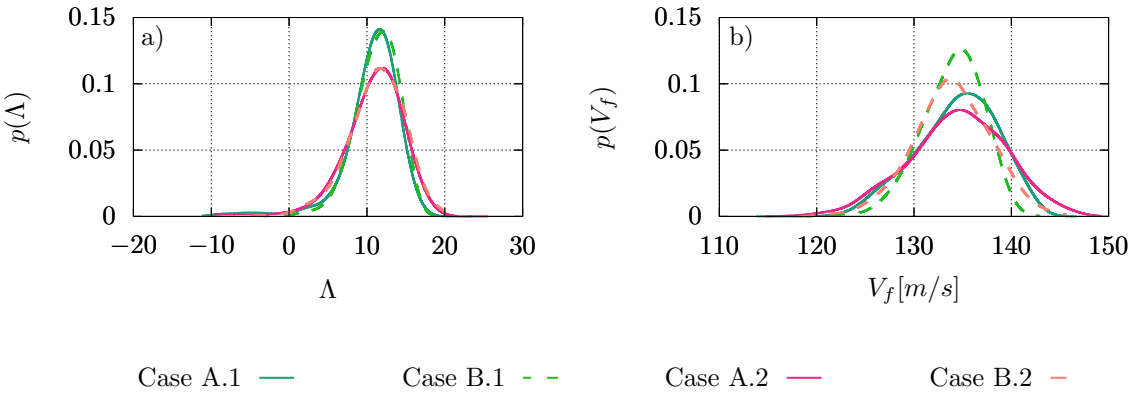

FIGURE 6.16: comparison of RBDO configurations with $V_{design} = 125m/s$. a) pdfs of stability margin and b) pdfs of flutter velocity.

It can be concluded that the uncertainty over the ply thicknesses results in wider pdfs with higher standard deviations. The latter increases the probability of failure and renders the configuration less reliable. As the RBDO is based on the probability of failure, the impact of this parameter cannot be neglected.

6.3.3 Influence of symmetric uncertainties over ply angles

All the uncertainty studies carried out until this step, were non-symmetric meaning that with a given symmetric sequence, the uncertainties considered on each angle is not the same as its symmetric counterpart. This study is done with the help of polar parameters as they permit to express coupled and non-symmetric configurations using the mentioned 6 parameters. On the other hand, most similar works use the lamination parameters to reduce the number of uncertainties which do not allow the study of non-symmetric laminates and therefore a symmetry on the uncertainties has to be imposed. The former assumption is not physically correct as the uncertain parameters cannot be symmetrically distributed during the manufacturing process. In this section, the influence of the imposed symmetry on the uncertainties will be studied. Two RBDO analyses have been conducted considering $V_{design} = 125m/s$, one with imposed symmetry on the uncertainties during the evaluation of the aeroelastic stochastic behaviour and releasing his constraint for the second case.

- Case A: Optimisation while considering non-symmetric uncertainties over angles

$$\underset{\Theta}{\text{minimize}} \quad P(\Lambda(V_{design}, \delta\Theta) < 0) \tag{6.18}$$

- Case B: Optimisation while considering imposed symmetry on the uncertainties over angles

$$\underset{\Theta}{\text{minimize}} \quad P(\Lambda(V_{design}, \delta\Theta_{sym}) < 0) \tag{6.19}$$

As shown in table 6.7, a small difference of 2% is observed between the flutter velocities which translates into the augmentation of the flutter frequency.

Type of uncertainty	$R_0[GPa]$	$R_1[GPa]$	$\Phi_1[^\circ]$	$V_f[m/s]$	$\omega_f[rad/s]$	Nominal Sequence
Case A	12.88	1.54	-24.09	137.1	424.2	$[-45, 40, -55, 35, 40, 10, -60, -50]_s$
Case B	7.63	3.35	4.9	134.1	496.0	$[-40, 25, 55, 20, -50, 80, -40, -15]_s$

TABLE 6.7: Optimal results obtained by the RBDO algorithm for two optimal cases with non-symmetric uncertainties (Case A) and with imposed symmetry over the uncertainties (Case B) with $V_{design} = 125m/s$.

The evolution of the damping and frequency for both optimal cases have been compared in figure 6.17. For both cases, the second aeroelastic mode becomes unstable. The third modes have quite different trends with respect to the second modes. These differences in the damping of each mode can be seen on the frequency plot as well. The frequencies of the non-symmetric optimal configuration (Case A), have the tendency of approaching each other as the velocity grows. On the other hand, the symmetric optimal configuration (Case B) has diverging frequencies as the speed increases.

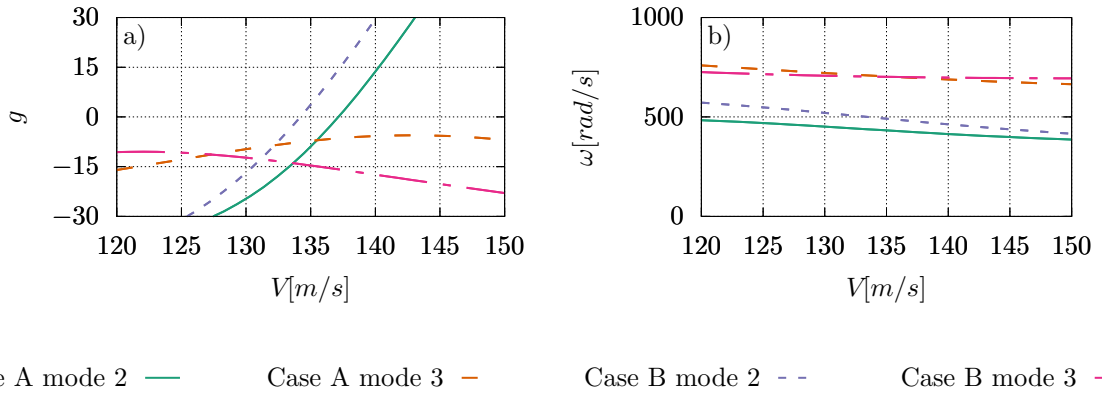

FIGURE 6.17: Comparison of RBDO configurations described in table 6.7. a) damping diagram and b) frequency diagram.

A comparison between mode shapes in carried out in figure 6.18, confirming the similarity between the unstable modes in different velocities.

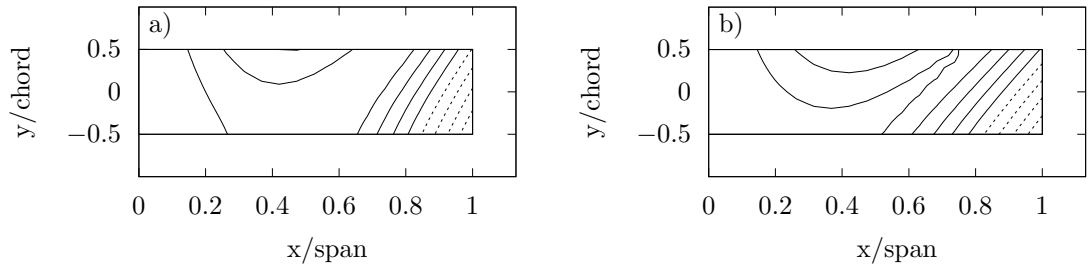

FIGURE 6.18: Mode shapes corresponding to the unstable mode for each optimal case. a) Case A (non-symmetric) and b) Case B (imposed symmetry).

Given the values of the polar parameters and the shape of elastic moduli in figure 6.19, both cases result in anisotropic laminates with close properties to orthotropic symmetries meaning with two dominated directions of symmetry. On the other hand, the young modulus of both cases do not have similar shapes and their shear moduli have strong differences in shapes and values.

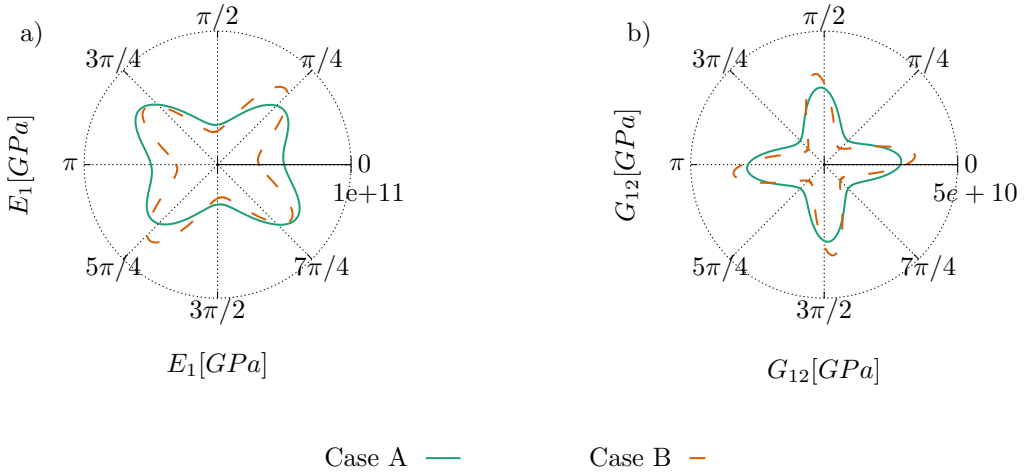

FIGURE 6.19: Elastic properties for RBDO cases with $V_{design} = 125m/s$. Case A (non-symmetric) and Case B (imposed symmetry).

The two optimal cases mentioned beforehand, are now subject to a posteriori stochastic analysis to further investigate the impact of symmetry on each configuration. Four study cases are finally evaluated and the pdf of Λ and V_f are compared with each other. All studies are summarised in the following

1. Case A.1: RBDO considering non-symmetric uncertainties over angles and a posteriori Uncertainty Quantification using non-symmetric uncertainties

$$\underset{\Theta}{\text{minimize}} \quad P(\Lambda(V_{design}, \delta\Theta) < 0) \quad \Rightarrow \quad \text{a posteriori} \quad UQ(P(\Lambda(V_{design}, \delta\Theta)) \tag{6.20}$$

2. Case B.1: RBDO considering symmetric uncertainties over angles and a posteriori Uncertainty Quantification using non-symmetric uncertainties

$$\underset{\Theta}{\text{minimize}} \quad P(\Lambda(V_{design}, \delta\Theta_{sym}) < 0) \quad \Rightarrow \quad \text{a posteriori} \quad UQ(P(\Lambda(V_{design}, \delta\Theta)) \tag{6.21}$$

3. Case A.2: RBDO considering non-symmetric uncertainties over angles and a posteriori Uncertainty Quantification using symmetric uncertainties

$$\underset{\Theta}{\text{minimize}} \quad P(\Lambda(V_{design}, \delta\Theta) < 0) \quad \Rightarrow \quad \text{a posteriori} \quad UQ(P(\Lambda(V_{design}, \delta\Theta_{sym})) \tag{6.22}$$

4. Case B..2: RBDO considering symmetric uncertainties over angles and a posteriori Uncertainty Quantification using symmetric uncertainties

$$\underset{\Theta}{\text{minimize}} \quad P(\Lambda(V_{design}, \delta\Theta_{sym}) < 0) \quad \Rightarrow \quad \text{a posteriori} \quad UQ(P(\Lambda(V_{design}, \delta\Theta_{sym})) \tag{6.23}$$

The stochastic properties for both stability margin and flutter velocity are presented in table 6.8. The nominal stability margin increases for the case with non-symmetric uncertainties during the optimisation process (Case B). On the other hand, the mean and the standard deviation of both optimal cases remain very close in each Uncertainty Quantification strategy. The mean values decrease by about 1% for the symmetric UQ cases (a posteriori) and the standard deviation increases by more than 40% for this strategy. Similar observations are made for the flutter velocity. The nominal value of the non-symmetric optimal case (Case A) is higher by about 2%. This difference remains the same amongst the mean values in each UQ strategy. The mean flutter velocities obtained symmetric uncertainties (Cases marked by .2) are also lowered by about 2% with respect to the ones obtained with non-symmetric uncertainties (Cases marked by .1). On the other hand, the mean values of both optimal cases are lower with the symmetric uncertainties (Cases marked by .2) than non-uncertainties (Cases marked by .1) a posteriori. The standard deviations of the flutter velocity are close for both optimal cases in the non-symmetric uncertainties. They present a large increase for the symmetric uncertainties and this time, the optimal cases have standard deviations that are further apart. The

PoF increases for cases with symmetric uncertainty propagation. The flutter velocity calculated at the 0.01th percentile decreases for Case B in both uncertainty propagation strategies. This observation as well as the value of the PoF show the overestimation of the probability of failure for symmetric cases.

Type of uncertainty	Λ	μ_Λ	σ_Λ	$V_f[m/s]$	$\mu_f[m/s]$	$\sigma_f[m/s]$	$P(\Lambda < 0)$	$(V_f[m/s], 0.01)$
Case A.1	12.8	10.4	4.3	137.1	134.4	4.1	0.03	120.8
Case B.1	10.7	10.4	4.2	134.1	132.3	3.9	0.02	90.6
Case A.2	12.8	8.8	8.4	137.1	132.9	5.4	0.07	111.8
Case B.2	10.7	9.0	7.0	134.1	130.2	7.8	0.09	78.5

TABLE 6.8: Stochastic properties of the optimal cases obtained by RBDO with and without imposed symmetry over the uncertainties with $V_{design} = 125m/s$.

In order to confirm our previous results, the pdfs of Λ and V_f are compared for both optimal cases in figure 6.20.

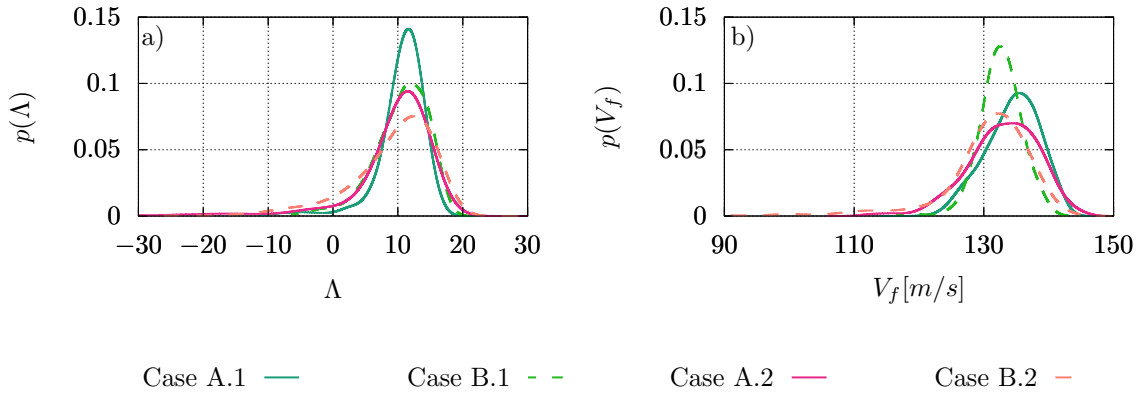

FIGURE 6.20: Comparison of RBDO configurations with $V_{design} = 125m/s$. a) pdf of stability margin and b) pdf of velocity.

Figure 6.20.a) shows that the cases with imposed symmetry a posterior (cases with .2) have lower peaks over the mean values and thus a wider pdf. This impact is more present for Case B as its uncertainties were also symmetric during the RBDO. Figure 6.20.b) also exhibits wider pdfs for symmetric uncertainty propagation a posteriori (cases with .2) over both optimal cases. It can be concluded that symmetric uncertainty propagation overestimates the probability of failure (due to wider pdfs.). On the other hand, the symmetric optimal case with non-symmetric uncertainty propagation a posteriori (Case B.1) has a very narrow V_f pdf with high probabilities over the peak. It can be said that the large standard deviation σ_f of this case presented in table 6.8 is due to its long tail.

6.4 RBDO using polar parameters

As shown in chapter 3, the use of polar parameters during the optimisation process give the advantage of limiting the investigation domain to the desired elastic symmetry as well as providing a faster convergence. The latter is justified by the reduced number of optimisation variables which can vary between 2 to 4 polar parameters given the domain of study instead of 8 to 16 ply angles for the laminates studied in this work. One disadvantage of using the polar parameters is that the aleatory uncertainties cannot be considered directly over the parameters. The reason for this limit is that the six polar parameters depend highly on one another and may exhibit a non-gaussian behaviour. These two properties were studied in details in the work of Nitschke et al. [29] by conducting an uncertainty propagation study over the composite laminates. They imposed 1° uncertainties over the angles of various stacking sequences and obtained the stochastic response of the six corresponding polar parameters. They obtained non-gaussian behaviours in multiple configurations and demonstrated the high dependance between these parameters. These observations and the similar works in literature [31] influenced the previous studies conducted using the ply angles.

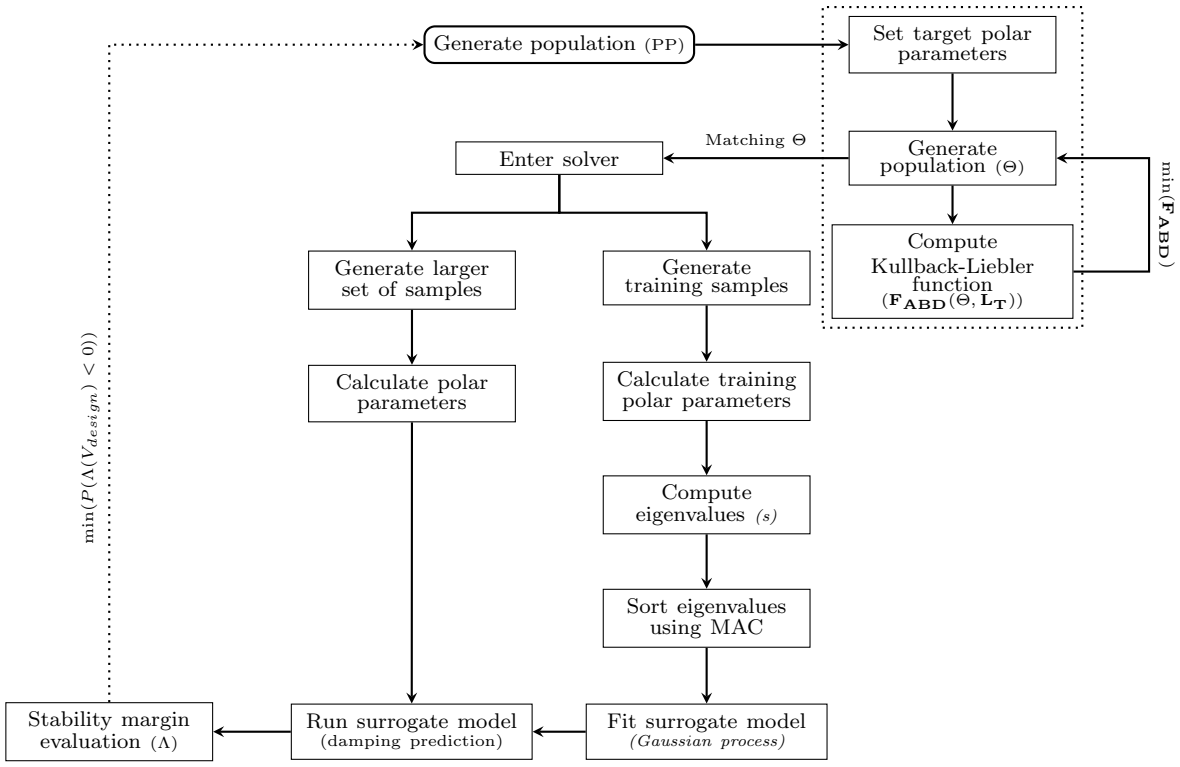

FIGURE 6.21: Reliability-Based Design Optimisation (RBDO) algorithm using polar parameters.

While the results obtained in this section present improvements compared to the deterministic studies concerning the reliability aspect, the optimisation process remains computationally expensive and the convergence rate is very slow. In an attempt to rectify these issues, a new formulation which employs the polar parameters in the RBDO is proposed in figure 6.21.

The same process as the previous cases is followed with and additional step for each individual which retrieves a matching stacking sequence to the corresponding polar parameters. The previous step has a very low computational cost (4 sec) as mentioned in section 3.2

$$\begin{aligned} \underset{R_K,R_1,\Phi_1}{\text{minimize}} \quad & P(\Lambda(R_K, R_1, \Phi_1, V_{design}) < 0) \\ \text{subject to} \quad & -(\rho_0) + 2(\rho_1^2) - 1 \leq 0, \end{aligned} \tag{6.24}$$

Limiting the optimisation domain to the orthotropic symmetry, the RBDO problem defined in (6.24) was carried out using the polar parameters. Table 6.9 compares the results of RBDO limited to the orthotropy using ply angles or polar parameters as optimisation variables. It needs to be noted that the stacking sequences were considered symmetric during the optimisation with angles in order to reduce the number of optimisation variables. The stacking sequence retrieval process of the optimal polar parameters works directly with 16 plies but can be limited to symmetric laminates if intended. An initial comparison of the elastic properties of these two cases using their polar parameters indicates that the two optimal laminates come from different regions of the anisotropic domain. This difference directly impacts the aeroelastic response of the structures. The flutter velocity of the case obtained using the polar parameters is about 5% higher than the case obtained by the ply angles. The flutter frequency of the former case is significantly higher than the latter which can indicate a difference in the unstable aeroelastic mode.

Type of parameters	$R_0[GPa]$	$R_1[GPa]$	$\Phi_1[^\circ]$	$V_f[m/s]$	$\omega_f[rad/s]$	Nominal Sequence
Angles	12.88	1.54	-24.09	137.1	424.2	$[-45, 40, -55, 35, 40, 10, -60, -50]_s$
Polar parameters	13.03	2.36	42.0	144.1	691.0	[-43, 37, -49, 45, 29, 35, 44, -26, -43, -44, -53, 36, -48, 37, 39, -39]

TABLE 6.9: Optimal results obtained by the RBDO algorithm using ply angles and polar parameters with $V_{design} = 125m/s$.

Figure 6.22 compares the damping and frequency of two aeroelastic modes corresponding to the cases presented in table 6.9. The plot of the damping confirms the difference in the unstable modes. The second mode becomes unstable for the case obtained by ply angles but the third mode is far from the flutter boundary (zero axis). On the other hand, the case obtained by the polar parameters

shows instability over the third mode and the second mode becomes unstable immediately after. The third mode corresponds to a hump mode and while it becomes unstable, it comes back to stability in higher velocities. The frequency evolution of both modes resembles amongst the two optimal cases and decreases as the velocity rises.

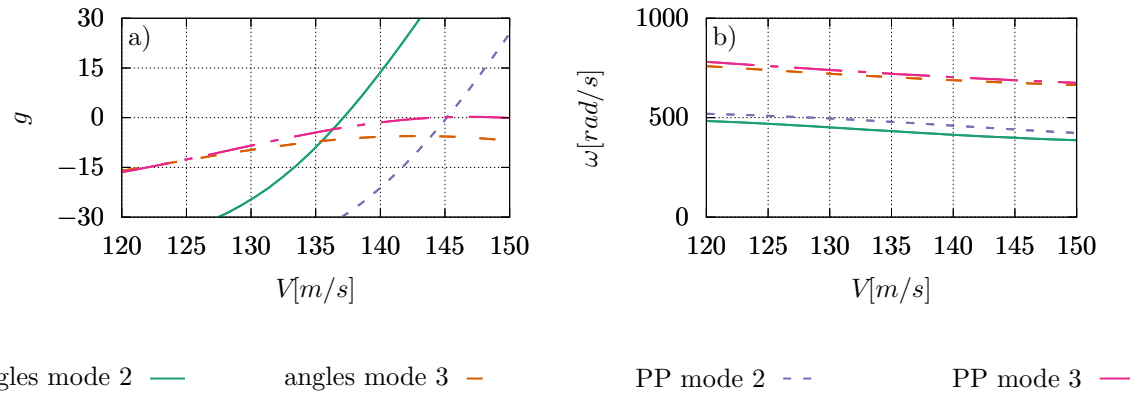

FIGURE 6.22: Comparison of the evolution of a) damping and b) frequency as a function of velocity for optimisation formulations with angle plies and Polar Parameters (PP).

The corresponding mode shapes of the unstable modes are presented for each case in figure 6.23. The unstable mode related to the optimal case obtained by the ply angles presents a second aeroelastic mode as a combination of the first torsion and second bending modes. The third aeroelastic mode is associated to the unstable mode of the optimal case obtained by the polar parameters and is a combination of the third bending the first torsion mode.

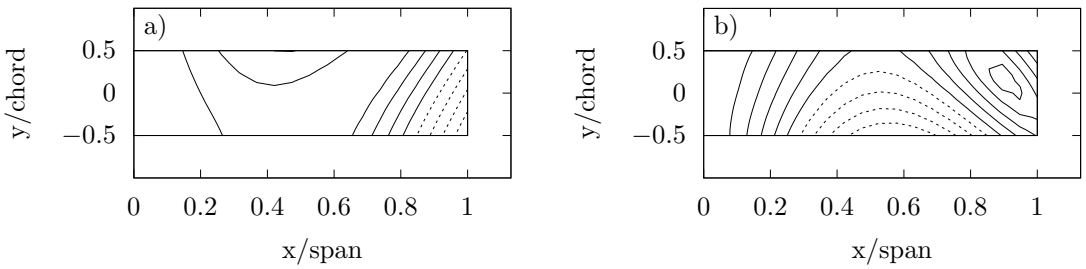

FIGURE 6.23: Mode shapes corresponding to the unstable mode for each optimal case. a) ply angles and b) polar parameters.

In order to highlight the stochastic behaviour of these two cases, first the optimal, mean and standard deviation of the stability margins and the flutter velocities are compared in table 6.10. The optimal stability margin of both cases are similar with about 1% difference. The same observation can

be done for the mean stability margins which are about 15% lower than the optimal stability margins. On the other hand, the standard deviation of the case obtained by the ply angles is significantly higher than the one obtained using the polar parameters. This 30% difference can indicate a wider pdf which affects the reliability of the configuration. As mentioned previously, the optimal flutter velocity of the configuration obtained by the polar parameters is 5% higher than the ply angle optimal case. A smaller difference is observed over the mean velocities which is approximately of 2% and similarly between the standard deviations which is nearly of 12%. These two observations can indicate a wider pdf for the flutter velocity of the optimal case obtained by the polar parameters. The probability of failure of the former is significantly smaller than the case obtained by the ply angles which given its higher flutter velocity can be considered the more reliable case with higher aeroelastic performance. On the other hand, the flutter velocities at 0.01th percentile are very close between the two cases (less than 1% difference). This result can be due to the long tail of the pdf of both cases which is also indicated by the value of the standard deviation.

Type of parameters	Λ	μ_Λ	σ_Λ	$V_f[m/s]$	$\mu_f[m/s]$	$\sigma_f[m/s]$	$P(\Lambda < 0)$	$(V_f[m/s], 0.01)$
Angles	12.8	10.4	4.3	137.1	134.4	4.1	0.03	120.8
Polar parameters	12.6	10.7	3.0	144.1	136.8	4.6	< 0.01	120.4

TABLE 6.10: Stochastic properties of the optimal cases obtained by RBDO for two optimisation formulations with $V_{design} = 125m/s$.

The stochastic behaviour of the two optimal cases are exhibited in figure 6.24 for both stability margin Λ and flutter velocity V_f.

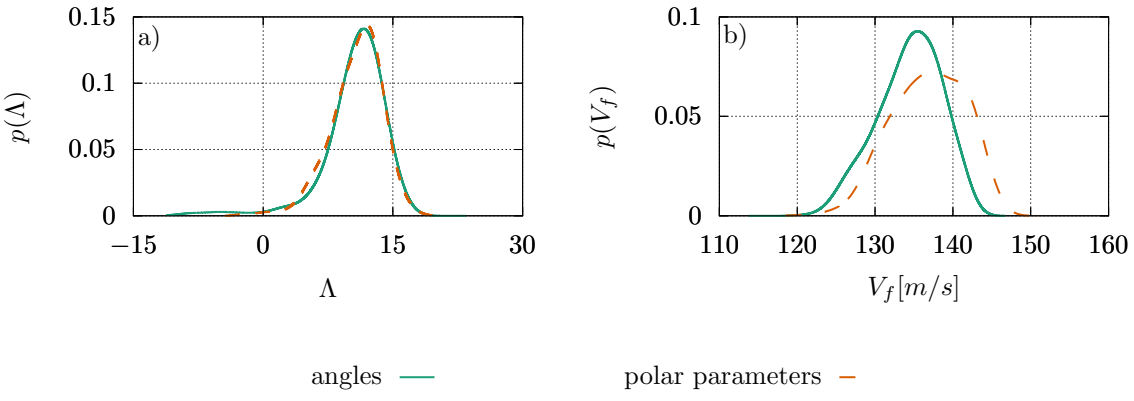

FIGURE 6.24: Comparison of RBDO configurations with $V_{design} = 125m/s$ obtained with angles and polar parameters. a) pdf stability margin and b) pdf of velocity.

Figure 6.24.a) shows that the stability margin pdf of the two formulations are very similar in shape. However, the pdf obtained by the ply angles formulation has a longer tail which explains the large difference of the standard deviations. The pdfs of the flutter velocities compared in figure 6.24.b) show very different shapes. The ply angles optimal case has a narrower pdf with higher probabilities over the peak, the polar parameters optimal configuration remains the more reliable case with a higher flutter velocity and thus with better performance.

6.5 Conclusion

In this chapter, the aeroelastic behaviour of a composite structure has been optimised in the stochastic framework. The ply angles have been used as optimisation variables throughout the study. Symmetric composite laminates have been considered in order to reduce the number of optimisation variables. The polar parameters have been used in order to reduce the dimensionality of the problem as they allow to express the bending behaviour of the structure using only 6 parameters. The stability margin was used to circumvent the difficulty associated to the use of non-smooth variable of interest such as the flutter velocity. Stability margin is a function of aeroelastic dampings which are continuous function of polar parameters and can easily be emulated using the chosen surrogate model.

The stochastic aeroelastic response of the composite structure was approximated using a surrogate model. The latter was then employed in a Reliability-Based Design Optimisation (RBDO) framework. The results of the deterministic optimisation process have been compared to the optimal cases of RBDO. A clear advantage of the RBDO is observed particularly in the stochastic analysis regarding the safety of the final design.

Next, the influence of random thicknesses and imposed symmetric uncertainties during the optimisation process and in the Uncertainty Quantification a posteriori has been investigated. Uncertainty over ply thicknesses lead to a more dispersed pdf and higher probability of failure. On the other hand, imposed symmetry on the uncertainties gave place to configurations with lower performance and an under-estimated probability of failure.

Finally, the proposed RBDO algorithm has been modified in order to include a higher control over the elastic properties of the structures under study. To this end, the intermediate step of stacking sequence retrieval has been added to the RBDO process while modifying the optimisation variables to the polar parameters. The comparison of the stochastic response of the cases obtained by ply angles and the polar parameters showed a significant improvement in the final results of the RBDO. The probability of failure was reduced by at least 70% when using the polar parameters while the flutter

velocity was increased by 5%. The elastic properties of the final result was determined beforehand as the optimisation domain was limited to orthotropy which resulted in a more reliable structure with higher performance.

7

Conclusions and Perspectives

7.1 Conclusion

The main objective of this work was to conduct the aeroelastic optimisation of composite structures using a 2-level method based on the polar formulation. Both deterministic and stochastic frameworks were considered and compared for this purpose. The purpose of this optimisation was the maximisation of the critical velocity which is defined as the velocity in which the dynamic (flutter) or static (divergence) instabilities can take place. The composite structures employed were constructed using stacking sequences with Uniform-Stiffness or Variational-Stiffness plies with Uni-Directional or Tow-Steered fibre paths respectively.

Initially, the Uniform-Stiffness composite laminates were directly optimised using the ply angles as the optimisation variables. Using the Genetic Algorithm as the optimisation method and a 16-ply composite laminate, the use of ply angles implied an optimisation process with 16 variables. Each variable could have an independent value in an interval of $-90°$ to $90°$ with a $5°$ increment which did not impose any limitations over the elastic symmetry of the stacking sequences. This study was then compared to similar cases with a constraint over the coupled membrane-bending condition and another case with imposed symmetry on the laminate under study (this reduced the number of optimisation parameters to 8). The optimisation variables were then replaced by the polar parameters which helped

to reduce the number of variables significantly (in this case 4 instead of 16). The investigation of the anisotropic domain with the help of polar parameters accelerated the convergence of the optimisation process while giving satisfactory results.

The results obtained during the anisotropic optimisation study using symmetric ply angles suggested optimal cases with orthotropic symmetries which triggered the idea of restraining the optimisation domain to orthotropy. Polar parameters demonstrated an improvement in the optimisation process in terms of the convergence to the optimal objective function. Moreover, they allowed the definition of elastic symmetries in a geometrical domain for which the boundaries are expressed analytically. Three geometries (straight, swept-backward and swept-forward wings) have been subject to this optimisation process. Using three polar parameters (R_K, R_1 and Φ_1) to represent all admissible orthotropic laminates, the maximum flutter velocity for each geometrical configuration was obtained. These results suggested an alignment between the orthotropic and reference wing axis for the straight wing, while the importance of optimising the polar angle Φ_1, i.e. the direction of the orthotropy axis, was demonstrated for the swept wings. While the polar parameters improve the optimisation process (by both accelerating and restraining the domain), they require a second step which consists on retrieving the stacking sequence corresponding to the optimal set of polar parameters. This step can be done either analytically or numerically, which was explained and demonstrated with multiple cases.

Next, the deterministic optimisation was expanded to Tow-Steered laminates. The polar parameters were again employed to express the elastic properties of the composite structures. The variable rigidity of the Tow-Steered plies were expressed by different strategies which were mainly based on the anisotropic moduli (R_K and R_1). The parameters were imposed over the chosen control points throughout the structure and were then interpolated by the B-spline curves in order to obtain the rigidity matrix over each finite element node. The anisotropic moduli were either chosen over the angle-ply curve or the entire orthotropic domain and the optimisation process was conducted for the same three geometries as previously mentioned. The variation over the angle-ply curve resulted in a $2-4\%$ improvement for the straight and the swept-backward wing in comparison to their Uniform-Stiffness counterpart. On the other hand, the variation of the anisotropic moduli inside the orthotropic domain achieved an increase of 3% for the swept-forward wing compared to its Uniform-Stiffness counterpart.

Once the deterministic optimisation of all cases was carried out, the stochastic response of these optimal configurations was studied. First a convergence study using the Latin Hypercube Sampling (LHS) was conducted in order to obtain the best compromise between the accuracy and the computational time. Using 1000 LHS samples the probability density function of all Uniform-Stiffness optimal cases were compared. While the optimal flutter velocity corresponded to the straight wing,

the stochastic analysis proved the swept-backward wing to be more reliable. Next, the Tow-Steered laminated were subject to the same analysis but this time a stochastic process needed to be put in place in order to propagate uncertainties with spatial dependencies. The Karhunen-Loève expansion was employed for this purpose using 40 modes of the covariance function. The pdf of the Tow-Steered laminates were compared to their Uniform-Stiffness counterparts and proved to be significantly more reliable for some geometries.

Finally, given the results obtained in the previous chapters, particularly considering the insight on the reliability degradation of deterministic optima when analysed in a stochastic framework, the parametric uncertainties were included in the optimisation process. The latter implied a stochastic optimisation with a probabilistic objective function. While multiple methods exist for this type of study, the Reliability-Based Design Optimisation (RBDO) was chosen in this work using this time the ply angles as the optimisation variables. RBDO consists of minimising the probability of failure which was defined as the probability of having flutter velocities lower than a given design velocity. This process was found to be computationally expensive particularly due to the calculation of probability of the objective function. It was thus decided to employ a surrogate model such as Gaussian Process Regression (GPR) in order to reduce the computational time. The main difficulty risen from the use of GPR was the discontinuity on the response surface of the domain of study which was overcome by changing the objective function. Stability margin which is a function calculated from the aeroelastic damping values at a given design velocity, solves the problem of discontinuity as the damping values are a continuous function of the composite material properties. The RBDO was conducted using GPR and the stability margin which helped define the probability of failure for cases with negative values of the latter. Multiple design velocities and different types of uncertainties were tested for the straight wing and their results were compared to one another. A new formulation was tested using the polar parameters which included a supplementary step of stacking sequence retrieval into the optimisation process. The latter was then compared to the original algorithm using the ply angles and showed to be more efficient both in convergence speed and the control over the elastic properties of the final result.

7.2 Perspectives

The optimisation process conducted in this work was tested for three different geometries. While the swept wings allowed a better understanding of the parametric study, the proposed methodology can easily be applied to more complex geometries. Configurations such as the T-tail wing [178] or even a simple whole airplane body [179] could be modelled using the tools presented in this work at a subsonic flow and adequate results for a pre-design step can be obtained. As far as the aerodynamic model is

concerned, while some studies mention the low accuracy of the original Doublet Lattice Method for these types of simulation, small variations in the latter could significantly enhance the results [180]. Another common aeroelastic instability, often taking place in supersonic regimes, is the panel flutter [35]. Simple models such as piston theory could be developed and coupled to the existing structural model in order to study this phenomenon in supersonic flows [181, 182].

In order to further improve the results obtained by the Doublet Lattice Method (DLM) presented in this work for compressible subsonic flows, higher fidelity models such as Euler or RANS can be employed. While these methods have proven to achieve higher precision results, they are computationally expensive. One way to reduce this computational cost is to solve the coupled equation in a frequency domain using linearised aerodynamic models [183, 184]. In order to obtain further time reduction, in the case of small-amplitude motions, an alternative solution is the flutter derivative, which is based on defining the aerodynamic forces as a function of the structural motions. The coefficients of the structural terms are the flutter derivatives which can be obtained by experimental or numerical methods [185, 186]. While these methods significantly reduce the computational time of high-fidelity models, they remain costly for an iterative optimisation framework. Multi-fidelity methods are more and more popular as a solution to reduce the computational cost. These types of procedures usually consist in conducting a few high fidelity simulations in order to obtain either a correction factor [187, 188] or a surrogate model [189, 190] to improve the results of the lower fidelity model. In an optimisation framework similar to the study presented in this work, another type of multi-fidelity analysis can be employed: it is based on a first analysis of the domain of study using a low-fidelity model in order to obtain the regions of interest which can then be exploited using a higher fidelity model which will investigate a significantly smaller domain [191].

Naturally, with more realistic models, different aspects of the structure or the aerodynamic forces need to be taken into account during the optimisation. A Multi-Disciplinary Optimisation (MDO) could help with the formulation of these types of studies in order to find the best compromise amongst multiple objective functions [192]. Furthermore, in the framework of the single objective optimisation problem conducted in this work using the polar parameters, some variations on the elastic properties of the final stacking sequence can be made. The latter is mainly during the numerical retrieval due to the choice of the function which is the Kullback-Liebler function in this work and is based on the rigidity matrices. Other functions can be defined by the matching of the polar parameters of one specific matrix such as bending or membrane or even the membrane-bending coupling matrix in order to put more emphasis on the desired property.

Another step that adds numerical error to the final result is the stacking sequence retrieval, particularly during the Reliability-Based Design Optimisation (RBDO) process. One solution to skip this step is to impose directly the uncertainties over the polar parameters. However, the latter has been an obstacle during this work as the parametric uncertainties over the stacking sequences do not have a direct relationship with the polar parameters. Moreover, the six polar parameters are co-dependant which further complicates the consideration of uncertainties over these variables. Few analysis have been conducted over the uncertainties of the quasi-trivial sequences and their impact on the distribution of the polar parameters. The latter has demonstrated a strong dependance of the polar parameters distribution on the family of the quasi-trivial sequences. This could be a starting point into imposing uncertainties directly over the polar parameters.

Another manner into the improvement of RBDO has been the replacement of the optimisation variables by polar parameters. As a result, a stacking sequence retrieval step has been included during the optimisation process. The latter has been based on the numerical optimisation of the Kullback-Liebler function for every polar parameter chosen by the optimisation algorithm. On the other hand, it was demonstrated that the right choice of retrieval method significantly reduces the differences between the target polar parameters and the resulting stacking sequence. The addition of an automatic analysis of the polar parameters inside the domain can help choose an appropriate method during the RBDO process.

The main objective of this work was to maximise the flutter velocity as well as ensuring a reliable stochastic response (low probability of failure) of the optimal structure. The latter has been made possible but resulted into a decrease of the flutter velocity. During the parametric analysis of the response surfaces for different geometries, it was observed that the mode switch of the optimal case is generally between the second and the third aeroelastic mode. The damping values of the second mode increase with the airspeed and remain unstable for all speeds beyond the flutter velocity. On the other hand, the third mode has damping values that become positive at the flutter velocity but soon after become stable at large velocities associating the latter to a hump mode. This type of behaviour can be eliminated with the help of flutter control and thus increase the flutter velocity. Active or passive flutter control [193, 194] have been the subject of interest in aeroelastic design in the recent years. Methods such as mass damper [195] or piezoelectric actuators [196] are some popular approaches to active flutter control. To further insure the safety of the structure, particularly due to the absence of high-fidelity models, active robust control has been developed as a solution which includes various uncertainties present in the aeroelastic system [197, 198].

A

Uniform-Stiffness Laminates: Tapered Wing

As a continuation to the results presented in chapter 3, the purpose of this appendix is optimisation of the orthotropic and geometrical properties of a tapered plate under study

$$\begin{aligned} \underset{R_K, R_1, \Phi_1, \alpha_{swept}, \lambda_t}{\text{maximize}} \quad & V_f \\ \text{subject to} \quad & -(\rho_0) + 2(\rho_1^2) - 1 \leq 0, \end{aligned} \tag{A.1}$$

where the tapered ratio can be defined as $\lambda_t = c_{tip}/c_{root}$ with c_{tip} representing the chord of the wing at the tip and c_{root} the chord of the wing at the root for which the value is constant throughout the optimisation process $c_{root} = 0.0762m$.

Table A.1 summarises the results of this optimisation study.

Case ID	Wing configuration	$R_K[GPa]$	$R_1[GPa]$	$\Phi_1[^\circ]$	$\alpha_{swept}[^\circ]$	λ_t	$V_f[m/s]$	$\omega_f[rad/s]$
tp1	tapered	13.27	1.06	36.	-20.	0.13	261.3	1425.9

TABLE A.1: Results of deterministic optimisation for tapered US configuration using polar parameters, swept-angle and the tapered ratio as optimisation variables.

The anisotropic moduli R_K and R_1 indicate that this optimal configuration is in the right side of the orthotropic domain near the cross-ply border. This property is similar to both optimal cases obtained for swept wings when the polar angles was included in the optimisation process. The value of the optimised swept angle α_{swept} corresponds to a swept-backward wing and unlike the swb2 Uniform-Stiffness case ($\alpha_{swept} = -15°$ and $\Phi_1 = -56°$), the polar angle of tp1 is in the opposite direction of the swept angle ($\alpha_{swept} = -20°$ and $\Phi_1 = 36°$). The optimised tapered ratio allows the calculation of the wing chord at the tip $c_{tip} = 0.0101m$. This value indicates that the optimal aeroelastic behaviour of a plate wing corresponds to a delta configuration. Finally, the flutter velocity of the optimal case is calculated which is significantly higher than the cases studied in section 3.1.2. The highest flutter velocity previously obtained corresponds to the straight wing ($V_f = 146.5$ m/s) which is 48% lower than the optimal flutter velocity of the tapered case. The flutter frequency of the tapered case is considerable higher than any value obtained previously for different modes. It can indicate the appearance of the instability on a different mode than the ones observed for other optimal cases.

Figure A.1 demonstrates the evolution of aeroelastic damping and frequency of the optimal tapered wing. The third mode becomes unstable and the fourth mode approaches the flutter boundary which has not been the case for the previous geometries studied previously. The first and the second modes are far from the instability which proves that at large values of velocity, higher modes are more favourable to become unstable. The aeroelastic frequencies of the modes increase for higher orders but at large velocities the frequencies of the fifth mode converge towards the fourth.

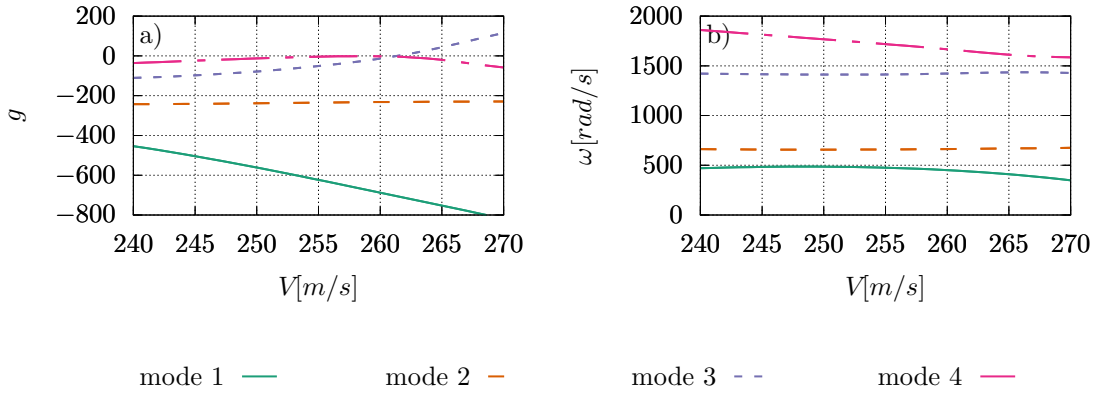

FIGURE A.1: The evolution of a) aeroelastic damping and b) aeroelastic frequency of case *tp1*.

The unstable mode shape is presented in figure A.2. It is the third aeroelastic mode which for this case is obtained by coupling between the third bending and second torsion mode.

Finally, the elastic moduli are presented in figure A.3. The symmetry in the young moduli plot

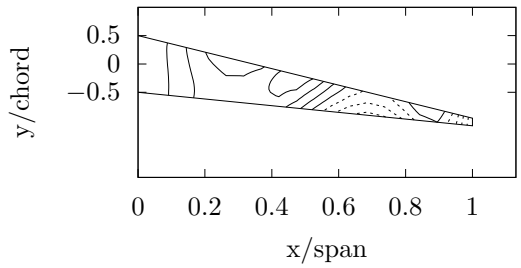

FIGURE A.2: The aeroelastic mode shape for case *tp1* resulting from the optimisation presented in table A.1.

confirms the orthotropic nature of the optimal configuration and the deviation from $\frac{\pi}{2}$ demonstrates the polar angle orientation.

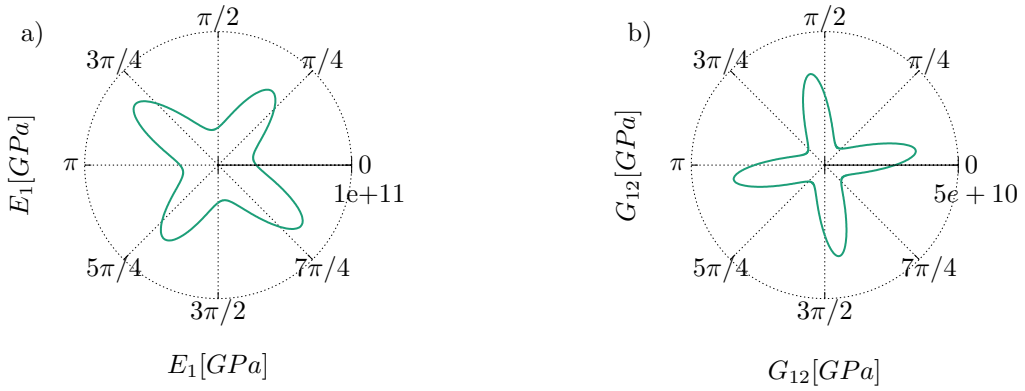

FIGURE A.3: Young moduli of the optimisation results for the optimal tapered wing presented in table A.1.

B

Variable-Stiffness Laminates: Complementary Results

This appendix includes complementary results of the Tow-Steered study. An optimisation strategy using the polar angle Φ_1 and some 2D results of the two strategies from chapter 4 are presented. Similar formulation of the Tow-Steered composite laminates has been employed as explained in chapter 4. Three different strategies are put in place for modelling these variable stiffness laminates where two of them were previously presented. In this section all three strategies are explained and the results of multiple cases are demonstrated. The three strategies are as followed:

- Anisotropic moduli (R_K and R_1) optimised but constant throughout the structure only the polar angle (Φ_1) optimised and variable per finite element node
- Anisotropic moduli (R_K and R_1) optimised over the angle-ply curve and variable per finite element node
- Anisotropic moduli (R_1 and R_K) optimised over the whole orthotropic domain and variable per finite element node

Each strategy is applied to three different geometries, one straight and two swept wings. For each geometry, two types of stiffness variations are considered, one along the span (1D) and one along both span and chord (2D).

B.1 Optimisation by varying the polar angle

The first strategy consists on optimisation of three polar parameters, the anisotropic moduli (R_K and R_1) in the orthotropic domain and the polar angle (Φ_1). While anisotropic moduli are optimised for each laminate, their values stay constant throughout the structure. On the other hand, the variation of the stiffness is presented by different values of the polar angle (Φ_1) per finite-element node. As explained before, these values are not set directly for each node but interpolated using the B-spline interpolation method. The optimisation algorithm, generates two values for each anisotropic moduli and 6 or 24 values of the polar angle on the control points depending on 1D or 2D variations of the stiffness.

Table B.1, summarises the results obtained for different configurations. It needs to be noted that for each geometry, two optimisation problems have been conducted. Cases with the variation of Φ_1 only along the span are indicated by (1D) and along both span and chord by (2D). Similarly to the optimisation problems conducted in the previous chapter, 100 individuals are optimised over 50 generations. For 2D cases the number of individuals is increased to 150 as the number of variables is significantly higher.

Case ID	Wing configuration	$R_K[GPa]$	$R_1[GPa]$	$\Phi_1[^\circ]$	$\alpha_{swept}[^\circ]$	$V_f[m/s]$	$\omega_f[rad/s]$
st1	straight (1D)	13.97	0.53	variable	**0.**	145.2	417.3
st2	straight (2D)	-13.97	1.28	variable	**0.**	138.1	478.4
swb1	swept-backward (1D)	12.18	5.15	variable	**-15.**	139.1	656.5
swb2	swept-backward (2D)	-13.33	1.04	variable	**-15.**	134.6	440.8
swf1	swept-forward (1D)	13.13	8.88	variable	**15.**	138.0	402.3
swf2	swept-forward (2D)	14.19	7.09	variable	**15.**	138.0	416.8

TABLE B.1: Deterministic optimisation results of the Tow-Steered configurations obtained by optimised anisotropic moduli (R_K and R_1) and variations of polar angle (Φ_1) throughout the structure with red coloured variables indicating constant parameters during the study.

For the straight case, optimised in the span-wise direction, the maximum flutter velocity (V_f) reaches similar values as the one obtained using Uniform-Stiffness (US) laminates. On the other hand, the anisotropic moduli are on the opposite part of the domain compared to the US configuration. The 2D (chord-wise and span-wise) variation of Φ_1 did not improve the results and could not reach the maximum value obtained with the 1D case. The reason is mainly due to the number of optimisation variables which were higher and thus more complicated for the algorithm to converge to the maximum value. Comparing the values of the flutter frequencies, the 2D variations have higher frequencies for smaller values of velocity.

For both straight wing cases (1D and 2D), figure B.1 represents the variation of Φ_1 throughout the structure. The arrows show the direction of the latter, while the colour map indicates the value of Φ_1 over each finite-element node. For the 1D case, the polar angle is not aligned with the reference axis but it does not show important variations except near the wing tip when the orthotropic axis has a notable change of direction and gets values closer to zero. On the other hand, the 2D case has remarkable patterns along both the chord-wise and the span-wise directions. These observations, confirm that in case of a straight wing, large variations of the orthotropic axis do not increase the flutter velocity and as demonstrated in the US case, the optimal configuration corresponds to $\Phi_1 = 0°$.

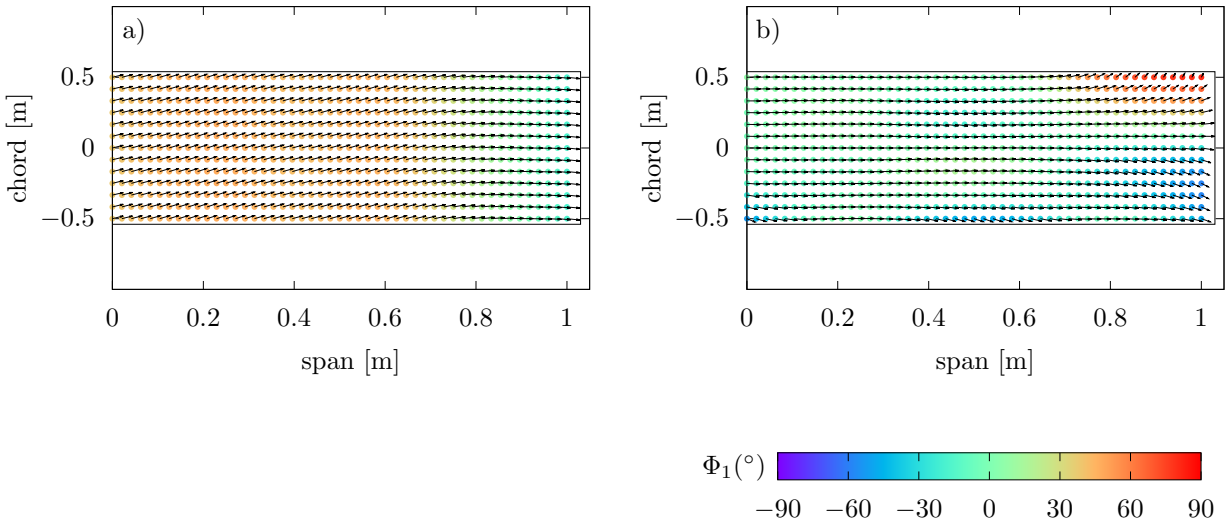

Figure B.1: Variation of value and orientation of the ply angle (Φ_1) indicated by the colour map and the arrows. a) over the span (case *st1*) and b) over both span and chord (case *st2*) for a straight wing.

The evolution of the aeroelastic damping and frequency of both straight cases in figure B.2, demonstrates the same behaviour as the US configurations. The instability occurs on the second mode while the third mode stays close to the zero axis as well. The mode shapes of the unstable cases are presented in figure B.3. The second aeroelastic mode with second bending and first torsion coupled modes occurs for both cases while the amplitude of the mode for each case is slightly different.

The same type of study was carried out for both swept-backward and swept-forward cases presented in table B.1. For 1D variation of Φ_1, the swept-backward case, reaches similar values than the US laminates but again with anisotropic moduli that belong to a different zone on the orthotropic domain. The 2D variation of the polar angle over the span and the chord, reduces the flutter velocity which as stated before is related to the large number of variables and the number of possibilities. On the other hand, the flutter frequency of the 2D case is significantly lower than the 1D case. This difference can

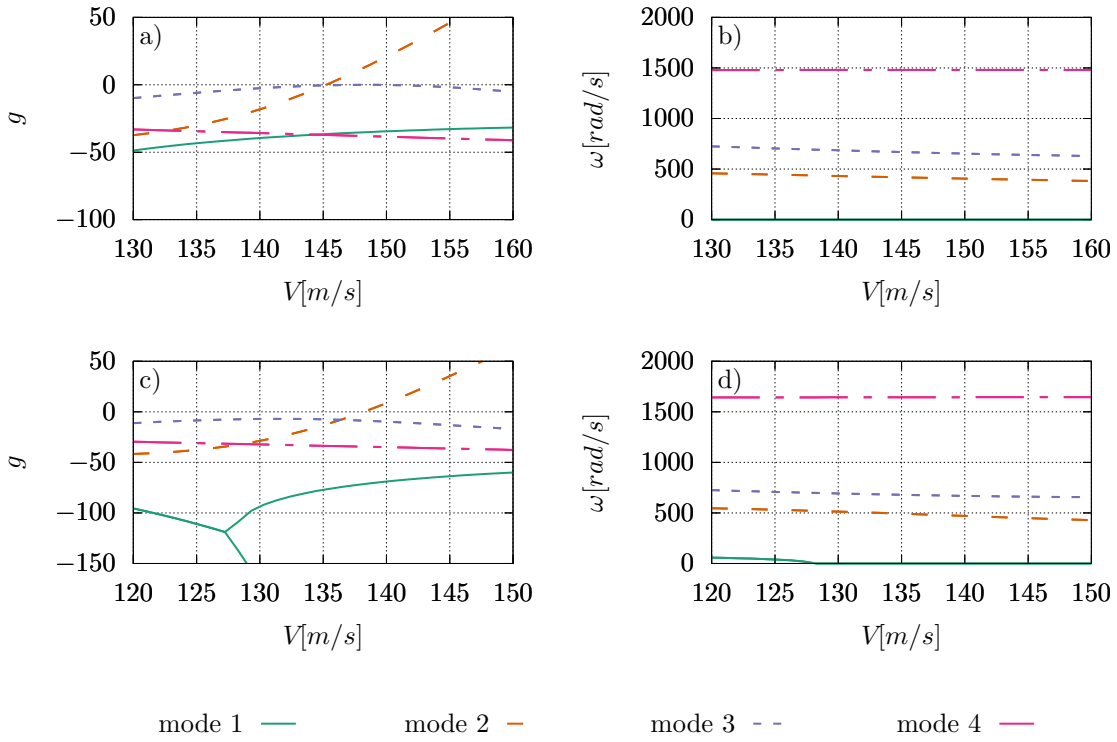

FIGURE B.2: Evolution of (a,c) aeroelastic damping and (b,d) aeroelastic frequency of the TS straight wings with variations of Φ_1. (a,b) for case *st1* and (c,d) for case *st2*.

indicate the instability on two different modes.

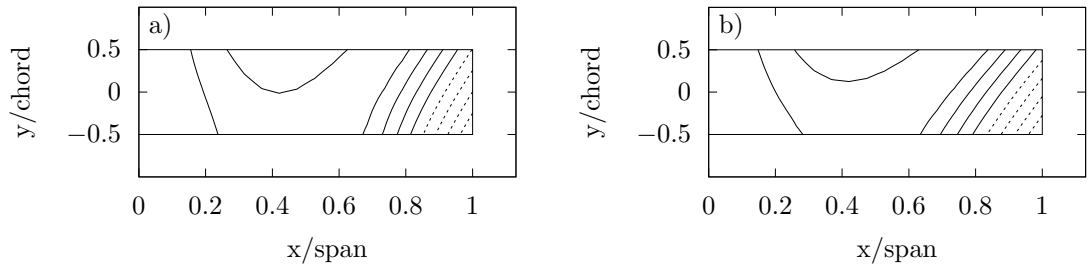

FIGURE B.3: Aeroelastic mode shapes of the TS straight wings for variation of Φ_1. a) for case *st1* and b) for case *st2*.

The variation of Φ_1 is now demonstrated for the swept-back configurations in figure B.4. Similarly to the straight case, for the 1D case, orientation of the polar angle over the structure remains roughly unchanged and has a significant variations towards the tip of the wing. Unlike the straight case, the

values of Φ_1 at the tip are not close to zero. For the case with a 2D variation of Φ_1, the deviation of the angle throughout the structure is more present but the interval in which the variations take value is limited.

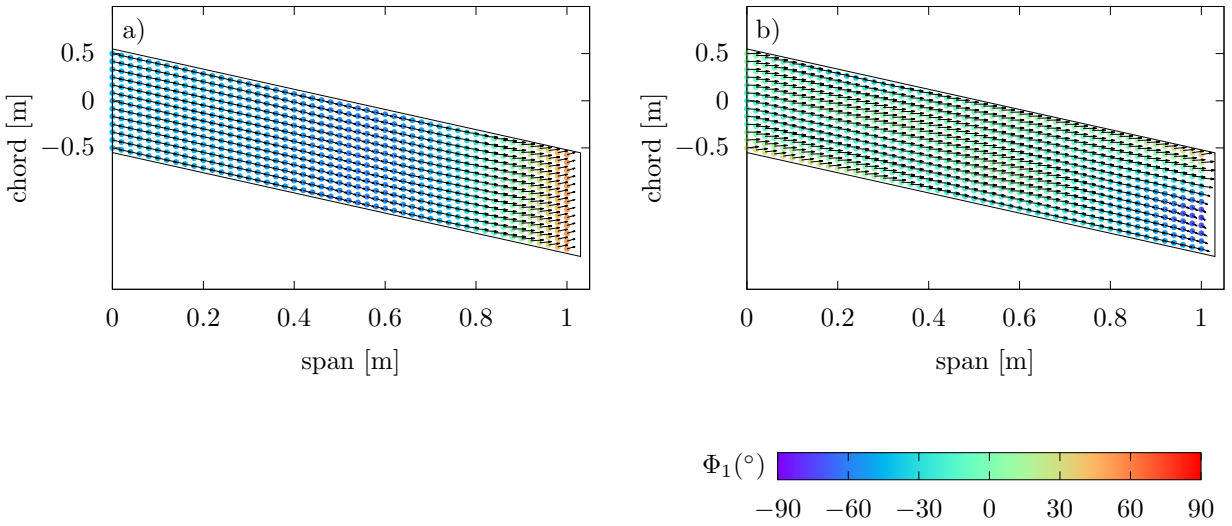

Figure B.4: Variation of value and orientation of the ply angle (Φ_1) indicated by the colour map and the arrows. a) over the span (case *swb1*) and b) over both span and chord (case *swb2*) for a swept-backward wing.

The aeroelastic damping and frequency evolution for the swept-backward wing are presented in figure B.5 . The instability takes place on the third mode for the 1D case while the second mode becomes unstable soon after. On the other hand, for the 2D case the latter becomes close to instability but stays stable even after the flutter velocity. Another points to remark on this figure, is the first mode which corresponds to divergence. The latter is closer to instability for the 1D case compared to the 2D configuration.

Concerning the mode shapes, figure B.6, demonstrates the third aeroelastic mode for the 1D case which is a combination of the second torsion and the first bending mode. for the 2D case, the second aeroelastic mode is presented which is a combination of the second bending and the first torsion mode.

The next geometry to consider is the swept-forward wing. The variation of the polar angle Φ_1 over a swept-forward wing demonstrates slightly different results in table B.1. The optimal flutter velocity is moderately higher than the US configurations. Furthermore, the 2D variation of Φ_1 reaches approximately identical values of velocity and frequency as the 1D case. The reason for this difference can be due to the large influence of the orientation of orthotropic axis over the aeroelastic response of swept-forward configurations. As observed in the previous chapter, swept-forward wings have the highest increase of the flutter velocity for the variation of Φ_1.

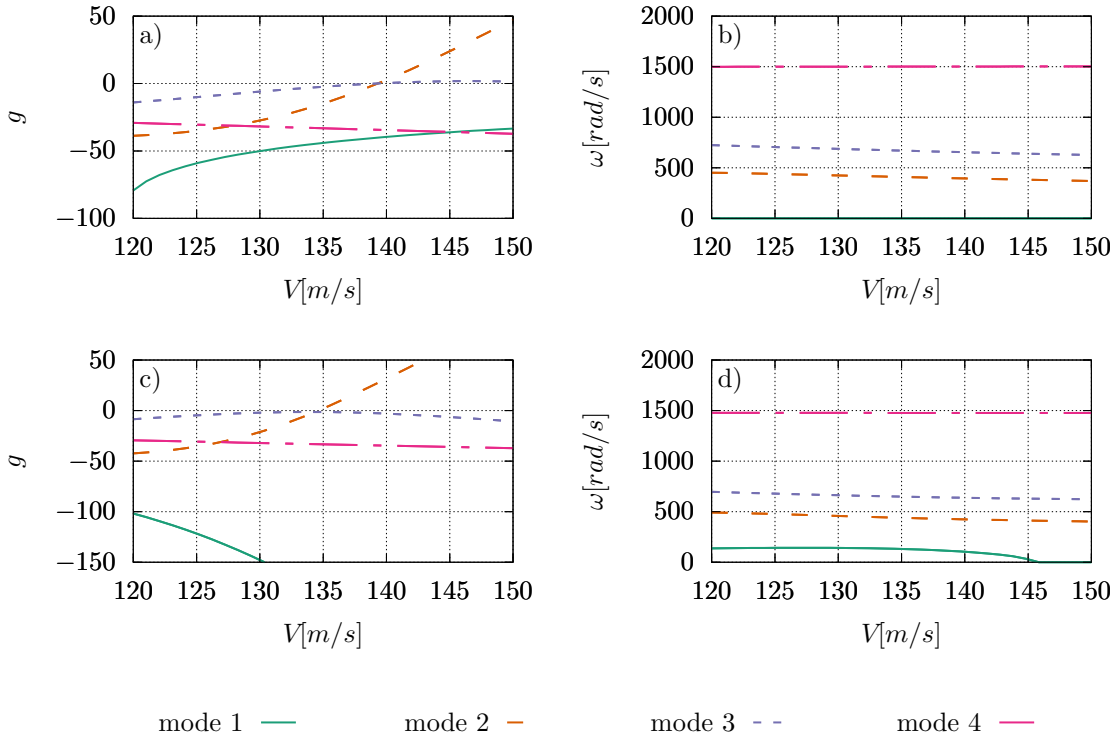

FIGURE B.5: Evolution of (a,c) aeroelastic damping and (b,d) aeroelastic frequency of the TS swept-backward wings with variations of Φ_1. (a,b) for case *swb1* and (c,d) for case *swb2*.

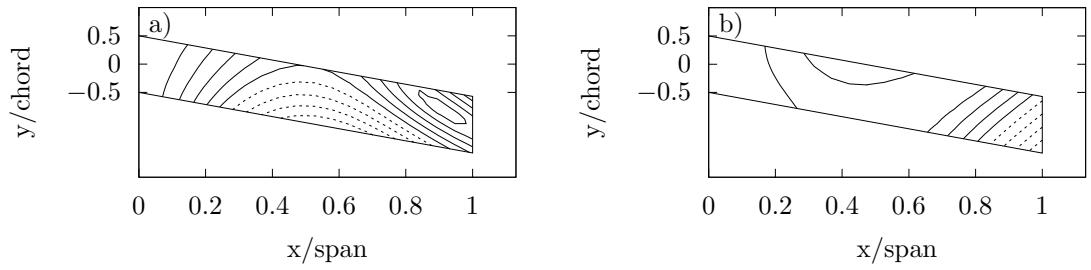

FIGURE B.6: Aeroelastic mode shapes of the TS swept-backward wings for variation of Φ_1. a) for case *swb1* and b) for case *swb2*.

Figure B.7 presents the distribution of the polar angle throughout the structure. The variation of Φ_1 over this case is highly uni-directional for the 1D case. Unlike the previous cases, the angles near the wing tip keep the same tendency as the rest of the structure. In the 2D case, the variation of the polar angle stays the same in the mid section of the wing and some variabilities towards the tip and the lower root.

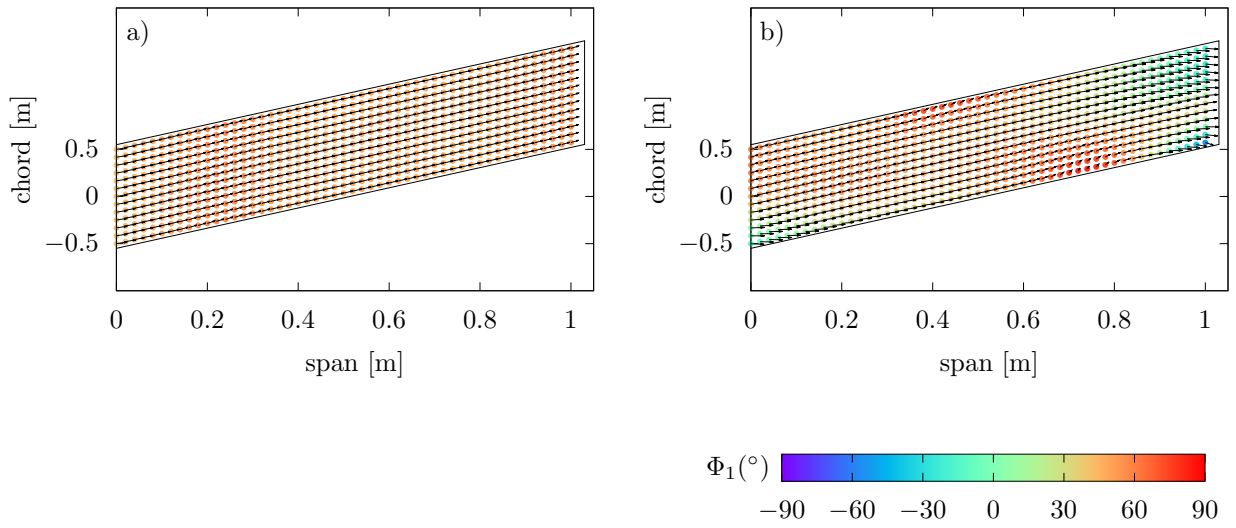

Figure B.7: Variation of value and orientation of the ply angle (Φ_1) indicated by the colour map and the arrows. a) over the span (case *swf1*) and b) over both span and chord (case *swf2*) for a swept-forward wing.

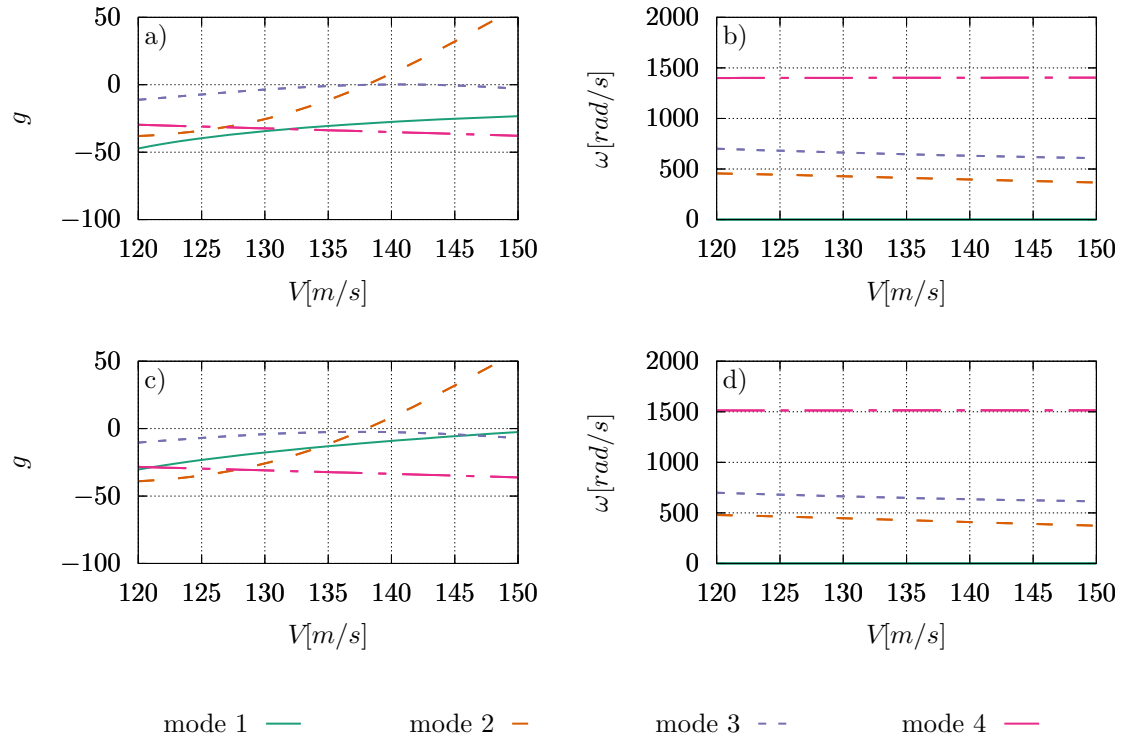

Figure B.8: Evolution of (a,c) aeroelastic damping and (b,d) aeroelastic frequency of the TS swept-forward wings with variations of Φ_1. (a,b) for case *swf1* and (c,d) for case *swf2*.

As for the aeroelastic damping and frequencies of the corresponding swept-forward cases B.8, the instability is again present on the second mode and the third mode is close to instability for both 1D and 2D cases. However, the first mode which corresponds to the divergence and was the unstable mode in the US case, is close to the axis zero and therefore the instability for the 2D configuration.

The mode shapes corresponding to instability are also presented in figure B.9. Both unstable modes are the second aeroelastic mode with a coupling between the second bending and the first torsion mode.

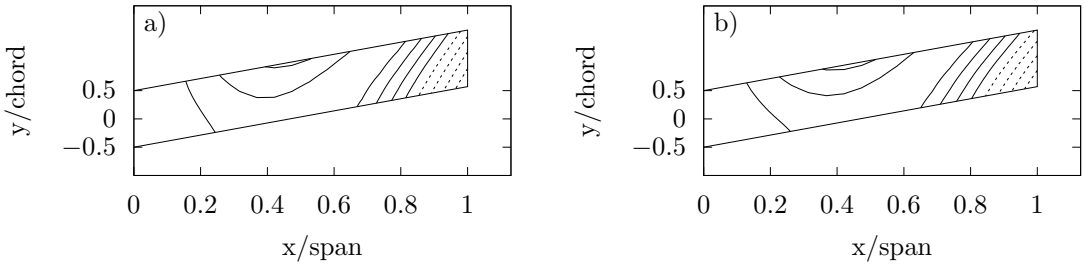

FIGURE B.9: Aeroelastic mode shapes of the TS swept-forward wings for variation of Φ_1. a) for case *swf1* and b) for case *swf2*.

The optimisation of the TS laminates by variation of the polar angle Φ_1 did not improve the aeroelastic behaviour of the considered structures. In an attempt to further maximise this velocity and study the influence of other parameters over the aeroelastic response of these laminates, other optimisation strategies are considered which will be explained in details in the next sections.

B.2 Optimisation over the angle-ply curve

As explained in chapter 4 the high number of optimal US laminates on the angle-ply curve influence the choice of this strategy. The optimisation variables are thus 6 or 24 values of R_1 over the control points. As the optimisation is restrained to the angle-ply curve, the values of R_K can be obtained analytically from R_1 using the relationship expressed in euqation (4.12). It needs to be pointed out that for cases presented here during this optimisation strategy, the polar angle is fixed and aligned to the reference axis of the wing.

Similarly to the previous strategy three geometries have been studied with both 1D and 2D variation of the laminate properties. Table B.2 presents these cases with the orthotropic axis aligned to the principle axis. For the straight 1D case, the flutter velocity is increased beyond any values

Case ID	Wing configuration	$R_K[GPa]$	$R_1[GPa]$	$\Phi_1[^\circ]$	$\alpha_{swept}[^\circ]$	$V_f[m/s]$	$\omega_f[rad/s]$
st1	straight (1D)	variable	variable	**0.**	**0.**	151.8	499.5
st2	straight (2D)	variable	variable	**0.**	**0.**	152.2	468.2
swb1	swept-backward (1D)	variable	variable	**-15.**	**-15.**	132.6	440.1
swb2	swept-backward (2D)	variable	variable	**-15.**	**-15.**	135.5	448.6
swf1	swept-forward (1D)	variable	variable	**15.**	**15.**	95.0	0.
swf2	swept-forward (2D)	variable	variable	**15.**	**15.**	108.7	0.

Table B.2: Deterministic optimisation results of the Tow-Steered configurations obtained by variation of anisotropic moduli (R_K and R_1) over the angle-ply curve throughout the structure, with red bold coloured variables indicating constant parameters during the study.

obtained previously for the straight wing and has a 4% gain compared to the US configuration. The 2D optimisation does not have a remarkable influence on the value of the flutter velocity as seen in the last strategy. The flutter frequencies for both 1D and 2D cases remain in close intervals but as the speed increases for the 2D configuration, its flutter frequency decreases.

Figure B.10 represents the variation of these moduli over the structure. The colour map demonstrates the value of each variable. As explained before in section 2.2, the stacking sequence of a set of polar parameters over the angle-ply curve can be calculated analytically using equation (2.56). As this sequence is only the variation of the sign of one angle ($\pm\alpha$) thus the orientation of this value can be presented on the figures. The arrows over each node represent this value that can be then used to build the corresponding stacking sequence. In the 1D case, the variations of both moduli and the sequence angle, stay limited to a small interval, except for both tip and the root of the wing. The drastic difference in the values of the borders to the mid section of the structure, creates a curved pattern of the tow-angle throughout the ply that differs from the US configurations. The effect of the wing tip and root disappears for the 2D case and the values of the anisotropic moduli remain limited and the path that the fibres follow, is less exaggerated than the 1D case.

In case of a 1D variation, the evolution of aeroelastic damping and frequency demonstrated in figure B.11, follows the same behaviour as the previous cases with the second mode that becomes unstable and the third mode close to instability. In case of a 2D variation, the instabilities take place over the second mode and the third mode remains close to the zero axis but the first mode which corresponds to static instabilities, approaches the zero axis and becomes unstable immediately after the second mode.

The isolines of the unstable modes are presented in figure B.12 which again displays a combination

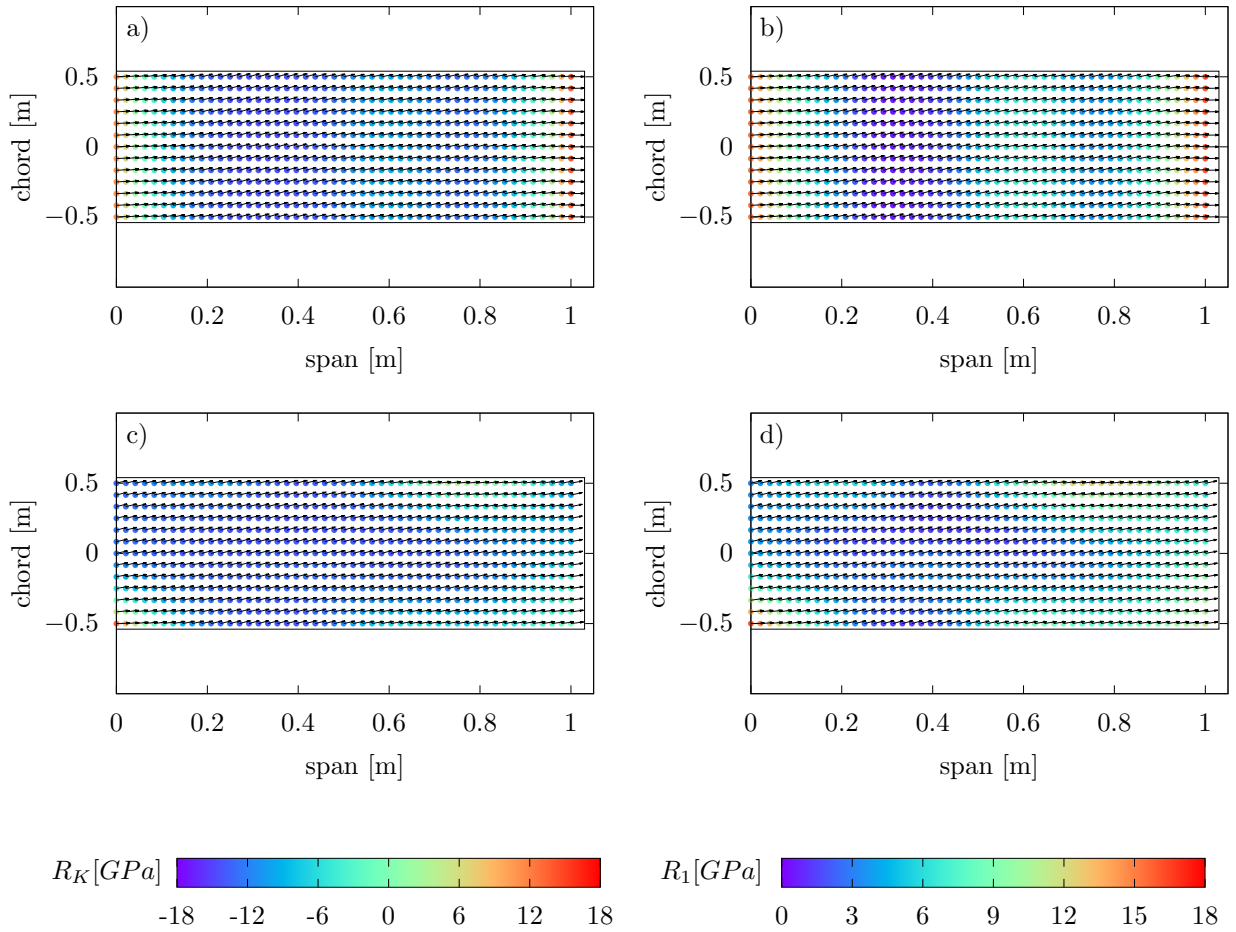

FIGURE B.10: Variation of R_K, R_1 and the orientation of ply angle presented by the colour map and the arrows. (a,b) over the span (case *st1*) and (c,d) over both span and chord (case *st2*) for a straight wing.

of the second bending and first torsion modes. This time the difference in amplitude of each mode is more significant.

For the swept-backward wing with an aligned orthotropic axis to the reference axis of the wing, the flutter velocity does not increase compared to the previous strategy for neither the 1D nor the 2D case as presented in table 4.1. On the other hand, for the 1D variation, the velocity is increased by 1% with respect to the US case with an aligned orthotropic and the reference axis. It needs to be noted that the 2D variation demonstrates a slight increase of the flutter velocity compared to the 1D case and even a further augmentation of 3% compared to the US case. It is therefore advantageous to consider the 2D variation of anisotropic moduli in this strategy unlike the previous optimisation problem. Unlike the straight configurations, the increase in the velocity of the 2D case results in a

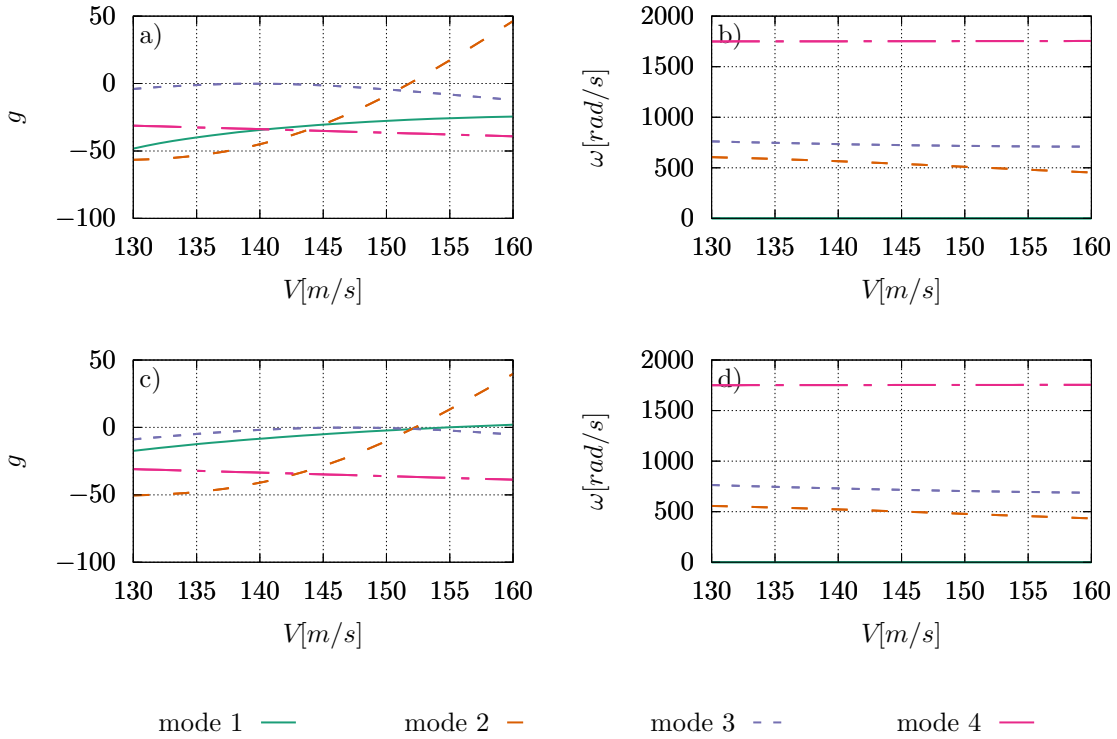

Figure B.11: Evolution of (a,c) aeroelastic damping and (b,d) aeroelastic frequency of the TS straight wings with variations of R_K R_1 over the angle-ply curve. (a,b) for case *st1* and (c,d) for case *st2*.

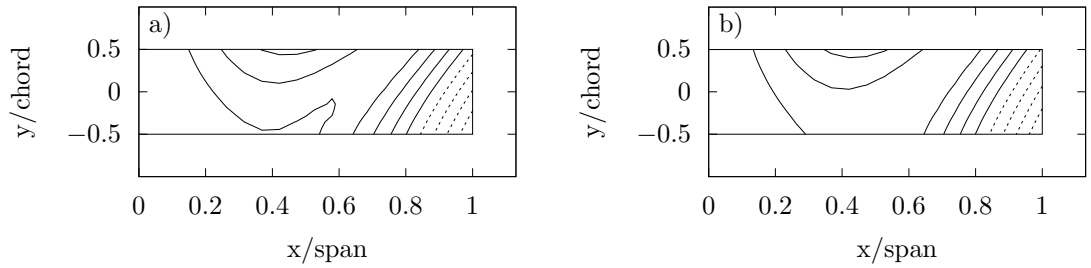

Figure B.12: Aeroelastic mode shapes of the TS straight wings for variation of R_K R_1 over the angle-ply curve. a) for case *st1* and b) for *st2*.

higher flutter frequency.

Figure B.14 represents variation in anisotropic moduli and the ply angles on the swept-backward wing with the orthotropic and the principle axis aligned. For the 1D case, the values of R_K and R_1

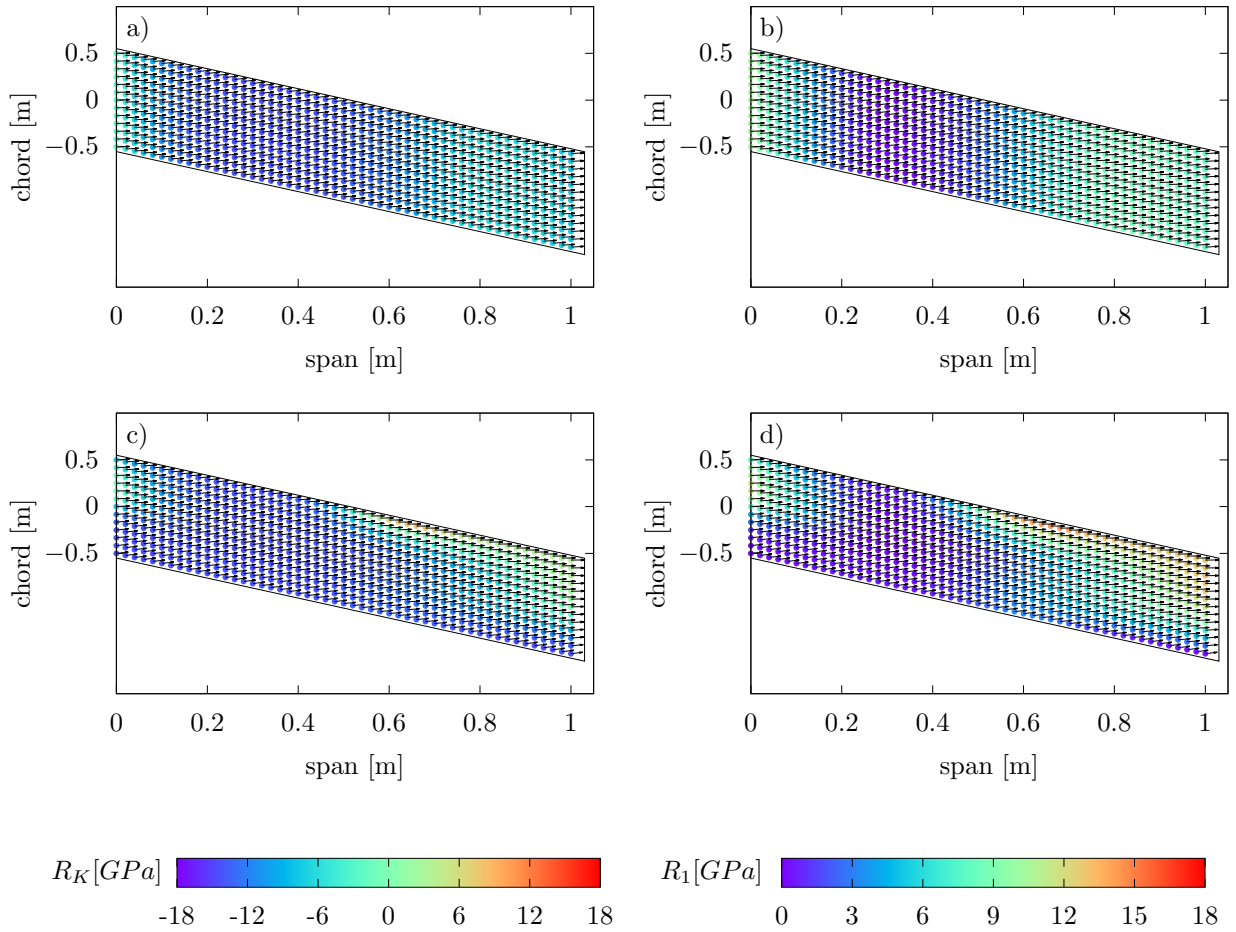

FIGURE B.13: Variation of R_K, R_1 and the orientation of ply angle presented by the colour map and the arrows. (a,b) over the span (case *swb1*) and (c,d) over both span and chord (case *swb2*) for a swept-backward wing.

are limited limited to a small zone over the ply-angle curve. This behaviour gives place to small variations of the tow-angles throughout the structure. For the case with a 2D variation, a more noticeable deviation is observed, this time mostly over the higher boundaries of the wing which gives place to a noticeable curve in the path of the fibres.

The aeroelastic damping and frequency of the both these configurations are presented in figure B.14. Comparable behaviours are observed concerning the unstable modes to the previous configurations. The instability occurs on the second mode for both 1D and 2D variations but the third mode is not as close to instability as the previous cases. The evolution of modes in damping and frequency are very close to the US case which can be explained by the small variations of the anisotropic moduli.

The representation of the second aeroelastic mode in figure B.15 confirms the coupling of the second bending and the first torsion modes.

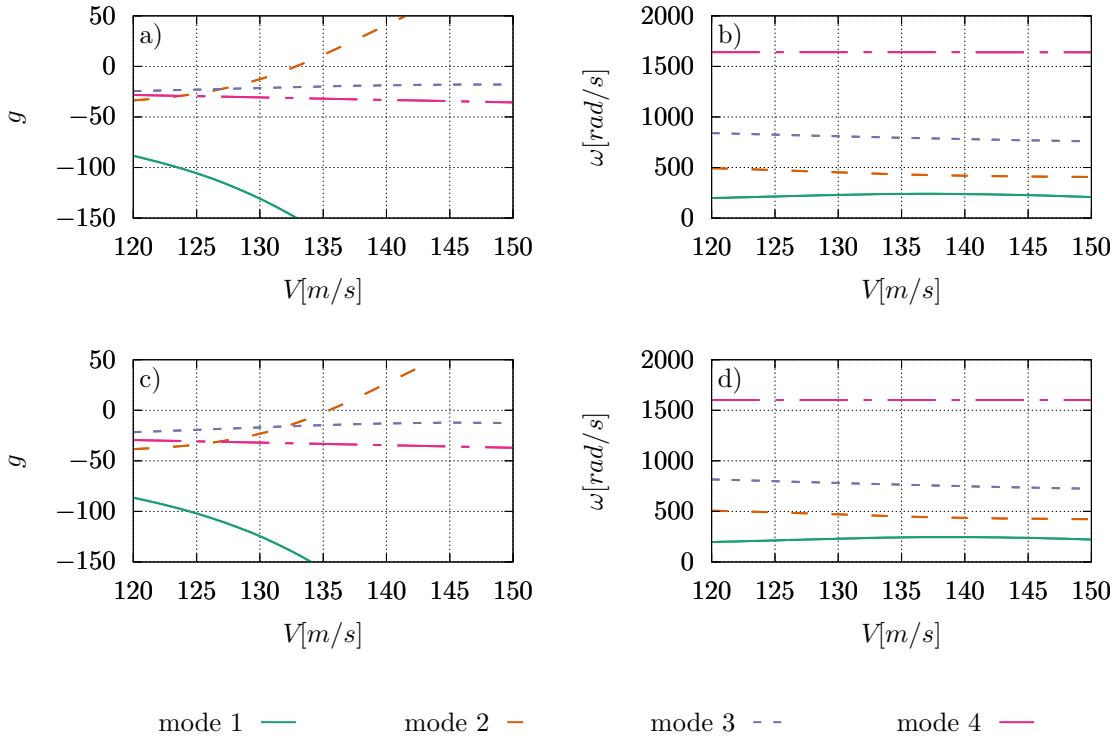

Figure B.14: Evolution of (a,c) aeroelastic damping and (b,d) aeroelastic frequency of the TS swept-backward wings with variations of R_K R_1 over the angle-ply curve. (a,b) for case *swb1* and (c,d) for case *swb2*.

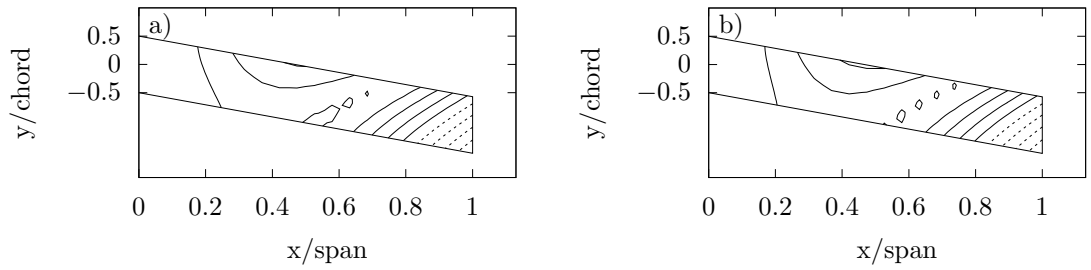

Figure B.15: Aeroelastic mode shapes of the TS swept-backward wings for variation of R_K R_1 over the angle-ply curve. a) for case *swb1* and b) for *swb2*.

In the same manner, for the swept-forward wing with the aligned orthotropic and principle axis,

no increase is indicated comparing to the previous strategy in table 4.1. A slight augmentation of 3% is observed in the flutter velocity of the 1D case with respect to the US configuration but even a more important increase of 16% in the 2D configuration. Both flutter frequencies are zero which indicates a divergence instability.

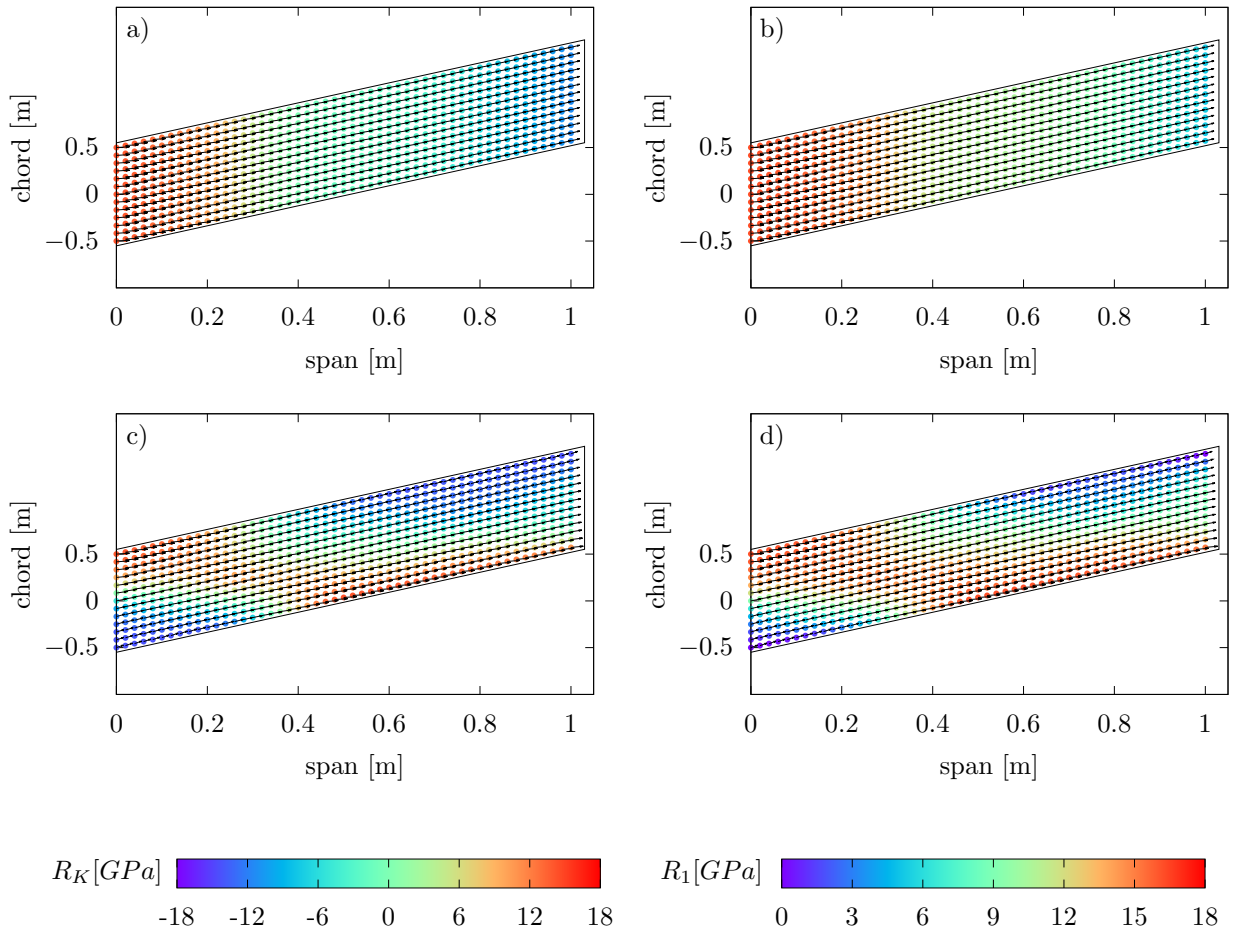

FIGURE B.16: Variation of R_K, R_1 and the orientation of ply angle presented by the colour map and the arrows. (a,b) over the span (case *swf1*) and (c,d) over both span and chord (case *swf2*) for a swept-forward wing.

Contrary to the previous cases, the swept-forward configurations, have a significant variation throughout the structure, for both 1D and 2D cases presented in figure B.16. These variation translate into more complicated patterns of the fibres. Unlike other configurations, the swept-forward wing does not have significant changes only over the boundaries and has a more dispersed variation throughout the structure.

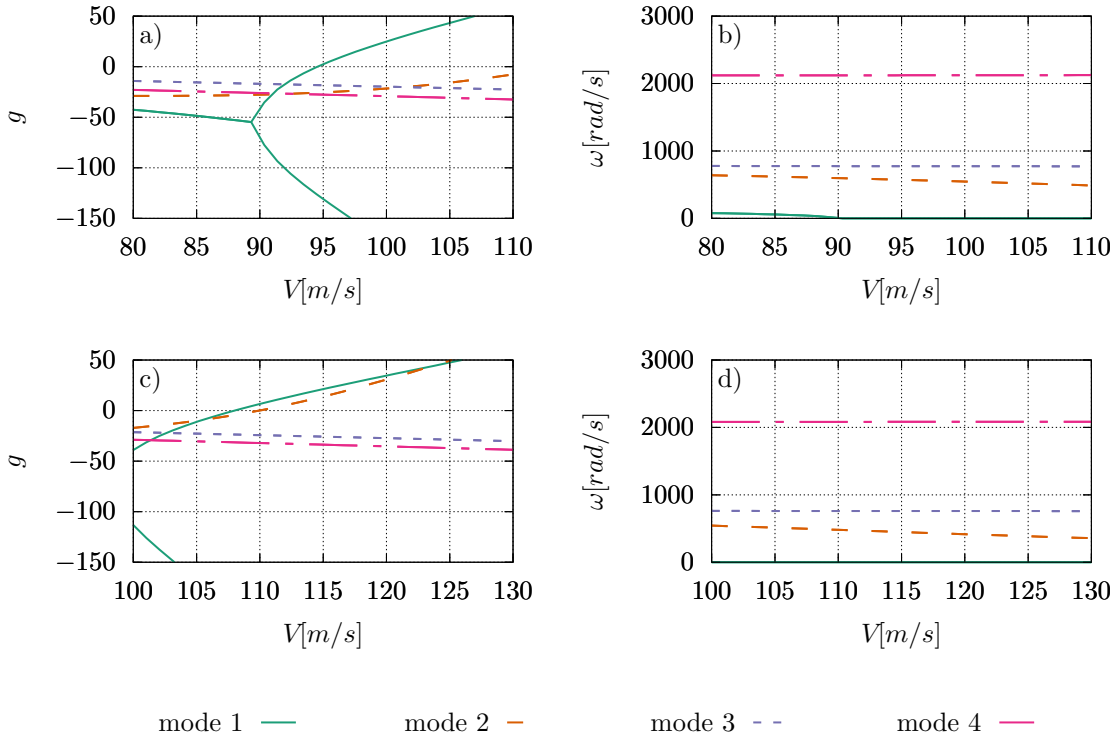

Figure B.17: Evolution of (a,c) aeroelastic damping and (b,d) aeroelastic frequency of the TS swept-forward wings with variations of R_K R_1 over the angle-ply curve. (a,b) for case *swf1* and (c,d) for case *swf2*.

The optimal configurations obtained for the swept-forward wings with $\Phi_1 = 0$, demonstrate a rather different aeroelastic behaviour in comparison to other geometries. The 1D variation of anisotropic moduli over the angle-ply curve results in a divergence, while the second mode becomes unstable in higher velocities. The 2D configuration, keeps the divergence instability but this time the second mode shows instabilities right after the first mode. Both divergence modes are presented in figure B.18 which correspond to the first natural bending mode.

While some improvements have been observed during this optimisation strategy, the question on the impact of the other orthotropic symmetries on the aeroelastic behaviour of the TS laminates, is still present. For this purpose the next strategy is formulated to further explore this domain for the three chosen geometries.

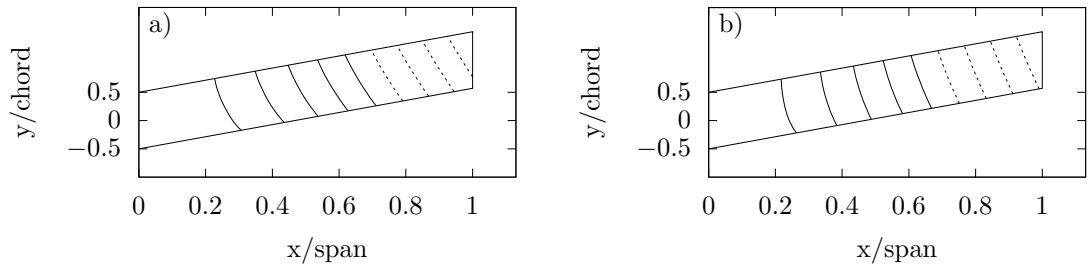

FIGURE B.18: Aeroelastic mode shapes of the TS swept-forward wings for variation of R_K R_1 over the angle-ply curve. a) for case *swf1* and b) for *swf2*.

B.3 Optimisation inside the orthotropic domain

In this section, the optimisation of the TS laminates is defined in the entire orthotropic domain, using the anisotropic moduli. The difference between this strategy and the one defined in the previous section is the domain of investigation. In the previous optimisation problem the anisotropic moduli were dependent on one another as the domain was limited to the angle-ply curve. In this strategy, both moduli can vary independently inside the orthotropic domain and do not have any dependencies on each other. The optimisation variables are therefore R_K and R_1 which gives place to 12 or 48 parameters (2 variables per control point).

Case ID	Wing configuration	$R_K[GPa]$	$R_1[GPa]$	$\Phi_1[°]$	$\alpha_{swept}[°]$	$V_f[m/s]$	$\omega_f[rad/s]$
st1	straight (1D)	variable	variable	**0.**	**0.**	146.9	502.7
st2	straight (2D)	variable	variable	**0.**	**0.**	139.0	496.5
swb1	swept-backward (1D)	variable	variable	**-15.**	**-15.**	132.1	444.0
swb2	swept-backward (2D)	variable	variable	**-15.**	**-15.**	129.4	467.5
swf1	swept-forward (1D)	variable	variable	**15.**	**15.**	94.5	0.
swf2	swept-forward (2D)	variable	variable	**15.**	**15.**	106.0	0.

TABLE B.3: Deterministic optimisation results of the Tow-Steered configurations obtained by variation of anisotropic moduli (R_K and R_1) inside the orthotropic domain throughout the structure, with red bold coloured variables indicating constant parameters during the study..

Table B.3 presents all the results obtained with this strategy. The orthotropic axis in considered aligned with the main axis of the wing unless it is mentioned as an optimisation variable. Each geometry is subject to 1D or 2D variations of the tow-angles and all the results will be compared to the previous cases obtained in other TS strategies or the US laminates.

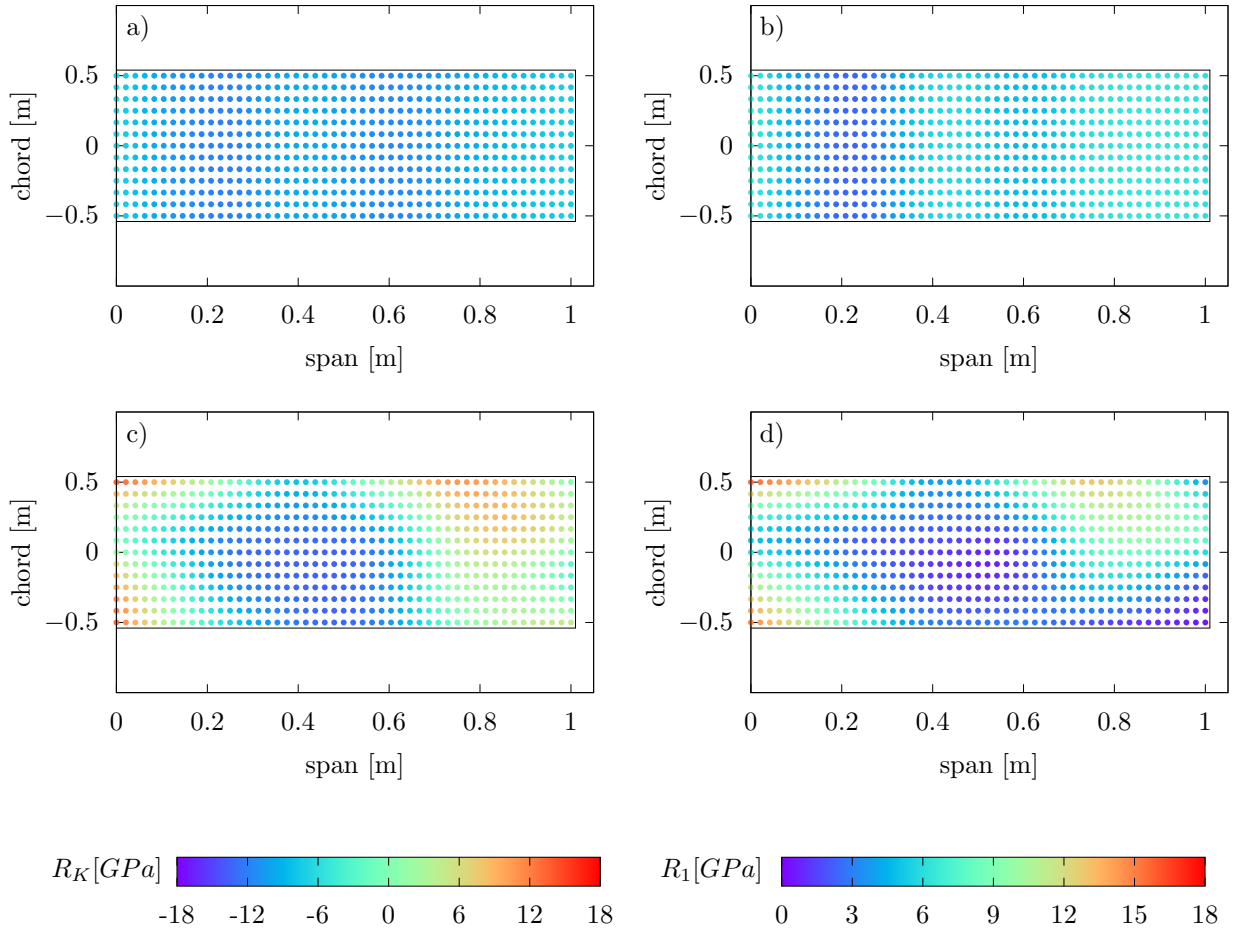

Figure B.19: Variation of R_K and R_1 presented by the colour map. (a,b) over the span (case *st1*) and (c,d) over both span and chord (*st2*) for a straight wing.

The optimisation study is first applied to a straight wing. The anisotropic moduli are chosen in the entire orthotropic domain but the maximum flutter velocity, corresponding to the 1D case, fails to surpass the previous TS results and can only rise as high as the US case. The 2D optimisation indicates a lower value of the flutter velocity. As mentioned for the first TS strategy using the polar parameters, the 2D variation has more difficulty to converge to a maximum V_f due to the large number of variables and possibilities. The flutter frequencies of both cases remain close to each other and previous cases.

Figure B.19 represents the variations of the anisotropic moduli over the studied structure. In this strategy the arrows corresponding to the orientation of the layers are not present. The reason is that

the orientations can no longer be analytically calculated for all the nodes and each layer has therefore a different direction which is not possible to present with only one value. The colormap on this figure indicates nearly uniform values for R_K and R_1. The variation for both moduli is limited to a given zone which has similar values to the optimal case of the US configuration. The 1D case has therefore converged toward a US optimal configuration. Concerning the 2D case, both moduli vary in large zones and take the values in the extremities of their domain of definition. This behaviour can explain the lower value of the flutter velocity for this configuration.

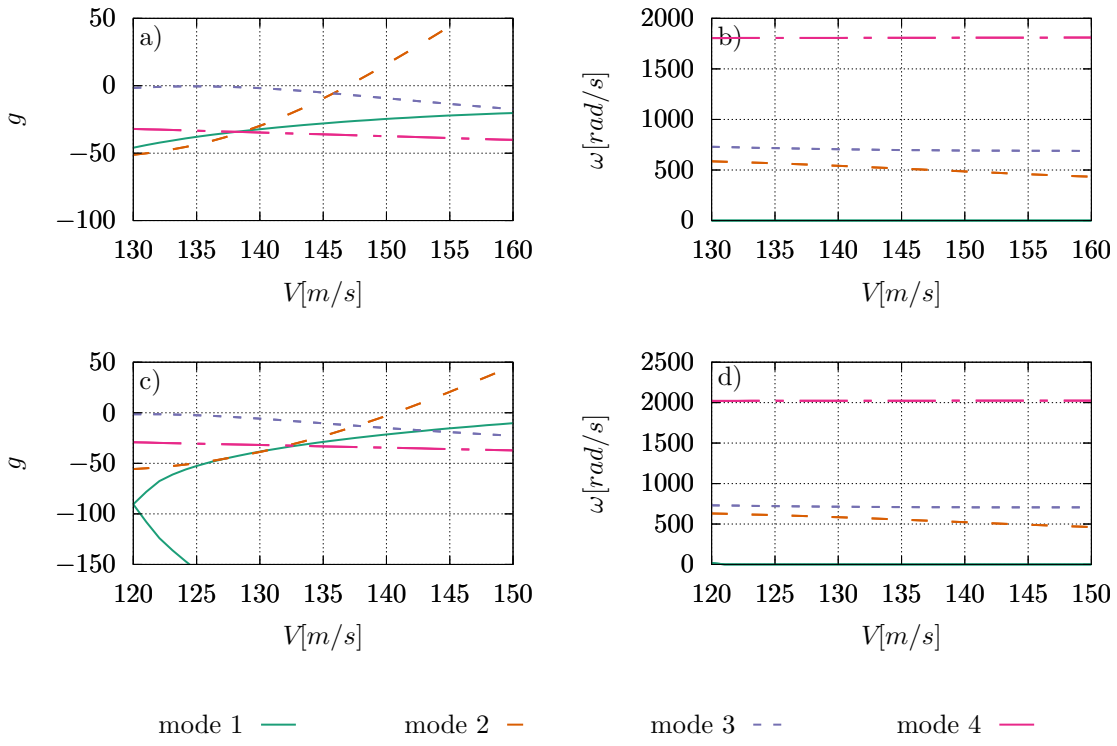

FIGURE B.20: Evolution of (a,c) aeroelastic damping and (b,d) aeroelastic frequency of the TS straight wings with variations of R_K R_1 in the orthotropic domain. (a,b) for case *st1* and (c,d) for case *st2*.

The aeroelastic damping and frequency presented in figure B.20 have similarities to the previous optimal cases obtained with different strategies. The 1D case has instabilities over the second mode and the third mode which is close to the axis zero. In this case, the divergence mode, approaches instabilities more than previous 1D cases. In the 2D configuration, this behaviour is further exaggerated with the first mode closer to instability in velocities near V_f. The mode shapes presented in figure B.21 demonstrate the unstable modes for both 1D and 2D straight optimal configurations. They both have similar shapes with a combination of the second bending and first torsion modes but a difference

in amplitude is observed.

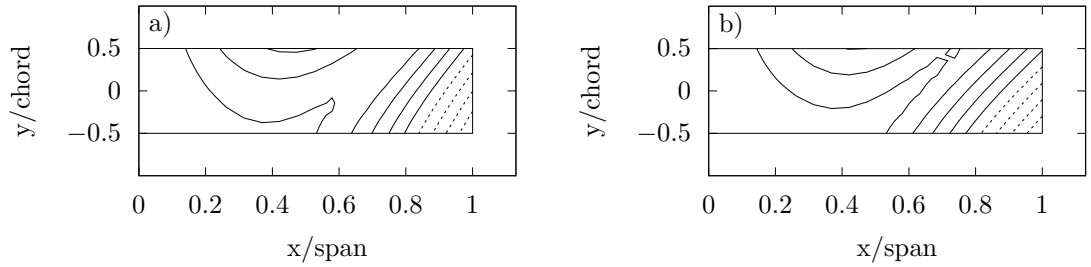

Figure B.21: Aeroelastic mode shapes of the TS straight wings for variation of R_K R_1 in the orthotropic domain. a) for case *st1* and b) for *st2*.

The swept-backward wing has been subject to the same optimisation studies with both 1D and 2D variations. The results of this study are presented in table B.3 .The values have again not exceeded any of the results in the previous strategies. Compared to the US case a small augmentation of 1% is observed. This time the 2D variation has closer values to the flutter velocity of the 1D case similar to what had been obtained in the US optimisation. The flutter frequencies indicate similar unstable modes between the two cases.

Figure B.22 represents the variation of the anisotropic moduli over each finite element node using a colour map. As observed in the previous case, the variations of both moduli are limited to a small interval for the 1D case. These values vary around the optimal US moduli of the swept-backward wing with an aligned orthotropic and reference axis. The 2D case presents wider range of variations but they have not contributed to the optimisation of the aeroelastic response of the structure but have only complicated the process of construction.

The aeroelastic response of the structure is presented in figure B.23. The instability occurs once again over the second mode. Other aeroelastic modes are not close to instability in the same manner as the previous cases. The 2D case shows similar behaviours as the 1D configuration over smaller velocities and can thus be concluded that it was not able to converge to the optimal configuration in the domain of investigation. the mode shapes of both configurations are presented in figure B.24. They both represent the second aeroelastic mode similarly to other cases demonstrated for previous strategies.

The swept-forward wing is the next geometry for which the TS laminates are optimised in the

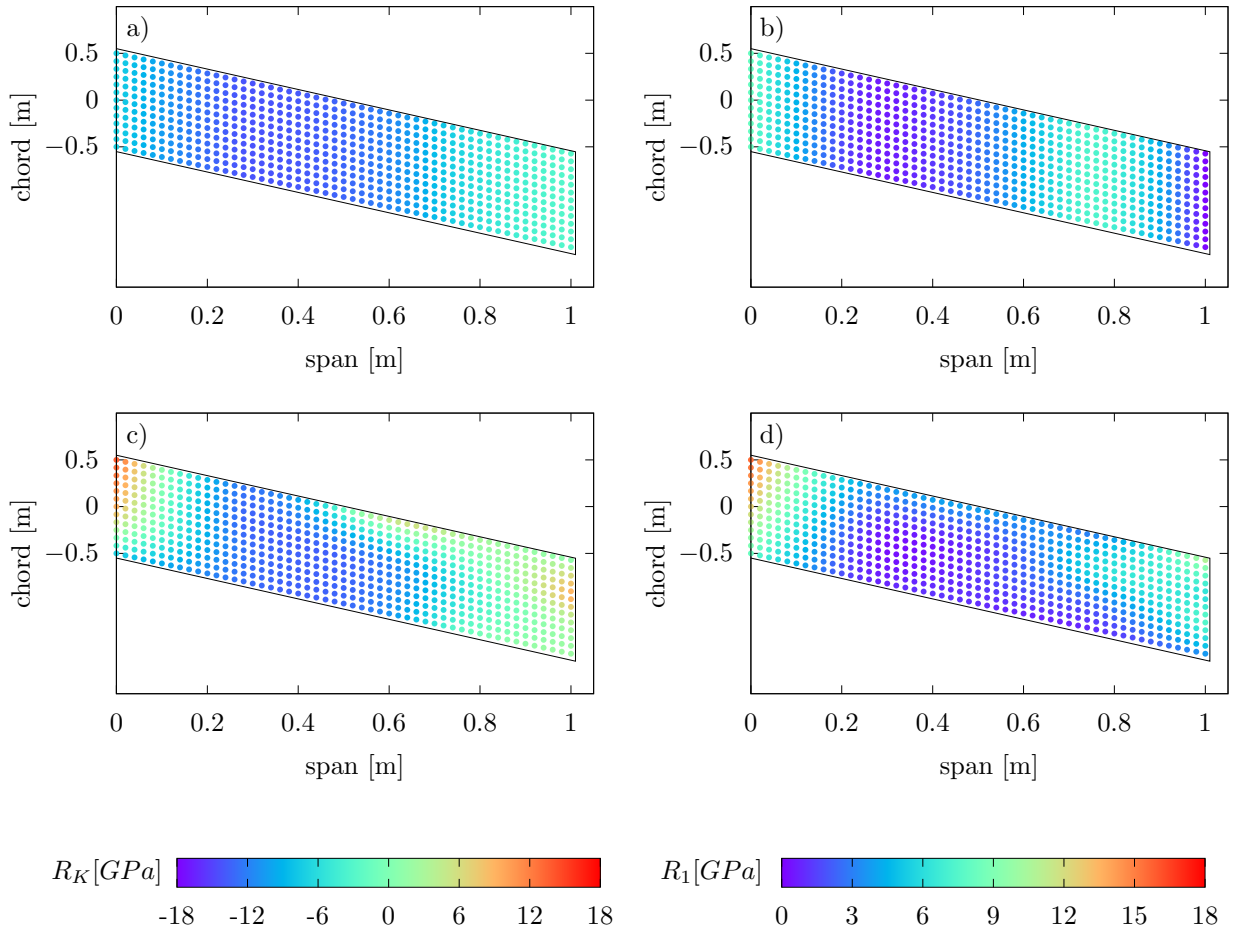

FIGURE B.22: Variation of R_K and R_1 presented by the colour map. (a,b) over the span (case *swb1*) and (c,d) over both span and chord (*swb2*) for a swept-backward wing.

orthotropic domain. The results of both 1D and 2D optimisations are similar to the cases obtained in the previous strategy. They do not increase compared to the TS laminate obtained with variation of the polar angle Φ_1. On the other hand some augmentation is observed compared to the US laminates with aligned orthotropic and reference axis. It can be concluded that for this configuration the optimal values are position over the angle-ply curve. It is noteworthy that the swept-forward wing is the only case where the value of V_f is higher for the 2D case compared to the 1D case. For both configurations a steady mode becomes unstable which is suggests a divergence.

The variation of the anisotropic moduli are demonstrated in figure B.25. Unlike the previous geometries, for the 1D case, both moduli vary in the entire domain of study and take values from the smallest to the largest margin. The effect of the borders is again present here and drastically changes

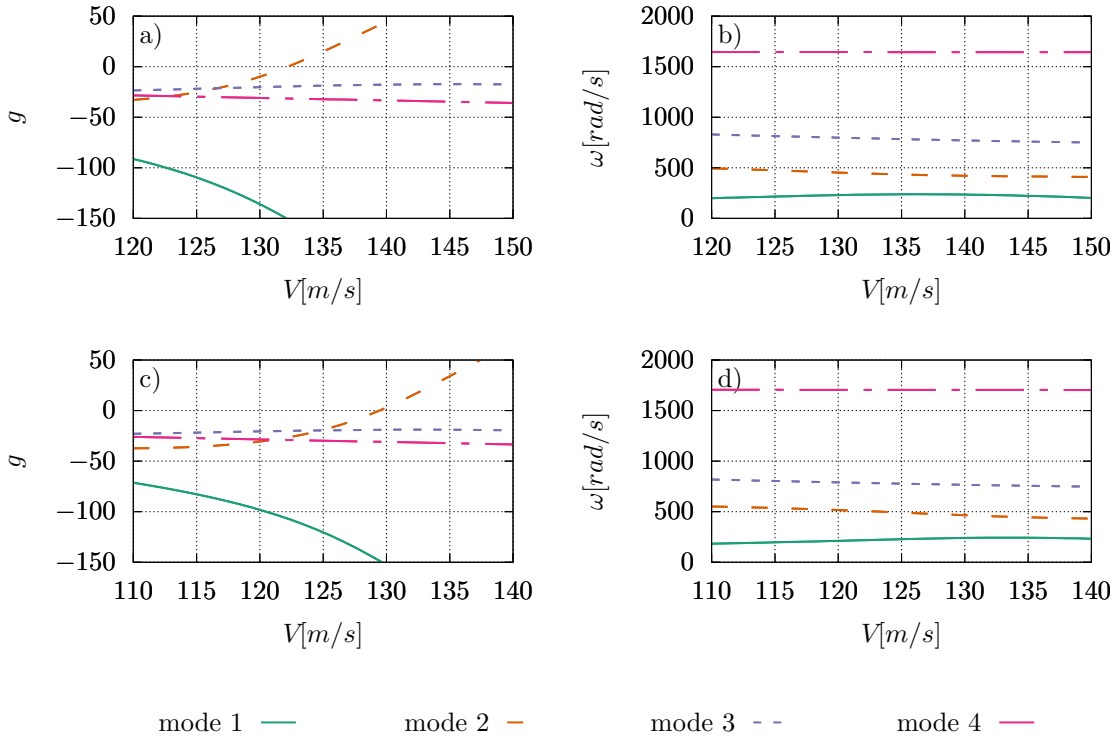

Figure B.23: Evolution of (a,c) aeroelastic damping and (b,d) aeroelastic frequency of the TS swept-backward wings with variations of R_K R_1 in the orthotropic domain. (a,b) for case *swb1* and (c,d) for case *swb2*.

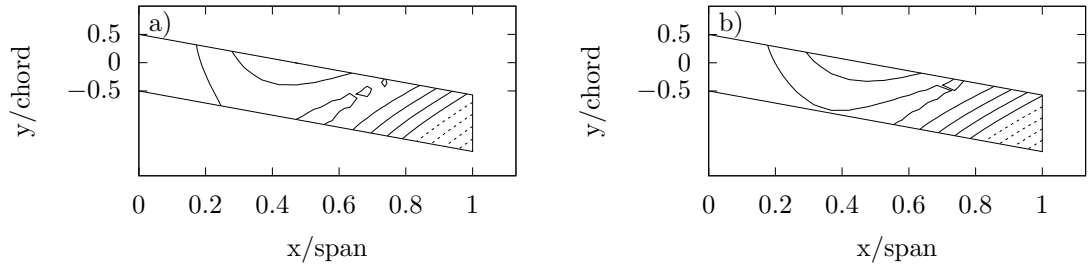

Figure B.24: Aeroelastic mode shapes of the TS swept-backward wings for variation of R_K R_1 in the orthotropic domain. a) for case *swb1* and b) for *swb2*.

the values towards the tip of the wing. The 2D case has also large variations of the anisotropic moduli but with more complicated patterns throughout the structure.

The aeroelastic response of the system is presented in figure B.26. For the 1D case the first mode

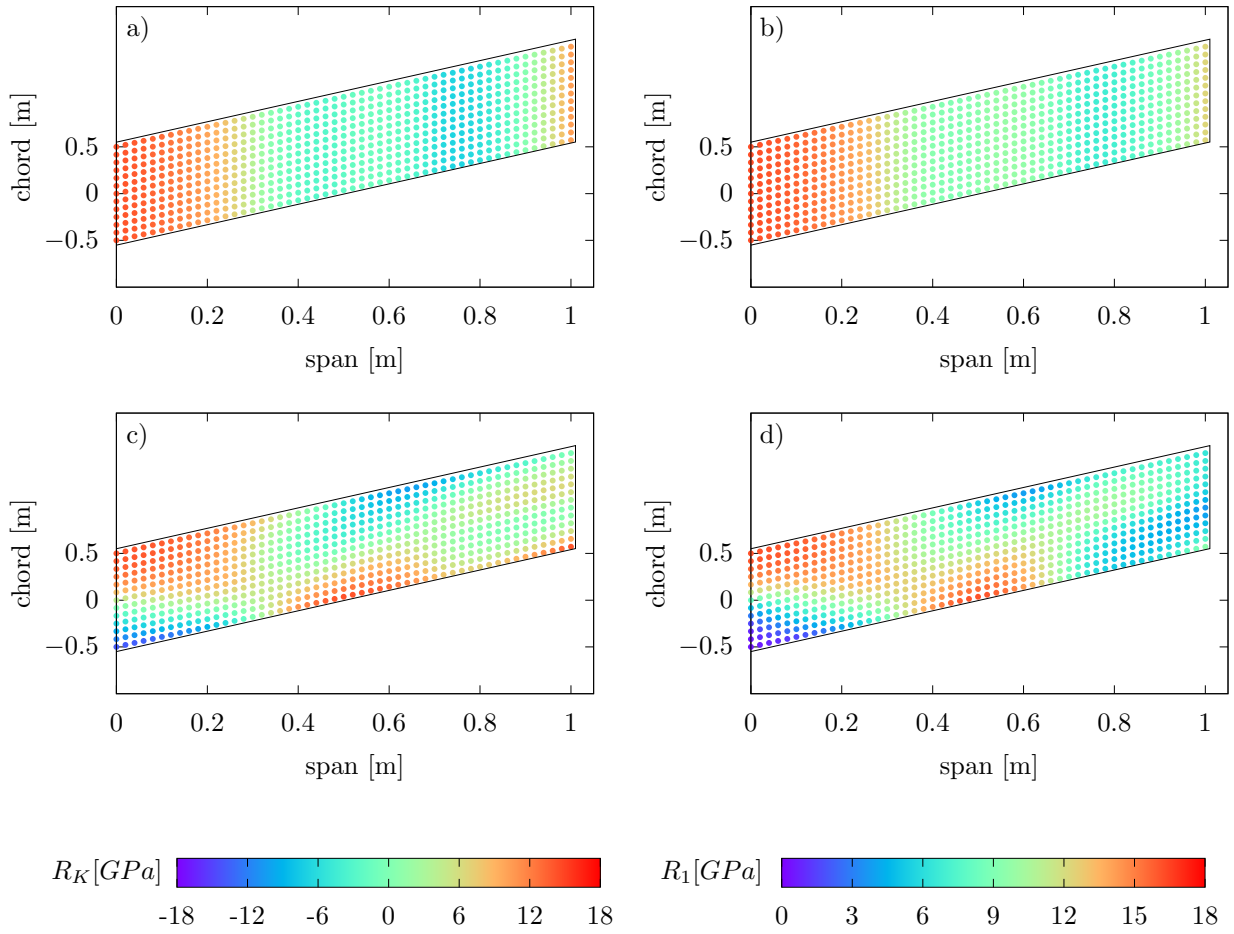

FIGURE B.25: Variation of R_K and R_1 presented by the colour map. (a,b) over the span (case *swf1*) and (c,d) over both span and chord (*swf2*) for a swept-forward wing.

which corresponds to divergence becomes unstable but the damping of the second mode increases with the speed and becomes unstable further on. For the 2D case, the divergence mode becomes unstable in higher velocities compared to the 1D case and the second mode becomes positive and thus unstable immediately after. The unstable modes for both cases are presented in figure B.27. They correspond to divergence which is due to instability of the first bending mode.

The optimisation inside the orthotropic domain was conducted for all three geometries. No improvement has been shown regarding the cases with aligned orthotropic and reference axis.

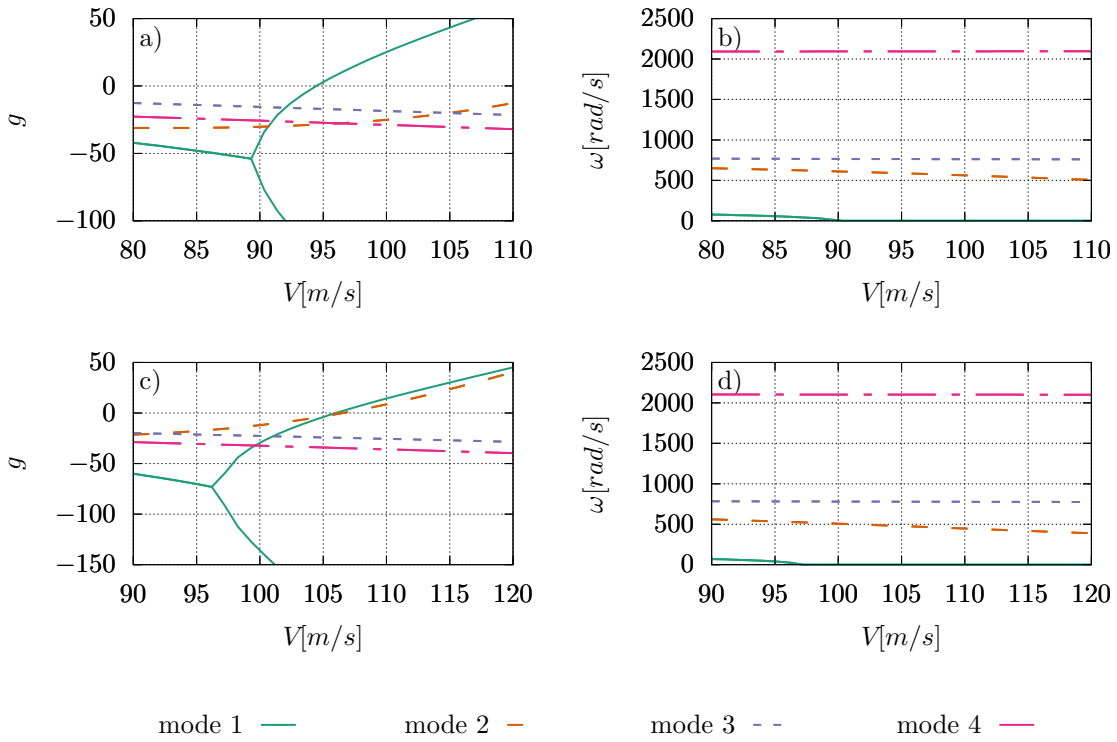

Figure B.26: Evolution of (a,c) aeroelastic damping and (b,d) aeroelastic frequency of the TS swept-forward wings with variations of R_K R_1 in the orthotropic domain. (a,b) for case *swf1* and (c,d) for case *swf2*.

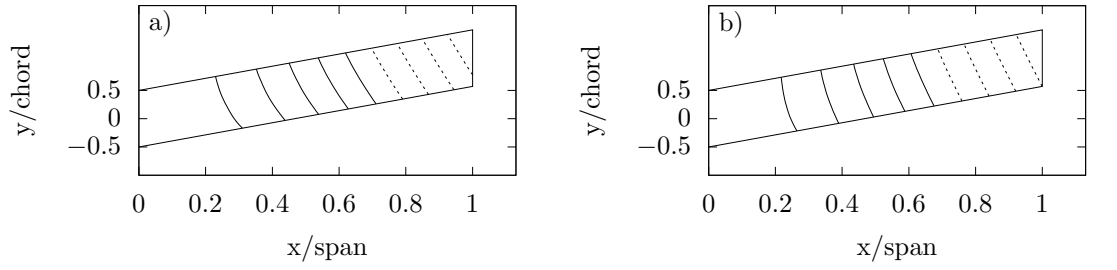

Figure B.27: Aeroelastic mode shapes of the TS swept-forward wings for variation of R_K R_1 in the orthotropic domain. a) for case *swf1* and b) for *swf2*.

C

Uncertainty Quantification: Complementary Results

For the optimal Tow-Steered cases presented in appendix B, the same stochastic analysis deployed in chapter 5 was conducted. As explained previously, three optimisation strategies based on variation of different polar parameters were considered for the optimisation of Tow-Steered laminates. Each strategy requires a different method of stacking sequence retrieval. The numerical and analytical methods explained in section 3.2 are employed over each finite-element node in the case of Variable Stiffness (VS) laminates

- **Variation of the polar angle :**
  The first optimisation strategy to construct a TS laminate uses Φ_1 to impose the variation of the stiffness throughout the structure. The anisotropic moduli are optimised in this case but kept constant over the entire structure. This is the most simple case of stacking sequence retrieval for a TS laminate, as R_K and R_1 are constant. Similarly to US configurations, these methods consist on first, positioning the optimal R_K and R_1 over the orthotropic domain and next, depending on the placement of the optimal case, an analytical or numerical approach can be employed to extract the corresponding stacking sequence. It needs to be noted that for this step, the value of the polar angle is fixed to $\Phi_1 = 0°$ and once the stacking sequence is obtained, the ply angles are rotated with respect to the value of Φ_1 over each finite-element node.

Figure C.1 presents the anisotropic moduli of all the optimal cases obtained by this strategy in the orthotropic domain. The first observation regarding the placement of the optimal cases indicates the proximity of the configurations to the border of the domain. The corresponding stacking sequences can thus be retrieved by analytical formulations if near the angle-ply curve or by limiting the numerical model to 0° and 90° values in the numerical model for cross-ply laminates.

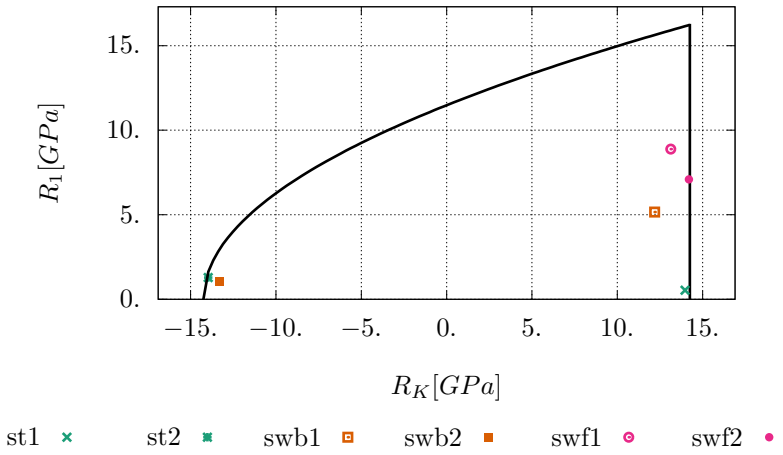

FIGURE C.1: Placement of the anisotropic moduli of Tow-Steered optimal cases obtained by variation of Φ_1 in the orthotropic domain.

Following this logic, the stacking sequences presented in table C.1 are retrieved, which will be rotated on each finite-element node with respect to the corresponding value of Φ_1. It needs to be noted that the sequences obtained analytically over the angle-ply curve are rounded to an integer due to manufacturing constraints.

Case ID	stacking sequence [°]	$R_K[GPa]$	$R_1[GPa]$	$V_f[m/s]$	$\omega_f[rad/s]$
st1	$[0, 90_2, 0, 90, 0_2, 90, 0, 90_2, 0_2, 90_2, 0]$	14.25 + ∼ 2%	0.38 − ∼< 1%	145.5 + ∼< 1%	414.1 − ∼< 1%
st2	$[42_2, -42_4, 42_2, -42_2, 42_4, -42_2]$	-13.94 − ∼< 1%	1.69 + ∼ 2%	137.6 − ∼< 1%	483.0 + ∼< 1%
swb1	$[0, 90, 0, 90, 0_4, 90, 0_3, 90_2, 0_2]$	14.24 + ∼ 14%	5.41 + ∼ 2%	138.3 − ∼< 1%	671.3 + ∼ 2%
swb2	$[40_2, -40_4, 40_2, -40_2, 40_4, -40_2]$	-13.39 + ∼< 1%	2.81 + ∼ 11%	132.9 − ∼ 1%	458.3 + ∼ 4%
swf1	$[0_2, 90, 0_3, 90, 0, 90, 0_5, 90, 0]$	14.25 + ∼ 8%	9.06 + ∼ 1%	138.9 + ∼< 1%	387.5 + ∼ 4%
swf2	$[90, 0_5, 90, 0, 90, 0, 90, 0_2, 90, 0_2]$	14.25 + ∼< 1%	7.13 + ∼< 1%	137.9 + ∼< 1%	416.2 + ∼< 1%

TABLE C.1: Stacking sequence retrieval results for optimal TS configurations obtained with variable Φ_1.

- **Variation of the anisotropic moduli over the angle-ply curve :**
  The second strategy is based on variation of R_K and R_1 over the structure and within the limits of the angle-ply curve. The stacking sequences over each finite element node are thus calculated using analytical formulations presented in section 5.2.1.

- **Variation of the anisotropic moduli inside the orthotropic domain :**
  Finally, the third strategy which employs both anisotropic moduli but this time, the variations are inside the entire orthotropic domain. The stacking sequence retrieval for this case is computationally expensive and the final result might cause challenges during the manufacturing process.

Using the retrieved stacking sequence and the Karhunen-Loève expansion explained in section 5.2.2, the stochastic analysis of the optimal Tow-Steered laminates is carried out.

C.1 Variation of the ply angle Φ_1

In this section the laminates obtained by variation of the polar angle throughout the structure are studied. Table C.2 summarises the optimal flutter velocity, mean and standard deviation corresponding to each case.

Case ID	Wing configuration	$V_f[m/s]$	$\mu_f[m/s]$	$\sigma_f[m/s]$
st1	straight (1D)	145.2	139.6	3.7
st2	straight (2D)	138.1	136.0	2.1
swb1	swept-backward (1D)	139.1	136.0	3.0
swb2	swept-backward (2D)	134.6	130.5	1.9
swf1	swept-forward (1D)	138.0	133.2	3.4
swf1	swept-forward (2D)	138.0	131.5	5.0

Table C.2: Stochastic properties of the optimal cases obtained with TS ply laminates while varying the polar angle.

The straight wing was subject to both 1D and 2D optimisation of Φ_1 and it was demonstrated that the flutter velocity for the 2D case cannot reach the optimal value obtained by the span-wise optimisation. As indicated in table C.2, the mean velocity of the 2D case remains lower than the 1D configuration but the difference between these two values is of 2% and smaller than the difference of the optimal V_f which is 5%. Moreover, the standard deviation corresponding to the 2D pdf is about 4% lower than the 1D case, making the former a more reliable configuration.

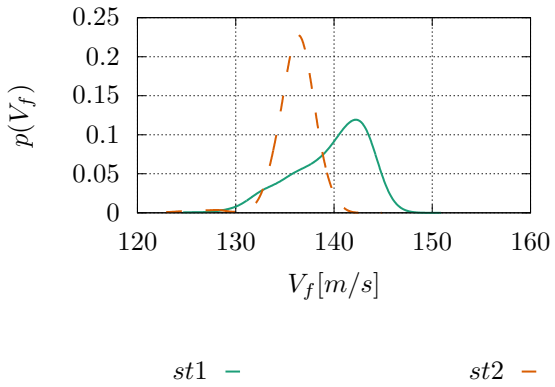

FIGURE C.2: Comparison of probability distribution function of flutter velocity corresponding to the optimal straight TS cases with 1D and 2D variations of Φ_1.

Figure C.2 compares the probability density function of both straight cases and confirms the observations made previously on the mean and the standard deviation values. The pdf of the 1D case has a large variance and while its mean value is higher than the 2D case, the probability that flutter velocities takes place at lower speeds remains significant. On the other hand, the pdf of the 2D case is much narrower with a high probability near the optimal V_f which becomes negligible at lower speeds.

Conducting the same analysis for the swept-backward wings, similar observations are made. The optimal and the mean flutter velocities of the 1D case are higher than the 2D configuration but this difference if of 3% for the optimal values and of 4% for the mean values. Furthermore, the standard deviation of the latter is about 40% smaller than the 1D case.

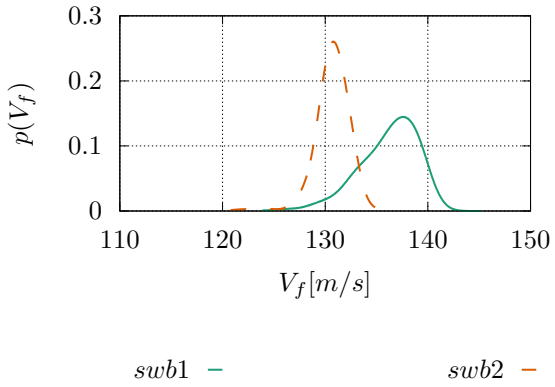

FIGURE C.3: Comparison of probability distribution function of flutter velocity corresponding to the optimal backward TS cases with 1D and 2D variations of Φ_1.

The pdfs of both these cases are compared in figure C.3. As a result of the higher variance of the

1D case, a wider pdf with lower probabilities on the optimal V_f is observed. This type of behaviour renders this configuration less reliable with a higher probability of flutter failure during the flight regime. On the other hand, the narrow pdf of the 2D case insures a high probability over the optimal velocity with a reliable safety margin to avoid instabilities during the flying conditions.

Unlike the previous cases, the swept-forward wing shows a different behaviour compared to the previous configurations. The optimal flutter velocities of both 1D and 2D cases are identical but the mean V_f of the latter is 1% lower than the former. Both cases have rather high standard deviations compared to other geometries which can indicate a wide probability density function. The standard deviation of the 1D case is 30% lower than the 2D case.

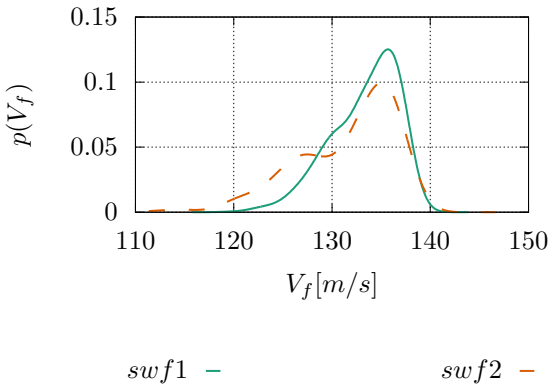

Figure C.4: Comparison of probability distribution function of flutter velocity corresponding to the optimal swept-forward TS cases with 1D and 2D variations of Φ_1.

Figure C.4 confirms the results presented in table C.2. These pdfs both demonstrate a bi-modal behaviour which has not been observed for other geometries in this optimisation strategy. On the other hand, the lower peak is closer to the optimal flutter velocity for the 1D case which explains the smaller variance of the latter. The second peak is more visible on the pdf of the 2D case with higher probabilities over the lower velocities.

Finally, the pdfs of the all optimal cases obtained with span-wise variation of Φ_1 are compared for different geometries. As observed in the optimisation results, the straight wing has the highest mean velocity but the swept-backward wing shows a narrower pdf with the smallest variance. This configuration can be identified as the best compromise between the aeroelastic performance and reliability amongst the 1D cases. On the other hand, referring to table C.2, the lowest standard deviation corresponds to the 2D swept-backward wing. The latter is only 1% lower than the standard deviation of the 2D straight wing while the mean flutter velocity of the straight case is about 4% higher. These

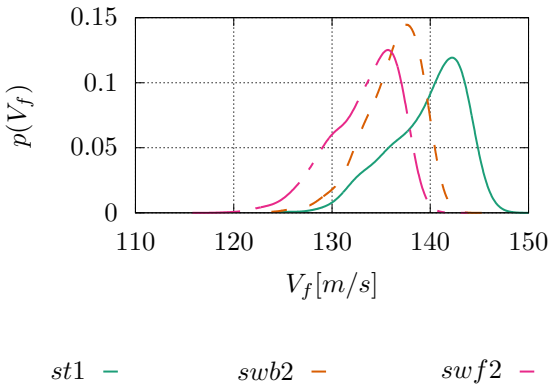

FIGURE C.5: Comparison of probability distribution function of flutter velocity corresponding to all optimal TS cases with 1D variation of Φ_1.

observations lead to the conclusion that the 2D straight wing is the most robust case but it needs to be noted that the variation of tow angles along both span and chord can make the construction of this case more difficult. It is thus necessary to take into account other parameters and uncertainties before finding the optimal laminate.

C.2 Variation of the anisotropic moduli over the angle-ply curve

Using similar methods and parameters as the previous case, the stochastic analysis for Tow-Steered laminates obtained by the variation of the anisotropic moduli over the angle-ply curve is conducted.

Case ID	Wing configuration	$V_f[m/s]$	$\mu_f[m/s]$	$\sigma_f[m/s]$
st1	straight (1D)	151.8	138.4	10.4
st2	straight (2D)	152.2	139.0	8.5
swb1	swept-backward (1D)	132.6	131.2	2.0
swb2	swept-backward (2D)	135.5	133.8	2.0
swf1	swept-forward (1D)	95.0	94.2	2.8
swf2	swept-forward (2D)	108.7	106.1	2.9

TABLE C.3: Stochastic properties of the optimal cases obtained with TS ply laminates while varying the anisotropic moduli over the angle-ply curve.

Both optimal straight wings with 1D and 2D tow angle variations, reach similar flutter velocities as well as the mean values of V_f but there is a difference of more than 8% between the optimal and mean values. On the other hand, while the standard deviation (std) of both cases are relatively large,

the std of the 2D case is about 2% smaller than the 1D configuration.

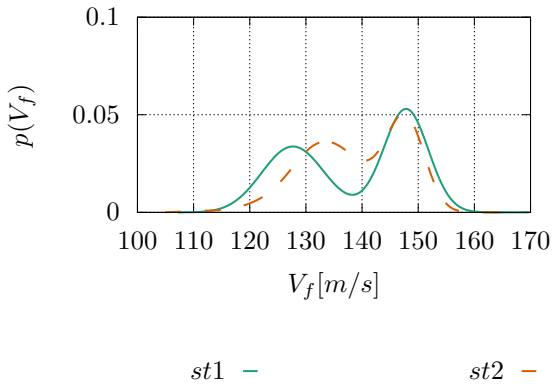

Figure C.6: Comparison of probability distribution function of flutter velocity corresponding to the optimal straight TS cases with 1D and 2D variations of R_K and R_1 over the angle-ply curve.

This difference translates directly on the pdfs of these laminates in figure C.6. Both cases possess a bi-modal pdf but for the 2D case, the smaller peak approaches the main peak around the optimal flutter velocity. In this case the probability over other velocities between the two peaks is higher than the 1D case. It cannot be said that the 2D configuration is a reliable case but the probability of having a flutter failure during the flying regime is reduced.

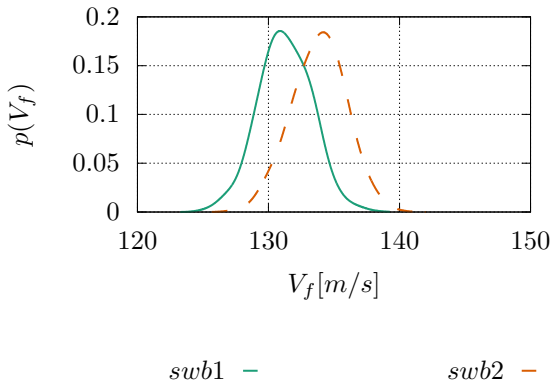

Figure C.7: Comparison of probability distribution function of flutter velocity corresponding to the optimal backward TS cases with 1D and 2D variations of R_K and R_1 over the angle-ply curve.

Concerning the swept-backward wing, an increase of 2% is observed in the optimal V_f as well as the mean flutter velocity for 2D variation of fibre paths. On the other hand, the standard deviation of both cases are identical. The latter observation on the mean and variance of the flutter velocity of swept-backward wings is also demonstrated in figure C.7 as the pdfs have approximately identical

shapes. Both cases have narrow shapes with high probability around the mean value, near the optimal velocity and thus can be considered as reliable structures.

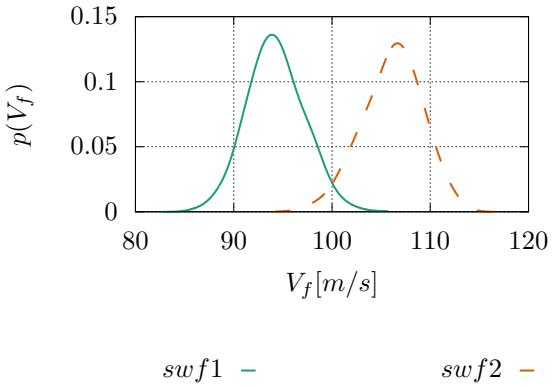

FIGURE C.8: Comparison of probability distribution function of flutter velocity corresponding to the optimal swept-forward TS cases with 1D and 2D variations of R_K and R_1 over the angle-ply curve.

Similarly to the previous strategy, the swept-forward wing has an increase of about 13% in V_f for the 2D configuration both in the optimal and mean flutter velocity. The standard deviation of both cases remain approximately identical and similar pdf shapes are expected as for the previous geometry. Figure C.8 compares the pdf of both 1D and 2D optimal cases. Narrow pdfs with high probabilities around the mean values are observed. Both cases are considered as reliable with respect to the deterministic results but the 2D case indicates a superior aeroelastic performance.

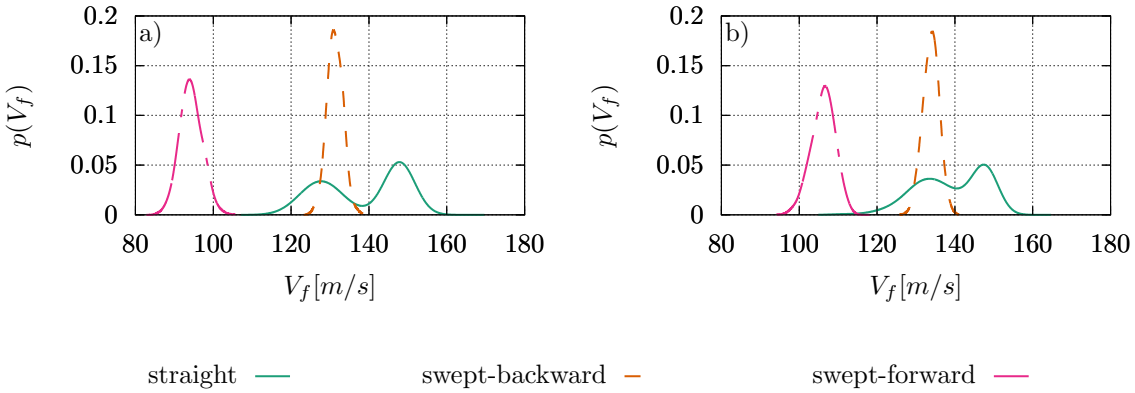

FIGURE C.9: Comparison of probability distribution function of flutter velocity corresponding to all optimal Tow-Steered cases with variation of R_K and R_1 over the angle-ply curve. a) for 1D cases and b) for 2D cases.

Figure C.9 compares the pdf of optimal configurations for all three geometries in case of 1D and 2D variations. The same conclusion can be extracted from both cases. The mean flutter velocity of

the straight case is higher than the swept wings but the latter has the highest standard deviation as it has a bi-modal pdf. The best compromise between all cases, can be the swept-backward wing as it has the lowest variance and a relatively high mean value of flutter velocity.

Taking into account all the cases studied in table C.3, the highest value of flutter velocity corresponds to the straight wings. Swept-backward configurations with aligned orthotropic and main axis have the lowest standard deviation. When optimising the polar angle, the mean flutter velocity of the swept-backward wing surpasses the mean V_f of the straight wings. The standard deviation of this case is higher than the two other swept-backward cases but remains lower than both straight wings. The robustness of this case in performance and reliability needs to be evaluated with respect to other parameters and fields of investigation.

C.3 Comparison between US and TS

The analysis conducted up to this point, concerned each case separately and within the strategy in which it was carried out. In order to evaluate the best strategy to optimise a given structure, the optimal deterministic value, the mean and the standard deviation of the flutter velocities amongst all optimisation methods are compared.

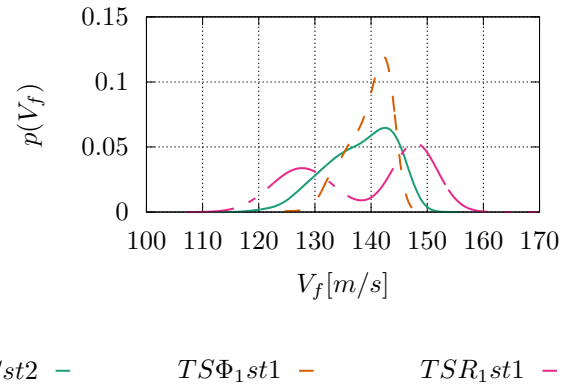

Figure C.10: Comparison of probability distribution function of flutter velocity corresponding to the US case, the TS case with 1D variation of Φ_1 and 1D variation of R_K and R_1 over the angle-ply curve for a straight wing.

Figure C.10 compares the pdfs of the US and the TS optimal cases obtained with two different strategies (variation of Φ_1 and variation of R_K and R_1 over the angle-ply curve) in span-wise direction. The highest deterministic optimal flutter velocity is achieved by variation of anisotropic moduli over the angle-ply curve. On the other hand, the highest mean flutter velocity corresponds to the TS laminate obtained by variation of the polar angle. The latter also owns the lowest variance compared

to the two other cases. While the differences in the optimal and the mean flutter velocity of the three cases does not exceed 10%, the optimal TS configuration obtained by variation of Φ_1 has a std that is more than 60% lower in comparison to the other TS case and about 30% lower than the US configuration. The low variance and a comparable mean value of flutter velocity makes this case the most reliable of the three configurations.

The same comparison is conducted amongst the 2D TS cases with the US configuration in figure C.11. This time, the optimal TS laminate obtained with the variation of the polar angle, has an optimal flutter velocity that is 9% lower than the case obtained with the variation of anisotropic moduli. The mean flutter velocity of the former is this time the lowest amongst the three but its standard variation is smaller than the other two cases and 60% lower than the 1D case. On the other hand, the 2D variations of the fibre path can make the realisation of this configuration harder and thus the compromise between reliability and manufacturing difficulties needs to be further assessed with other parameters for this case.

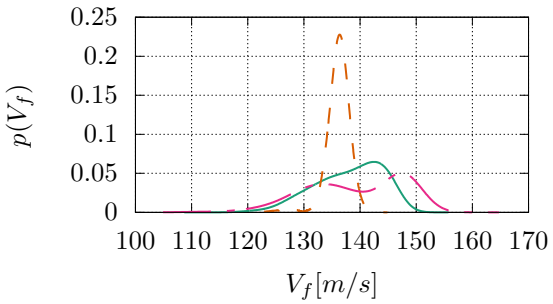

FIGURE C.11: Comparison of probability distribution function of flutter velocity corresponding to the US case, the TS case with 2D variation of Φ_1 and 2D variation of R_K and R_1 over the angle-ply curve for a straight wing.

Figure C.12 includes the pdfs of the US configuration and the two TS cases for a swept-backward wing. In this case, the pdfs of the US configuration and the TS laminate obtained by span-wise variation of Φ_1 are remarkably similar. The TS case obtained by variation of anisotropic moduli has a lower optimal and mean flutter velocity compared to these two cases but a slightly lower variance. It can be said that given the difficulties in the manufacturing of TS laminates, the US configuration can be the optimal case amongst the three.

Conducting the same analysis with the 2D variation of the TS cases. The US configuration has higher optimal and mean flutter velocity amongst all cases but its std remains the largest in comparison

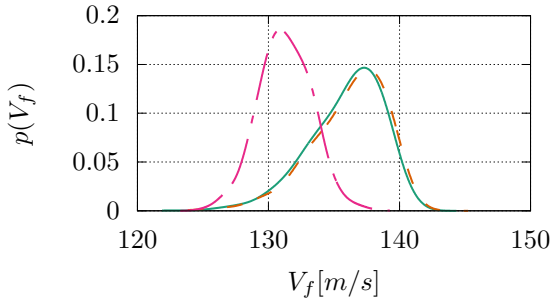

Figure C.12: Comparison of probability distribution function of flutter velocity corresponding to the US case, the TS case with 1D variation of Φ_1 and 1D variation of R_K and R_1 over the angle-ply curve for a swept-backward wing.

to the other two pdfs. As the 2D cases have lower optimal and mean values of flutter velocity compared to their analogous 1D configurations, it can be concluded that the US laminate remains the optimal case in comparison to the TS configurations.

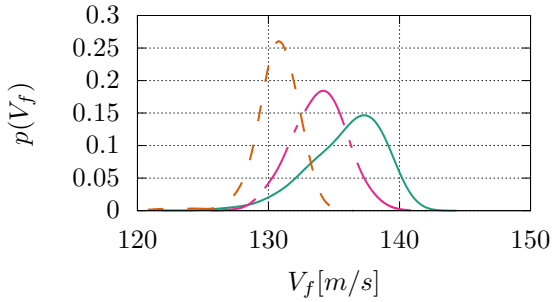

Figure C.13: Comparison of probability distribution function of flutter velocity corresponding to the US case, the TS case with 2D variation of Φ_1 and 2D variation of R_K and R_1 over the angle-ply curve for a swept-backward wing.

Concerning the swept-forward wing, the same analysis as other geometries is made. The comparison of the US case to the TS configuration obtained by span-wise variation of Φ_1 and 1D variation of R_K and R_1 respectively is made in figure C.14. The pdf of the TS case with variable anisotropic moduli is remarkably separated as its optimal and mean flutter velocity are about 30% lower than the two other cases. Between the US and the TS configuration obtained by variation of Φ_1, the optimal flutter velocities are less than 1% apart but the mean V_f of the TS case is 2% higher than the US case while its std is about 20% smaller. These properties render the TS configuration with variable polar angle a more robust case.

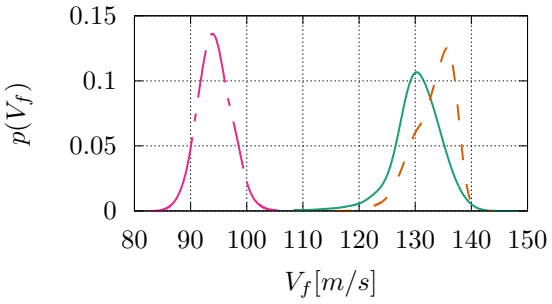

FIGURE C.14: Comparison of probability distribution function of flutter velocity corresponding to the US case, the TS case with 1D variation of Φ_1 and 1D variation of R_K and R_1 over the angle-ply curve for a swept-forward wing.

Similarly the pdfs for the TS laminates obtained by 2D variation of the polar parameters are presented in figure C.15. The case obtained by varying the anisotropic moduli over the angle-ply curve has a significantly lower flutter velocity once again. Comparing the two other cases, while the TS laminate with variable polar angle has a slightly higher optimal and mean flutter velocity in comparison to the US case, the std of the former is about 15% higher than the latter. It can thus be said that the US laminate is more robust amongst the three.

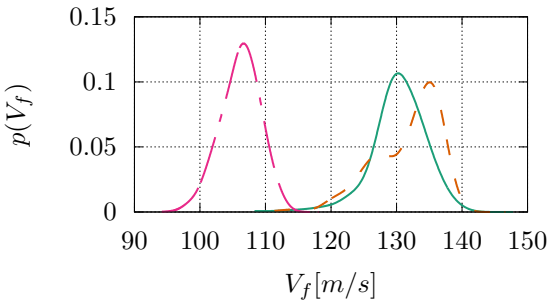

FIGURE C.15: Comparison of probability distribution function of flutter velocity corresponding to the US case, the TS case with 2D variation of Φ_1 and 2D variation of R_K and R_1 over the angle-ply curve for a swept-forward wing.

References

[1] D. H. Hodges and G. A. Pierce, *Introduction to structural dynamics and aeroelasticity*, vol. 15. cambridge university press, 2011. 1, 2, 3, 7

[2] A. R. Collar, "The expanding domain of aeroelasticity," *The Aeronautical Journal*, vol. 50, no. 428, pp. 613–636, 1946. vii, 1

[3] E. H. Dowell, R. Scanlan, F. Sisto, H. Curtiss Jr, and H. Saunders, "A modern course in aeroelasticity," 1981. 2, 21

[4] J. R. Wright and J. E. Cooper, *Introduction to aircraft aeroelasticity and loads*. Chichester: Wiley, 2. ed ed., 2015. 2, 3, 4, 22

[5] H. Zhan and T. Fang, "Flutter stability studies of great belt east bridge and tacoma narrows bridge by cfd numerical simulation," in *Proceedings of the7th International Colloquium on Bluff Body Aerodynamics and Applications (BBAA7)*, 2012. 2

[6] D. Laxalde and F. Thouverez, "Complex non-linear modal analysis for mechanical systems: Application to turbomachinery bladings with friction interfaces," *Journal of sound and vibration*, vol. 322, no. 4-5, pp. 1009–1025, 2009. 2

[7] M. O. L. Hansen, J. N. Sørensen, S. Voutsinas, N. Sørensen, and H. A. Madsen, "State of the art in wind turbine aerodynamics and aeroelasticity," *Progress in aerospace sciences*, vol. 42, no. 4, pp. 285–330, 2006. 2

[8] O. H. Amman, T. Von Kármán, and G. B. Woodruff, "The failure of the tacoma narrows bridge," 1941. vii, 2

[9] I. Garrick and W. H. Reed III, "Historical development of aircraft flutter," *Journal of Aircraft*, vol. 18, no. 11, pp. 897–912, 1981. 2, 3, 4

[10] T. A. Weisshaar, "Aeroelasticity, an introduction to fundamental problems-with an historical perspective, examples and homework problems," 2012. vii, 3

[11] F. Lanchester, "Torsional vibrations of the tail of an aeroplane," *Aeronaut. Research Com. R & M*, vol. 276, 1916. 3

[12] L. Bairstow and A. Fage, "Oscillations of the tail plane and body of an aeroplane in flight," *Aeronaut. Research Com. R & M*, vol. 276, 1916. 3

[13] R. L. Bisplinghoff, H. Ashley, and R. L. Halfman, *Aeroelasticity*. Courier Corporation, 2013. 3, 7

[14] H. Glauert, "The force and moment on an oscillating aerofoil. r. & m. no. 1242," *British ARC*, 1929. 3

[15] T. Theodorsen, "General theory of aerodynamic instability and the mechanism of," *Annual Report of the National Advisory Committee for Aeronautics*, vol. 268, p. 413, 1935. 3, 5, 22

[16] L. Mathijssen, "An experimental study on supersonic panel flutter using simultaneous digital image correlation and schlieren," 2022. 3

[17] G. H. Jordan, N. J. McLeod, and L. D. Guy, *Structural Dynamic Experiences of the X-15 Airplane*. National Aeronautics and Space Administration, 1962. 3

[18] A. Boyd, R. Murphy, C. Gurney, G. Minetty, and W. Gillilland, "Aircraft accident report braniff airways, t, le., lockheed slectra, n 9705c, buffalo, texas," tech. rep., SEPTEMBER 29, 1959. Technical report, Civil Aeronautics Board, 1961. 3

[19] A. Boyd, R. Murphy, C. Gurney, G. Minetty, and W. Gillilland, "Aircraft accident report northwest airlines lockheed electra, n 121us, near cannelton, indiana," tech. rep., MARCH 17, 1960. Technical report, Civil Aeronautics Board, 1961. 3

[20] E. Dowell, J. Edwards, and T. Strganac, "Nonlinear aeroelasticity," *Journal of aircraft*, vol. 40, no. 5, pp. 857–874, 2003. 4

[21] R. W. Bunton and C. M. Denegri Jr, "Limit cycle oscillation characteristics of fighter aircraft," *Journal of aircraft*, vol. 37, no. 5, pp. 916–918, 2000. 4

[22] D. Durmuş, *Aeroelastic analysis of variable-span morphing wing*. PhD thesis, Institute of Science And Technology, 2020. vii, 4

[23] J. A. Grauer and M. Boucher, "System identification of flexible aircraft: lessons learned from the x-56a phase 1 flight tests," in *AIAA SciTech 2020 Forum*, p. 1017, 2020. 4

[24] B. Kirsch, O. Montagnier, E. Bénard, and T. M. Faure, "Tightly coupled aeroelastic model implementation dedicated to fast aeroelastic tailoring optimisation of high aspect ratio composite wing," *Journal of Fluids and Structures*, vol. 94, p. 102930, 2020. 4

[25] T. E. Noll, J. M. Brown, M. E. Perez-Davis, S. D. Ishmael, G. C. Tiffany, and M. Gaier, "Investigation of the helios prototype aircraft mishap volume i mishap report," *Downloaded on*, vol. 9, p. 2004, 2004. vii, 4

[26] J. J. Ryan and J. T. Bosworth, "Current and future research in active control of lightweight, flexible structures using the x-56 aircraft," in *52nd Aerospace Sciences Meeting*, p. 0597, 2014. 4

[27] F. S. Tse, I. E. Morse, and R. T. Hinkle, *Mechanical vibrations*. Allyn and Bacon Boston, 1963. 5

[28] W. T. Thomson, *Theory of vibration with applications*. CrC Press, 2018. 5

[29] C. Nitschke, A. Vincenti, and J.-C. Chassaing, "Influence of stochastic perturbations of composite laminate layups on the aeroelastic flutter of a cantilevered plate wing," *Composite Structures*, vol. 220, pp. 809–826, 2019. vii, 5, 9, 12, 22, 36, 89, 92, 110, 134

[30] C. T. Nitschke, P. Cinnella, D. Lucor, and J.-C. Chassaing, "Model-form and predictive uncertainty quantification in linear aeroelasticity," *Journal of Fluids and Structures*, vol. 73, pp. 137–161, 2017. 5, 10, 22

[31] C. Scarth and J. E. Cooper, "Reliability-based aeroelastic design of composite plate wings using a stability margin," *Structural and Multidisciplinary Optimization*, vol. 57, no. 4, pp. 1695–1709, 2018. 5, 11, 14, 108, 110, 134

[32] M. Goland, "The flutter of a uniform cantilever wing," *Journal of Applied Mechanics*, 1945. 5

[33] E. H. Dowell and H. Voss, "Theoretical and experimental panel flutter studies in the mach number range 1.0 to 5.0.," *AIAA Journal*, vol. 3, no. 12, pp. 2292–2304, 1965. 5

[34] E. H. Dowell, "Flutter of infinitely long plates and shells. i-plate.," *AIAA journal*, vol. 4, no. 8, pp. 1370–1377, 1966. 5

[35] E. H. Dowell, "Panel flutter-a review of the aeroelastic stability of plates and shells," *AIAA journal*, vol. 8, no. 3, pp. 385–399, 1970. 5, 144

[36] B. J. Landsberger and J. Dugundji, "Experimental aeroelastic behavior of unswept and forward-swept cantilever graphite/epoxy wings," *Journal of Aircraft*, vol. 22, pp. 679–686, Aug. 1985. 5

[37] M. N. Bismarck-Nasr, "Finite element analysis of aeroelasticity of plates and shells," *Applied Mechanics Reviews*, vol. 45, no. 12, 1992. 5

[38] P. A. de Carvalho Pastilha, "Structural optimization for flutter instability problems," 2007. 5

[39] A. H. Modaress-Aval, F. Bakhtiari-Nejad, E. H. Dowell, H. Shahverdi, H. Rostami, and D. A. Peters, "Aeroelastic analysis of cantilever plates using peters' aerodynamic model, and the influence of choosing beam or plate theories as the structural model," *Journal of Fluids and Structures*, vol. 96, p. 103010, 2020. 5

[40] C. V. Jutte, B. K. Stanford, and C. D. Wieseman, "Internal structural design of the common research model wing box for aeroelastic tailoring," tech. rep., 2015. 5

[41] H. Wagner, "Über die entstehung des dynamischen auftriebes von tragflügeln," *Journal of Applied Mathematics and Mechanics*, 1924. 5

[42] R. T. Jones, "Operational treatment of the nonuniform-lift theory in airplane dynamics," tech. rep., 1938. 5

[43] S. Shams, H. Haddadpour, M. S. Lahidjani, and M. Kheiri, "An analytical method in computational aeroelasticity based on wagner function," in *25th International Congress of the Aeronautical Science, Hamburg, Germany*, 2006. 5

[44] D. A. Peters, S. Karunamoorthy, and W.-M. Cao, "Finite state induced flow models. i-two-dimensional thin airfoil," *Journal of aircraft*, vol. 32, no. 2, pp. 313–322, 1995. 6

[45] E. Albano and W. P. Rodden, "A doublet-lattice method for calculating lift distributions on oscillating surfaces in subsonic flows.," *AIAA journal*, vol. 7, no. 2, pp. 279–285, 1969. 6, 22

[46] M. Petrolo, "Flutter analysis of composite lifting surfaces by the 1d carrera unified formulation and the doublet lattice method," *Composite Structures*, vol. 95, pp. 539–546, 2013. 6

[47] A. Pagani, M. Petrolo, and E. Carrera, "Flutter analysis by refined 1d dynamic stiffness elements and doublet lattice method," *Advances in aircraft and spacecraft science*, vol. 1, no. 3, p. 291, 2014. 6

[48] M. Parenteau and E. Laurendeau, "A general modal frequency-domain vortex lattice method for aeroelastic analyses," *Journal of Fluids and Structures*, vol. 99, p. 103146, 2020. 6

[49] C. de Souza, R. G. da Silva, and C. Cesnik, "Nonlinear aeroelastic framework based on vortex-lattice method and corotational shell finite element," in *53rd AIAA/ASME/ASCE/AHS/ASC Structures, Structural Dynamics and Materials Conference 20th AIAA/ASME/AHS Adaptive Structures Conference 14th AIAA*, p. 1976, 2012. 6

[50] G. Dimitriadis, N. Giannelis, and G. Vio, "A modal frequency-domain generalised force matrix for the unsteady vortex lattice method," *Journal of Fluids and Structures*, vol. 76, pp. 216–228, 2018. 6

[51] S. D. Pesmajoglou and J. Graham, "Prediction of aerodynamic forces on horizontal axis wind turbines in free yaw and turbulence," *Journal of Wind Engineering and Industrial Aerodynamics*, vol. 86, no. 1, pp. 1–14, 2000. 6

[52] B. K. Stanford and K. E. Jacobson, "Transonic aeroelastic modeling of the naca 0012 benchmark wing," *AIAA Journal*, vol. 59, no. 10, pp. 4134–4143, 2021. 6

[53] M. Smith, M. Patil, and D. Hodges, "Cfd-based analysis of nonlinear aeroelastic behavior of high-aspect ratio wings," in *19th AIAA Applied Aerodynamics Conference*, p. 1582, 2001. 6

[54] T. Tamura and Y. Ono, "Les analysis on aeroelastic instability of prisms in turbulent flow," *Journal of wind engineering and industrial aerodynamics*, vol. 91, no. 12-15, pp. 1827–1846, 2003. 6

[55] P. S. Beran, D. J. Lucia, and C. L. Pettit, "Reduced-order modelling of limit-cycle oscillation for aeroelastic systems," *Journal of Fluids and Structures*, vol. 19, no. 5, pp. 575–590, 2004. 6

[56] A. S. Thelen, L. T. Leifsson, and P. S. Beran, "Aeroelastic flutter prediction using multi-fidelity modeling of the aerodynamic influence coefficients," in *AIAA Scitech 2019 Forum*, p. 0609, 2019. 6

[57] R. ROSENBAUM and R. H. SCANLAN, "A note on flight flutter testing," *Journal of the Aeronautical Sciences*, vol. 15, no. 6, pp. 366–370, 1948. 6

[58] H. J. Hassig, "An approximate true damping solution of the flutter equation by determinant iteration.," *Journal of Aircraft*, vol. 8, no. 11, pp. 885–889, 1971. 7

[59] W. P. Rodden, R. L. Harder, and E. D. Bellinger, *Aeroelastic addition to NASTRAN*, vol. 3094. National Aeronautics and Space Administration, Scientific and Technical Information Branch, 1979. 7, 14

[60] M. Kameyama and H. Fukunaga, "Optimum design of composite plate wings for aeroelastic characteristics using lamination parameters," *Computers & structures*, vol. 85, no. 3-4, pp. 213–224, 2007. 7, 8, 9, 41

[61] R. M. Ajaj, E. I. Saavedra Flores, M. Amoozgar, and J. E. Cooper, "A parametric study on the aeroelasticity of flared hinge folding wingtips," *Aerospace*, vol. 8, no. 8, p. 221, 2021. 7

[62] D. Borglund, "Robust aeroelastic stability analysis considering frequency-domain aerodynamic uncertainty," *Journal of aircraft*, vol. 40, no. 1, pp. 189–193, 2003. 7

[63] D. Pitt, "A new non-iterative pk match point flutter solution," in *40th Structures, Structural Dynamics, and Materials Conference and Exhibit*, p. 1353, 1999. 7

[64] W. G. Roeseler, B. Sarh, M. U. Kismarton, J. Quinlivan, J. Sutter, and D. Roberts, "Composite structures: the first 100 years," in *16th International Conference on Composite Materials*, pp. 1–41, Japan Society for Composite Materials Kyoto, Japan, 2007. 7

[65] L. P. Kollar and G. S. Springer, *Mechanics of composite structures*. Cambridge university press, 2003. vii, 7

[66] P. Vannucci, "General anisotropic elasticity," in *Anisotropic Elasticity*, pp. 19–73, Springer, 2018. 8

[67] K.-J. Lin, P.-J. Lu, and J.-Q. Tarn, "Flutter analysis of cantilever composite plates in subsonic flow," *AIAA journal*, vol. 27, no. 8, pp. 1102–1109, 1989. 8

[68] M. Mahran, A. ELsabbagh, and H. Negm, "A comparison between different finite elements for elastic and aero-elastic analyses," *Journal of advanced research*, vol. 8, no. 6, pp. 635–648, 2017. 8

[69] C. Scarth, J. E. Cooper, P. M. Weaver, and G. Silva, "Uncertainty quantification of aeroelastic stability of composite plate wings using lamination parameters," *Composite Structures*, vol. 116, pp. 84–93, Sept. 2014. 8, 9, 18, 33, 45, 89

[70] K. Koo and I. Lee, "Aeroelastic behavior of a composite plate wing with structural damping," *Computers & structures*, vol. 50, no. 2, pp. 167–176, 1994. 8

[71] G. Karpouzian and L. Librescu, "Nonclassical effects on divergence and flutter of anisotropic swept aircraft wings," *AIAA journal*, vol. 34, no. 4, pp. 786–794, 1996. 8

[72] R. K. Kapania and S. Raciti, "Recent advances in analysis of laminated beams and plates. part i-sheareffects and buckling.," *AIAA journal*, vol. 27, no. 7, pp. 923–935, 1989. 8

[73] A. Chattopadhyay, S. Zhang, and R. Iha, "Structural and aeroelastic analysis of composite wing box sections using higher-order laminate theory," in *37th Structure, Structural Dynamics and Materials Conference*, p. 1567, 1996. 8

[74] M. Patil, D. Hodges, and C. Cesnik, "Nonlinear aeroelastic analysis of aircraft with high-aspect-ratio wings," in *39th AIAA/ASME/ASCE/AHS/ASC Structures, Structural Dynamics, and Materials Conference and Exhibit*, p. 1955, 1998. 8

[75] S. W. Tsai and H. T. Hahn, *Introduction to composite materials*. Lancaster, Pa.: Technomic Publ, 1980. 8, 33

[76] G. Verchery, "Les invariants des tenseurs d'ordre 4 du type de l'élasticité," in *Comportment Méchanique des Solides Anisotropes*, vol. 115, (Villard-de-Lans), pp. 93–104, Editions du CNRS, Paris, 1979. 8, 31

[77] S. W. Tsai and N. J. Pagano, "Invariant properties of composite materials," tech. rep., AIR FORCE MATERIALS LAB WRIGHT-PATTERSON AFB OH WRIGHT-PATTERSON AFB, 1968. 8

[78] S. Nagendra, S. Kodiyalam, J. Davis, and V. Parthasarathy, "Optimization of tow fiber paths for composite design," in *36th structures, structural dynamics and materials conference*, p. 1275, 1995. 9

[79] M. Montemurro and A. Catapano, "On the effective integration of manufacturability constraints within the multi-scale methodology for designing variable angle-tow laminates," *composite structures*, vol. 161, pp. 145–159, 2017. 9, 10, 36, 41, 59, 67

[80] M. Montemurro and A. Catapano, "A general b-spline surfaces theoretical framework for optimisation of variable angle-tow laminates," *Composite Structures*, vol. 209, pp. 561–578, 2019. 9, 36, 41, 67

[81] T. R. Brooks and J. R. Martins, "On manufacturing constraints for tow-steered composite design optimization," *Composite structures*, vol. 204, pp. 548–559, 2018. vii, 9

[82] A. Viglietti, E. Zappino, and E. Carrera, "Free vibration analysis of variable angle-tow composite wing structures," *Aerospace Science and Technology*, vol. 92, pp. 114–125, 2019. 10, 87

[83] D. Pereira, T. Sales, and D. Rade, "Multi-objective frequency and damping optimization of tow-steered composite laminates," *Composite Structures*, vol. 256, p. 112932, 2021. 10

[84] M. Montemurro and A. Catapano, "A new paradigm for the optimum design of variable angle tow laminates," in *Variational analysis and aerospace engineering*, pp. 375–400, Springer, 2016. 10, 15

[85] O. Stodieck, J. E. Cooper, P. M. Weaver, and P. Kealy, "Improved aeroelastic tailoring using tow-steered composites," *Composite Structures*, vol. 106, pp. 703–715, Dec. 2013. 10, 18, 20, 45

[86] H. Haddadpour and Z. Zamani, "Curvilinear fiber optimization tools for aeroelastic design of composite wings," *Journal of Fluids and Structures*, vol. 33, pp. 180–190, 2012. 10, 67, 87

[87] T. A. Guimarães, S. G. Castro, C. E. Cesnik, and D. A. Rade, "Supersonic flutter and buckling optimization of tow-steered composite plates," *AIAA Journal*, vol. 57, no. 1, pp. 397–407, 2019. 10

[88] T. R. Brooks, J. R. Martins, and G. J. Kennedy, "High-fidelity aerostructural optimization of tow-steered composite wings," *Journal of Fluids and Structures*, vol. 88, pp. 122–147, 2019. 10

[89] S. Setoodeh, M. M. Abdalla, and Z. Gürdal, "Design of variable–stiffness laminates using lamination parameters," *Composites Part B: Engineering*, vol. 37, no. 4-5, pp. 301–309, 2006. 10

[90] M. Montemurro, A. Vincenti, and P. Vannucci, "A two-level procedure for the global optimum design of composite modular structures—application to the design of an aircraft wing," *Journal of Optimization Theory and Applications*, vol. 155, no. 1, pp. 1–23, 2012. 10

[91] M. Montemurro, A. Vincenti, and P. Vannucci, "A Two-Level Procedure for the Global Optimum Design of Composite Modular Structures — Application to the Design of an Aircraft Wing: Part 2: Numerical Aspects and Examples," *Journal of Optimization Theory and Applications*, vol. 155, pp. 24–53, Oct. 2012. 10, 43

[92] M. A. Albazzan, R. Harik, B. F. Tatting, and Z. Gürdal, "Efficient design optimization of non-conventional laminated composites using lamination parameters: A state of the art," *Composite Structures*, vol. 209, pp. 362–374, 2019. 10, 13

[93] S. Setoodeh, A. Blom, M. Abdalla, and Z. Gürdal, "Generating curvilinear fiber paths from lamination parameters distribution," in *47th AIAA/ASME/ASCE/AHS/ASC Structures, Structural Dynamics, and Materials Conference 14th AIAA/ASME/AHS Adaptive Structures Conference 7th*, p. 1875, 2006. 10

[94] S. Kucherenko, D. Albrecht, and A. Saltelli, "Exploring multi-dimensional spaces: A comparison of latin hypercube and quasi monte carlo sampling techniques," *arXiv preprint arXiv:1505.02350*, 2015. 11

[95] S. Kawai and K. Shimoyama, "Kriging-model-based uncertainty quantification in computational fluid dynamics," in *32nd AIAA Applied Aerodynamics Conference*, p. 2737, 2014. vii, 11

[96] N. Wiener, "The Homogeneous Chaos," *American Journal of Mathematics*, vol. 60, no. 4, pp. pp. 897–936, 1938. 11, 89

[97] D. Xiu and G. E. Karniadakis, "Modeling uncertainty in steady state diffusion problems via generalized polynomial chaos," *Computer Methods in Applied Mechanics and Engineering*, vol. 191, pp. 4927–4948, Sept. 2002. 11

[98] A. Manan and J. Cooper, "Design of composite wings including uncertainties: a probabilistic approach," *Journal of Aircraft*, vol. 46, no. 2, pp. 601–607, 2009. 11, 14

[99] S. Murugan, R. Chowdhury, S. Adhikari, and M. Friswell, "Helicopter aeroelastic analysis with spatially uncertain rotor blade properties," *Aerospace Science and Technology*, vol. 16, no. 1, pp. 29–39, 2012. 11

[100] C. Scarth, P. N. Sartor, J. E. Cooper, P. M. Weaver, and G. H. C. Silva, "Robust and Reliability-Based Aeroelastic Design of Composite Plate Wings," *AIAA Journal*, vol. 55, pp. 3539–3552, Oct. 2017. 11, 14, 107

[101] J.-C. Chassaing, D. Lucor, and J. Trégon, "Stochastic nonlinear aeroelastic analysis of a supersonic lifting surface using an adaptive spectral method," *Journal of sound and vibration*, vol. 331, no. 2, pp. 394–411, 2012. 12

[102] W. Becker, K. Worden, and J. Rowson, "Bayesian sensitivity analysis of bifurcating nonlinear models," *Mechanical Systems and Signal Processing*, vol. 34, no. 1-2, pp. 57–75, 2013. 12

[103] J. Ashton and M. Waddoups, "Analysis of Anisotropic Plates," *Journal of Composite Materials*, vol. 3, pp. 148–165, Jan. 1969. 12

[104] Noor, A. K., "Free vibrations of multilayered composite plates.," *AIAA Journal*, vol. 11, pp. 1038–1039, July 1973. 12

[105] D. X. Lin, R. G. Ni, and R. Adams, "Prediction and measurement of the vibrational damping parameters of carbon and glass fibre-reinforced plastics plates," *Journal of composite materials*, vol. 18, no. 2, pp. 132–152, 1984. 12

[106] Y. Narita and A. W. Leissa, "Buckling studies for simply supported symmetrically laminated rectangular plates," *International Journal of Mechanical Sciences*, vol. 32, no. 11, pp. 909–924, 1990. 12

[107] N. Khot, V. Venkayya, C. Johnson, and V. Tischler, "Optimization of fiber reinforced composite structures," *International Journal of Solids and Structures*, vol. 9, no. 10, pp. 1225–1236, 1973. 12

[108] Y. Nshanian and M. Pappas, "Optimal laminated composite shells for buckling and vibration," *AIAA journal*, vol. 21, no. 3, pp. 430–437, 1983. 12

[109] S. Adali, "Optimization of fibre reinforced composite laminates subject to fatigue loading," in *Composite Structures 3*, pp. 43–55, Springer, 1985. 12

[110] R. Ramkumar and T. Weisshaar, "Flutter of flat rectangular anisotropic plates in high mach number supersonic flow," *Journal of Sound and Vibration*, vol. 50, pp. 587–597, Feb. 1977. 12

[111] T. A. Weisshaar, "Aeroelastic Tailoring of Forward Swept Composite Wings," *Journal of Aircraft*, vol. 18, pp. 669–676, Aug. 1981. 12

[112] D. Sadagopan and R. Pitchumani, "Application of genetic algorithms to optimal tailoring of composite materials," *Composites Science and Technology*, vol. 58, no. 3-4, pp. 571–589, 1998. 12, 13

[113] F. Eastep, V. Tischler, V. Venkayya, and N. Khot, "Aeroelastic tailoring of composite structures," *Journal of aircraft*, vol. 36, no. 6, pp. 1041–1047, 1999. 12

[114] S. Guo, W. Cheng, and D. Cui, "Aeroelastic tailoring of composite wing structures by laminate layup optimization," *Aiaa Journal*, vol. 44, no. 12, pp. 3146–3150, 2006. 12, 42

[115] S. Guo, D. Li, and Y. Liu, "Multi-objective optimization of a composite wing subject to strength and aeroelastic constraints," *Proceedings of the Institution of Mechanical Engineers, Part G: Journal of Aerospace Engineering*, vol. 226, no. 9, pp. 1095–1106, 2012. 13

[116] A. Attaran, D. Majid, S. Basri, A. Mohd Rafie, and E. Abdullah, "Structural optimization of an aeroelastically tailored composite flat plate made of woven fiberglass/epoxy," *Acta mechanica*, vol. 196, no. 3, pp. 161–173, 2008. 13

[117] J. Grenestedt and P. Gudmundson, "Layup optimization of composite material structures," *Optimal design with advanced materials*, pp. 311–336, 1993. 13

[118] A. Muc, J. Flis, and M. Augustyn, "Optimal design of plated/shell structures under flutter constraints—a literature review," *Materials*, vol. 12, no. 24, p. 4215, 2019. 13, 41, 107

[119] A. Manan, G. Vio, M. Harmin, and J. Cooper, "Optimization of aeroelastic composite structures using evolutionary algorithms," *Engineering Optimization*, vol. 42, no. 2, pp. 171–184, 2010. 13

[120] H. Ghiasi, D. Pasini, and L. Lessard, "Optimum stacking sequence design of composite materials part i: constant stiffness design," *Composite Structures*, vol. 90, no. 1, pp. 1–11, 2009. 13

[121] H. Ghiasi, K. Fayazbakhsh, D. Pasini, and L. Lessard, "Optimum stacking sequence design of composite materials part ii: Variable stiffness design," *Composite structures*, vol. 93, no. 1, pp. 1–13, 2010. 13

[122] A. Vincenti, M. R. Ahmadian, and P. Vannucci, "Bianca: a genetic algorithm to solve hard combinatorial optimisation problems in engineering," *Journal of Global Optimization*, vol. 48, no. 3, pp. 399–421, 2010. 13, 47

[123] A. Vincenti, M. R. Ahmadian, and P. Vannucci, "Optimization of laminated composites by using genetic algorithm and the polar description of plane anisotropy," *Mechanics of Advanced Materials and Structures*, vol. 20, no. 3, pp. 242–255, 2013. 13

[124] A. Catapano, B. Desmorat, and P. Vannucci, "Stiffness and strength optimization of the anisotropy distribution for laminated structures," *Journal of Optimization Theory and Applications*, vol. 167, no. 1, pp. 118–146, 2015. 13

[125] R. L. Riche and R. T. Haftka, "Optimization of laminate stacking sequence for buckling load maximization by genetic algorithm," *AIAA journal*, vol. 31, no. 5, pp. 951–956, 1993. 13

[126] N. Kogiso, L. T. Watson, Z. Gürdal, R. T. Haftka, and S. Nagendra, "Design of composite laminates by a genetic algorithm with memory," *MECHANICS OF COMPOSITE MATERIALS AND STRUCTURES An International Journal*, vol. 1, no. 1, pp. 95–117, 1994. 13

[127] S. Nagendra, D. Jestin, Z. Gürdal, R. T. Haftka, and L. T. Watson, "Improved genetic algorithm for the design of stiffened composite panels," *Computers & Structures*, vol. 58, no. 3, pp. 543–555, 1996. 13

[128] J. Park, J. Hwang, C. Lee, and W. Hwang, "Stacking sequence design of composite laminates for maximum strength using genetic algorithms," *Composite Structures*, vol. 52, no. 2, pp. 217–231, 2001. 13

[129] T. N. Massard, "Computer sizing of composite laminates for strength," *Journal of reinforced plastics and composites*, vol. 3, no. 4, pp. 300–345, 1984. 13

[130] B. Farshi and R. Rabiei, "Optimum design of composite laminates for frequency constraints," *Composite structures*, vol. 81, no. 4, pp. 587–597, 2007. 13

[131] M. Montemurro, A. Pagani, G. A. Fiordilino, J. Pailhès, and E. Carrera, "A general multi-scale two-level optimisation strategy for designing composite stiffened panels," *Composite Structures*, vol. 201, pp. 968–979, 2018. 13

[132] X. Liu, C. A. Featherston, and D. Kennedy, "Buckling optimization of blended composite structures using lamination parameters," *Thin-Walled Structures*, vol. 154, p. 106861, 2020. 13

[133] M. Nikbay and P. Acar, "Robust aeroelastic design optimization of wing/store configurations based on flutter criteria," in *12th AIAA aviation technology, integration, and operations (ATIO) conference and 14th AIAA/ISSMO multidisciplinary analysis and optimization conference*, p. 5455, 2012. 14

[134] C. L. Pettit and R. V. Grandhi, "Optimization of a wing structure for gust response and aileron effectiveness," *Journal of aircraft*, vol. 40, no. 6, pp. 1185–1191, 2003. 14

[135] B. Stanford and P. Beran, "Computational strategies for reliability-based structural optimization of aeroelastic limit cycle oscillations," *Structural and Multidisciplinary Optimization*, vol. 45, no. 1, pp. 83–99, 2012. 14

[136] M. Allen and K. Maute, "Reliability-based design optimization of aeroelastic structures," *Structural and Multidisciplinary Optimization*, vol. 27, no. 4, pp. 228–242, 2004. 14

[137] M. F. Othman, G. H. Silva, P. H. Cabral, A. P. Prado, A. Pirrera, and J. E. Cooper, "A robust and reliability-based aeroelastic tailoring framework for composite aircraft wings," *Composite Structures*, vol. 208, pp. 101–113, 2019. 14

[138] W. Stein, "A summary of Classical Lamination Theory." 2010. 18

[139] M. D. Minich and C. C. Chamis, "Analytical displacements and vibrations of cantilevered unsymmetric fiber composite laminates," in *AIAA, ASME, and SAE, Structures, Structural Dynamics, and Materials Conference*, (Denver, Colorado), Jan. 1975. 20

[140] A. W. Leissa, "The free vibration of rectangular plates," *Journal of Sound and Vibration*, vol. 31, pp. 257–293, Dec. 1973. 20

[141] J. S. Hale, M. Brunetti, S. P. Bordas, and C. Maurini, "Simple and extensible plate and shell finite element models through automatic code generation tools," *Computers & Structures*, vol. 209, pp. 163–181, 2018. 21

[142] A. Logg and G. N. Wells, "Dolfin: Automated finite element computing," *ACM Transactions on Mathematical Software (TOMS)*, vol. 37, no. 2, pp. 1–28, 2010. 21

[143] A. Logg, K.-A. Mardal, and G. Wells, *Automated solution of differential equations by the finite element method: The FEniCS book*, vol. 84. Springer Science & Business Media, 2012. 21

[144] G. P. Guruswamy, "Unsteady aerodynamic and aeroelastic calculations for wings using euler equations," *AIAA journal*, vol. 28, no. 3, pp. 461–469, 1990. 22

[145] D. M. Schuster, J. Vadyak, and E. Atta, "Static aeroelastic analysis of fighter aircraft using a three-dimensional navier-stokes algorithm," *Journal of Aircraft*, vol. 27, no. 9, pp. 820–825, 1990. 22

[146] L. Morino and C.-C. Kuo, "Subsonic potential aerodynamics for complex configurations: a general theory," *AIAA journal*, vol. 12, no. 2, pp. 191–197, 1974. 22

[147] L. H. van Zyl, "Convergence of the subsonic doublet lattice method," *Journal of aircraft*, vol. 35, no. 6, pp. 977–979, 1998. 23

[148] M. L. Guertin, *The application of finite element methods to aeroelastic lifting surface flutter*. Rice University, 2012. 25

[149] S. J. Hollowell and J. Dugundji, "Aeroelastic flutter and divergence of stiffness coupled, graphite/epoxy cantilevered plates," *Journal of Aircraft*, vol. 21, no. 1, pp. 69–76, 1984. vii, xvii, 28, 29, 30

[150] P. Vannucci, "Plane Anisotropy by the Polar Method," *Meccanica*, vol. 40, pp. 437–454, Dec. 2005. xvii, 31, 32, 33, 34, 35, 37, 73

[151] Z. Gurdal, R. Haftka, and P. Hajela, *Design and optimization of laminated composite materials*. New York: Wiley, 1999. 33

[152] P. Vannucci, "A Special Planar Orthotropic Material," *Journal of elasticity and the physical science of solids*, vol. 67, no. 2, pp. 81–96, 2002. 34

[153] P. Vannucci, X. Gong, and G. Verchery, "Determination des stratifies quasi-homogènes par l'approche polaire," *Comptes-rendus Onzième Journées Nationales sur les Matériaux Composites, JNC11, à Arcachon*, pp. 18–20, 1998. 36

[154] P. Vannucci and G. Verchery, "A special class of uncoupled and quasi-homogeneous laminates," *Composites Science and Technology*, vol. 61, no. 10, pp. 1465–1473, 2001. 36

[155] P. Vannucci and G. Verchery, "Stiffness design of laminates using the polar method," *International Journal of Solids and Structures*, vol. 38, no. 50-51, pp. 9281–9294, 2001. 36

[156] Y. Narita, "Layerwise optimization for the maximum fundamental frequency of laminated composite plates," *Journal of Sound and Vibration*, vol. 263, no. 5, pp. 1005–1016, 2003. 42

[157] Y. Narita and J. Hodgkinson, "Layerwise optimisation for maximising the fundamental frequencies of point-supported rectangular laminated composite plates," *Composite Structures*, vol. 69, no. 2, pp. 127–135, 2005. 42

[158] O. Erdal and F. O. Sonmez, "Optimum design of composite laminates for maximum buckling load capacity using simulated annealing," *Composite Structures*, vol. 71, no. 1, pp. 45–52, 2005. 43

[159] M. Moakher, "On the averaging of symmetric positive-definite tensors," *Journal of Elasticity*, vol. 82, no. 3, pp. 273–296, 2006. 59

[160] O. Stodieck, J. Cooper, P. Weaver, and P. Kealy, "Aeroelastic tailoring of a representative wing box using tow-steered composites," *AIAA journal*, vol. 55, no. 4, pp. 1425–1439, 2017. 67

[161] L. Piegl and W. Tiller, *The NURBS book*. Springer Science & Business Media, 1996. 68

[162] M. I. Izzi, A. Catapano, and M. Montemurro, "Strength and mass optimisation of variable-stiffness composites in the polar parameters space," *Structural and Multidisciplinary Optimization*, vol. 64, no. 4, pp. 2045–2073, 2021. 71

[163] M. Montemurro, G. A. Fiordilino, and E. Carrera, "Multi-level optimisation of composite structures through a global-local modelling approach based on high-order theories," *Computers & Structures*, vol. 275, p. 106932, 2023. viii, 71, 72

[164] B. Sudret, "Global sensitivity analysis using polynomial chaos expansions," *Reliability engineering & system safety*, vol. 93, no. 7, pp. 964–979, 2008. 89

[165] D. Xiu and G. E. Karniadakis, "Modeling uncertainty in flow simulations via generalized polynomial chaos," *Journal of computational physics*, vol. 187, no. 1, pp. 137–167, 2003. 89

[166] C. Scarth and S. Adhikari, "Modeling spatially varying uncertainty in composite structures using lamination parameters," *AIAA Journal*, vol. 55, no. 11, pp. 3951–3965, 2017. 97

[167] T. de Larrard, J.-B. Colliat, F. Benboudjema, J.-M. Torrenti, and G. Nahas, "Effect of the young modulus variability on the mechanical behaviour of a nuclear containment vessel," *Nuclear engineering and Design*, vol. 240, no. 12, pp. 4051–4060, 2010. 97

[168] T. A. Guimarães, H. L. Silva, D. A. Rade, and C. E. Cesnik, "Aeroelastic stability of conventional and tow-steered composite plates under stochastic fiber volume," *AIAA Journal*, vol. 58, no. 6, pp. 2748–2759, 2020. 97

[169] K. Phoon, S. Huang, and S. Quek, "Implementation of karhunen–loeve expansion for simulation using a wavelet-galerkin scheme," *Probabilistic Engineering Mechanics*, vol. 17, no. 3, pp. 293–303, 2002. 100

[170] R. Ghanem and P. D. Spanos, *Stochastic finite elements: a spectral approach*. New York: Springer-Verlag, 1991. 100

[171] C. Zang, M. Friswell, and J. Mottershead, "A review of robust optimal design and its application in dynamics," *Computers & structures*, vol. 83, no. 4-5, pp. 315–326, 2005. 107

[172] S.-K. Choi, R. A. Canfield, and R. V. Grandhi, *Reliability-Based Structural Optimization*. Springer, 2007. 107

[173] C. Rasmussen, "Cki williams gaussian processes for machine learning," 2006. 108

[174] E. Schulz, M. Speekenbrink, and A. Krause, "A tutorial on gaussian process regression: Modelling, exploring, and exploiting functions," *Journal of Mathematical Psychology*, vol. 85, pp. 1–16, 2018. 109

[175] M. Pastor, M. Binda, and T. Harčarik, "Modal assurance criterion," *Procedia Engineering*, vol. 48, pp. 543–548, 2012. 111

[176] C. Beaverstock, M. Friswell, S. Adhikari, T. Richardson, and J. Du Bois, "Automatic mode tracking for flight dynamic analysis using a spanning algorithm," *Aerospace Science and Technology*, vol. 47, pp. 54–67, 2015. 111

[177] M. Montemurro, P. Vannucci, and A. Vincenti, "Bianca, a genetic algorithm for engineering optimisation - user guide," 03 2011. 119

[178] J. Murua, P. Martínez, H. Climent, L. van Zyl, and R. Palacios, "T-tail flutter: Potential-flow modelling, experimental validation and flight tests," *Progress in Aerospace Sciences*, vol. 71, pp. 54–84, 2014. 143

[179] R. Bombardieri, R. Cavallaro, R. Castellanos, and F. Auricchio, "On the dynamic fluid–structure stability response of an innovative airplane configuration," *Journal of Fluids and Structures*, vol. 105, p. 103347, 2021. 143

[180] L. H. Van Zyl and E. H. Mathews, "Aeroelastic analysis of t-tails using an enhanced doublet lattice method," *Journal of Aircraft*, vol. 48, no. 3, pp. 823–831, 2011. 144

[181] W.-W. Zhang, Z.-Y. Ye, C.-A. Zhang, and F. Liu, "Supersonic flutter analysis based on a local piston theory," *AIAA Journal*, vol. 47, no. 10, pp. 2321–2328, 2009. 144

[182] H. F. Ganji and E. H. Dowell, "Panel flutter prediction in two dimensional flow with enhanced piston theory," *Journal of Fluids and Structures*, vol. 63, pp. 97–102, 2016. 144

[183] Z. Zhang, S. Yang, and P. Chen, "Linearized euler solver for rapid frequency-domain aeroelastic analysis," *Journal of Aircraft*, vol. 49, no. 3, pp. 922–932, 2012. 144

[184] H.-P. Kersken, G. Ashcroft, C. Frey, N. Wolfrum, and D. Korte, "Nonreflecting boundary conditions for aeroelastic analysis in time and frequency domain 3d rans solvers," in *Turbo Expo: Power for Land, Sea, and Air*, vol. 45615, p. V02BT39A010, American Society of Mechanical Engineers, 2014. 144

[185] R. H. Scanlan and J. J. Tomko, "Airfoil and bridge deck flutter derivatives," *Journal of the engineering mechanics division*, vol. 97, no. 6, pp. 1717–1737, 1971. 144

[186] O. Le Maıtre, R. Scanlan, and O. Knio, "Estimation of the flutter derivatives of an naca airfoil by means of navier–stokes simulation," *Journal of Fluids and Structures*, vol. 17, no. 1, pp. 1–28, 2003. 144

[187] M. Berci and F. Torrigiani, "Multifidelity sensitivity study of subsonic wing flutter for hybrid approaches in aircraft multidisciplinary design and optimisation," *Aerospace*, vol. 7, no. 11, p. 161, 2020. 144

[188] A. S. Thelen, L. T. Leifsson, and P. S. Beran, "Multifidelity flutter prediction using local corrections to the generalized aic," *Aerospace Science and Technology*, vol. 106, p. 106032, 2020. 144

[189] A. N. Marques, M. M. Opgenoord, R. R. Lam, A. Chaudhuri, and K. E. Willcox, "Multifidelity method for locating aeroelastic flutter boundaries," *AIAA Journal*, vol. 58, no. 4, pp. 1772–1784, 2020. 144

[190] M. P. Rumpfkeil and P. Beran, "Multi-fidelity surrogate models for flutter database generation," *Computers & Fluids*, vol. 197, p. 104372, 2020. 144

[191] D. Leusink, D. Alfano, and P. Cinnella, "Multi-fidelity optimization strategy for the industrial aerodynamic design of helicopter rotor blades," *Aerospace Science and Technology*, vol. 42, pp. 136–147, 2015. 144

[192] H. Hoenlinger, J. Krammer, and M. Stettner, "Mdo technology needs in aeroelastic structural design," in *7th AIAA/USAF/NASA/ISSMO Symposium on Multidisciplinary Analysis and Optimization*, p. 4731, 1998. 144

[193] R. Huang, Y. Zhao, and H. Hu, "Wind-tunnel tests for active flutter control and closed-loop flutter identification," *AIAA Journal*, vol. 54, no. 7, pp. 2089–2099, 2016. 145

[194] Z. Yan, S. A. Ragab, and M. R. Hajj, "Passive control of transonic flutter with a nonlinear energy sink," *Nonlinear Dynamics*, vol. 91, no. 1, pp. 577–590, 2018. 145

[195] X. Chen and A. Kareem, "Efficacy of tuned mass dampers for bridge flutter control," *Journal of Structural Engineering*, vol. 129, no. 10, pp. 1291–1300, 2003. 145

[196] S. Raja, A. Pashilkar, R. Sreedeep, and J. Kamesh, "Flutter control of a composite plate with piezoelectric multilayered actuators," *Aerospace Science and Technology*, vol. 10, no. 5, pp. 435–441, 2006. 145

[197] J. Theis, H. Pfifer, and P. J. Seiler, "Robust control design for active flutter suppression," in *AIAA Atmospheric Flight Mechanics Conference*, p. 1751, 2016. 145

[198] M. R. Waszak, "Robust multivariable flutter suppression for benchmark active control technology wind-tunnel model," *Journal of Guidance, Control, and Dynamics*, vol. 24, no. 1, pp. 147–153, 2001. 145